

DANIEL S. NIELSEN  
PhD thesis, Niels Bohr Institute, University of Copenhagen

# IN SEARCH OF NEW HIGGS BOSONS



This thesis has been submitted to the PhD School of The Faculty of Science, University of Copenhagen

SUPERVISOR	Associate Professor Troels C. Petersen, Niels Bohr Institute
CO-SUPERVISOR	Assistant Professor Flavia de Almeida Dias, University of Amsterdam
INTERNAL COMMITTEE MEMBER	Associate Professor Stefania Xella, Niels Bohr Institute
EXTERNAL COMMITTEE MEMBER	Professor Alex Lincoln Read, University of Oslo
EXTERNAL COMMITTEE MEMBER	Professor Peter Christiansen, University of Lund

© Daniel S. Nielsen 2020

In search of new Higgs bosons

PhD Thesis, Niels Bohr Institute, University of Copenhagen

184 pages + bibliography + appendices

Made using pdfL<sup>A</sup>T<sub>E</sub>X with a modified Tufte-L<sup>A</sup>T<sub>E</sub>X package

Available online at <https://gitlab.com/Daniel-Dane/phd-thesis>

Thesis submitted on the 31<sup>st</sup> of October 2020 to the PhD School

*First printing, October 2020*

# Contents

Abstract . . . . .	7
Dansk resumé . . . . .	7
Disclaimer . . . . .	8
Acknowledgments . . . . .	9
Introduction . . . . .	10
<b>I Background</b>	<b>13</b>
<b>1 Theory</b>	<b>15</b>
1.1 The Standard Model of Particle Physics . . . . .	15
1.2 2HDM: Beyond the Standard Model . . . . .	19
1.3 Hadron collider physics . . . . .	27
<b>II Experimental setup</b>	<b>33</b>
<b>2 The ATLAS experiment</b>	<b>35</b>
2.1 The inner detector . . . . .	37
2.1.1 The Pixel and Semiconductor trackers . . . . .	37
2.1.2 The Transition radiation tracker . . . . .	38
2.2 The calorimeters . . . . .	39
2.3 The muon spectrometer . . . . .	40
2.4 Trigger and data acquisition . . . . .	42
<b>3 Reconstruction</b>	<b>43</b>
3.1 Tracks and vertices . . . . .	44
3.2 Electrons . . . . .	45
3.3 Muons . . . . .	47
3.4 Jets . . . . .	48
3.5 Event reconstruction quality . . . . .	50
<b>III Performance analysis: TRT electron identification</b>	<b>51</b>
<b>4 Analysis overview</b>	<b>53</b>
4.1 Particle identification . . . . .	54
<b>5 Selections</b>	<b>57</b>
5.1 Event and lepton selections . . . . .	57
5.1.1 Event pre-selections . . . . .	57
5.1.2 Lepton selections . . . . .	58

5.1.3	Cut-flow for both selections . . . . .	59
5.2	Preparation prior to analysis . . . . .	61
<b>6</b>	<b>Analysis and results</b>	<b>63</b>
6.1	Calibration tuning . . . . .	63
6.2	Correction factors (CFs) . . . . .	65
6.3	Final performance . . . . .	67
6.4	Additional analysis . . . . .	68
6.4.1	ROC curves for different occupancies . . . . .	68
6.4.2	Applying simulation-tuned calibration on data . . . . .	69
<b>7</b>	<b>Discussion</b>	<b>71</b>
<b>IV</b>	<b>Physics analysis: Off-alignment Higgs bosons search</b>	<b>75</b>
<b>8</b>	<b>Analysis overview</b>	<b>77</b>
8.1	Data and simulated samples . . . . .	82
<b>9</b>	<b>Object definitions and preselection</b>	<b>85</b>
9.1	Leptons . . . . .	86
9.2	Jets . . . . .	86
9.3	Overlap removal . . . . .	87
9.4	Event preselection . . . . .	88
<b>10</b>	<b>Object and event selection</b>	<b>89</b>
10.1	Initial event selection . . . . .	90
10.2	Resolving jet combinatorics . . . . .	91
10.2.1	Deriving the selections . . . . .	92
10.2.2	Applying the selections . . . . .	94
10.3	Optimization of the $J$ variable . . . . .	97
10.4	$m_{4q}$ window optimization . . . . .	99
10.4.1	Window optimization in 2D . . . . .	100
10.5	Final selection and summary . . . . .	101
10.5.1	Cut-flow tables . . . . .	104
<b>11</b>	<b>Background modeling</b>	<b>107</b>
11.1	Mismodeling . . . . .	112
11.2	$t\bar{t}$ modeling . . . . .	115
<b>12</b>	<b>Signal modeling</b>	<b>119</b>
12.1	Shape interpolation . . . . .	120
12.1.1	Large-width signals . . . . .	125
12.2	Acceptance interpolation . . . . .	126
<b>13</b>	<b>Systematic uncertainties</b>	<b>129</b>
13.1	Detector uncertainties . . . . .	130
13.1.1	Signal detector uncertainties interpolation . . . . .	133
13.2	Modeling uncertainties on signal . . . . .	133
13.2.1	Scale . . . . .	133
13.2.2	Tune (ISR/FSR/MPI) . . . . .	134

13.2.3 PDF . . . . .	136
13.3 Background modeling uncertainties . . . . .	137
<b>14 Fit model</b>	<b>139</b>
14.1 The likelihood function . . . . .	141
14.2 Model inspection with Asimov . . . . .	143
14.2.1 NP reduction campaign . . . . .	146
14.3 Blinded model inspection with real data . . . . .	147
14.4 Model inspection with real data . . . . .	148
<b>15 Results</b>	<b>153</b>
15.1 Large-width and 2HDM limits . . . . .	157
<b>16 Discussion</b>	<b>161</b>
<b>V Conclusion and bibliography</b>	<b>165</b>
<b>17 Conclusion</b>	<b>167</b>
<b>Bibliography</b>	<b>169</b>
<b>VI Appendix</b>	<b>185</b>
<b>18 Performance analysis</b>	<b>187</b>
18.A Calibration results for all gases and TRT parts . . . . .	188
18.B z-scores between raw and fitted $p_{HT}$ . . . . .	198
18.C Probability ratio on data before and after simulation-tuned fit . . . . .	200
18.D Correction factors (CFs) . . . . .	202
18.E Probabilities for all CF configurations . . . . .	205
18.F CFs for different occupancy intervals . . . . .	206
18.G Performance for different CF configurations . . . . .	211
18.H Momentum to $\gamma$ factor . . . . .	213
18.I Track-based $p_{HT}$ method . . . . .	214
<b>19 Physics analysis</b>	<b>219</b>
19.A "Hardest jets" limits . . . . .	220
19.B Kinematic variables . . . . .	220
19.C Fitted parameterized signals . . . . .	223
19.D Asimov pulls and ranks . . . . .	225
19.E Unblinded post-fits, pull plots, and NP ranks . . . . .	232
19.F Unblinded 1D limit slices . . . . .	243



## Abstract

The abundance of matter to antimatter in the universe is not explained by the Standard Model (SM). Two Higgs Doublet Models (2HDMs), which introduce additional Higgs particles, and in particular the  $A \rightarrow ZH$  channel may partly explain the origin of the matter asymmetry.

A search for the  $A \rightarrow ZH$  signature is done using  $139 \text{ fb}^{-1}$  of integrated luminosity at a center-of-mass energy of  $\sqrt{s} = 13 \text{ TeV}$  recorded by ATLAS during 2015–2018 proton–proton collisions at the LHC. The heavy  $A$  boson ( $300 < m_A < 800 \text{ GeV}$ ) is produced by gluon–gluon fusion. The heavy  $H$  boson ( $200 < m_H < 700 \text{ GeV}$ ) decays to  $WW$  that further decay to  $qqqq$ .  $Z$  decays to a pair of electrons or muons. The individual  $W$  bosons are reconstructed from the final state quarks. Signal shapes are interpolated from Monte Carlo simulations. The rates of known (background) processes are constrained by dedicated control regions in data. No excess above the SM predictions is found. The upper limits at the 95% confidence level for  $\sigma(gg \rightarrow A) \times \text{BR}(A \rightarrow ZH) \times \text{BR}(H \rightarrow WW)$  are set to 0.023–8.9 pb, depending on mass. Using the results and taking the natural width of  $A$  into account, exclusions are placed on the phase space of type-I 2HDMs.

In a separate performance analysis, the electron identification of the ATLAS Transition Radiation Tracker is calibrated using  $Z \rightarrow ee, \mu\mu$  events obtained by the tag and probe method applied to LHC data recorded by ATLAS in 2016 as well as simulated data. The new calibration solves the issue of a rising number of electrons with low probabilities. The background efficiency is reduced by 1.45 (3.31) percentage points in data (simulation) at 95% signal efficiency compared to the previous calibration.

## Dansk resumé

Overvægten af stof i forhold til antistof i universet er ikke forklaret af standardmodellen (SM). To Higgs Doublet-modeller (2HDM'er), der introducerer yderligere Higgs-partikler og især  $A \rightarrow ZH$ -kanalen kan delvist forklare oprindelsen af stofasymmetrien.

En søgning efter  $A \rightarrow ZH$ -signaturen udføres ved hjælp af  $139 \text{ fb}^{-1}$  af integreret luminositet ved en massecenterenergi på  $\sqrt{s} = 13 \text{ TeV}$  optaget af ATLAS under proton–proton-kollisioner ved LHC i løbet af 2015–2018. Den tunge  $A$ -boson ( $300 < m_A < 800 \text{ GeV}$ ) er produceret af gluon–gluon-fusion. Den tunge  $H$ -boson ( $200 < m_H < 700 \text{ GeV}$ ) henfalder til  $WW$ , der yderligere henfalder til  $qqqq$ .  $Z$  henfalder til et elektron- eller muonpar. De enkelte  $W$ -bosoner rekonstrueres af kvarker i sluttilstanden. Signalformer interpoleres fra Monte Carlo-simuleringer. Rater for kendte (baggrunds-)processer begrænses af dedikerede kontrolregioner i data. Resultaterne er i overensstemmelse med SM's forudsigelser. Øvre grænser på  $\sigma(gg \rightarrow A) \times \text{BR}(A \rightarrow ZH) \times \text{BR}(H \rightarrow WW)$  ved 95 % konfidensniveau sættes til 0.023–8.9 pb, afhængig af masse. Ved at bruge resultaterne og tage den naturlige bredde af  $A$  i betragtning placeres der udelukkelser i faseområdet for type-I 2HDM'er.

I en separat teknisk analyse kalibreres elektronidentifikationen af ATLAS's Transition Radiation Tracker ved hjælp af  $Z \rightarrow ee, \mu\mu$ -begivenheder opnået ved hjælp af "tag and probe"-metoden benyttet på LHC-data optaget af ATLAS i 2016 samt simuleret data. Den nye kalibrering løser problemet med et stigende antal elektroner med lave sandsynligheder. I data og simulering reduceres baggrundseffektiviteten med hhv. 1,45 og 3,31 procentpoint ved 95 % signaleffektivitet sammenlignet med den tidligere kalibrering.

## Disclaimer

The calibration in data of the TRT's electron identification was the entirety of my qualification task. All work presented is an adaptation of the technical note that was written on the matter. The likelihood with its correction factors is still the original work made by none other than my supervisor, Troels C. Petersen. The work on the tag and probe was done in collaboration with Nikita Smirnov who was also working on his qualification task in the TRT.

The Higgs analysis is the second iteration of a previous analysis, which originally only considered the  $\ell\ell b\bar{b}$  channel, which is near alignment. The approach taken in this analysis is much the same as before, and much experience and code have therefore been transferred to the new analysis. The off-alignment  $\ell\ell WW$  channel presented in this thesis is a novel addition to the analysis. I was responsible for the  $\ell\ell WW$  channel after the creation of its datasets, but I also worked a great deal on the  $\ell\ell b\bar{b}$  channel. While much of the work on this channel is mine, I have reused a great deal of the same frameworks and code that was used in the previous analysis as well as code made for the current analysis.

Figures produced for the internal notes and eventual paper bear the *ATLAS* mark in the figures. In this thesis, the mark (as well as "Internal", "Work in Progress", etc.) has been removed, as the thesis would otherwise have had to be approved by ATLAS.

Unedited figures from other sources will be referenced with a "From [X]" at the end of the caption. Manipulated figures (typically irrelevant information removed, text made to conform to the notation in the thesis, or updated colors) will reference sources with "Adapted from [X]".

## Acknowledgments

For the TRT analysis, I have adopted a great deal of code from my supervisor, Troels C. Petersen, who is the original author of the likelihood-based electron identification in the TRT. The tag and probe framework was developed in collaboration with Nikita Smirnov with whom I was working on my qualification task. I, along with the rest of the TRT group, owe a great thanks to Troels for the excellent electron likelihood, which still stands the test of time against the ML models being trained to replace it.

For the Higgs analysis, there are many people to thank for the various frameworks in use as well as the work that was put into the previous iteration of the analysis of which much has been reused.<sup>1</sup> I would like to thank my PhD collaborators, Wai Yuen Chan (Alan) and Shyam Balaji, for the help in making this analysis as well as Xiaohu Sun, Nikolaos "Nikos" Rompotis, Flavia Dias, and of course my supervisor for their work on and supervision of the analysis.

It goes without saying that few people can work alone in an office for years. A special thanks therefore goes to the numerous Master's and PhD students with whom I have socialized, collaborated, and maybe even tutored a little over the years. So thank you, Nicolas, Milena, Stefan, Rosanna, Christian, Benjamin, Lukas, Frederik, Helle, and all those I embarrassingly have forgotten to mention here. If it weren't for all your *neutral tracks*, life would be a little dull.

<sup>1</sup> The full author list of the previous analysis can be found for the internal note in Ref. [1].

## Introduction

The nineteen-sixties was a fruitful decade for the particle physics community. The Higgs mechanism was formulated in an attempt to explain why elementary particles have mass, and this work evolved into the Standard Model (SM) of today. It was also the decade where CP violation was first discovered. Just a few years later, Andrei Sakharov proposed his three conditions [2] that must be met in order to generate a baryon asymmetry: baryon number violation, C and CP violation, and a phase transition. With the discovery of the Higgs boson in 2012, an important piece of the puzzle was put into place, but the puzzle is far from finished, and several questions are still unanswered to this day. Among the questions is, why does matter even exist today?

Shortly after the Big Bang, as the universe expanded and cooled, matter and antimatter were created in equal numbers. As the universe further expanded, they stopped annihilating, and the universe would then contain equal numbers of matter and antimatter.

This is not the case, and the question is why that is. To answer this, many hypotheses have been presented. Perhaps they separated into different galaxies and "anti-galaxies", or perhaps the antimatter moved outside the observable universe? Since we have not observed any interaction between matter and antimatter (there should be a wall of light at their border from the annihilations), other mechanisms must be at play that lead the initial baryon symmetry to become asymmetric. If so, any mechanism able to explain this must follow Sakharov's three conditions.

The current level of CP violation in the SM is not enough to explain the level of asymmetry observed. An extension to the SM known as the Two Higgs Doublet Model (2HDM) introduces a new Higgs doublet with which 4 new Higgs bosons are hypothesized. The 2HDM model is able to fulfill the phase transition and possibly the CP violation conditions for some parts of its parameter space. One specific case is the  $A \rightarrow ZH$  decay, which may be considered the smoking gun for electroweak baryogenesis.

This thesis covers two studies, a performance analysis and a physics analysis.

In the performance analysis, the electron identification of ATLAS's Transition Radiation Tracker (TRT) is calibrated in data in order to improve its identification performance and its scaling with multiple interactions per bunch crossing. As the LHC moves towards higher instantaneous luminosity, the number of multiple interactions per bunch crossing increases, which in turn increases the occupancy in the TRT. The TRT electron identification tool had also shown regressions in its identification of electrons towards the low end of the electron probability distribution. It was therefore necessary to calibrate the tool anew. The calibration has been done in real and simulated data separately using  $Z \rightarrow ee$  and  $Z \rightarrow \mu\mu$  events obtained using the tag and probe method.

The physics analysis is a search for additional Higgs bosons beyond the SM. The analysis has searched for the  $A \rightarrow ZH$  signature where  $Z$  decays to leptons and  $H$  decays as  $H \rightarrow WW \rightarrow qqqq$ , where  $A$  and  $H$  ( $m_H > 125$  GeV) are heavier cousins to the SM Higgs. A discovery of new Higgs bosons in the context of 2HDM may be used to explain the baryon asymmetry that is observed in the universe. The  $WW$  channel covers one part of phase space that is away from the alignment limit and is a novel search in the context of 2HDM.

The physics analysis is the second iteration of a 2HDM analysis in ATLAS, which originally only considered the  $A \rightarrow ZH \rightarrow \ell\ell bb$  channel. I contributed to the first iteration (and am an author on the paper), but my main work lies in the second iteration. As I have worked extensively in  $\ell\ell WW$  channel of this analysis, results will primarily be from this channel. I have been a part of a great deal of the  $\ell\ell bb$  channel as well, and the thesis will refer to this channel at times.



**Part I**

**Background**



# 1 Theory

The theoretical foundation for the two analyses in this thesis is laid out in this chapter. We will go through a short introduction of the Standard Model of particle physics and the Two Higgs Doublet Model. The final section is dedicated to physics at hadron colliders including particle production in collisions and their interactions with detectors. The concepts will be used in the following chapters on the ATLAS experiment and the reconstruction of objects recorded by ATLAS.

## Contents

---

<b>1.1 The Standard Model of Particle Physics</b> . . . . .	<b>15</b>
<b>1.2 2HDM: Beyond the Standard Model</b> . . . . .	<b>19</b>
<b>1.3 Hadron collider physics</b> . . . . .	<b>27</b>

---

In the field of particle physics, one wants to explain the properties and interactions of matter at any energy scale using the most elementary particles, e.g. the mass of electrons and the electromagnetic forces between them. The *Standard Model* is the framework that accomplishes this, and it is a more fundamental theory, which is able to explain as much as previous theories in some limit (slow particles, low energy, etc.) while also being able to make new predictions. Maxwell's equations can be derived from the electromagnetic interactions of the Standard Model in the same way that Newtonian mechanics can be derived from special relativity in the limit  $v \ll c$ . While the Standard Model has been able to predict and explain a great deal, there are still unanswered questions. One of these is the evident asymmetry of particles and antiparticles in the universe (baryon asymmetry). In the following sections, the Standard Model is introduced along with an extension that can explain the baryon asymmetry.

## 1.1 The Standard Model of Particle Physics

The Standard Model (SM) of particle physics is an ensemble of quantum field theories (QFTs), which describes all *fundamental* particles and their *interactions*. The interactions are described as *fermions* (matter particles) exchanging *gauge bosons* (force carriers), where fermions and bosons are the usual half-integer and integer spin particles, respectively. The particles are listed in Fig. 1.1. Apart from the fermions and force carriers, there is the Higgs boson, which is the particle that is associated with the Higgs field. The Higgs boson has 0 spin in con-

Figure 1.1: The Standard Model of particle physics. The matter particles (first three columns) are given in purple for the quarks and green for the leptons. The bosons (last two columns) are given in red for the gauge bosons and yellow for the Higgs boson. The interactions between the matter particles and the gauge bosons are indicated by the light gray outline with light beige background: The quarks "feel" the strong force (gluons), the quarks and charged leptons feel the electromagnetic force (photons), and every matter particle feels the weak interactions (Z and W bosons). Adapted from [3].

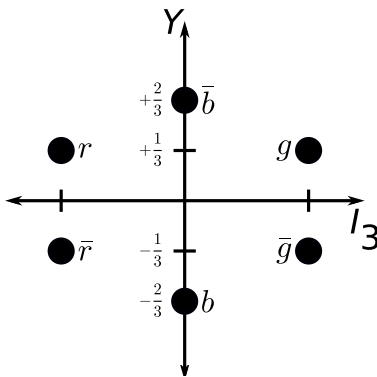
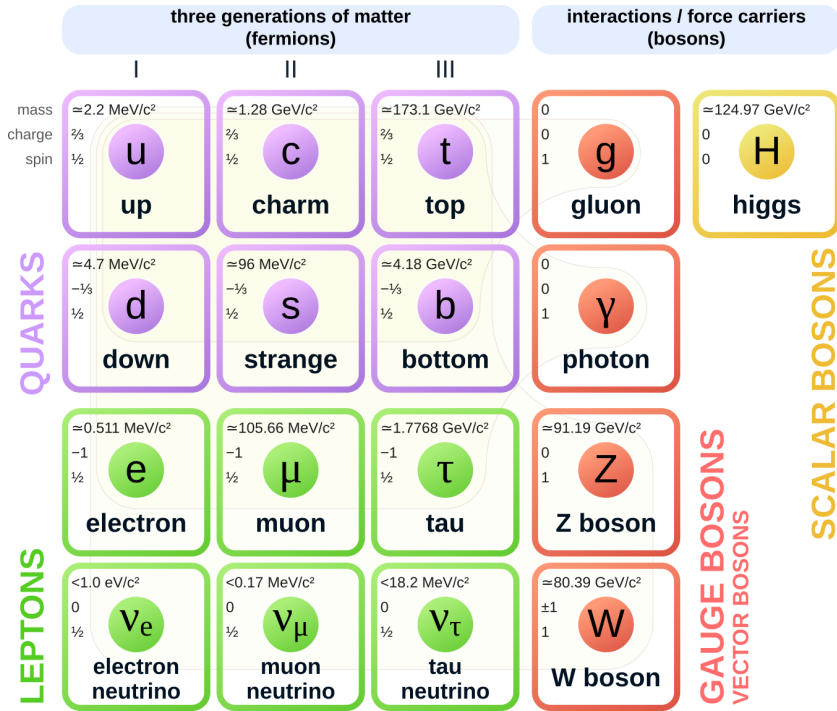


Figure 1.2: Representation of the color charge as a function of the quantum numbers isospin  $I_3$  and hypercharge  $Y$ .

<sup>1</sup> The Lagrangian  $L$  of classical mechanics operates on generalized coordinates  $q_i$  and their time derivatives, often written using Newton's notation  $\dot{q}_i$ . The Lagrangian density (or just Lagrangian for short)  $\mathcal{L}$  replaces the discrete coordinates with continuous fields  $q_i \rightarrow \phi_i(t, x, y, z)$  and the time derivatives by derivatives to all four space-time coordinates  $x^\mu$ , written as  $\partial_\mu \phi_i \equiv \frac{\partial \phi_i}{\partial x^\mu}$ .

trast to the gauge bosons, which are spin 1. Three of the four forces of nature — electromagnetic, weak, and strong, but not gravity — are each described by Quantum Electrodynamics (QED), weak interactions, and Quantum Chromodynamics (QCD), respectively. The electromagnetic and weak interactions are together described by the Electroweak Theory (EW).

In QFTs, every particle and interaction is associated with a field. Electrons are quantized excitations of the electron field, and they interact electromagnetically with each other using photons through their couplings to the photon field. Such couplings require interaction terms in the Lagrangian density<sup>1</sup> between electrons and photons. QFTs are gauge theories, meaning their Lagrangians are invariant (do not change) under local gauge transformations [4]. In ordinary words, this means that the model is independent of the underlying mathematical formulation. Each invariance is a symmetry of the model (e.g. invariance under a small rotation  $\phi \rightarrow \phi' = \phi + \delta\phi$  means rotational symmetry). Noether's theorem states that this symmetry leads to a conserved quantity, in this case, conservation of angular momentum. To construct a QFT, one starts with an equation for a free matter particle and requires that it is invariant under a local gauge transformation  $\phi(x) \rightarrow \phi'(x) = \exp(i\theta(x))\phi(x)$ . Consequently, this requirement implies that one has to introduce additional *gauge* fields. The gauge field is introduced by replacing the derivative  $\partial_\mu$  with the *covariant derivative*  $\partial_\mu \rightarrow D_\mu = \partial_\mu + X$ , where  $X$  is the generator of the symmetry group. This extra term describes the interaction between the particle and the gauge field. In the case of QED,  $X = iqA_\mu$  and the field  $A_\mu$  is identified as the photon.

QCD [4] is a Quantum Field Theory (QFT) with an  $SU(3)$  symmetry. The strong interaction between particles with *color* charge (with the three states red, green, and blue) is mediated by *gluons*. Particles with color charge include quarks but also gluons, and since gluons themselves have color, they will self-interact (shown later in Fig. 1.13b). The quarks carry two quantum numbers related to the strong interaction, the (third component of the) isospin  $I_3$  and hypercharge  $Y$ . See Fig. 1.2 for the representation of the color charges. Color is overall conserved in the exchange of gluons between quarks, ie. a red quark sends an  $r\bar{g}$  gluon to a green quark while at the same time the green quark sends a  $g\bar{r}$  gluon to the red quark, which effectively swaps their colors (while a  $\frac{1}{\sqrt{2}}(r\bar{r} - g\bar{g})$  exchange will not change color).

The lack of existence of free quarks is hypothesized to be due to *color confinement*, which states that objects with a net color charge cannot exist freely. This also explains why gluons, seeing as they carry color charge, do not propagate freely either. The color confinement can be understood as coming from gluon self-interactions between gluons exchanged between quarks, which lead to a potential linearly increasing with the distance between the quarks. This potential will increase until the energy stored allows for the creation of additional quarks that combine into separate quark pairs. The color confinement implies that colored particles must be colorless singlets, ie. only *hadrons* (bound states of quarks) that become colorless can exist freely. Being a colorless singlet is not sufficient; the color ladder operators applied to the color wave functions must yield zero as well.

The gluon self-interactions have further consequences for the strong force. The interactions between quarks can be expressed as the exchange of gluons to the first order. However, the interactions have higher-order terms that include both quark and gluon loops, which lead to a *decrease* in the effective strength or *coupling* of the strong force at higher energies. This is known as *asymptotic freedom*. The consequences of color confinement and asymptotic freedom will be explained later (Sect. 1.3).

Combinations of colors for *mesons* (bound states of a quark and an antiquark) give  $3 \otimes \bar{3} = 8 \oplus 1$  color states, which are a colored octet and a colorless singlet. The singlet is the state  $\psi = 1/\sqrt{3}(r\bar{r} + g\bar{g} + b\bar{b})$ . The octet and singlet are shown in Fig. 1.3. Combinations of colors for *baryons* (three quarks) also produce colorless singlets. Larger permitted hadrons include tetraquarks  $q\bar{q}q\bar{q}$  [5] and the pentaquarks  $qqq\bar{q}\bar{q}$  recently discovered by LHCb [6]. LHCb has also very recently discovered a possible  $c\bar{c}c\bar{c}$  [7].

QED [4] is the QFT for the electromagnetic interactions with the photon ( $\gamma$  for the particle or  $A$  for the field) associated with the  $U_{EM}(1)$  symmetry, which couples to the electric charge. Photons do not carry electric charge themselves and do therefore not self-couple. The weak interactions are mediated by the heavy  $W^\pm$  ("charged current") and  $Z$  ("neutral current") bosons and couple to the weak isospin  $I_W^3$ .

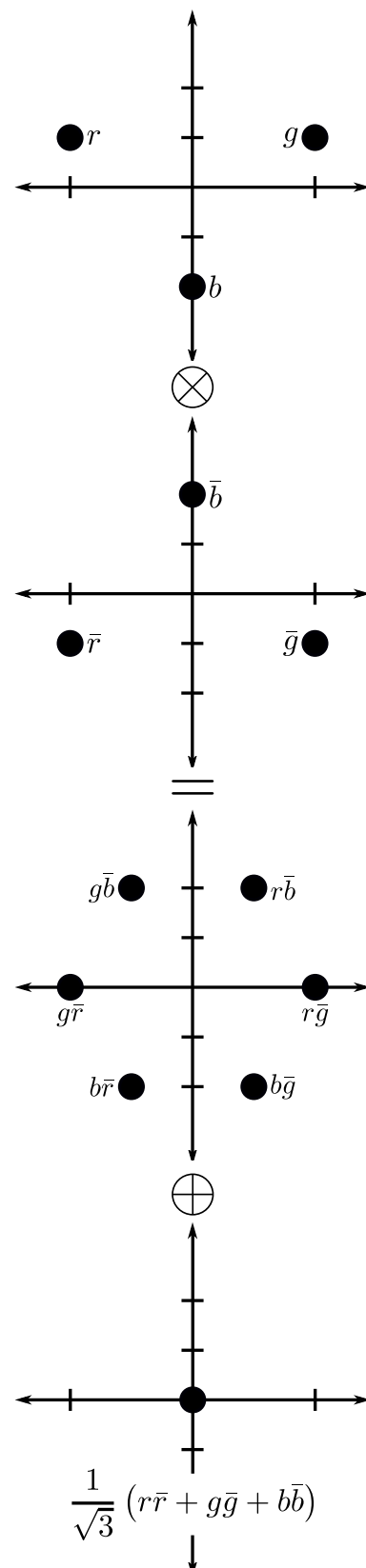


Figure 1.3: The colored octet and colorless singlet formed by combinations of colors and anticolor. The octet is the same for gluons but missing labels for the two gluons at the origin,  $(\frac{1}{\sqrt{2}}(r\bar{r} - g\bar{g}))$  and  $\frac{1}{\sqrt{6}}(r\bar{r} + g\bar{g} - 2b\bar{b})$ .

The weak interactions couple differently to particles of different *chirality*. The field of a particle can be decomposed into *left-handed* and *right-handed* components by use of the chiral projection operators,

$$\begin{aligned}\psi_R &= P_R \psi, & P_R &= \frac{1}{2}(1 + \gamma^5), \\ \psi_L &= P_L \psi, & P_L &= \frac{1}{2}(1 - \gamma^5),\end{aligned}$$

$${}^1\gamma^5 \equiv i\gamma^0\gamma^1\gamma^2\gamma^3 = \begin{pmatrix} 0 & 0 & 1 & 0 \\ 0 & 0 & 0 & 1 \\ 1 & 0 & 0 & 0 \\ 0 & 1 & 0 & 0 \end{pmatrix}$$

where  $\gamma^5$  is the fifth gamma matrix<sup>1</sup>. Chirality is analogous to helicity, which is defined as the direction of the projection of a particle's spin on its momentum vector. For massive particles, helicity is not invariant under boost. However, for massless particles (or approximately so for massive particles with  $E \gg m$ ), the eigenstates of helicity are identical to those of chirality.

The weak interactions couple to left-handed particles (and right-handed antiparticles) in weak isospin doublets,  $\begin{pmatrix} \nu_l \\ l \end{pmatrix}_L$  ( $l = e, \mu, \tau$ ) as well as  $\begin{pmatrix} u \\ d' \end{pmatrix}_L$ ,  $\begin{pmatrix} c \\ s' \end{pmatrix}_L$ , and  $\begin{pmatrix} t \\ b' \end{pmatrix}_L$ , where the first components have  $I_W^3 = 1/2$  and the second components  $I_W^3 = -1/2$ . The weak isospin doublets allow for particles to transform/rotate between each other within a doublet (e.g.  $\ell \rightarrow W\nu_\ell$ ). The primed quarks are weak eigenstates, which are linear combinations of the mass eigenstates of the quarks as given by the CKM matrix,

$$\begin{pmatrix} d' \\ s' \\ b' \end{pmatrix} = \begin{pmatrix} V_{ud} & V_{us} & V_{ub} \\ V_{cd} & V_{cs} & V_{cb} \\ V_{td} & V_{ts} & V_{tb} \end{pmatrix} \begin{pmatrix} d \\ s \\ b \end{pmatrix}. \quad (1.1)$$

The CKM matrix contains complex phases and is the only known source of CP violation in the quark sector in the SM. The mixing provided by the CKM matrix allows quarks to change generation under weak interactions (e.g.  $s \rightarrow Wu$ ). The weak interactions do not couple to right-handed particles (nor left-handed antiparticles), making the symmetry group for the weak interactions  $SU_L(2)$ , where the subscript  $L$  indicates that the gauge bosons only interact with left-handed particles.

However, the  $Z$  boson does couple to right-handed particles. This issue is solved in the EW Glashow–Salam–Weinberg model [4], which mixes the symmetries  $U_Y(1) \otimes SU_L(2)$  to give four generators,  $W^{(1)}$ ,  $W^{(2)}$ ,  $W^{(3)}$ , and  $B$ . The first two are associated with the  $W^+$  and  $W^-$  bosons,

$$W_\mu^\pm = \frac{1}{\sqrt{2}}(W_\mu^{(1)} \mp iW_\mu^{(2)}). \quad (1.2)$$

The latter two are linearly combined to give the  $Z$  and  $\gamma$  bosons,

$$A_\mu = B_\mu \cos \theta_W + W_\mu^{(3)} \sin \theta_W, \quad (1.3)$$

$$Z_\mu = -B_\mu \sin \theta_W + W_\mu^{(3)} \cos \theta_W, \quad (1.4)$$

where  $\theta_W$  is the Weinberg angle. The  $U(1)$  component of the  $Z$  boson can now interact with right-handed particles, though not as strongly as it interacts with left-handed particles.  $U_Y(1)$  introduces the quantum number weak hypercharge  $Y_W$ , which together with the weak isospin gives the electric charge  $Q = \frac{1}{2}Y_W + I_W^3$ . Unfortunately, the

gauge bosons are massless, which is in disagreement with the known masses for the  $W$  and  $Z$  bosons.

The Higgs mechanism is responsible for giving mass to the fermions through their couplings to the Higgs field<sup>1</sup>. The Higgs mechanism is also responsible for giving mass to the weak gauge bosons,  $W^\pm$  and  $Z$ . For the massive gauge bosons to obtain masses, the symmetry must be *spontaneously broken* [4]. This is achieved in the Higgs mechanism by introducing a complex doublet field  $\phi = \begin{pmatrix} \phi^+ \\ \phi^0 \end{pmatrix} = \frac{1}{\sqrt{2}} \begin{pmatrix} \phi_1 + i\phi_2 \\ \phi_3 + i\phi_4 \end{pmatrix}$  in a Lagrangian of the form,

$$\mathcal{L} = (\partial_\mu \phi)^\dagger (\partial^\mu \phi) - \mu^2 (\phi^\dagger \phi) + \lambda (\phi^\dagger \phi)^2, \quad (1.5)$$

which must give masses to the weak bosons and a boson associated with the Higgs field (but not the photon).

For the potential to have a finite minimum,  $\lambda > 0$ . For  $\mu^2 > 0$ , the minimum is at  $\phi^+ = \phi^0 = 0$ . For  $\mu^2 < 0$ , the potential will take on the characteristic "wine-bottle" potential<sup>2</sup> shown in Fig. 1.4, and the minimum will be at  $v^2 = \frac{-\mu^2}{2\lambda}$ , where  $v = 246$  GeV is the vacuum expectation value (vev). The non-zero vacuum has broken the symmetry of the Lagrangian. For the photon to remain massless, only the neutral component  $\phi^0$  can remain non-zero. This gives  $\langle \phi \rangle = \frac{1}{\sqrt{2}} \begin{pmatrix} 0 \\ v \end{pmatrix}$  using the unitary gauge, in which a proper gauge transformation transforms additional Goldstone bosons into polarizations of the weak bosons<sup>3</sup>. This can be expanded about the minimum as  $\phi(x) = \frac{1}{\sqrt{2}} \begin{pmatrix} 0 \\ v + h(x) \end{pmatrix}$ , where the scalar field  $h$  will be associated with the Higgs boson. By replacing the derivatives in the Lagrangian with the covariant derivatives with generators from  $U_Y(1)$  and  $SU_L(2)$ ,

$$\partial_\mu \rightarrow D_\mu = \partial_\mu + \frac{1}{2} i g_W \vec{\sigma} \cdot \vec{W}_\mu + i g' \frac{Y}{2} B_\mu, \quad (1.6)$$

and having the covariant derivative act on the Higgs doublet  $\phi(x)$  (following Eq. (1.5)), one can identify mass terms generated by  $(D_\mu \phi)^\dagger (D^\mu \phi)$  by the terms that are quadratic in the fields. For the  $W^{(1)}$  and  $W^{(2)}$  terms, one obtains  $m_W = \frac{1}{2} g_W v$ . The  $W^{(3)}$  and  $B$  terms are written in matrix form and diagonalized giving  $m_A = 0$  and  $m_Z = \frac{1}{2} v \sqrt{g_W^2 + g'^2}$ , where  $A_\mu$  and  $Z_\mu$  are identified as Eq. (1.3) and Eq. (1.4) with  $\tan \theta_W = \frac{g'}{g_W}$ .

Triple field terms in  $(D_\mu \phi)^\dagger (D^\mu \phi)$  such as  $VVh$ , where  $V = W^\pm, Z$ , give couplings between the weak bosons and the Higgs boson  $h$ ,

$$g_{hVV}^{\text{SM}} = g_V m_V. \quad (1.7)$$

Additional Yukawa couplings let the Higgs field give masses to the massive fermions.

## 1.2 2HDM: Beyond the Standard Model

The SM as it stands does not explain dark matter, which makes up the majority of the matter in the universe; the masses of the neutrinos, which are now known to have masses due to their flavor

<sup>1</sup> The neutrinos are considered massless in the SM. This is one of several known, significant shortcomings of the SM since neutrinos are experimentally known to have mass due to their flavor oscillations.

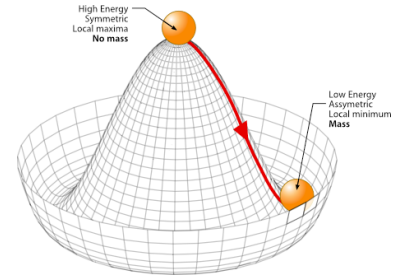


Figure 1.4: The characteristic Higgs potential. From [8].

<sup>2</sup> The potential may be better known as the Sombrero or "Mexican hat" potential.

<sup>3</sup> This is (in)famously referred to as the gauge "eating" the Goldstone bosons.

oscillations; nor the baryon asymmetry observed in the universe, among other things [4, 9]. Slightly after the Big Bang, baryonic matter was at equilibrium with the photons  $\gamma + \gamma \rightleftharpoons p + \bar{p}$ . As the universe cooled, the forward direction ceased. Then, with further expansion, the density of baryons and antibaryons fell, and the backwards process also fell, eventually freezing the number of baryons and antibaryons (known as baryogenesis) with a number density ratio of  $\frac{n_B - n_{\bar{B}}}{n_\gamma} \approx 10^{-9}$ , which is calculated from measurements [4, 9]. The amount of matter today is not explained by the limited CP violation provided by the CKM matrix. A successful extension of the SM must explain the baryon asymmetry as the universe transitioned from thermal equilibrium.

Simple extensions of the SM include adding one [10] or two [11] real, scalar singlets; one complex singlet [12]; or one complex doublet. The Two-Higgs-Doublet-Models (2HDMs) [13, 14] are the latter. 2HDM introduces 5 new bosons and consists of several types, both of which will be introduced in a moment. It is a popular and versatile extension, which can be used as a general benchmark for additional Higgs bosons or as part of the Minimal Supersymmetric Standard Model [14, 15]. 2HDMs may be used to explain the baryon asymmetry [16–19] through electroweak baryogenesis [20], and similar models with two complex Higgs doublets are also part of some dark matter [21] and neutrino mass [22] models.

The discovery [23, 24] and precise measurements [25–32] of the SM Higgs boson [33–38] have put some constraints on the possible phase space of extensions. Previous LHC searches for single 2HDM particles include heavy  $H \rightarrow WW/ZZ$  [39–44],  $H \rightarrow hh$  [45, 46],  $A \rightarrow Zh$  [47, 48], and  $A/H \rightarrow \tau\tau/bb$  [49–51]. However, the focus in this thesis will be on the heavy  $A$  decaying to a  $Z$  boson and another heavy Higgs  $H$ , which has been covered by CMS in the  $A \rightarrow ZH \rightarrow \ell\ell bb/\ell\ell\tau\tau$  channels<sup>1</sup> [52, 53] as well as ATLAS in the  $A \rightarrow ZH \rightarrow \ell\ell bb$  channel [54].

<sup>1</sup>The quoted references also consider the  $H \rightarrow ZA$  decays, and they only quote exclusions for type-II.

In 2HDM, an additional complex SU(2) doublet is added to the Higgs sector. After symmetry breaking, the two Higgs doublets each obtain their vacuum expectation value (vev) [14]:

$$\langle \Phi_1 \rangle = \frac{1}{\sqrt{2}} \begin{pmatrix} 0 \\ v_1 \end{pmatrix}, \quad \langle \Phi_2 \rangle = \frac{1}{\sqrt{2}} \begin{pmatrix} 0 \\ v_2 \end{pmatrix},$$

where  $v_1$  ( $v_2$ ) is the vev for the  $\Phi_1$  ( $\Phi_2$ ) doublet, and  $v_1^2 + v_2^2 = v^2 = (246 \text{ GeV})^2$ . Other vevs are possible, including "inert" models where one doublet is 0 at the minimum or vevs with complex phases [14]. While these vevs may be interesting as well, the "normal" SM-like minimum is chosen in this case. The potential for the two doublets is [14],

$$\begin{aligned} V = & m_{11}^2 \Phi_1^\dagger \Phi_1 + m_{22}^2 \Phi_2^\dagger \Phi_2 - m_{12}^2 (\Phi_1^\dagger \Phi_2 + \Phi_2^\dagger \Phi_1) \\ & + \lambda_1/2 (\Phi_1^\dagger \Phi_1)^2 + \lambda_2/2 (\Phi_2^\dagger \Phi_2)^2 + \lambda_3 \Phi_1^\dagger \Phi_1 \Phi_2^\dagger \Phi_2 \\ & + \lambda_4 \Phi_1^\dagger \Phi_2 \Phi_2^\dagger \Phi_1 + \lambda_5 \left[ (\Phi_1^\dagger \Phi_2)^2 + (\Phi_2^\dagger \Phi_1)^2 \right], \end{aligned}$$

where some parameters may be complex and therefore provide CP-violating phases.

The 2HDM types include (see also Fig. 1.5),

- type-I, in which the right-handed (RH) up- and down-type quarks and the RH charged leptons couple to  $\Phi_2$ ;
- type-II, in which only the RH up-type quarks couple to  $\Phi_2$  and the RH down-type quarks and the RH charged leptons couple to  $\Phi_1$
- lepton-specific, where to the RH quarks couple to  $\Phi_2$  and the RH charged leptons  $\Phi_1$ ; and
- flipped, where the RH up-type quarks and the RH charged leptons couple to  $\Phi_2$  and RH down-type quarks  $\Phi_1$ .

It is common to assume or enforce that CP is conserved, that CP is not spontaneously broken (which *may* happen if one of the vevs include a complex phase), and that discrete symmetries suppress flavor-changing neutral currents (FCNCs) at leading order to match what is seen experimentally. The latter is ensured by imposing the  $Z_2$  symmetry  $\Phi_1 \rightarrow -\Phi_1$  in type-I and type-II. Type-II additionally needs  $d_R^i \rightarrow -d_R^i$  [14]. This leads to the classification of models into these types. The  $Z_2$  symmetry is *softly* broken in the aforementioned potential by not setting  $m_{12}^2$  to zero while otherwise keeping the Lagrangian invariant under the  $\Phi_1 \rightarrow -\Phi_1$  interchange to ensure CP conservation.

The 8 degrees of freedom from the two complex doublets give rise to the same three weak bosons as well as 5 Higgs bosons, two charged ( $H^\pm$ ), two CP-even ( $h$  and  $H$ ), and one CP-odd ( $A$ ) [16]. The two light CP-even bosons are found by mixing the Goldstone bosons  $h_1$  and  $h_2$ , and  $A$  is found by mixing  $h_3$  and  $h_4$ :

$$h = -h_1 \sin \alpha + h_2 \cos \alpha, \quad (1.8)$$

$$H = h_1 \cos \alpha + h_2 \sin \alpha, \quad (1.9)$$

$$A = h_3 \sin \beta - h_4 \cos \beta, \quad (1.10)$$

where  $\alpha$  ( $-\pi/2 < \alpha < \pi/2$ ) is the mixing angle after diagonalizing the mass matrix for the neutral scalars, and  $\tan \beta \equiv \frac{v_2}{v_1}$  is the ratio of vevs and also the mixing angle for the pseudoscalars. It is important to note that the literature has different definitions of  $\alpha$ , and the convention used in this thesis follows Branco [14]. However, the benchmark models are taken from Dorsch [16], which uses a different convention, where  $\alpha$  is shifted by  $\pi/2$ . Therefore,  $\cos(\beta - \alpha) = 0$  is the *alignment limit* (or *weak decoupling limit*) [55], in which  $h$  obtains SM-like properties.

The coupling of  $H$  to a pair of vector bosons follows the SM with an additional factor of  $\cos(\beta - \alpha)$  [14], and  $A$  couples to  $V$  and either of the neutral scalars as,

$$g_{HVV} = \cos(\beta - \alpha) g_{hVV}^{\text{SM}}, \quad (1.11)$$

$$g_{AZh} \propto \cos(\beta - \alpha), \quad (1.12)$$

$$g_{AZH} \propto \sin(\beta - \alpha). \quad (1.13)$$

For type-I and lepton-specific, the gluon-gluon fusion production for  $A$  dominates (as for the SM Higgs) in proton-proton collisions,

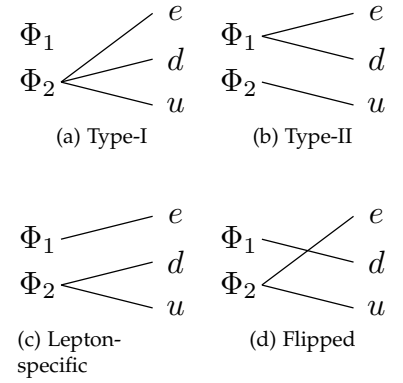


Figure 1.5: The four 2HDM types that suppress flavor-changing neutral currents (FCNCs) at leading order.  $e$  symbolizes the charged leptons.  $d$ ,  $u$ , and  $e$  are all right-handed.

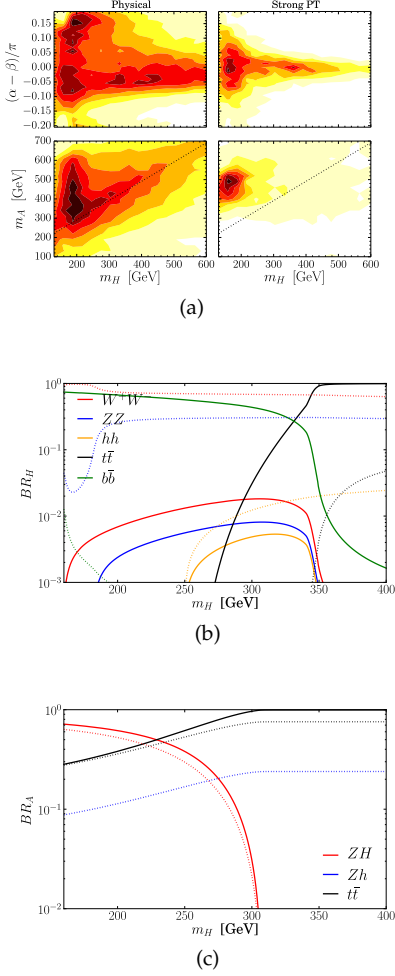


Figure 1.6: (a) Heat map of physical points (left column) and points with a strong phase transition (right column). The points are shown as a function of  $\alpha - \beta$  (Ref. [16] convention) or  $m_A$  as well as  $m_H$ . (b) Major branching ratios for the  $H$  decay as a function of  $m_H$  for  $m_A = m_{H^\pm} = 400$  GeV,  $\tan \beta = 2$ ,  $\alpha - \beta = 0.001\pi$  (solid lines; near alignment) and  $\alpha - \beta = 0.1\pi$  (dotted lines; away from alignment), again using the convention from Ref. [16]. (c) Major branching ratios for the  $A$  decay as a function of  $m_H$  following the same setup as for middle figure. All adapted from [16].

while  $b$ -associated production ( $b$ -quark fusion) becomes important for the other two models for large  $\tan \beta$  [14, 56].

The ability for 2HDM to generate a strong phase transition is found through Monte Carlo simulations with a wide range of  $m_A$ ,  $m_{H^\pm}$ ,  $\tan \beta$ , and  $\alpha - \beta$  [57]. Any point satisfying unitarity and perturbativity as well as precision constraints and collider bounds are considered *physical*, while points also passing  $v_c/T_c > 1$  ( $v_c$  being the magnitude of the broken vev at  $T_c$ ) will lead to a *strong phase transition*. The results are shown in Fig. 1.6a as heat maps visualizing the density of points passing the criteria. In general, models near alignment are favored, especially for higher  $m_H$ ; a relatively large difference in  $A$  and  $H$  masses is also favored with a clear preference for  $m_A > m_H$ .

Figs. 1.6b and 1.6c show the branching ratios for  $H$  and  $A$  close to and away from alignment as a function of  $m_H$ . For the  $H$  decay,  $WW$  dominates away from alignment. For the  $A$  decay, the alignment matters less, and  $A \rightarrow t\bar{t}$  becomes dominant at  $m_H \approx 250$  GeV and beyond in either case. The last figure especially gives some preliminary indications on the expected sensitivity for the  $A \rightarrow ZH \rightarrow \ell\ell WW$  decay; one should expect falling sensitivity past  $m_H \approx 250$  GeV. There is one ATLAS study on the  $A \rightarrow t\bar{t}$  channel using limited Run 1 data [58], but extra care has to be taken on the interference with SM  $t\bar{t}$  decay.

Further assumptions are made on the properties of the Higgs bosons. The lightest CP-even boson ( $h$ ) is assumed to be the SM Higgs at  $m_h = 125$  GeV with  $m_H > m_h$ , the heavier CP-even boson is lighter than the CP-odd ( $m_H < m_A$ ), and the charged bosons have the same mass as the CP-odd ( $m_{H^\pm} = m_A$ ).  $m_{12}^2$  is defined as,

$$m_{12}^2 \equiv m_A^2 \tan \beta / (1 + \tan^2 \beta),$$

following ATLAS recommendation. Production cross-sections are calculated by SusHi 1.7.0 [59–65] using the LHAPDF 6.3.0 [66] library, and partial widths and branching ratios are calculated by 2HDMC 1.7.0 [67]. These values have been calculated for  $\cos(\beta - \alpha)$  between  $-1$  and  $1$  in steps of  $0.1$ ,  $\tan \beta$  between  $0.5$  and  $3.0$  in steps of  $0.5$ , and  $(m_A, m_H) = (300, 200)$  to  $(800, 700)$  GeV in steps of  $50$  GeV in both masses and with the condition that  $m_A > m_H$ . Under these constraints, the  $A \rightarrow ZH$  decay dominates [16, 68].

Fig. 1.6b from Ref. [16] with  $m_A = 400$  GeV,  $\tan \beta = 2$ ,  $\alpha - \beta = 0.1\pi$  (their convention) is recreated with  $m_A = 400$  GeV,  $\tan \beta = 2$ , and  $\cos(0.1\pi - \pi/2) \approx 0.3$  in Fig. 1.7, where  $-\pi/2$  is to convert from their convention. The calculated branching ratios are plotted against the figure and shows perfect agreement until  $m_H = 250$  GeV, where the  $hh$  decay becomes kinematically allowed. The  $H \rightarrow WW$  branching ratio falls at about the same  $m_H = 250$  GeV where  $A \rightarrow t\bar{t}$  becomes dominating, further reducing the sensitivity beyond this point.

The cross-section for  $gg \rightarrow A$  times branching ratios for  $A \rightarrow ZH$  and  $H \rightarrow WW$  is shown in Fig. 1.9 for different  $A$  and  $H$  masses as a function of the tunable parameters  $\tan \beta$  and  $\cos(\beta - \alpha)$ . For

$m_H < 250$  GeV, where  $H \rightarrow hh$  is forbidden, the branching ratio for  $H \rightarrow WW$  becomes constant (at least for  $\cos(\beta - \alpha) > 0.3$ ) as expected [14]. Since  $g_{AZH} \propto \sin(\beta - \alpha)$  but  $g_{HVV} \propto \cos(\beta - \alpha)$ , the peak will be "somewhere in the middle". The highest sensitivity is expected for low  $\tan \beta$ , medium to low  $\cos(\beta - \alpha)$ , and very low  $m_H$ , which is consistent with the observations on the  $A$  and  $H$  branching ratios.

Using the same configuration, the relative  $H$  width is shown in Fig. 1.10. Darker colors are  $< 1\%$  width and may be considered narrow-width compared to the detector and reconstruction resolutions. However, the width may be up to 35% for high  $m_H$  with some dependence on  $\cos(\beta - \alpha)$  and  $\tan \beta$ . Regardless, for large parts of the phase space, the  $H$  width may be considered narrow-width. The case is different for the  $A$  width in Fig. 1.11 where the width is several percent even for low masses and especially for very low  $\tan \beta$ , which is part of the phase space in which the analysis is sensitive.

Current limits on  $\alpha$  and  $\beta$  are shown in Figs. 1.8a–1.8c. The result from Fig. 1.8a is made at alignment. The results from Figs. 1.8b and 1.8c are not directly comparable to Fig. 1.8a and the results of the AZH analysis in this thesis, as the former papers are indirect searches that assume very high masses for  $A$  and  $H$ , making it possible to integrate out the heavy fields [14]. No CMS result for type-I was found.

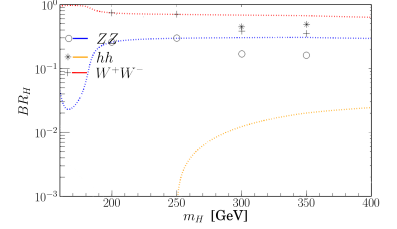
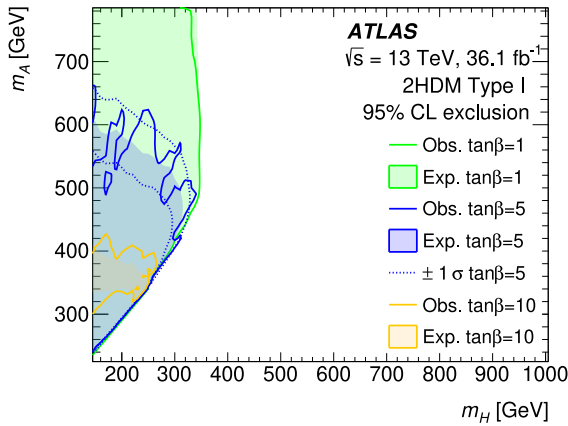
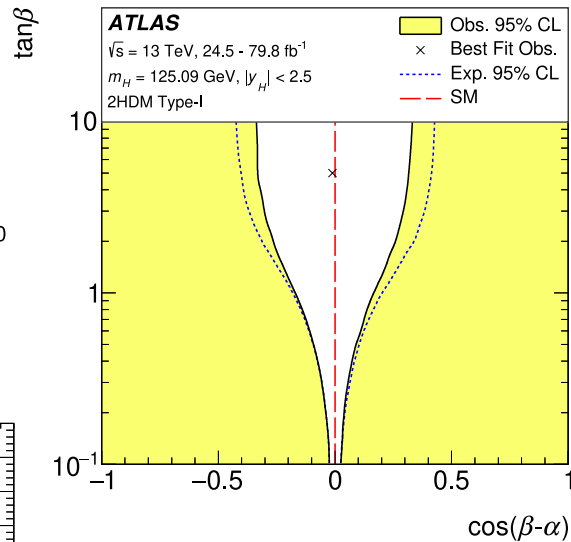


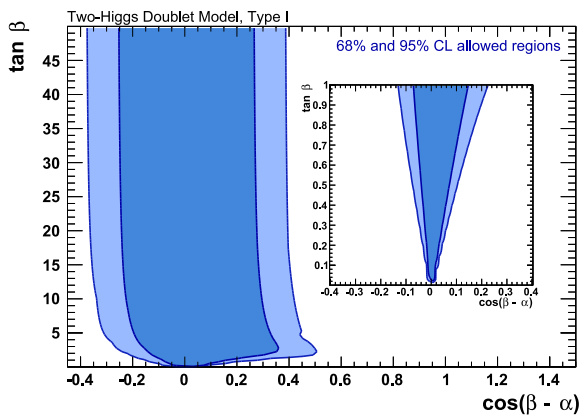
Figure 1.7: Major branching ratios for the  $A$  decay as a function of  $m_H$  for  $m_A = 400$  GeV,  $\tan \beta = 2$ ,  $\alpha - \beta = 0.1\pi$  (dotted lines; their convention). The result of the calculation in the text is plotted against the figure and shown as points. The  $WW$  (pluses) and  $ZZ$  (open circles) channels fit the curves for  $m_H = 200$  and 250 GeV. They deviate after 250 GeV when the  $hh$  (asterisks) decay becomes possible. Adapted from [16] and augmented. Original figure shown in Fig. 1.6b.



(a) Limits from previous paper



(b) Latest ATLAS results



(c) Limits from global fits of ATLAS+CMS data

Figure 1.8: Exclusions for type-I for (a) the previous iteration of the AZH analysis (from [54]), (b) combined results from ATLAS and CMS (from [69]), and (c) latest ATLAS results (from [25]).

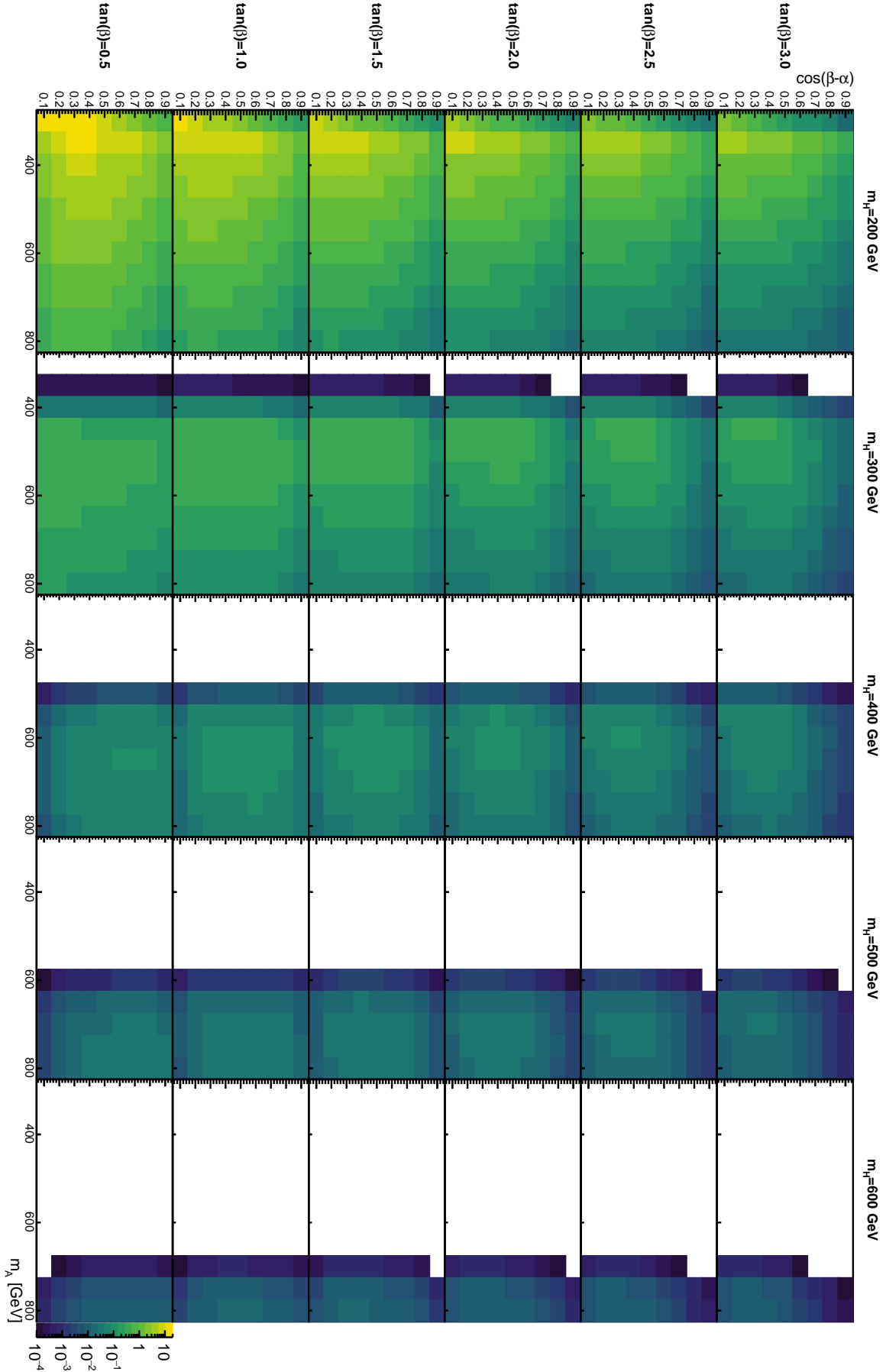


Figure 1.9:  $\sigma(gg \rightarrow A) \cdot \text{BR}(A \rightarrow ZH) \cdot \text{BR}(H \rightarrow WW)$  in pb (scale up to 20 pb) as a function of  $\cos(\beta - \alpha)$  and  $m_A$  in slices of  $m_H$  (columns) and  $\tan \beta$  (rows). Empty bins are either due to the  $m_H < m_A$  requirement or values below  $10^{-4}$  pb.

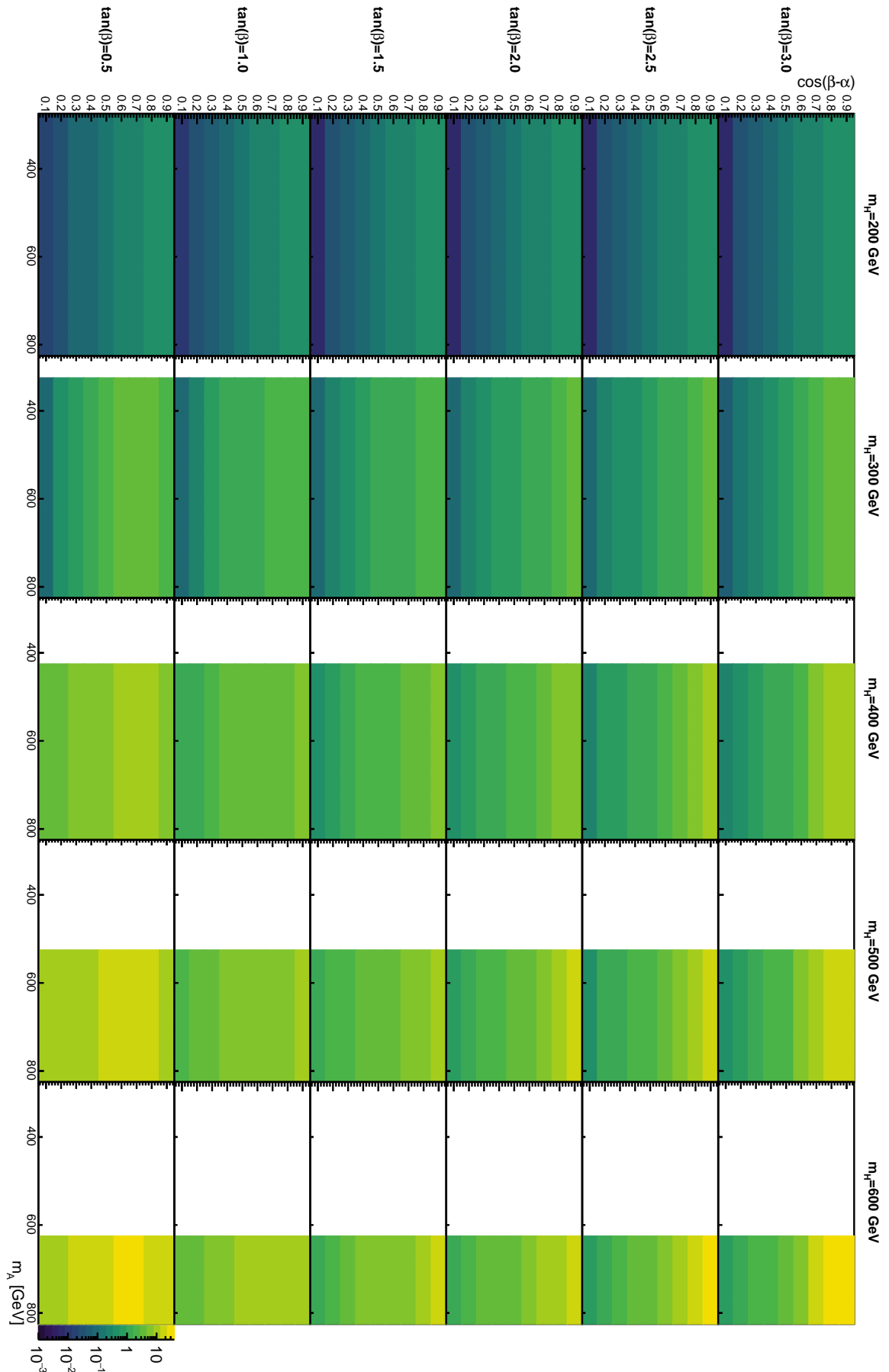


Figure 1.10:  $H$  width divided by its mass in percent (scale up to 40%) as a function of  $\cos(\beta - \alpha)$  and  $m_A$  in slices of  $m_H$  (columns) and  $\tan \beta$  (rows). Empty bins are due to the  $m_H < m_A$  requirement. The decay width does not depend on the  $A$  mass. The width increases up to  $\approx 35\%$  for  $\tan \beta = 3.0$  and  $\cos(\beta - \alpha) \geq 0.9$ .

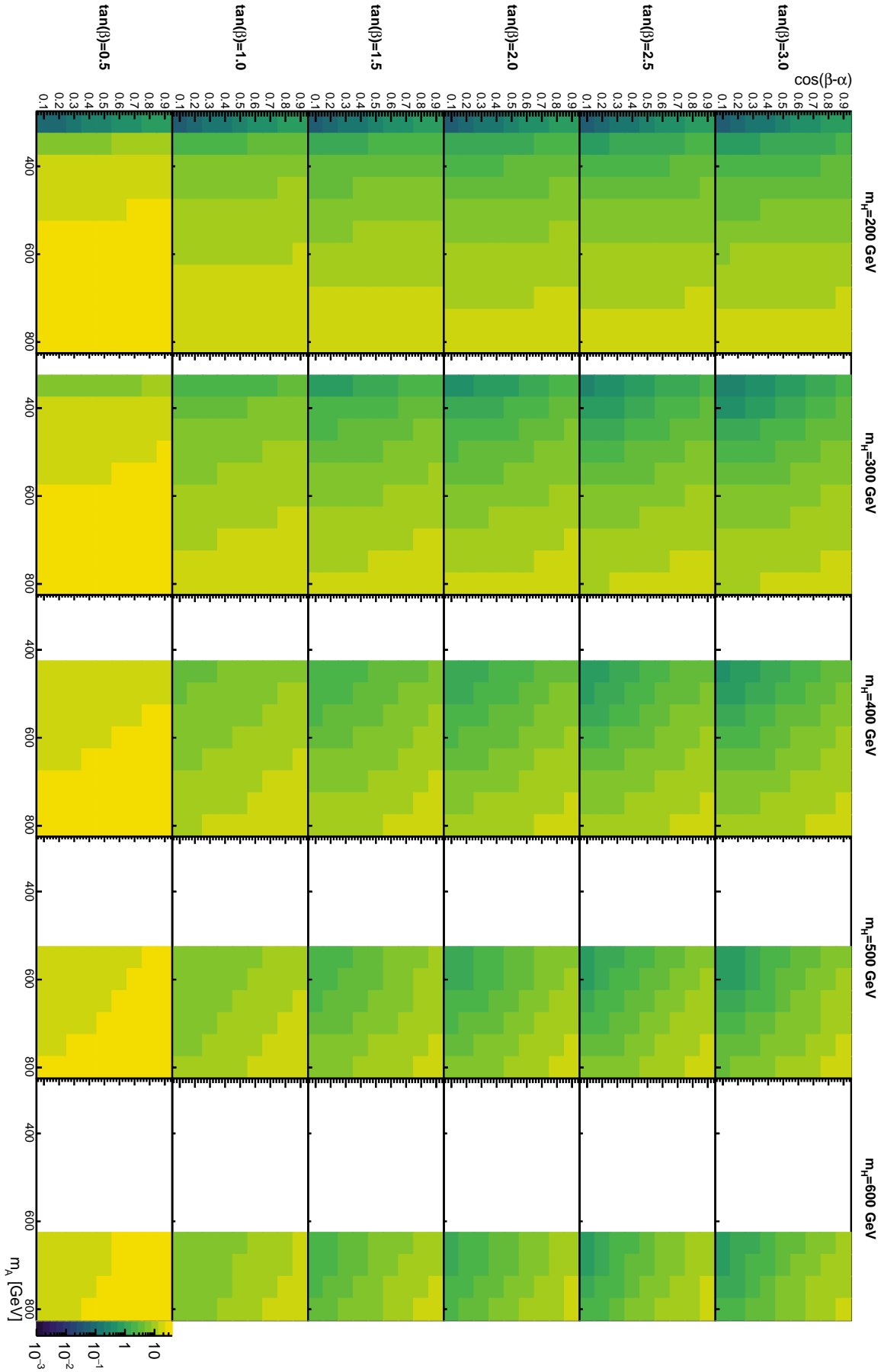


Figure 1.11: A width divided by its mass in percent (scale up to 40%) as a function of  $\cos(\beta - \alpha)$  and  $m_A$  in slices of  $m_H$  (columns) and  $\tan \beta$  (rows). Empty bins are due to the  $m_H < m_A$  requirement. The width increases up to  $\approx 35\%$  for  $\tan \beta = 0.5$ .

### 1.3 Hadron collider physics

Circular accelerators will accelerate two counter-rotating sets of particles to great energies and bring them to collision inside experiments on the ring. Many particles produced in the collisions are unstable and decay before even reaching the first layer of the detector. The Z boson, for instance, has a mass<sup>1</sup> of about 91 GeV and an extremely short lifetime. For an ensemble of unstable particles (e.g. radioactive isotopes), the number of particles falls as  $\exp(-t/\tau)$ , where  $\tau$  is the lifetime. The lifetime is related to the *total decay width* through  $\Gamma = 1/\tau$  for single particles. This affects the shape of the probability distribution of the observed invariant mass of the Z boson, which is described by the Breit-Wigner distribution shown in Fig. 1.12 [4, 70]. The full-width-at-half-maximum of the distribution is  $\Gamma/2$  away from the median.

The probability to produce a pair of particles from a two-to-two process can be calculated from the *differential cross-section*  $d\sigma$  that is determined using Fermi's golden rule, which can be expressed in the form,

$$d\sigma \propto |\mathcal{M}|^2 d\Omega, \quad (1.14)$$

where  $\mathcal{M}$  is the matrix elements and  $\Omega$  is the solid angle over which the integration is done in the center of mass frame, neglecting normalization and momentum factors [4]. Integrating over  $\Omega$  gives the *cross-section*  $\sigma$  for a process. At the lowest order, the matrix elements are given by<sup>2</sup>  $\mathcal{M} \propto \langle f|\hat{\mathcal{H}}'|i\rangle$  for initial states  $i$  and final states  $f$ , where  $\hat{\mathcal{H}}'$  is the Hamiltonian of the perturbation.

The expansion of the matrix elements can be expressed in terms of *Feynman diagrams*. Fig. 1.13a describes the lowest-order, or *leading order* (LO; also known as *tree level*), term in  $\mathcal{M}$  for two-to-two interactions. Higher-order terms include an increasing number of vertices and are named *next-to-leading order* (NLO), NNLO, etc. An example of an NLO process is shown in Fig. 1.13b. Terms in the matrix elements can be reduced to coupling constants depending on the interaction between two particles. The coupling  $\alpha(q^2)$  for the electroweak interactions is the fine structure constant, approximately  $1/137$ , at the energy  $q^2 = 0$ , and it only slowly increases for higher energies. As each higher-order term gains an additional factor of  $\alpha(q^2)$ , they quickly become insignificant.  $\alpha_S(q^2)$  for the strong interaction is around 1 at low energies and non-perturbative (the expansion of the matrix elements will contain many significant terms), but  $\alpha_S(q^2)$  decreases asymptotically for higher  $q^2$  to about 0.1 at relevant energies (typically set to the mass of the Z boson), which makes QCD perturbable at higher energies. However, 0.1 is still not small, so higher-order QCD terms are still significant [4]. The falling  $\alpha_S(q^2)$  for higher energies is the asymptotic freedom mentioned earlier.

<sup>1</sup> Particle physicists often use *natural units*, where  $\hbar = c = 1$ , meaning masses are given in units of eV instead of  $\text{eV}/c^2$ .

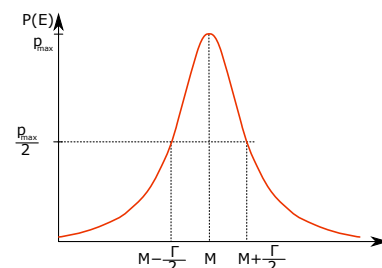


Figure 1.12: The Breit-Wigner distribution. From [71].

<sup>2</sup>  $\mathcal{M}$  is analogous to the wave functions entering Schrödinger's equation and may be called the *amplitude*.  $|\mathcal{M}|^2$  is similarly the probability.

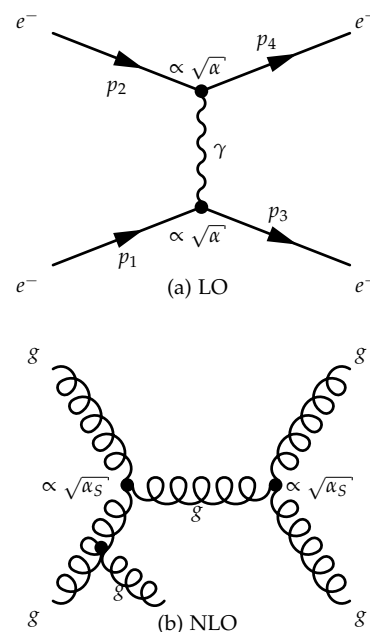


Figure 1.13: (a) Coulomb scattering between two electrons through the exchange of a virtual photon. The strength of the interaction is related to the product of the vertices,  $\alpha_{\text{EM}}$ . (b) Example of an NLO process. Adapted from [72].

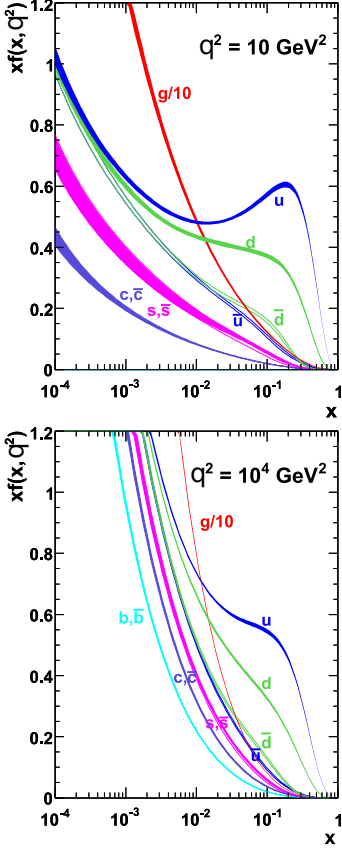


Figure 1.14: The pdfs for quarks and gluons at two energy scales. Adapted from [74].

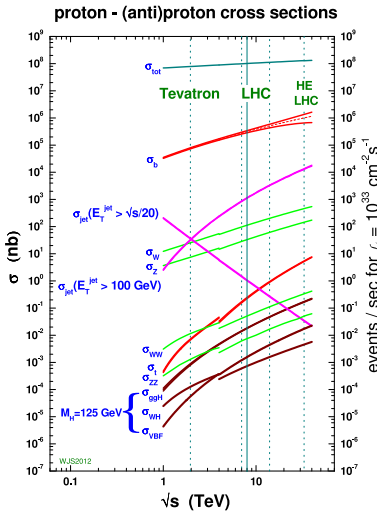


Figure 1.15: The cross-sections for producing various particles (for different production mechanisms for the Higgs boson) as well as the total cross-section. The discontinuity at 4 TeV is due to the switch from proton-antiproton to proton-proton collisions. High-energy (HE) LHC is included. From [76].

Partial decay widths for one-to-two processes can be expressed similar to Eq. (1.14),

$$\Gamma_i \propto \int |\mathcal{M}|^2 d\Omega. \quad (1.15)$$

Unstable particles may decay to different final state particles, yielding an  $\mathcal{M}$  and hence  $\Gamma_i$  for each *decay channel*. The total decay width is found from the sum of the partial decay widths. The relative frequency of a partial decay width is given by the *branching ratio*,  $BR_i = \Gamma_i/\Gamma$ . For the  $Z$  boson, the branching ratios are approximately 70% to quarks, 20% to neutrinos, and 10% to leptons [73].

The probability to extract specific partons (quarks and gluons) from the proton-proton collision and having these interact to form a specific particle can be calculated independently and is known as the *factorization theorem* [9, 75],

$$\sigma_X = \sum_{a,b=q,g} \int_0^1 dx_1 dx_2 f_a(x_1, \mu_F^2) f_b(x_2, \mu_F^2) \times \hat{\sigma}_{ab \rightarrow X}(x_1, x_2, \{p_i^\mu\}; \alpha_S(\mu_R^2), \alpha(\mu_R^2), q^2/\mu_R^2, q^2/\mu_F^2). \quad (1.16)$$

The function  $f_a(x)$  is the probability distribution for extracting parton  $a$  with a momentum fraction  $x$  from the parent proton; these *parton distribution functions* (pdfs) are shown in Fig. 1.14 at two energy scales  $q^2$ . At low energy scales ( $q^2 = 10 \text{ GeV}^2$ ), the *valence* quarks of protons ( $uud$ ) are more probable at high  $x$  than the virtual *sea* quarks. Note that the  $y$ -axis is scaled by the momentum fraction; it is most probable to extract very low momentum partons, especially gluons, for which reason most proton-proton collisions produce results in *soft* scatter of little interest to high-energy physicists. The first term in Eq. (1.16) integrates the pdfs over all momentum fractions. The second term in Eq. (1.16) gives the probability for forming particle  $X$  from the partons  $a$  and  $b$ , which (following Eq. (1.14)) contains the matrix elements for  $ab \rightarrow X$ . Finally, the full product is summed over for all gluons and quarks. The theorem depends on the factorization  $\mu_F$  and renormalization  $\mu_R$  scales, which are introduced to suppress divergences. The dependence of these *unphysical* scales decreases when including higher-order Feynman diagrams [9].

Interactions can be classified into two categories, annihilations and scatterings. Since four-momentum is conserved at every vertex, the following are equivalent for two-to-two interactions [4],

$$s = (p_1 + p_2)^2 = (p_3 + p_4)^2, \quad (1.17)$$

$$t = (p_1 - p_3)^2 = (p_2 - p_4)^2, \quad (1.18)$$

$$u = (p_1 - p_4)^2 = (p_2 - p_3)^2, \quad (1.19)$$

where  $p_1$  and  $p_2$  are the four-momenta of the initial state particles and  $p_3$  and  $p_4$  are the four-momenta of the final state particles. The  $s$ -channel refers to an annihilation (Fig. 1.13b) and the  $t$ -channel refers to scattering (Fig. 1.13a). The  $u$ -channel refers to scattering with identical final state particles where  $p_3$  and  $p_4$  are indistinguishable but the

momentum transfer is different between the two. At high energies where the mass of the proton can be ignored, the invariant mass of a proton–proton interaction is, therefore,  $M^2 \approx x_1 x_2 \sqrt{s}$  [4].

The sum of cross-sections for all possible processes, including diffractive, gives  $\sigma_{\text{tot}}$ . The total event rate is known as the *instantaneous luminosity*  $\mathcal{L}(t)$  and its integral is the *integrated luminosity*  $L = \int \mathcal{L}(t) dt$ . From these, one can calculate the total number of interactions,  $N = \sigma_{\text{tot}} L$  [4]. The instantaneous luminosity depends on many factors, including the collision frequency  $f = 1/(25 \text{ ns}) = 40 \text{ MHz}$ , the number of particles in the colliding bunches, and the cross-sectional area of the beams. Using the equation for the total number of interactions, one can calculate the cross-section of a given process by,  $\sigma = N/(L\epsilon)$ , where  $\epsilon$  contains selection efficiencies as well as the detector acceptances. Fig. 1.15 shows the vast scale for the cross-sections (and event rates at a given luminosity) of various processes; every about 100 seconds, one Higgs boson is produced by gluon fusion at the LHC. However, in the same time frame,  $10^{10}$  events have occurred, which must be filtered out by careful analysis.

ATLAS uses a right-handed Cartesian coordinate system. The  $x$ -axis points from the center of the detector, the interaction point (IP), towards the center of the LHC ring. The  $y$ -axis points upwards from the IP. The  $z$ -axis is along the beamline [77]. ATLAS uses cylindrical coordinates when referring to reconstructed objects in the transverse plane.  $p_T$  is defined as the momentum in the transverse plane to the beamline. The azimuthal angle,  $\phi$ , is defined to be around the beamline. The pseudorapidity,  $\eta$ , is defined as  $\eta = -\ln \tan(\theta/2)$ . For massless particles, the pseudorapidity is identical to the rapidity  $y = \frac{1}{2} \ln \frac{E+p_z}{E-p_z}$  [4]. This relation holds approximately for particles with  $E \gg m$ . The coordinate system is drawn in Fig. 1.16. These cylindrical coordinates are natural in hadronic colliding beams because differences in rapidity are invariant under boost along the beamline. As such, different collision events<sup>1</sup> can be directly compared (or filled into histograms) without needing to know the center-of-mass energy. A bonus is the interval of  $\eta$  or rapidity that spans from approx  $-2.5$  to  $2.5$  (or beyond for *forward* physics), close to the range  $-\pi$  to  $\pi$  for  $\phi$ , making clusters in  $\eta - \phi$  circular and the  $\Delta R = \sqrt{\Delta\eta^2 + \Delta\phi^2}$  measure<sup>2</sup> meaningful without needing to transform.

Partons cannot exist as free particles due to color confinement as explained in Sect. 1.1. Instead, a final state quark will radiate gluons that split into gluons or quarks, leading to a cascade or *shower* of quarks that cluster together to form hadrons when they reach energies below a few GeV. The final step of the process is known as *hadronization* [9] and is phenomenologically modeled by the Cluster Model [79] or the Lund String Model [80], the latter which is used by Pythia [81], where the clusters generated by the particle showers are still connected by QCD color strings. The Cluster Model forms independent clusters from the particle showers. The full theoretical picture is very complex and incomplete due to the non-perturbative nature of low-energy QCD [4].

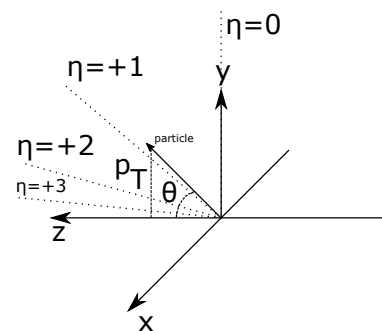
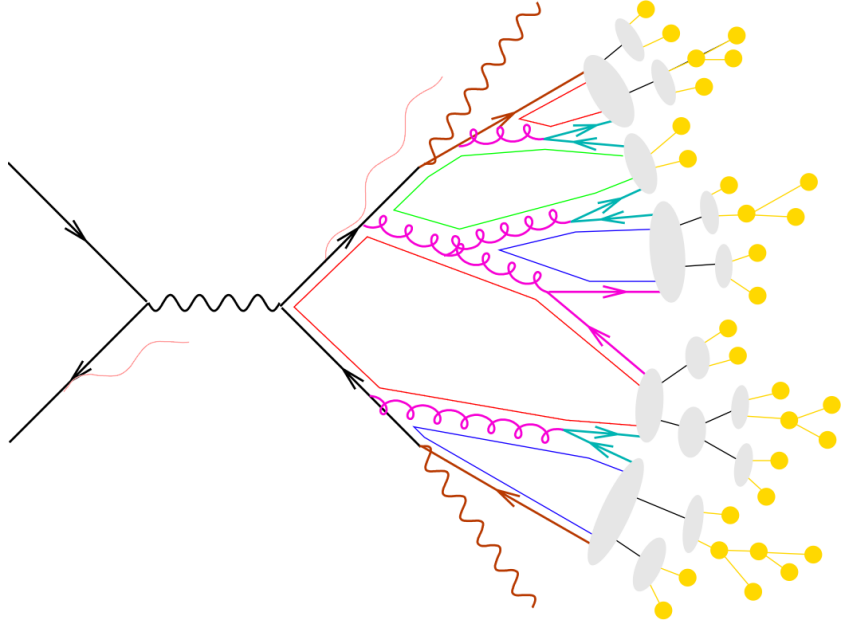


Figure 1.16:  $\eta$  is related to the angle  $\theta$  through  $\eta = -\ln \tan(\theta/2)$ . The  $x$ -axis points towards the center of LHC, the  $y$ -axis points upwards, and the  $z$ -axis points along the beam axis. The angle  $\phi$  (not drawn) is defined from the positive  $x$ -axis in the  $xy$ -plane. From [72].

<sup>1</sup> Henceforth simply referred to as events.

<sup>2</sup> The parentheses are omitted; the deltas of the values are squared.

Figure 1.17: Hard scatter (the two-to-two interaction) including ISR/FSR, particle showering (from the hard scatter until the gray ellipses), and hadronization (gray ellipses and yellow circles). Adapted from [78].



Barring color connections between the incoming partons, terms that are relevant to this work include (cf. Fig. 1.17) [9]:

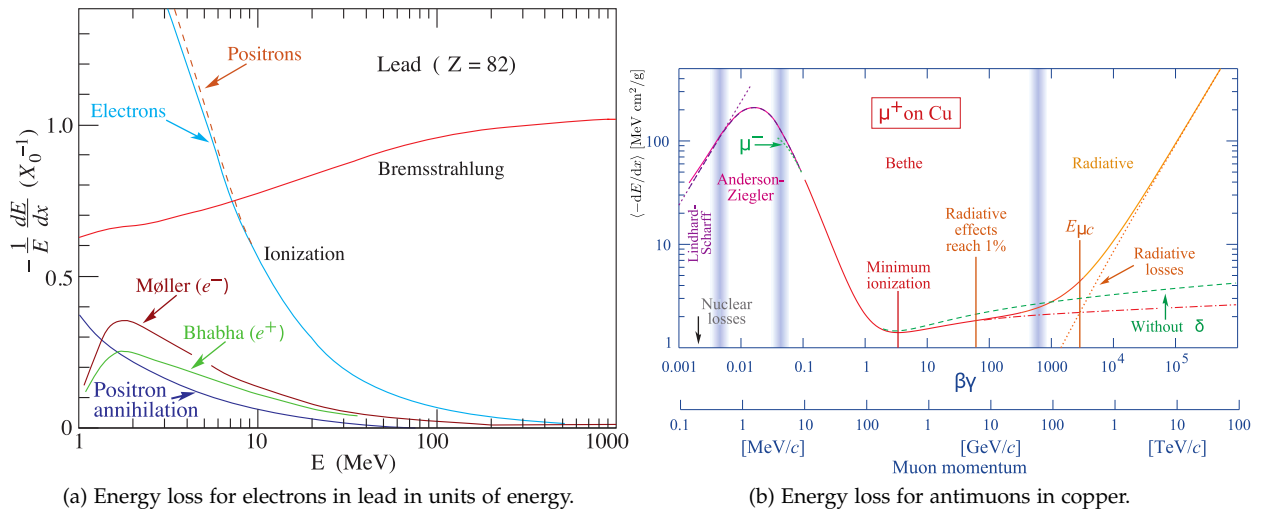
**The hard scatter/process (black lines):** A fraction of momentum ( $x$ ) is carried by the partons from the colliding protons (left-most lines). These partons interact and form a virtual particle known as the propagator (wavy line), which decays to two particles.

**Underlying event:** The remnants of the protons after the hard scatter as well as soft particles produced in the color field between the hard scatter and the remnants. This includes photons or gluons radiated by the incoming (initial state radiation (ISR)) and outgoing (final state radiation (FSR)) particles, shown as light pink wavy lines. The underlying event may contain additional interactions between the partons, known as multiple (parton) interactions (MPI), which may produce additional high- $p_T$  particles.

**Minimum bias:** A collision not producing any hard scatter. Most collisions are minimum bias (>99.99%). Multiple protons interact in ATLAS with up to about 55 [82] interactions per bunch-crossing in Run 2, known as "pileup". The term "pileup" also covers the average number of interactions per bunch-crossing  $\langle\mu\rangle$ .<sup>1</sup> These interactions happen a distance from the hard interaction along the beamline and can be somewhat suppressed by reconstructing the coordinates of the individual proton-proton interactions. Minimum bias from an earlier or later collision may interfere with measurements in the detectors and are known as out-of-time pileup.

<sup>1</sup> In other words, the loose term "pileup" is jargon for all non-hard-scatter collisions in an event as well as the term for the average number of these. To further the confusion, "pileup" may sometimes include the underlying event.

Electrons, with their very low mass, will primarily lose energy through bremsstrahlung ("braking radiation") at  $E > 7$  MeV when passing through absorbing matter (Fig. 1.18a). This effect is suppressed by a factor of  $1/m^2$ , which makes it negligible for heavier particles, e.g. it does not become relevant for muons until at least



several hundred GeV as shown in the last part of Fig. 1.18b as radiative losses [4, 70, 73]. In general, the energy loss per traversed length for intermediate energies can be described by the Bethe formula shown in the middle of Fig. 1.18b for muons. The formula depends, among others, on the element of the matter and the momentum of the projectile. The Bethe graph shows that muons are *minimum ionizing particles* (mips) in a rather large range of approximately 100 MeV to 100 GeV, meaning that they will pass through even dense detectors with minimal energy loss. Muons with higher momenta will lose some energy to bremsstrahlung, but will then reach energies where they become mips. At very low energies, particles (focusing on electrons in Fig. 1.18a) quickly lose energy by ionizing the traversed matter.

A characteristic traversal length through matter is the *radiation length*  $X_0$  defined as the distance a particle travels to reduce the energy by a factor of  $1/e$ . As electrons travel through (dense) matter, they will radiate bremsstrahlung photons, which will travel a distance before producing a pair of electrons from their interactions with the matter. This creates a cascade of pair-producing bremsstrahlung photons, which is the main loss of energy for the electrons. After traveling a distance of  $x$  radiation lengths, an electron will on average have an energy of  $E/2^x$ . This continues, until the energy of the electron becomes so low that it quickly loses all energy to ionization. In a detector, the energy of the radiated photons can be transferred by scintillators to be measured by photomultiplier tubes. For hadrons, the length scale is called (*nuclear*) *interactions lengths*.

Other sources of energy losses are delta rays coming from liberated matter electrons that ionize the matter and Coulomb scattering. Coulomb scattering only cause significant energy loss for electrons, but all particles will scatter randomly multiple times, which contributes significantly to the momentum uncertainty [70].

Figure 1.18: The mean stopping power ( $\langle -dE/dx \rangle$ ) for (a) electrons and (b) muons. Adapted from [73].



## **Part II**

# **Experimental setup**

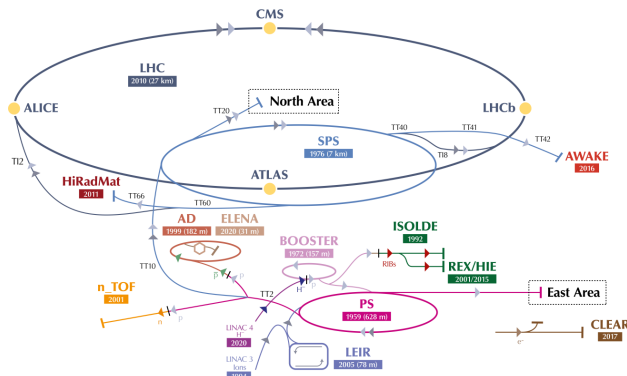


## 2 The ATLAS experiment

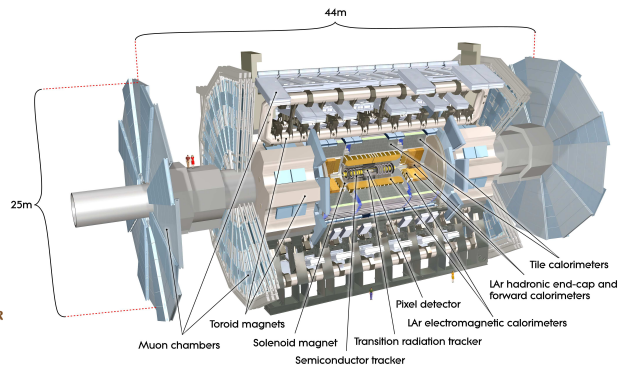
In this chapter, we will go through a short introduction to the Large Hadron Collider (LHC), on which ATLAS is one of four main detectors. Then we will see an overview of the ATLAS detector and delve into details regarding the relevant sub-detectors for this thesis.

### Contents

<b>2.1 The inner detector</b> . . . . .	<b>37</b>
2.1.1 The Pixel and Semiconductor trackers . . . . .	37
2.1.2 The Transition radiation tracker . . . . .	38
<b>2.2 The calorimeters</b> . . . . .	<b>39</b>
<b>2.3 The muon spectrometer</b> . . . . .	<b>40</b>
<b>2.4 Trigger and data acquisition</b> . . . . .	<b>42</b>



(a) The CERN detector complex



(b) The ATLAS experiment

The Large Hadron Collider (LHC), located at CERN, is a circular particle accelerator that accelerates counter-rotating beams of protons to 6.5 TeV each (or ions at lower energies) and brings them to collision in the four main experiments located on the ring [84]. The LHC can be seen in Fig. 2.1a, in which it accepts accelerated particles from the SPS with energies of 450 GeV in case of protons. During normal operations, the LHC cycles between injection (filling of ring), ramp (increase of energies), squeeze (reduction of beam size), stable beams (collisions which typically lasts 10-15 hours), and dump followed by ramp down (the beam is diverted into the cavern and the magnets are ramped down). The protons are clumped together in *bunches* with  $1.1 \cdot 10^{11}$  protons each. There is about 2500 colliding bunches  $n_b$  in

Figure 2.1: (a) The CERN detector complex picturing the accelerators and connected experiments. The protons in the LHC ring are created in a linear accelerator and passed to several circular accelerators before entering the LHC. Adapted from [83]. (b) The ATLAS detector with its sub-detectors and magnet systems. From [77].

the ring during operation.  $n_b$  as well as the beam focusing  $\beta^*$  at the interaction points increased during Run 2 [82]. The numbers for  $n_b$  and  $\beta^*$  and their influence on the luminosity and hence pileup are listed in Tab. 2.1 per year. The 50 ns bunch spacing run of 2015 and the high-pileup run during 2017 are not included.

Table 2.1: Some beam parameters leading to larger instantaneous luminosity and therefore pileup. When the instantaneous luminosity is converted to pileup a reference inelastic cross-section of 80 mb is assumed. From [82].

Parameter	2015	2016	2017	2018
$n_b$	2232	2208	2544	2544
$\beta^*$ (m)	0.8	0.4	0.3	0.3–0.25
Peak $\mathcal{L}(t)$ ( $10^{33} \text{ cm}^{-2}\text{s}^{-1}$ )	5	13	16	19
Approximate peak $\langle\mu\rangle$	16	41	45	55

<sup>1</sup> ATLAS is formed from the silly backronym, A Toroidal LHC ApparatuS.

The ATLAS detector<sup>1</sup> is a general-purpose detector [77] placed on one of the four interaction points of the LHC. The cylindrically shaped detector is also forward-backward symmetric along the beam-line. It consists of a middle, or *barrel*, part and two end parts, named *end-caps*. For the cylindrically shaped barrel, particles travel mainly transverse to the beam pipe through sub-detectors. For the end-caps, on the other hand, the sub-detectors are constructed as disks around the beam pipe, and particles will travel mostly transverse to the disks. The detector mainly consists of three sub-detectors: the inner detector that is responsible for tracking charged particles, the calorimeters that are responsible for stopping particles and measuring their energies, and finally the muon spectrometer that measures the muon momenta<sup>2</sup>. The sub-detectors and magnet systems are pictured in Fig. 2.1b, which shows the inner detector (Pixel detector, Semiconductor tracker (SCT), Transition radiation tracker (TRT)), the solenoid magnet, the calorimeters (LAr electromagnetic and tile calorimeters in the barrel, LAr hadronic end-cap and forward calorimeters and tile calorimeters in the end-cap and forward region), the toroid magnets, and finally the muon chambers for the muon spectrometer in the order from the interaction point and out.

<sup>2</sup> Muons are the only *detectable*, fundamental particles that escape the calorimeters. Neutrinos escape the detector without ever being detected directly.

Charged particles in a magnetic field will bend their trajectory towards the magnetic field lines. The inner detector and the muon spectrometer can measure the transverse momentum of a particle as this scales linearly as a function of the curvature and the strength of the magnetic field [70]. To measure energetic particles with relatively low uncertainty, a strong magnetic field is required. For this task, ATLAS has installed four magnets, which are the central solenoid between the inner detector and the electromagnetic calorimeter and three toroids around the muon spectrometers in the barrel and the two end-caps. The solenoid provides a 2 T axial magnetic field, and the toroids provide 0.5 and 1 T toroidal magnetic fields for the barrel and end-cap regions, respectively [77].

Some sub-detectors must be cooled to lower thermally induced noise. The Pixel and SCT are cooled to  $-7^\circ\text{C}$ , but the TRT must be heated to stay at  $20^\circ\text{C}$  [77].

## 2.1 The inner detector

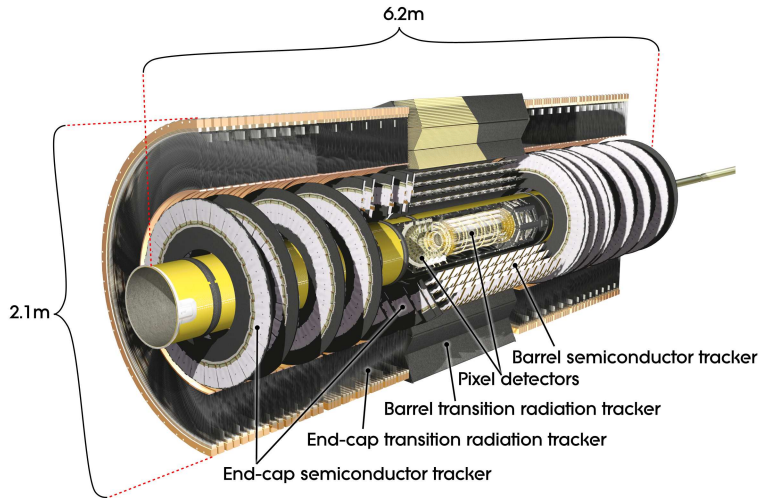


Figure 2.2: The inner detector. From [77].

The inner detector (shown in Fig. 2.2) consists of two silicon-based trackers (the Pixel and SCT) that provide precise tracking information, which consists of precise momentum resolution and especially precise angular resolution, and a straw tube tracker (the TRT) that adds similar momentum resolution due to its distance from the interaction point and the high number of hit straws on average. For the barrel and end-caps, the silicon trackers cover up to  $|\eta| < 2.5$ , while the TRT covers up to  $|\eta| < 2.0$ .

The silicon-based trackers can also measure the impact parameter of a track, which aids the identification of heavy quarks and  $\tau$  leptons. The TRT can detect transition radiation (TR) from high  $\gamma$  particles, which is used in electron identification.

### 2.1.1 The Pixel and Semiconductor trackers

The Pixel detector consists of 1744 individual pixel sensors with 47232 pixels each, totaling approximately 80 million readout channels. The sensors are made of  $n$ -type wafers [77]. The minimum pixel is  $50 \times 400 \mu\text{m}^2$  in  $R - \phi \times z$ . The modules are arranged in three layers in the barrel and three disks in each end-cap. The Pixel detector is placed close to the beam pipe; the first layer in the barrel is only 50 mm from the beamline (cf. Fig. 2.3). The Pixel modules have an intrinsic accuracy of  $10 \times 115 \mu\text{m}^2$  in  $R - \phi \times z$  in the barrel and in  $R - \phi \times R$  in the end-caps [77].

The Pixel additionally contains the Inner B-Layer (IBL) placed between the beam-pipe and the first layer of the Pixel detector. The IBL contributes significantly to the tracking performance as well as the identification of heavy quarks and  $\tau$  leptons.

In the barrel, the SCT sensors use strips of silicon parallel to the beamline with another set of strips crossing at a stereo angle of 40 mrad. The strip pairs are placed in four double layers in the barrel.

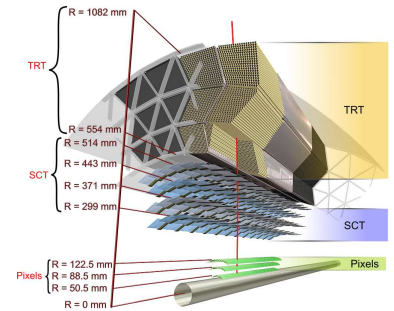


Figure 2.3: The layers of the sub-detectors of the inner detector. The IBL is not drawn. From [77].

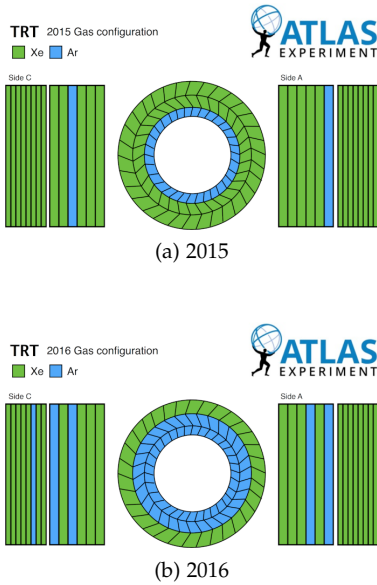


Figure 2.4: Gas configuration in the TRT modules for the years 2015 and 2016. From [85].

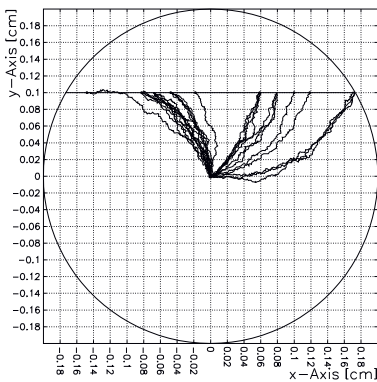


Figure 2.5: A simulation of electron drift in a 2 T field after an electron with 10 GeV energy passes through  $y = 0.1$  mm of the tube with standard xenon gas mixture at 20 °C and 1 atm pressure. The cascade near the wire is not shown. Adapted from [88].

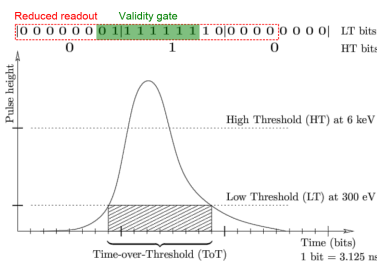


Figure 2.6: A pulse recorded by a straw and saved into the 27-bit word. From [89].

In the end-caps, the strips run radially with the second set of strips again crossing at an angle of 40 mrad. There are a total of 6.3 million readout channels. The SCT modules have an intrinsic accuracy of  $17 \times 580 \mu\text{m}^2$  in  $R - \phi \times z$  in the barrel and in  $R - \phi \times R$  in the end-caps [77].

### 2.1.2 The Transition radiation tracker

The TRT is a gas-filled straw tube tracker. The tubes are 4 mm diameter wide, 70  $\mu\text{m}$  thin-walled *straw tubes* of coated polymers with 31  $\mu\text{m}$  diameter gold-plated tungsten wires in the center [86, 87]. The wall is held at approximately  $-1500$  V with respect to the grounded wire. In the barrel, the approximately 140 cm long straws are parallel to the beamline and are split into two parts at  $\eta = 0$ . In the end-caps, the straws are placed radially in the wheels with a length of 37 cm. The TRT has approximately 350 000 readout channels [77]. Since the TRT straws only run along the beamline with no crossing straws, the TRT only provides  $R - \phi$  information in the barrel with an intrinsic accuracy of 130  $\mu\text{m}$  per straw [77].

The gas mixture is 70% xenon, 27%  $\text{CO}_2$ , and 3%  $\text{O}_2$ . During the years 2015 and 2016, the xenon gas has been replaced by argon in an increasing number of modules as shown in Fig. 2.4 due to leaks.

Charged particles traversing the straws, will create approximately 5 ionization clusters per mm [87]. The electrons will drift towards the wire due to the strong electric field and will end in a cascade close to the wire that amplifies the signal by 4 orders of magnitude. See Fig. 2.5 for a simulation of the ionization and drift.

For each straw, a 27-bit word is recorded over 75 ns [89], such that each bit is 3.125 ns. The word is split into three even windows (25 ns each), where the most significant bit is set if the high threshold was exceeded in that window and the remaining bits are set if the low thresholds were exceeded in the respective bits. The low threshold is set to around 300 eV and the high threshold (HT) is around 6 keV. See Fig. 2.6 for an example of this. Due to bandwidth limitations coming from increased luminosity, the four least significant bits are discarded and the signal must peak within the "validity gate" (green bits in figure). Only the middle HT is saved.

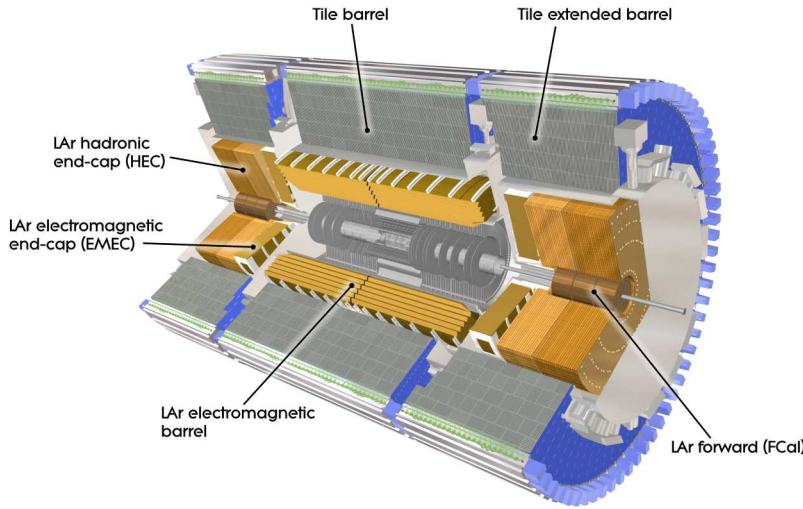
The TRT is capable of providing electron identification through the detection of TR photons created by ultra-relativistic ( $\gamma > 1000$ ) charged particles passing through the passive radiator material in front of the straws. This TR is identified by charge deposition that exceeds the HT, as xenon is efficient in absorbing the TR photons. Argon has a much lower efficiency in absorbing these photons but shows similar tracking capabilities [87]. The details of electron identification will be presented in Chap. 4.

The current TRT electron identification is calibrated using only simulated data. A study into deriving the calibration in data has been done. The study shows little improvement in identification but does eliminate issues with an increasing number of non-electrons at low

non-electron probability and correction factors that show regression in data only [90].<sup>1</sup>

Until recently, the TRT has only used the likelihood method for electron identification. A recent study [91] on simulated data using long short-term memory neural networks with all hits shows an improvement in background reduction of up to a factor of 2. The neural network is also less sensitive to increasing pileup.

## 2.2 The calorimeters



<sup>1</sup> This refers to the TRT analysis of this thesis.

Figure 2.7: The calorimeters. From [77].

The calorimeters consist of dense absorber material, with which particles will interact and lose energy through various radiative processes explained in Sect. 1.3, and active material, which will absorb the photons and convert them to electric signals.

The calorimeters of ATLAS serve different purposes. The high granularity liquid-argon (LAr) electromagnetic calorimeter with lead as passive material identifies and measures electrons and photons within  $|\eta| < 1.475$  in the barrel (ECAL) and  $1.375 < |\eta| < 3.2$  in the end-caps (EMEC), and the scintillator-tile hadronic calorimeter (Tile) with steel as passive material, which is split into a central part with extended parts on either side, measures hadrons within  $|\eta| < 1.7$  in the barrel [77]. In the end-caps, there is a LAr hadronic calorimeter in the ranges  $1.5 < |\eta| < 3.2$  (HEC). Beyond this, there is a LAr calorimeter (FCAL) for electromagnetic and hadronic energy measurements in the ranges  $3.1 < |\eta| < 4.9$ . The calorimeters can be identified in Fig. 2.7.

The ECAL is accordion-shaped to give full coverage in  $\phi$ . This can be seen in Fig. 2.8, which shows the three barrel layers of the ECAL. The first layer is only coarsely segmented in  $\phi$  but very finely in  $\eta$ . The read-out electronics is at the back for layers 2 and 3, but in front of the ECAL for layer 1. There is a pre-sampler – a layer 0

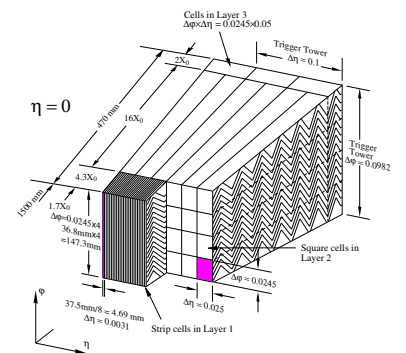


Figure 2.8: The three layers of the ECAL after the pre-sampler. From [77].

– in front of the ECAL up to  $|\eta| < 1.8$ , which measures the energy lost in front of the ECAL [77]. The second layer has a depth of  $16 X_0$ , which captures the majority of the electron and photons even at high energies.

The sizes of the calorimeters are determined by the containment of particle showers needed in terms of radiations lengths  $X_0$  (for electromagnetic particles) and interactions length  $\lambda$  (for hadronic particles). The ECAL extends to  $> 22X_0$  in the barrel and  $> 24X_0$  in the end-caps. The hadronic calorimeters cover approximately  $10\lambda$ .

### 2.3 The muon spectrometer

Figure 2.9: The muon spectrometer. From [77].

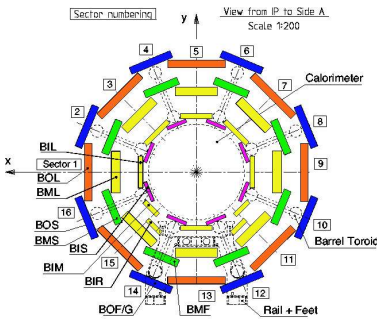
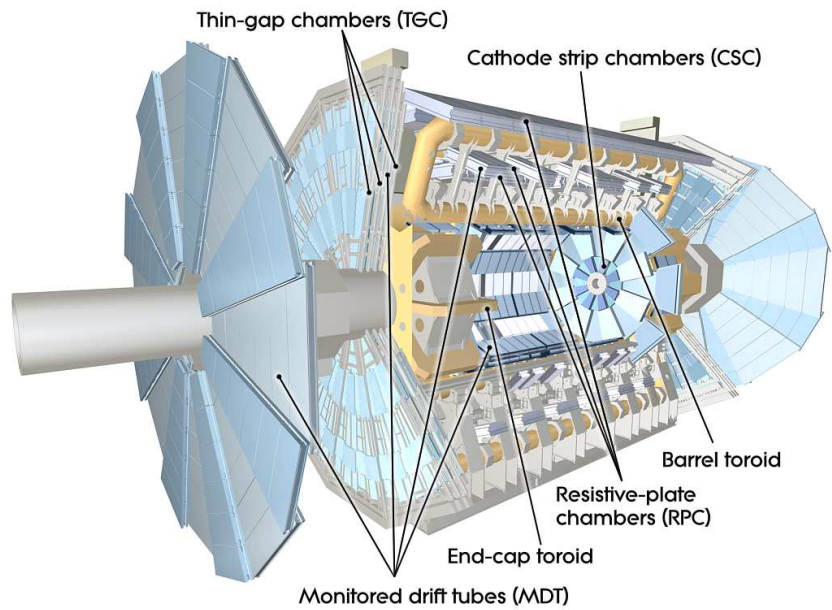


Figure 2.10: A cross-section of the MS in the barrel with the toroid magnet system in-between. From [77].

The muon spectrometer (MS) consists of several subsystems, which are mainly responsible for either tracking or triggering. The subsystems encompass the calorimeters together with the toroid magnet system (see Fig. 2.9). The muon chambers and toroid magnets are intertwined as seen in Fig. 2.10 with a gap at  $|\eta| < 0.1$  for cabling. This outer part is rather large and mainly responsible for giving ATLAS the diameter of 25 m compared to the 15 m of CMS.

Muons are mips (cf. Sect. 1.3), so they will traverse the calorimeters, and since they are the only known particles (except for the neutrinos, of course) to do so, one can measure the momenta of the tracks left in the MS by charged particles under the assumption that these are left by muons. The magnetic field to bend the muon tracks is provided by the barrel toroid for  $|\eta| < 1.4$ , by the end-cap toroids for  $1.6 < |\eta| < 2.7$ , and both the barrel and end-caps toroids in  $1.4 < |\eta| < 1.6$  [77].

The four subsystems, which will be detailed in a moment, are each placed in multiple layers in the barrel and end-caps. The first two

subsystems measure the track coordinates in the  $r - z$  plane (the bending plane), from which the muon momentum can be derived. The last two subsystems provide trigger information and additionally provide coordinate information in the  $r - \phi$  plane (the non-bending plane) [92].

The four subsystems are [77]:

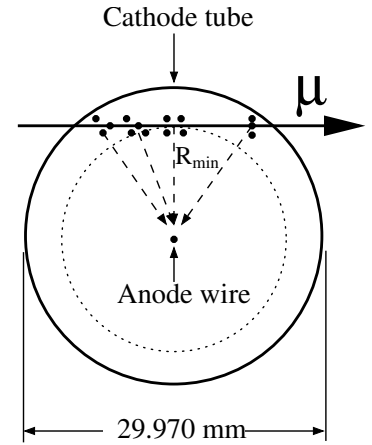
**Monitored Drift Tubes (MDTs):** These modules, consisting of several drift tubes, measure track coordinates with high precision – resolutions in  $z$  of approximately  $80\ \mu\text{m}$  per tube or  $35\ \mu\text{m}$  per module – within  $|\eta| < 2.7$  (though only  $|\eta| < 2.0$  for the innermost layer). The drift tubes are similar to those of the TRT as in they are held at a potential (about  $-3000\ \text{V}$ ) with respect to a tungsten-rhenium wire that will pull electrons that have been ionized by the gas (93% argon and 7  $\text{CO}_2$ ) towards the wire as drawn in Fig. 2.11a. The MDTs are unable to unambiguously provide coordinate information for more than one track per chamber, but collinear muons can still be unambiguously resolved using the inner detector (more on this in the reconstruction chapter, Sect. 3.3).

**Cathode Strip Chambers (CSCs):** These multiwire proportional chambers are placed in the end-caps only with wires running radially from the center with strips perpendicular to the wire, from which signals are read out, as shown in Fig. 2.11b. The chambers operate at  $1900\ \text{V}$  with a gas mixture of 80% argon and 20%  $\text{CO}_2$ . These strips measure track coordinates in the bending plane with resolutions of approximately  $60\ \mu\text{m}$  per plane or  $40\ \mu\text{m}$  per chamber in the range  $2.0 < |\eta| < 2.7$ . There are additional strips parallel to the wires that give  $\phi$  coordinates with resolutions of  $5\ \text{mm}$ . The CSCs are capable of disambiguating two tracks and provide accurate  $\eta$  and  $\phi$  information for each due to the different pulse heights left by the tracks.

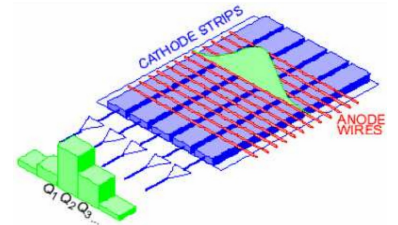
**Resistive Plate Chambers (RPCs):** The chambers consist of parallel resistive plates with a gas mixture of primarily  $\text{C}_2\text{H}_2\text{F}_4$ . The transverse and longitudinal strips shown in Fig. 2.12a provide triggering information as well as coarse track information within  $|\eta| < 1.05$  with  $10\ \text{mm}$  resolutions in  $z$  and  $\phi$ .

**Thin Gap Chambers (TGCs):** The TGC is also a multiwire proportional chamber (Fig. 2.12b). It contains 55%  $\text{CO}_2$  and 45% n-pentane with a  $2900\ \text{V}$  potential between its wires and the plates. It provide triggering information in the range  $1.05 < |\eta| < 2.4$  as well as track information with up to  $6\ \text{mm}$  in  $R$  and up to  $7\ \text{mm}$  in  $\phi$ .

All three chambers (the MDT is not included) have adequate time resolutions ( $7, 1.5,$  and  $4\ \text{ns}$  in the above order), making it possible to tag beam-crossings. The trigger chambers, the RPCs and TGCs, require coincidence between the last three layers to generate a trigger with the curvature of the track matching well-defined  $p_T$  thresholds, where the TGCs can provide this information up to  $|\eta| < 2.7$  [77].

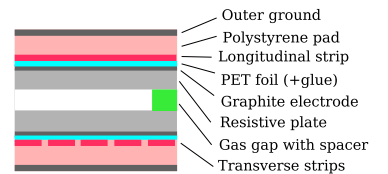


(a) A cross-section of an MDT tube. From [77]

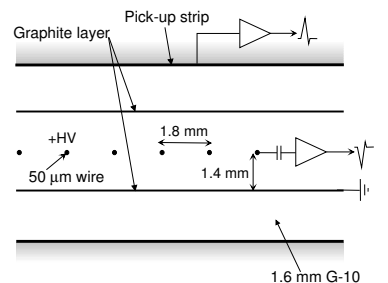


(b) The CSC wires and strips with a pulse across one wire. Adapted from [77]

Figure 2.11: The precision measurement subsystems of the MS.



(a) A cross-section of an RPC. Adapted from [77]

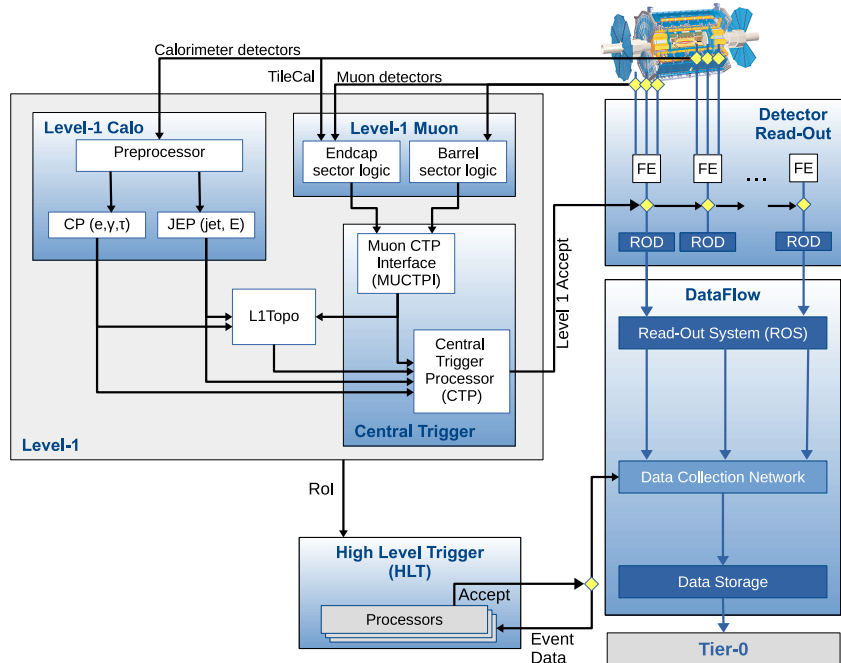


(b) The TGC structure with the wires and strips. From [77]

Figure 2.12: The triggering subsystems of the MS.

## 2.4 Trigger and data acquisition

Figure 2.13: The ATLAS TDAQ flow chart showing the process by which sub-detector information is handled by the L1 and passed to the HLT. Adapted from [84].



The ATLAS trigger and data acquisition (TDAQ) is responsible for deciding which collisions are saved as they occur every 25 ns (rate = 40 MHz) [84, 93, 94]. This is done in two steps that bring the initial 40 MHz down to approximately 100 kHz using an analog system named the first level trigger (L1) and further down to approximately 1 kHz using a software-based trigger running on a cpu farm named the high-level trigger (HLT). The L1 will evidently make fast decisions using rudimentary reconstructions of the events – by defining regions of interest (RoIs) – within the 2.5  $\mu$ s windows (to keep the output rate at 100 kHz) and pass these triggered events to the much slower HLT, which is capable of performing more complex reconstructions to reject more background.

The flow is shown in Fig. 2.13. The L1Calo takes input from the calorimeters and identifies candidates for electrons, photons,  $\tau$ -leptons, jets, and missing transverse energy from clusters in the calorimeter. The L1Muon determines curvatures from hits in RPCs and TGCs as mentioned in the previous section. For L1-triggered events, data from the sub-detectors is sent to the HLT along with the RoIs. The HLT has the full detector information available from the calorimeters, MS, and the ID, which are not available at L1. The HLT will reconstruct events within the RoIs. While the HLT uses the same software as the offline reconstruction, much work has gone into making it as fast as possible, including selecting particle candidates in steps and stopping immediately when a criterion is not met.

## 3 Reconstruction

The previous chapters introduced the particles of the Standard Model and their interactions in hadronic colliders (Chap. 1) as well as the sub-detectors of the ATLAS detector (Chap. 2), which record the results of these interactions. It is now time to connect these and look into how an event recorded by the ATLAS detector is related back to the fundamental particles that are produced in a collision. This act is called reconstruction. In this chapter, we will introduce vertices, tracks, and clusters, which are integral for the reconstruction of leptons and jets.

### Contents

<b>3.1 Tracks and vertices</b> . . . . .	<b>44</b>
<b>3.2 Electrons</b> . . . . .	<b>45</b>
<b>3.3 Muons</b> . . . . .	<b>47</b>
<b>3.4 Jets</b> . . . . .	<b>48</b>
<b>3.5 Event reconstruction quality</b> . . . . .	<b>50</b>

Collision events<sup>2</sup> are reconstructed several times from the raw data recorded by ATLAS into objects that are used in analysis, first by the triggers and then finally offline. In Sect. 2.4, the trigger system was introduced, in which it was stated that preliminary reconstruction is done already at the L1 trigger and afterwards in the HLT. The raw data as well as objects and decisions made by the triggers are written to disk.

The L1 and HLT triggers identify particles of specific types under given conditions using algorithms called "triggers", and their names follow this convention [94]:

[Trigger level]\_[object multiplicity][object type][minimum transverse energy in GeV],

with details listed in Tab. 3.1. The trigger level may refer to L1 or HLT and is often omitted. The object multiplicity is omitted for single-particle triggers. The type refers to photons "g" or electrons "e" for HLT triggers. The L1 trigger seeding the HLT trigger is sometimes added as a suffix. As an example, the trigger named e24\_lhmedium\_L1EM20VH fires when the HLT identifies an electron candidate with  $E_T > 24$  GeV and passing LHMedium identification coming from the L1 seed of an EM cluster with an average  $E_T$  of 20 GeV, depending on  $\eta$ , and with an additional hadronic veto.

To keep the output rate from the L1 and HLT triggers level, triggers that fire too often, due to increased activity, are ignored following a probabilistic decision-maker [94]. This is called *prescaling*, and

<sup>2</sup> Non-collision events such as cosmic muon calibration runs are not considered in this.

		Photons	Electrons
HLT	Identification	loose, medium, tight	lhvloose, lhloose, lhmedium, lhtight
	Isolation	icalovloose, icalotight	ivarloose
	"nod0"	-	Transverse impact parameter not used ("no d0")
	"etcut"	-	$E_T$ -only requirement applied in the HLT
L1	"V"	-	$\eta$ -dependence of $E_T$ threshold
	"H"	-	Veto on hadronic activity

Table 3.1: Some suffixes and their meanings for photon and electron triggers. From [94].

extra care in calculating the recorded luminosity must be taken when using prescaled triggers. Many analyses use *unprescaled* triggers since they often have higher  $p_T$  requirements anyway.

Triggers for electrons (and photons) at the L1 use a sliding window called a *trigger tower* of size  $4 \times 4$  and granularity  $0.1 \times 0.1$  in  $\eta \times \phi$  in the ECAL to build the RoI [94], in which the  $E_T$  is calculated and used as input for the different thresholds (20 GeV in the case of the previously named trigger). A similar tower is built in the hadronic calorimeter to apply the hadronic veto to electrons if the  $E_T$  in the hadronic tower exceeds an  $E_T$ -dependent threshold. Similarly, the isolation requirement fails the  $E_T$  of any tower around the RoI in the ECAL exceeds an  $E_T$ -dependent threshold.

Recorded events are processed using the full offline reconstruction framework using the raw and trigger data. This step reconstructs tracks, vertices, leptons, jets, and more, and saves these in datasets to disk. While these datasets can be used in analysis, they are incredibly large in size (at least hundreds of terabytes), due to the number of events recorded and the information recorded and constructed for the events. In ATLAS, these datasets are converted to the xAOD format, which keeps much less raw information. For analyses, even the xAOD datasets are too large, and derived datasets, or DxAODs, are made, which remove irrelevant events using simple selections in accordance with signal signatures (e.g. for signals with a leptonically decaying  $Z$ , at least two leptons with invariant mass above 50 GeV) and unused objects and lastly unused variables for the remaining objects. These DxAOD datasets will be on the order of percent in size compared to their xAOD parent datasets. Even then, an analysis may require many DxAODs with a total size of tens or hundreds of terabytes.

The remaining sections of this chapter are dedicated to the reconstruction of objects used by the analyses in this thesis and will end with some universal selections used to clean events.

### 3.1 Tracks and vertices

As charged particles pass through the ID, they are detected by the *hits* that they leave in the different layers. Their paths, or *tracks*, can be reconstructed by connecting the hits [95, 96]. The tracks are seeded by

three-dimensional coordinates, or *space points*, created from the hits in the Pixel and SCT sub-detectors and extrapolated through to hits in outer layers using the Kalman filter [97], which extrapolates tracks to the next layers by inverting small covariance matrices, compares the extrapolations to the actual hits, and detects outliers by their higher contribution to the  $\chi^2$  of the evolving fit [70, 96]. Tracks that fail reconstruction may be retried under an electron hypothesis that accounts for bremsstrahlung, if  $p_T > 1$  GeV and the track failed to gather at least 7 Pixel and SCT hits [95]. The first step creates many track candidates, which must be cleaned for shared hits, incomplete tracks, and fake tracks that do not originate from single charged particles (ie. noise or many crossing particles) [96]. Finally, the track candidates are extended into the TRT, and tracks are refitted using all sub-detectors.

Tracks can also be formed from seeds in the TRT in order to find particles from secondary decays and converted photons, which are photons that have pair-produced to real electron pairs [96]. These converted photons originate from secondary vertices within the ID and can be identified by regular or the TRT tracks.

Primary vertices are formed from tracks that are extrapolated back to the beam spot [70, 96]. Only tracks that pass the following criteria are considered in vertex formation [98]:

- $p_T > 400$  MeV
- $|\eta| < 2.5$
- Number of Pixel+SCT hits  $\geq 9$  for  $|\eta| \leq 1.65$  and  $\geq 11$  for  $|\eta| > 1.65$
- At least one IBL hit
- No Pixel holes<sup>1</sup>
- At most one SCT hole

A vertex requires at least two passing tracks.

Tracks are parameterized in  $(z_0, d_0, \theta, \phi, q/p)$  from the *perigee* point, which is defined as the point of closest approach to the beamline.  $z_0$  is the longitudinal impact parameter and is the distance from the perigee to the origin.  $d_0$  is the transverse impact parameter and is the shortest distance from the track to the beamline. Usually, the significance of  $d_0$  is used to suppress fake tracks.  $q/p$  is the track curvature defined as the inverse of the momentum, where the sign of  $q$  is the sign of the charge and hence the curvature of the track.

## 3.2 Electrons

Electrons and photons produce similar signatures in the ECAL, which is reflected in the reconstruction. During the reconstruction of electrons, several steps are taken to disambiguate them from converted and non-converted photons. Therefore, this section will occasionally cover photons when needed. Electron candidates are created from *superclusters* made from *topo-clusters*, which are topologically connected ECAL or HCAL cells, and matched to tracks from the ID. The steps

<sup>1</sup> A hole is a Pixel point, which is passed by the track but was not registered by the point. A veto on holes suppresses fake tracks.

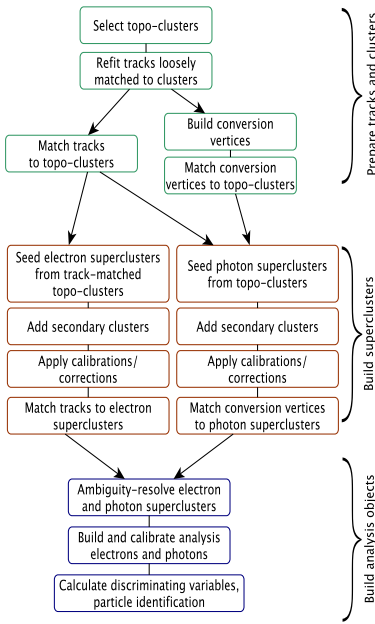
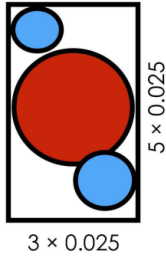


Figure 3.1: The steps in reconstruction of electrons and photons. Adapted from [99].

### All $e^\pm, \gamma$ :

Add all clusters within  $3 \times 5$  window around seed cluster.



### Electrons only:

Seed, secondary cluster match the same track.

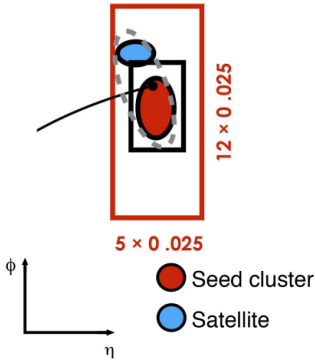


Figure 3.2: The electron supercluster. Adapted from [99].

leading up to the supercluster formations are as follows [99] (see also Fig. 3.1).

Topo-clusters [100] are formed by seed cells in the second layer of the ECAL. A cell with significance  $|\rho_{\text{cell}}^{\text{EM}}| > 4$ , where  $\rho_{\text{cell}}^{\text{EM}} = E_{\text{cell}}^{\text{EM}} / \sigma_{\text{noise,cell}}^{\text{EM}}$ , seeds a topo-cluster.  $\sigma_{\text{noise,cell}}^{\text{EM}}$  is the expected noise in that cell and includes electronic noise and noise from the level of pileup. All neighboring cells with  $|\rho_{\text{cell}}^{\text{EM}}| > 2$  are added until the cluster is surrounded by cells with  $|\rho_{\text{cell}}^{\text{EM}}| < 2$ . Clusters are combined if they merge at this step. Finally, all cells immediately neighboring the clusters are added. Clusters are split if they contain multiple cells with  $E_{\text{cell}}^{\text{EM}} > 500$  MeV, at least four neighbors and no neighbor with a larger signal. At this stage, the topo-clusters are formed.

Tracks that loosely match fixed-size clusters in the ECAL are refitted with the Gaussian Sum Filter (GSF) algorithm, which is more general than the Kalman filter and less sensitive to bremsstrahlung [101]. The tracks are then matched to the topo-clusters. If multiple tracks match the same topo-cluster, a ranking system is employed that, among other things, prioritizes tracks with more Pixel hits.

Conversion vertices for converted photons are reconstructed from the regular and TRT-seeded tracks, which are required to be identified as electrons by the TRT PID. Several steps are taken to identify single- and double-track conversions and lower the fraction of unconverted photons. The vertices are then matched to the topo-clusters.

Superclusters are then seeded by the  $E_T$ -leading topo-clusters, if they pass  $E_T$  and ID hit requirements and have not been used already in another supercluster. Topo-clusters in windows of  $0.075 \times 0.125$  in  $\Delta\eta \times \Delta\phi$  are added as satellites (first box of Fig. 3.2). Topo-clusters in a larger window of  $0.125 \times 0.300$  (second box) are added as satellites if their associated tracks are the same as the tracks associated to their seeding clusters.

Electron and photon superclusters are built independently and are therefore disambiguated by considering the possibly matched tracks and their number of hits and the possibly matched conversion vertices. This step may fail to disambiguate the clusters, and the failed objects are placed in both containers with the "ambiguity" author.

Calibrations are applied both before and after disambiguation, including calibrations on the energy scale. Variables pertaining to shower shapes, discrimination, etc. are calculated.

The quality of a candidate is asserted through different selection criteria that *identify* the object to some level. Electrons are identified using a series of likelihoods [99] for different energy and  $\eta$  ranges, which use shower shape variables calculated from their clusters, matching between cluster and track, and the TRT electron PID. The identification seeks to reject especially hadronic jets (for which a rejection factor of about 100 000 is needed at low energies, if memory serves). Three working points (WPs) offer an increasing level of signal purity at the expense of signal efficiency, namely *LooseLH*, *MediumLH*,

and *TightLH*. The target signal efficiencies are quoted as 93%, 88%, and 80%, respectively. However, the efficiencies of the selections depend on energy and  $\eta$  with the loose WP having a signal efficiency of at least 86% and the tight at least 58% for any  $\eta$  and energy [99].

A separate approach to the suppression of electrons from hadronic decays is known as *isolation* [99]. The hadronic decays lead to larger activity in the ID and calorimeters. Isolation is defined as the sum of  $p_T$  of tracks ( $p_T > 1$  GeV per track) or clusters, respectively, in a cone of size  $\Delta R = \sqrt{\Delta\eta^2 + \Delta\phi^2}$  around the object in question, where the object itself is not included in the sum. The isolation in the calorimeter must be less than 20% (6%) of the electron's  $p_T$  for a cone of size  $\Delta R = 0.2$  for the loose (tight) WP. The track isolation requires 15% (6%) for a cone of size  $\Delta R = \min(10 \text{ GeV}/p_T, 0.2)$ . A WP, *HighPtCaloOnly*, efficient for highly energetic electrons, has a threshold of 3.5 GeV on the sum of clusters in a cone of  $\Delta R = 0.2$ .

### 3.3 Muons

Muons are created from tracks reconstructed at least either in the muon spectrometer or inner detector.

Independent track segments are created in the various chambers of the MS. Muon track candidates are fitted using the hits of these segments. Muon tracks can share some of their segments with other muons to allow for very collinear muons. During the full  $\chi^2$  fits of candidates, hits may be removed or added. There are four types of muons that differ by the ability to reconstruct the muons' traversal through the whole detector [102]:

**Combined (CB) muons** are reconstructed from tracks in the MS and ID, which are refit as a combined track.

**Segment-tagged (ST) muons** match an ID track with track segments in the MDT or CSC<sup>1</sup> of the MS. These types of muons are created when only one MS layer can be matched to the muon.

**Calorimeter-tagged (CT) muons** are ID tracks matched with low energy deposit in the calorimeters left by mips. Due to their low purity, these types of muons are only reconstructed in  $|\eta| < 0.1$  to recover lost acceptance.

**Extrapolated (ME) or stand-alone (SA) muons** are MS tracks that, accounting for energy loss, loosely extrapolate back to the interaction point. These types of muons are created in the  $2.5 < |\eta| < 2.7$  range to compensate for the lack of the ID.

The order listed is the priority given to the different types when different types of muons share the same ID track.

Muon identification primarily relies on minimum requirements on the number of hits in the different sub-detectors. For all types but the extrapolated muons, a minimum number of Pixel and SCT hits are independently required as well as a successful TRT extension for the three inclusive WPs (loose, medium, and tight). Additionally, for the medium and tight WPs, the tracks must have a minimum number

<sup>1</sup> These are the two precision measurement subsystems.

of hits in the MS. Combined muons have further requirements on the significance of the  $q/p$  imbalance between the ID and MS tracks as well as the  $p_T$  imbalance between ID and MS tracks against their combined  $p_T$  to suppress fakes from hadronic activity. To further suppress fakes, the tight WP also selects on the normalized  $\chi^2$  of the combined fit [102]. All four muon types are considered for the loose WP. For the medium WP, only CB and ME muons are used. Finally, only CB muons can pass the tight WP. Almost all loose muons are combined. For  $20 < p_T < 100$  GeV, the signal efficiencies are approx. 98%, 96%, and 92% for loose, medium, and tight WPs, respectively, according to Ref. [102]. These values may have changed since the publication. Two special WPs can be used for very low  $p_T$  ( $p_T < 5$  GeV) and very high  $p_T$  muons ( $p_T > 300$  GeV).

Isolation for muons are similar to that of electrons. The isolation in the calorimeter must be less than 30% (6%) of the electron's  $p_T$  for a cone of size  $\Delta R = 0.2$  for the loose (tight) WP. The track isolation requires 15% (6%) for a cone of size  $\Delta R = \min(10 \text{ GeV}/p_T, 0.3)$ . The efficiency of the loose WP is 96% at 15 GeV and increases steadily for higher transverse momentum according to Ref. [102]. These values may also have changed since the publication. A WP, TightTrackOnly, has a threshold of 6% for a cone of size  $\Delta R = \min(10 \text{ GeV}/p_T, 0.2)$ .

### 3.4 Jets

The physical process of forming jets in the detector was covered in Sect. 1.3. In this section, the jets will be reconstructed from topo-clusters<sup>1</sup> in the HCAL [100, 103] by the anti- $k_t$  algorithm [104] with  $R = 0.4$  using Fastjet [105].

The anti- $k_t$  algorithm belongs to a class of sequential recombination algorithms along with the  $k_t$  [106] and Cambridge/Aachen [107] algorithms, differing only by the power of the energy scale in the distance measure [104]. The distance measure and its upper limit per jet are defined as,

$$d_{ij} = \min \left( k_{ti}^{2p}, k_{tj}^{2p} \right) \frac{\Delta R^2}{R^2}, \quad \Delta R^2 = (y_i - y_j)^2 + (\phi_i - \phi_j)^2, \quad (3.1)$$

$$d_{iB} = k_{ti}^{2p}, \quad (3.2)$$

where  $k_{ti}$ ,  $y_i$ , and  $\phi_i$  are the transverse momentum, rapidity, and azimuthal angle of particle  $i$ , respectively.  $p = 1$  and  $p = 0$  recover the  $k_t$  and Cambridge/Aachen algorithms, respectively, while  $p = -1$  is named the anti- $k_t$  algorithm.  $R = 0.4$  is the radius parameter. The distance metric  $d_{ij}$  has two parts, the energy scale and  $\Delta R$ . The algorithm combines two topo-clusters  $i$  and  $j$ , which have the smallest  $d_{ij}$ . The  $p = -1$  in the energy scale ensures that the size of the metric is determined by the hardest<sup>2</sup> particle, while  $d_{ij}$  between two soft particles will be larger. As such, soft topo-clusters will combine with harder topo-clusters. The process continues until  $d_{iB} < d_{ij}$ , at which point the combined topo-cluster is called a jet and is removed from the list. The combination then continues with the smallest  $d_{ij}$ . Due

<sup>1</sup>The process of forming topo-clusters was introduced in the previous section.

<sup>2</sup>Jargon for the  $p_T$ -leading.

to  $p = -1$ , jets will be circular around the leading topo-cluster component. If two jets are within  $2R$  of each other, the leading jet 1 will be circular, overlapping the sub-leading jet 2, in case of  $k_{t1} \gg k_{t2}$ . If their transverse momenta are similar, they will divide the area among them. The result of an example event is shown in Fig. 3.3.

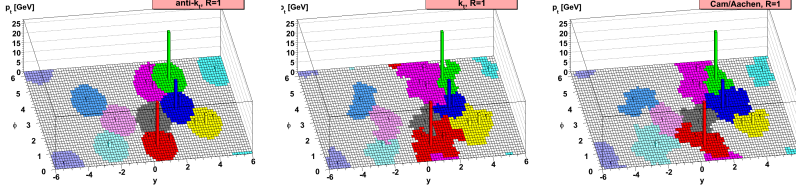


Figure 3.3: The jets formed by the anti- $k_t$ ,  $k_t$ , and Cambridge/Aachen algorithms, respectively. From [104].

The Cambridge/Aachen algorithm is used to make  $R = 1.0$  *large-R jets*, which better capture the soft substructures within their cones since the distance metric is independent of energy.

While the anti- $k_t$  algorithm is less sensitive to soft components, which may lead to large jet areas for the other algorithms [104], several steps are needed to correct for contributions from the underlying event, pileup, and detector effects [108]. They include, in the following order:

**Origin correction:** The origin of the jet is moved to the primary vertex of the hard scatter without changing the energy.

**Pileup correction:** The contribution from pileup jets is subtracted from the energy of the jet, based on the pileup of the event and jet area.

**Jet energy scale:** The jet energy scale (JES) is corrected by applying scale factors derived from simulation. An example is shown in Fig. 3.4.

**Global calibration:** The energy is further improved using calorimeter, MS, and track-based variables.

**In situ calibration:** A final correction is applied to jets in real data using calibrations derived in situ.

Jets originating from pileup are suppressed by the jet vertex tagger (JVT) [109], which assigns a probability for whether the jet originates from the hard scatter. It is applied to jets with  $p_T < 60$  GeV to improve purity in a regime otherwise dominated by pileup.

While there are means of identifying whether a gluon or a quark originally initiated the jet (although the distinction is ill-defined [110]), only discrimination between jets initiated by heavy and light quarks is efficient.

Some jets can be reconstructed from processes other than the hard scatter at the interaction point such as proton collision in the beam pipe, cosmic rays, and calorimeter noise [111]. Since these "fake" or "bad" jets do not originate from proton-proton collisions, they must be identified through *jet cleaning* and disregarded in the analysis. Jet cleaning has two WPs, LooseBad and Tight. The former is used in most analyses.

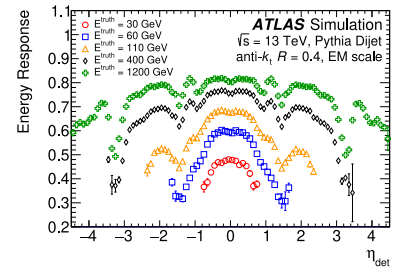


Figure 3.4: The jet energy response  $E_{\text{reco}}/E_{\text{truth}}$  as a function of the jet  $\eta$  calculated from the geometric center of the detector for jets at different energies. From [108].

### 3.5 Event reconstruction quality

Several factors from detector malfunction to improper reconstruction and non-collision backgrounds are taken into account when determining the quality of an event. The list includes but is not limited to:

**Good Runs List (GRL):** The GRL [112] marks parts of runs as bad at the luminosity block ("lumiblock", 1-minute intervals) level if they are deemed unusable by any sub-detector or data quality groups. There are many reasons to mark a lumiblock as bad such as bad calibrations, noisy channels, etc.

**Primary vertex:** An event may seldom be reconstructed with no vertex. An event must have at least one primary vertex with two tracks.

**Event cleaning:** Several defects not covered by the GRL are grouped into the selection known as "event cleaning". The event may contain corrupted data from the ECAL, the Tile calorimeter, the SCT, or due to a mid-run restart.

**Bad jet veto:** Since the fake jets (mentioned in the previous section) may interfere with the reconstruction of hadronic jets, an event must be discarded if a fake jet otherwise passes for a real jet [111]; if a jet passes the JVT and overlap removal<sup>1</sup> (as well as the kinematic selections,  $p_T > 20$  GeV and  $|\eta| < 2.8$ ), and is identified as a fake jet, the event is discarded.

<sup>1</sup>Disambiguating different objects built from the same information in the event, e.g. an electron and muon sharing the same ID track. The precise approach will be defined in Sect. 9.3.

## **Part III**

# **Performance analysis: TRT electron identification**



# 4 Analysis overview

We will obtain an overview of the calibration of the TRT PID from the theoretical to the technical aspect. The particle identification section is taken from Ref. [113].

## Contents

---

<b>4.1 Particle identification</b> . . . . .	<b>54</b>
--	-----------

---

The performance of particle identification (PID) using the TRT is measured using LHC data recorded by ATLAS during 2016 as well as simulated data. Calibrating in data allows for the full use of the correction factors used by the TRT's electron PID tool. Calibration of the PID tool using data is feasible due to the tag and probe (T&P) method, which provides *unbiased* and reasonably pure electron candidates as input for the calibration. T&P combines one tightly identified electron (which shall be called the tag) with one electron candidate for which no *TRT-provided* ID selection is applied (called the probe). Finally, the method requires that the invariant mass of the pair is close to the Z boson mass. Since the tool to be calibrated has not been used to select the probe, the selection is said to be unbiased, and the probe is then used in the calibration. For background (non-electrons), muons are used because their mass are similar to that of pions, and they leave similar tracks in the TRT<sup>2</sup>. Specifically, muons from Z decays are used as they have comparable kinematics to the selected electrons and can be similarly identified using the Z mass constraint.

<sup>2</sup> Any effect from hadronic interactions between actual non-electrons such as pions, kaons, protons, etc. and the TRT is assumed to be minor.

This analysis is separated into the following chapters, whose contents are shortly listed as well:

**Selections:** An initial event pre-selection is applied; electron and muon pairs are separately identified, and all electron probes per event are saved; finally, some preprocessing is done.

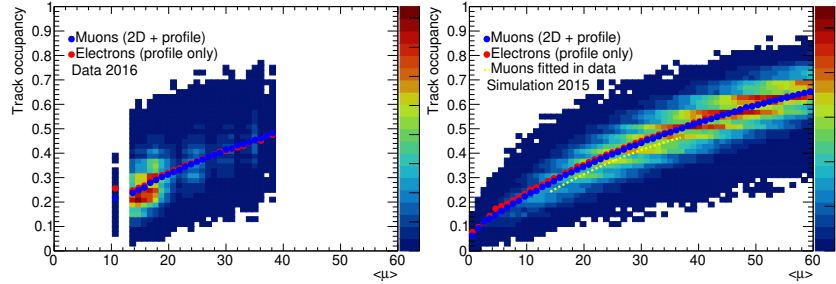
**Analysis and results:** The probes are filled into 2D histograms in bins of  $\gamma$  and occupancy with the HT probability on the z-axis; they are fitted using the expression later in this section, correction factors (explained in this section) are calculated, and the performance is compared to the previous calibration using ROC curves; some further checks are done, including testing the occupancy-independence of the correction factors.

**Discussion:** Several issues discovered during the calibration effort are discussed.

Activity in the vicinity of the straws is known as track occupancy (or sometimes wrongly known as local occupancy, which is not the

same). The global occupancy is an absolute measure of activity in the whole TRT. The global occupancy is roughly defined as the number of hit TRT straws out of the total number of TRT straws. The local occupancy is independently calculated in the 192  $\phi$  slices of the TRT. The track occupancy is a weighted average of the local occupancies from the  $\phi$  slices that the track crosses; each slice is weighted by the ratio of hits of the track in that region to the total number of hits that make up the track. See Ref. [114] (especially Eqs. 1 and 2) for in-depth explanations of the different occupancy definitions.

Figure 4.1: Track occupancy is plotted against  $\langle\mu\rangle$  with data on the left and simulation on the right. The 2D figure is for muons only with a profile along  $\langle\mu\rangle$  of muons and electrons plotted on top. The muons in data are fitted with a second-order polynomial and drawn in yellow on simulation figure.



The pileup  $\langle\mu\rangle$  is related to the track occupancy through Fig. 4.1. As track occupancy began surpassing 50% during data taking in 2017, it was crucial that the pileup-dependent behavior be well-modeled. The pileup and track occupancy of the available 2016 data as well as simulation is shown in the figure. The dashed, yellow line in the simulation sub-figure is fitted from the data on the data sub-figure. In simulation, the calculated track occupancy is consistently higher than in data. This discrepancy is not understood.

A second issue, which prompted this calibration, was that an increase in electron count at low electron probability was found. As will be shown later in Fig. 6.4, the electron probabilities for both electrons and muons in data and simulation are well-behaved with the new calibration.

## 4.1 Particle identification

Charged particles with very high  $\gamma$  factors ( $\gamma > 1000$ ) will, with some probability, produce transition radiation (TR) when entering a medium of different dielectric permittivity. This medium is the passive radiative material in the TRT. Energetic electrons, due to their very low mass, will often be ultra-relativistic in ATLAS and therefore produce TR to a greater degree compared to heavier particles such as muons/pions (which both have similar masses approximately 200 times greater than electrons). The xenon gas in the TRT is especially sensitive to the energetic TR photons, which in turn will deposit a high amount of charge in the straw when hit, as was explained in Sect. 2.1.2. Repeating the section a bit more, the TRT operates with two thresholds for charge deposition in straws. The low threshold (LT) is above noise and is sensitive to ionization deposits from pass-

ing charged particles, while the much higher high threshold (HT) is sensitive to larger deposits as well as TR. Therefore, the HT is the response to the combined effect of ionization and TR. Any track will on average produce approximately 35 LT hits in the TRT. Electrons have an approximately 30% chance of producing an HT hit compared to non-electrons (e.g. muons/pions) at 10%. For 35 hits, this discrepancy will give good separation power. The simple fraction  $f_{\text{HT}}$  was used for electron PID in the first half of Run 1:

$$f_{\text{HT}} = \frac{n_{\text{HT}}}{n_{\text{LT}}}, \quad (4.1)$$

where the number of HT hits are contained in the number of LT hits.

The HT count is influenced by the track occupancy. Thus, while the simple fraction is powerful, the lack of incorporating the occupancy as well as local corrections to HT hit probability will lead to sub-optimal performance. To improve on this, HT probabilities for electrons and non-electrons are individually constructed for single hits and combined into electron and non-electron likelihoods for a track,

$$\mathcal{L}^{e,\mu} = \prod_{\text{TRT hits}} \begin{cases} p_{\text{HT}}^{e,\mu} & \text{if HT hit} \\ 1 - p_{\text{HT}}^{e,\mu} & \text{else} \end{cases} \quad (4.2)$$

The electron probability for a track is found from the likelihood ratio,

$$\mathcal{P}^e = \frac{\mathcal{L}^e}{\mathcal{L}^e + \mathcal{L}^\mu}. \quad (4.3)$$

The hit probability depends mainly on the  $\gamma$  factor and the track occupancy with small correction factors (CFs) factorized out:

$$p_{\text{HT}}^{e,\mu} = p_{\text{HT}}^{e,\mu}(\gamma, occ) \cdot CF(SL) \cdot CF(ZR) \cdot CF(TW). \quad (4.4)$$

Of course, the factorization assumes that the correction factors do not depend on  $\gamma$  and occupancy, which will be shown to be correct for all cases except for  $TW > 1.8$  mm for muons in the barrel.

$CF(X)$  is computed by calculating the fraction of  $p_{\text{HT}}$  at a given  $X = x$  to the average  $p_{\text{HT}}$ :

$$CF(X = x) = \frac{p_{\text{HT},X}(x)}{p_{\text{HT,avg}}}. \quad (4.5)$$

The three correction factors are, respectively, the straw layer in the barrel/endcap, the Z distance from the xy-plane (barrel) or radial distance from the beam pipe (endcap), and the track-to-wire distance in millimeters (the straw tubes have a radius of approximately 2 mm).  $p_{\text{HT}}$  and the CFs are tuned in the barrel and two endcaps separately as well for tubes with xenon and argon, making a total of 6  $p_{\text{HT}}^{e,\mu}$  models.  $p_{\text{HT}}$ , as figures later will show, can be modeled by a sigmoid function in  $\gamma$ .

The expression used for the fitting is as follows:

$$p_{\text{HT}}(\gamma) = \begin{cases} p_2 + \frac{p_3}{1+\exp(-(p_0-p_4)/p_5)} + \frac{p_3}{(1+\exp(-(p_0-p_4)/p_5)^2)} \frac{\exp(-(p_0-p_4)/p_5)}{p_5} (\log_{10} \gamma - p_0) & \text{if } \log_{10} \gamma < p_0 \\ p_2 + \frac{p_3}{1+\exp(-(p_1-p_4)/p_5)} + \frac{p_3}{(1+\exp(-(p_1-p_4)/p_5)^2)} \frac{\exp-(p_1-p_4)/p_5}{p_5} (\log_{10} \gamma - p_1) & \text{if } \log_{10} \gamma > p_1 \\ p_2 + \frac{p_3}{1+\exp(-(\log_{10} \gamma - p_4)/p_5)} & \text{if } p_0 < \log_{10} \gamma < p_1 \end{cases} \quad (4.6)$$

The first line describes the behavior at low  $\gamma$  with no TR and is linear in  $\ln(\gamma)$ . The second line describes the very high  $\gamma$  particles with enough TR to be consistently above the HT and is also linear. The third line describes particles at the TR turn-on in the medium  $\gamma$  regime and is modeled by a sigmoid. The rather long expressions for the linear parts are for continuity of the function and their first derivatives between the two points,  $p_0$  and  $p_1$ . The equation describes the onset curve at zero occupancy. The dependency on occupancy can be modeled by a second order polynomial following the "Anatoli constraint". To model the occupancy dependency, the following substitutions must be made:

$$p_1 \rightarrow p_1 + p_6 \cdot \text{occ} \quad (4.7)$$

$$p_4 \rightarrow p_4 + p_7 \cdot \text{occ} \quad (4.8)$$

$$p_{\text{HT}}(\gamma, \text{occ}) = p_{\text{HT}}(\gamma) + (1 - p_{\text{HT}}(\gamma))(p_8 \cdot \text{occ} + p_9 \cdot \text{occ}^2) \quad (4.9)$$

## 5 Selections

In this section, the event pre-selection and lepton selections will be outlined, including the cut-flow diagrams. Afterwards, the output histograms and variables will be explained.

### Contents

<b>5.1</b>	<b>Event and lepton selections</b>	<b>57</b>
5.1.1	Event pre-selections	57
5.1.2	Lepton selections	58
5.1.3	Cut-flow for both selections	59
<b>5.2</b>	<b>Preparation prior to analysis</b>	<b>61</b>

The TRT group produces their own samples, listed below for completeness<sup>2</sup>:

group.det-indet.00303832.physics\_Main.daq.TRTxAOD\_Z.f716\_trt098-00\_EXT0  
group.det-indet.00304178.physics\_Main.daq.TRTxAOD\_Z.f716\_trt098-01\_EXT0  
group.det-indet.00304337.physics\_Main.daq.TRTxAOD\_f716\_Ztnp3\_EXT0  
group.det-indet.361106.PowhegPythia8EvtGen\_AZNLOCTEQ6L1\_Zee.recon.TRTxAOD.e3601\_s2876\_r7886\_trt093-00\_EXT0  
group.det-indet.361107.PowhegPythia8EvtGen\_AZNLOCTEQ6L1\_Zmumu.recon.TRTxAOD.e3601\_s2876\_r7886\_trt093-04\_EXT0

<sup>2</sup> The "trt" tags are documented internally, <https://twiki.cern.ch/twiki/bin/view/Atlas/TrtxAOD>.

### 5.1 Event and lepton selections

The selections are split into event pre-selections (event-level selections) and lepton selections (selections on the leptons being selected for). For any electron pair passing the final selection, the probe is kept. For any muon pair passing the final selection, both are kept. All combinations of pairs are attempted, and thus pairs with switched labels are also accepted if they pass the selections. Even when a pair has been accepted in the event, new pairs of (other) leptons are still accepted after this, also with switched labels.

The pre-selection is listed in Tab. 5.1, and the electron and muon selections are listed in Tab. 5.3. Some of the selections will be detailed in the paragraphs below. Numbers for the selections in the tables can be seen in Tab. 5.4, which uses shorter names for the selections.

#### 5.1.1 Event pre-selections

The event pre-selections are listed in Tab. 5.1. The selection skips new events if a previous event with the same event number has already been processed. Sometimes in the past, events were duplicated in production, so this selection ensures that duplicates

Table 5.1: Event pre-selections. The *lepton* corresponds to the lepton being selected for, not both. The selections are detailed in the text. <sup>1</sup>Trigger selection is not applied for simulated data because of reconstruction bugs at the time of sample production.

electron channel
HLT_e24_lhmedium_L1EM18VH
HLT_e24_lhmedium_L1EM20VH
HLT_e60_lhmedium
HLT_e120_lhloose
HLT_e5_lhvloose
HLT_e12_lhvloose_L1EM10VH
HLT_e12_lhvloose_nod0_L1EM10VH
HLT_e15_lhvloose_L1EM7
HLT_e20_lhvloose
HLT_e20_lhvloose_L1EM12
HLT_e20_lhvloose_nod0
HLT_e24_lhmedium_nod0_L1EM20VH
HLT_e24_lhtight_nod0_ivarloose
HLT_e26_lhtight_nod0_ivarloose
HLT_e26_lhtight_smooth_ivarloose
HLT_e28_lhmedium_nod0_L1EM20VH
HLT_e28_lhtight_nod0_ivarloose
HLT_e28_lhtight_smooth_ivarloose
HLT_e50_lhvloose_L1EM15
HLT_e60_medium
HLT_e60_lhmedium_nod0
HLT_e140_lhloose_nod0
HLT_e300_etcut
muon channel
HLT_mu26_imedium
HLT_mu26_ivarmedium
HLT_mu28_imedium
HLT_mu28_ivarmedium
HLT_mu40
HLT_mu50

Table 5.2: The single lepton triggers that have been used for the calibration. See Chap. 3 for the naming convention.

<sup>1</sup> The ATLAS Electron and Photon Performance Group uses 25 GeV and 15 GeV for tags and probes, respectively, in their tag and probe framework. Their framework was the baseline of this work.

Remove duplicated events
[Data] Event cleaning
[Data] Pass GRL
Any <i>lepton</i> trigger passed <sup>1</sup>
At least two <i>leptons</i> in the event

are not used (in the case that the duplicated events can be identified by their event number). Event cleaning refers to the usual veto on events due to problematic regions of the detector or incomplete events (cf. Sect. 3.5). The good runs list for the 2016 data is, data16\_13TeV.periodAllYear\_DetStatus-v88-pro20-21\_DQDefects-00-02-04\_PHYS\_StandardGRL\_All\_Good\_25ns.xml.

Finally, all triggers for the lepton being selected for are checked. Tab. 5.2 contains all regular electron triggers (even prescaled to increase electron count) and all unprescaled muon triggers for the years 2015 and 2016. If any trigger passes, the event is pre-selected, given that the event contains at least two of the leptons being selected for. For simulated data, no trigger selection was applied due to bugs in the sample production.

## 5.1.2 Lepton selections

With the pre-selection passed, all the leptons of a given type are paired in all combinations. For each pair, one candidate is tested as the tag and the other as the probe. As soon as the tag or the probe fails a selection, the next pair is tested. The selections in Tab. 5.3 are detailed below.

Truth-matching of electrons is done by using the truth information supplied by an algorithm during reconstruction. Prompt, FSR and bremsstrahlung electrons are all accepted. Due to a bug in the sample, no truth-matching is done for muons.

The  $p_T$  selections are set to 5 GeV for electrons and muons in order to keep efficiency high<sup>1</sup>. The invariant mass selection has an indirect selection on the momentum that anyway indirectly raises the lower momentum limit. The  $p_{T,\text{trk}} > 0.25 \cdot p_T$  selection ensures that the tracks of electrons passing with minimum  $p_T$  still have a decent  $p_{T,\text{trk}}$ .

The silicon hits are the sum of Pixel and SCT hits. All hits include dead sensors.

The LLH ID includes all variables for electron PID, while the "cut-based" ID has fewer variables and looser selections for looser PID. The "cut-based" loose PID does not include TRT information.

The electron probe ID and isolation selections at the bottom of the table are additional selections compared to the selections in the framework by the ATLAS Electron and Photon Performance Group to further clean the electron sample.

Electron channel	Muon channel
[Simulation] Both truth-matched	[Simulation] Both truth-matched <sup>1</sup>
$80 < m_{ee} < 100$ GeV	Both are combined muons with $\geq 2$ precision hits
Both pass author	$80 < m_{\mu\mu} < 100$ GeV
Tag $p_T > 5$ GeV	At least one match trigger object
Probe $p_T > 5$ GeV	Both $\eta < 2.0$
Probe $p_{T,\text{trk}} > 0.25 \cdot p_T$	Both $p_T > 5$ GeV
Both $\eta < 2.0$	Both $\text{hits}_{\text{pixel}} \geq 1$ , $\text{hits}_{\text{silicon}} \geq 7$ , $\text{hits}_{\text{TRT}} \geq 15$
Both pass OQ	Both pass tight track iso, $p_T^{\text{varcone30}}/p_T < 0.06$
Tag match trigger object	Both pass tight calo iso, $E_T^{\text{topocone20}}/p_T < 0.06$
Tag pass tight track iso, $p_T^{\text{cone20}}/p_T < 0.06$	Opposite sign (OS)
Tag pass tight calo iso, $E_T^{\text{topocone20}}/p_T < 0.06$	
Tag $\text{hits}_{\text{pixel}} \geq 1$ , $\text{hits}_{\text{silicon}} \geq 7$ , $\text{hits}_{\text{TRT}} \geq 15$	
Tag pass tight LLH ID	
Opposite sign (OS)	
Probe pass same hits and non-LLH loose ID	
Probe tight track iso	
Probe tight calo iso	

### 5.1.3 Cut-flow for both selections

The cut-flow diagrams can be found in Fig. 5.1. For both figures, the red bins show the number of *events* passing the *event pre-selection*, and blue bins show the number of *leptons* passing the *lepton selection*. Note that the "InitialElectronZ" and "InitialMuonZ" show every pair before any selection. They therefore get a contribution of  $n(n-1)$  per event with  $n$  being the number of leptons. Since the label switch is allowed, all electrons are tried as both tags and probes. If the switch was not allowed, the contribution would be  $n(n-1)/2$ . Since these are mostly low  $p_T$  pileup, the first selection will clear out the majority of the lepton pairs. The raw numbers are given in Tab. 5.4.

Table 5.3: Lepton selections for electrons (left) and muons (right) in the order that they are applied. Some selections are detailed in the text. <sup>1</sup>Muon truth-matching is not applied because of reconstruction bugs at the time of sample production.

Cut	Probes	Eff.	Acc. eff.	Cut	Probes	Eff.	Acc. eff.
InitialEvent	1953402			InitialEvent	603426		
RemoveDuplicates	1807815			RemoveDuplicates	603426		
EventCleaning	1806534			-			
GRL	1806360			-			
TriggerFired	725917			-			
EnoughLeptons	721161			EnoughLeptons	530642		
-----				-----			
InitialElectronZ	15994269			InitialElectronZ	5555704		
-				BothTruthmatching	649596		
MassWindow	789362			MassWindow	399638		
BothAuthor	789362	100.00	100.00	BothAuthor	399638	100.00	100.00
TagPt	748174	94.78	94.78	TagPt	399491	99.96	99.96
ProbePt	714111	95.45	90.47	ProbePt	399344	99.96	99.93
ProbeAtLeastRelPt	607149	85.02	76.92	ProbeAtLeastRelPt	361351	90.49	90.42
TagEta	510486	84.08	64.67	TagEta	307853	85.20	77.03
ProbeEta	432711	84.76	54.82	ProbeEta	269437	87.52	67.42
BothOQ	430250	99.43	54.51	BothOQ	267735	99.37	66.99
TagTrigger	255597	59.41	32.38	TagTrigger	267735	100.00	66.99
TagTrkIso	240406	94.06	30.46	TagTrkIso	261204	97.56	65.36
TagCaloIso	224465	93.37	28.44	TagCaloIso	223747	85.66	55.99
TagTrk	193578	86.24	24.52	TagTrk	187276	83.70	46.86
TagIDTight	178654	92.29	22.63	TagIDTight	140981	75.28	35.28
OS	158166	88.53	20.04	OS	139867	99.21	35.00
ProbeQuality	110369	69.78	13.98	ProbeQuality	110974	79.34	27.77
ProbeTrkIso	107763	97.64	13.65	ProbeTrkIso	108588	97.85	27.17
ProbeCaloIso	100383	93.15	12.72	ProbeCaloIso	95524	87.97	23.90

(a) Electrons, data

(b) Electrons, simulation

Cut	Probes	Eff.	Acc. eff.	Cut	Probes	Eff.	Acc. eff.
InitialEvent	1953402			InitialEvent	511614		
RemoveDuplicates	1807815			RemoveDuplicates	511614		
EventCleaning	1806534			-			
GRL	1806360			-			
TriggerFired	426292			-			
EnoughLeptons	425775			EnoughLeptons	430469		
-----				-----			
InitialMuonZ	2186928			InitialMuonZ	4810508		
quality	553615			quality	698389		
MassWindow	383286			MassWindow	463507		
trigger	382925	99.91	99.91	trigger	463507	100.00	100.00
eta	286866	74.91	74.84	eta	335984	72.49	72.49
pt	286463	99.86	74.74	pt	335554	99.87	72.39
trackQuality	279798	97.67	73.00	trackQuality	325725	97.07	70.27
MuonTrkIso	270278	96.60	70.52	MuonTrkIso	309651	95.07	66.81
MuonCaloIso	250736	92.77	65.42	MuonCaloIso	285078	92.06	61.50
OS	250292	99.82	65.30	OS	284937	99.95	61.47

(c) Muons, data

(d) Muons, simulation

Table 5.4: Cut-flow table for (a) electrons in data, (b) electrons in simulation, (c) muons in data, and (d) muons in simulation. The efficiency of a selection is only given for particles passing all previous selections. The dashed lines separate the event and lepton selections.

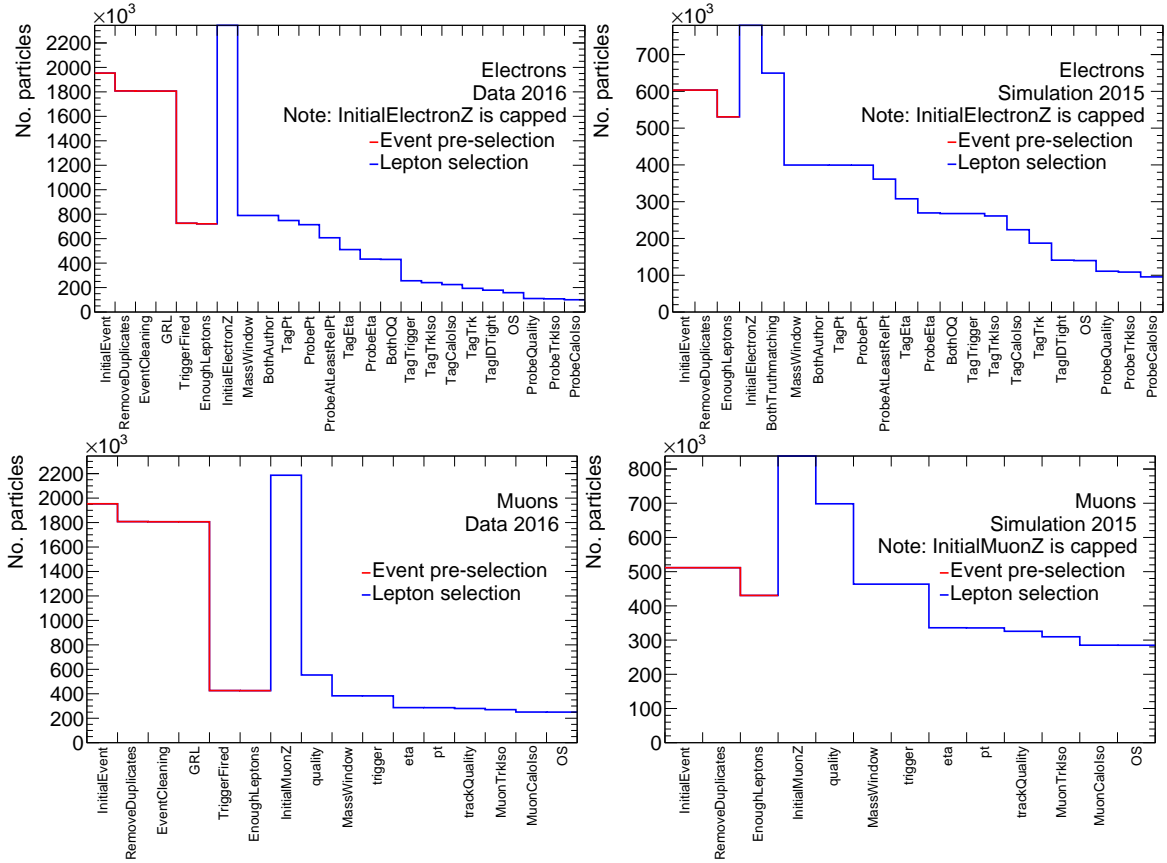


Figure 5.1: Cut-flow diagram for selections. The red histogram is the number of events passing the event pre-selection and the blue is the number of leptons passing their respective selections.

## 5.2 Preparation prior to analysis

The usual event information and particle kinematics are saved in the output, including the following used for recalculating the probabilities with the new tuning. The probe track variables are: `trackP`, `trackEta`, `trackOccupancy`, `electronProbabilityAth`. The probe track hit variables are: `HighThreshold`, `GasType`, `TRTPart`, `StrawLayer`, `TrackToWire`, `ZToR`. `electronProbabilityAth` is the TRT electron probability using the current calibration. This variable is shown in some figures as ‘previous calibration based on 2015 Simulation’.

2D Histograms, with  $\gamma$  factor and track occupancy as axes, are filled for each gas and TRT part. All hits are filled in the LT histogram, while only HT are filled into HT histograms. To calculate  $p_{HT}$ , the two histograms are divided. The average and per SL, TW, and ZR values of  $p_{HT}$  are also saved, from which the correction factors are derived. Finally, a few histograms for the appendix are also made. These include histograms with the HT fraction calculated per track and the correction factors as a function of occupancy.

The uncertainty of the fraction is recalculated for data. The binomial uncertainty for fractions is used:

$$\sigma^2 = f(1 - f)/n_{LT}, \quad f = n_{HT}/n_{LT}. \quad (5.1)$$

Bins in the 2D fraction histogram with fewer than 20 HT hits are removed. The simulation weights (“MC weights” given by the gen-

erators) have been normalized in the very beginning due to being very high. Now, bins with few hits and no hits are weight-wise closer. Events with negative weights are skipped to ease the computation of some histograms. The amount of simulation with negative weights is approximately 2 orders magnitudes smaller.

Following these selections, approximately 1.6 electron probes are saved per event when at least one electron probe passes. See Fig. 5.2. In data, much more so than in simulation, the occupancy (and hence the pileup) has a great influence on the selection efficiency of electrons (see Chap. 4 for definitions of the different occupancies). The stark difference between data and simulation makes data-driven calibration important for optimal performance.

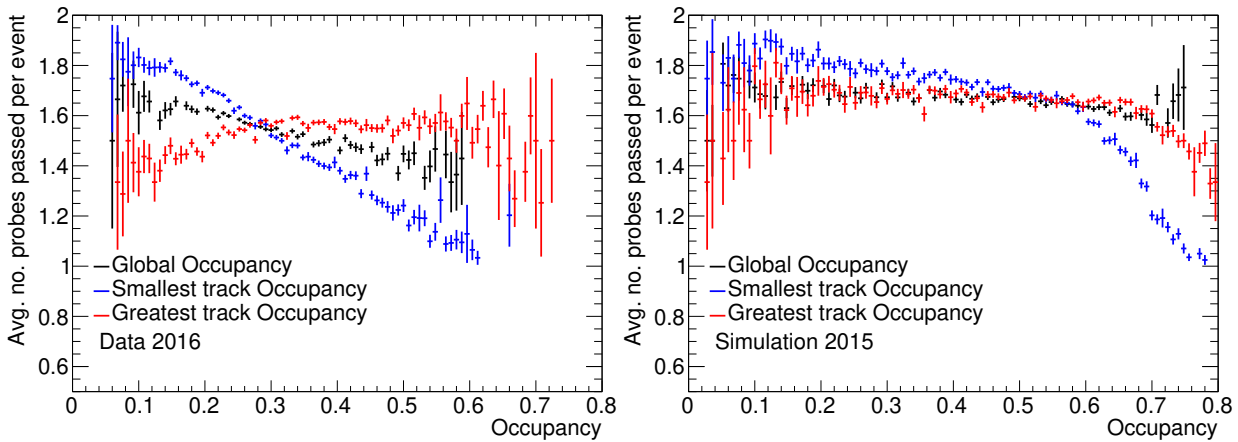


Figure 5.2: For events with at least one electron probe passing, the average number of selected electron probes per event is plotted against the global occupancy (black), the smaller track occupancy of the one or two electron probe(s) selected per any given event (blue), and the greater track occupancy of them (red).

# 6 Analysis and results

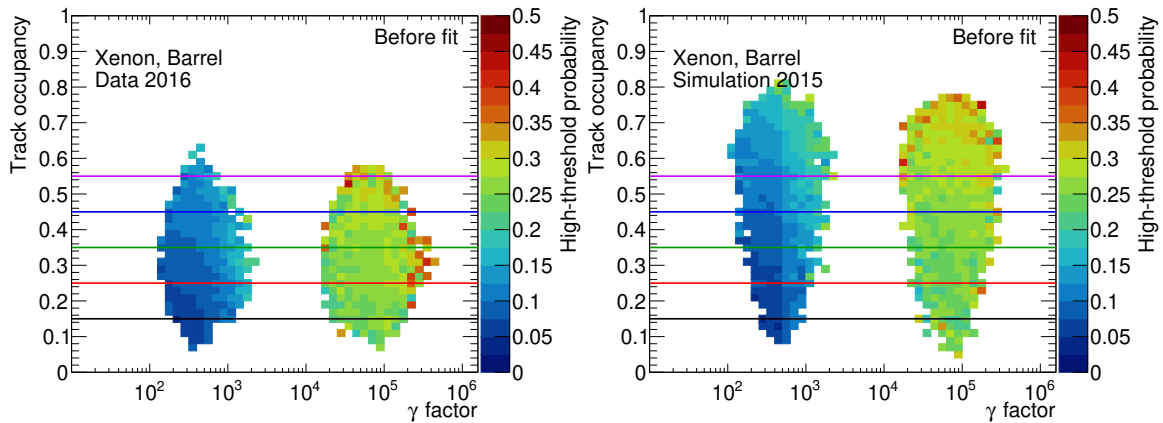
The tuning of the likelihood parameters will now follow. After this, the correction factors will be analyzed. Finally, the full PID tool is applied and ROC curves<sup>2</sup> are shown.

<sup>2</sup>[https://en.wikipedia.org/wiki/Receiver\\_operating\\_characteristic](https://en.wikipedia.org/wiki/Receiver_operating_characteristic)

## Contents

<b>6.1 Calibration tuning</b>	<b>63</b>
<b>6.2 Correction factors (CFs)</b>	<b>65</b>
<b>6.3 Final performance</b>	<b>67</b>
<b>6.4 Additional analysis</b>	<b>68</b>
6.4.1 ROC curves for different occupancies	68
6.4.2 Applying simulation-tuned calibration on data	69

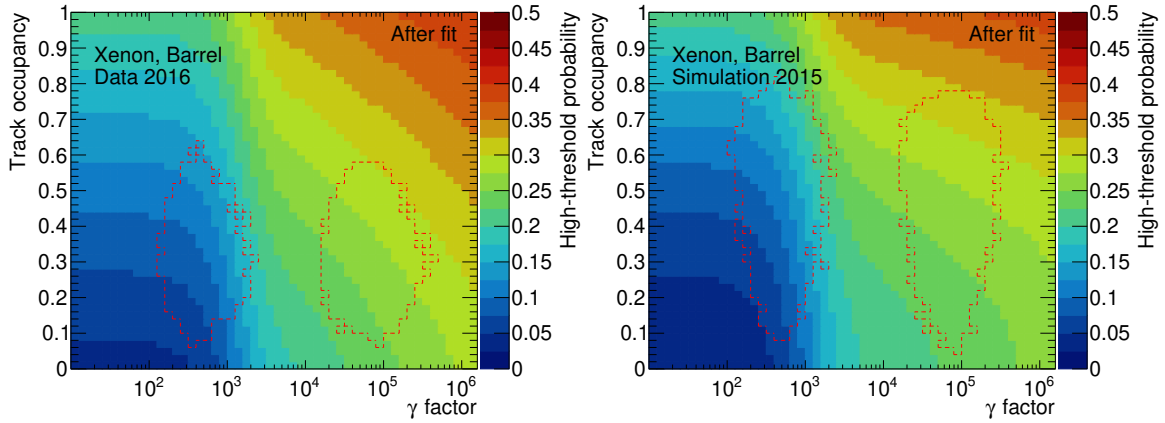
## 6.1 Calibration tuning



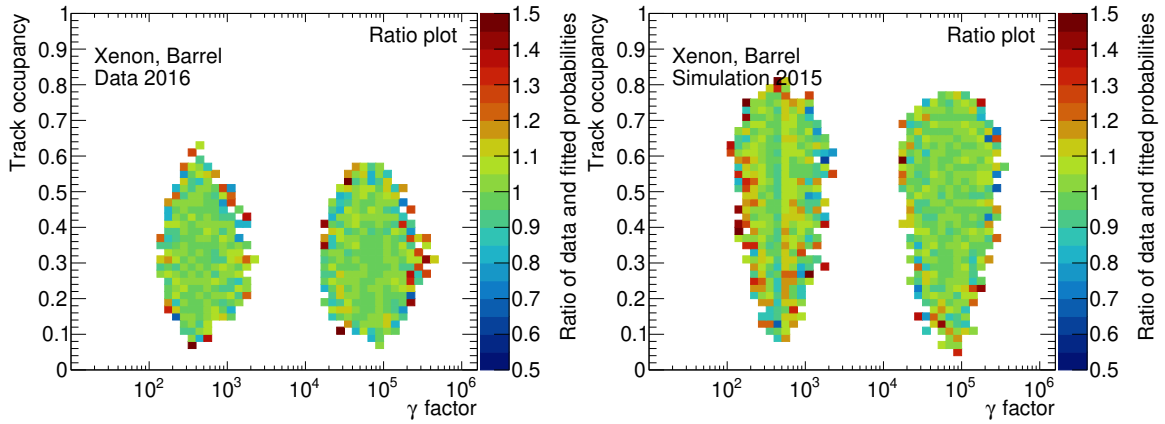
As explained in the previous section, each HT and LT hit is added to their respective 2D histograms, which are a function of the  $\gamma$  factor and the track occupancy. These histograms are separated into the barrel, endcap A, and endcap B parts and further into argon and xenon gases. When the histograms are filled, the HT and LT histograms are divided to give the HT fraction (or probability), since the LT histograms also contain the HT hits. These histograms can be seen in Fig. 6.1 and Figs. 6.2a–6.2c for xenon in the barrel. See App. 18.A for the other parts and gases.

Fig. 6.1 shows the fraction before fitting. The colored lines correspond to the colored points on the upper sub-figures of Fig. 6.2c.

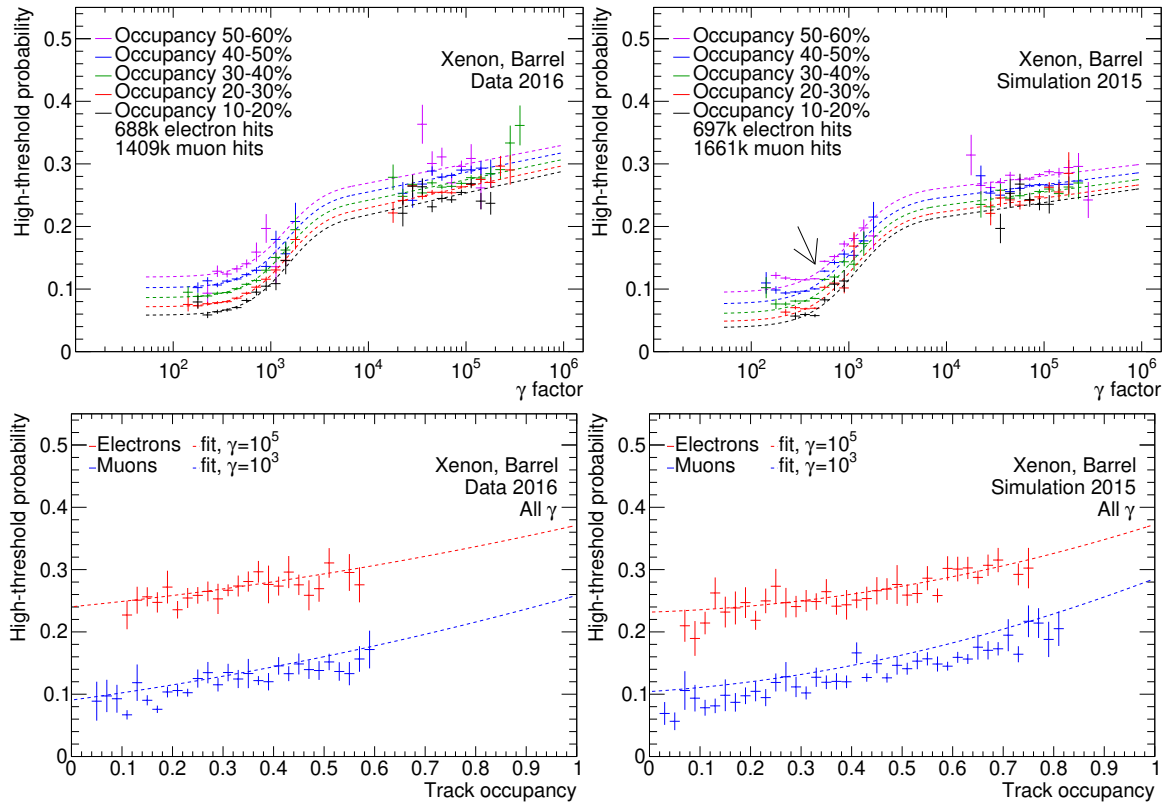
Figure 6.1: The HT fraction plotted as a function of the track occupancy and the  $\gamma$  factor with the left cluster in each sub-figure coming from muons and the right cluster coming from electrons. This figure is only for xenon straws in the barrel. The colored lines correspond to the colored points on the upper sub-figures of Fig. 6.2c.



(a) The HT fraction plotted as a function of the track occupancy and the  $\gamma$  factor after fitting Fig. 6.1. Muons are on the left and electrons are on the right. This figure is only for xenon straws in the barrel.



(b) Ratio of HT fractions before (Fig. 6.1) and after the fit (Fig. 6.2a).



(c) Onset curves after fitting in slices of occupancy. The above sub-figures show slices in track occupancy of the 2D histograms before (points) and after (lines) fitting. The lower sub-figures show the 2D histograms before fitting for all  $\gamma$  values (points) and after fitting for two choices of  $\gamma$  (lines). This figure is only for xenon straws in the barrel. The arrow in the upper-right sub-figure points to a jump most clearly seen in simulation in the barrel with xenon.

Figure 6.2: (a) The HT fraction after fitting. (b) The ratio of the fit to the raw values. (c) The fit shown in slices of occupancy (upper row) and  $\gamma$  factor (lower row).

$p_{\text{HT}}^{e,\mu}(\gamma, occ)$  is derived from these. The fast  $\gamma$  and slow occupancy dependency is also seen in this figure.

Fig. 6.2a shows the fraction predicted by the fit. The outlined area in red dashes shows the area that was used as input for the fit. The fit is also applied to the outside of the fit area to show the behavior of the model on unseen data.

Fig. 6.2b shows the ratio of the fraction before and after the fit. In data, the deviation seems no larger than 10% for the bulk with the edges being far off due to lower statistics (hence larger errors). App. 18.B shows figures of z-scores (significances) that take the uncertainties into account. They show no deviation in the edges.

Fig. 6.2c shows the 2D histograms before and after the fit in slices of track occupancy and  $\gamma$  factor, respectively. The upper sub-figures show  $p_{\text{HT}}$  in occupancy slices of 10% up to 60%. The left points in the two sub-figures show the onset of TR production for muons. For the most part, the data points conform well to the dashed lines from the fit. The electrons on the right has less statistics but for 20-40% occupancy, the points follow the dashed lines. The lower sub-figures show  $p_{\text{HT}}$  as a function of occupancy. The fitted model is drawn for two choices of  $\gamma$  that follow the electron and muon trends quite well. It is important to note that no selection on  $\gamma$  is made, so the muons from the onset on the upper sub-figure all go into the lower sub-figures, and that the dashed line is not fitted to the points but drawn from the fitted model.

Fig. 6.1 and Fig. 6.2b show a sudden, small jump in  $p_{\text{HT}}$  in simulation down the middle of the left cluster. This phenomenon is pointed at in Fig. 6.2c. It is also seen in some other gas/parts in simulation and real data, though most can be explained by statistical fluctuations. This systematic effect is not understood.

Overall, judging from the figures sliced in  $\gamma$  and occupancy (Fig. 6.2c), the model is quite well fitted to points with low uncertainty. The fits converge, so the model describes the behavior well. The only point of criticism would be that the model slightly overestimates the HT fraction for muons at  $\gamma = 10^3$  in simulation.

## 6.2 Correction factors (CFs)

The significant drivers of the PID tool are the  $\gamma$  factor and the track occupancy. As the previous figures show, they model the overall behavior very well. However, corrections to the electron probabilities of the hits are needed. These correction factors (CFs) were factorized out of the likelihood function. To be able to do this, the assumption is that the CFs will modify ever so slightly (at most  $\mathcal{O}(1)$ ) the electron probability of each hit.

The CFs are calculated as follows for each gas and part individually. The average HT fractions are filled into TProfiles<sup>1</sup>, and the HT fractions as a function of SL, ZR, and TW are filled into each their own TProfiles as well. The CFs are scaled by  $1/\text{avg}$  (cf. Eq. (4.5)) and then used in Eq. (4.4). Only tracks with momenta up to 80 GeV are

<sup>1</sup> Histograms that show the average value per bin instead of the sum of values per bin; <https://root.cern.ch/doc/master/classTProfile.html>

used. The previous limit was 50 GeV. This threshold is put in to limit the  $\gamma$  dependency that would otherwise follow into the correction factors which are supposed to be independent (cf. Eq. (4.4)).

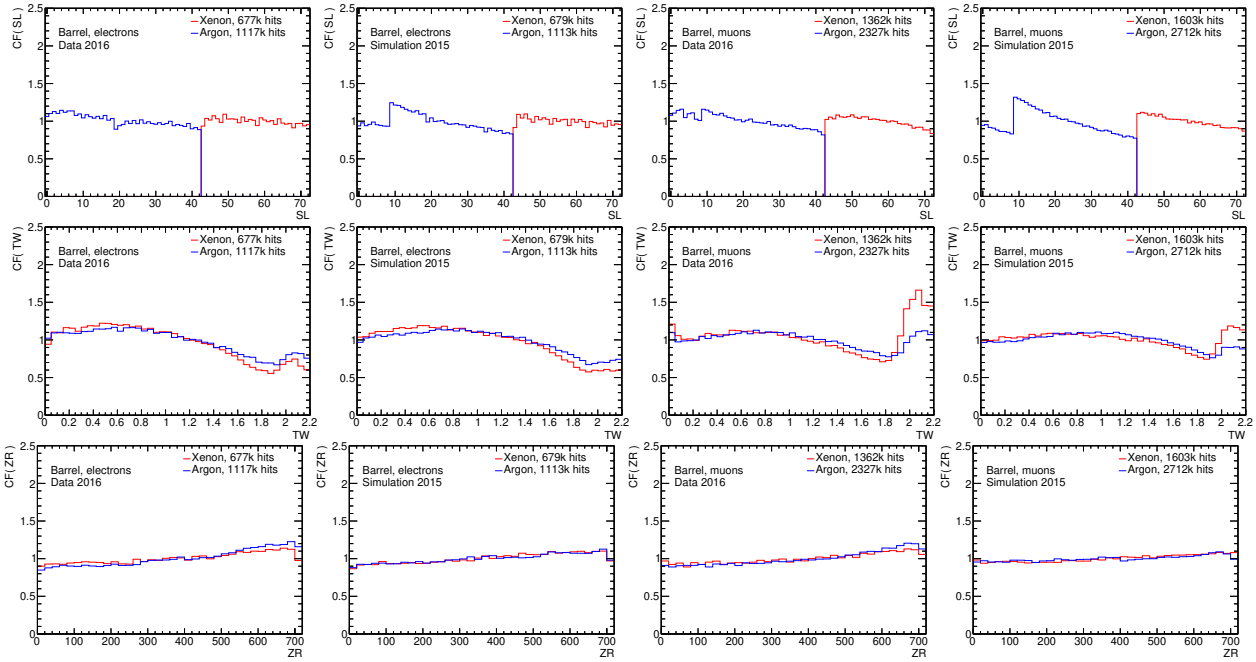


Figure 6.3: Correction factor (first row SL, second row TW, and third row ZR) for the barrel. The first two columns are electrons and the last two columns are muons. Columns 1 and 3 are data and columns 2 and 4 are simulation.

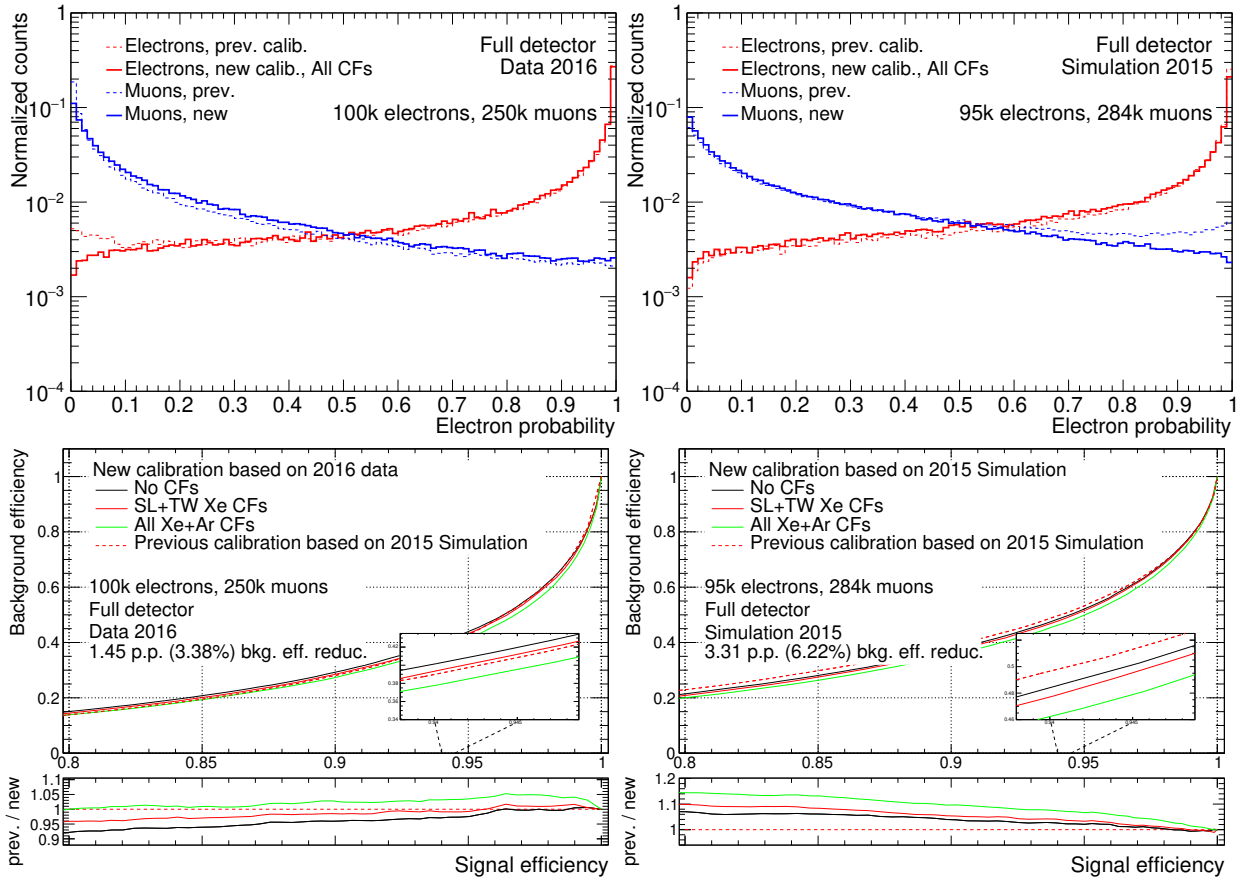
Figures for the three CFs are shown for the barrel in Fig. 6.3. The remaining CFs for the endcaps are attached in App. 18.D. The SL correction shows that the transition from short to long straws at  $SL = 9$  affects simulation much more than data. The TW correction also shows a great difference for muons between data and simulation at around 2.0 mm. The ZR correction is mostly flat.

Raising the threshold to 80 GeV will include the muons on the rising part of the onset function as seen in Fig. 18.42 in App. 18.H. Analysis shows that the high momentum limit leads to little occupancy dependency of the CFs; App. 18.F shows the CFs for low, medium, and high occupancy (all with equal number of entries). All figures show little discrepancy with the exceptions being low statistics (especially for endcap B and argon in general) and CF(TW) for muons in the barrel (Fig. 18.32). The dependency on occupancy for CF(TW) for muons will lead to slightly sub-optimal performance. However, Fig. 18.41 in App. 18.G shows that truncating TW at 2.0 mm reduces performance.

$TW > 2.0$  mm for a hit is unphysical, as the hit will be outside the straw tube. These unphysical hits may stem from uncertainty on the track position or from delta-rays knocked into the tube from nearby tracks.

The conclusion therefore is that, for optimal performance, all correction factors should be used and in the full range of values. The ROC curve in Fig. 6.4 in the next section will confirm this.

### 6.3 Final performance



$p_{\text{HT}}(\gamma, occ)$  and the CFs have been calculated. Fig. 6.2c shows the tuning without correction factors. The tool is applied back on the same sample from which the tuning is derived.

The probabilities given by the tool (using all CFs) are in the two upper sub-figures of Fig. 6.4 along with the predictions of the previous tuning in dashed lines. The upper left sub-figure shows the count of electrons in data now correctly going down at very low electron probability. The upper right sub-figure also shows the muons in simulation now correctly going down at very high electron probability.

From the probabilities, ROC curves have been calculated for a few CF combinations. These are shown in the lower sub-figures of Fig. 6.4. A zoomed-in window is shown to help tell the slight improvement given by the incrementally added CFs. See App. 18.A for ROC curves for the different parts and gases. For more combinations of CFs, see App. 18.G. As shown in the figure, with all CFs, the new calibration reduces the background efficiency by 1.45 percentage points (3.38%) in data and 3.31 p.p. (6.22%) in simulation at 95% signal efficiency.

The significant increase in performance in simulation is not due to the additional CFs (cf. App. 18.E). Rather, the performance was previously heavily degraded by the rising muon count at high electron probability, which lead to a worse background reduction at high sig-

Figure 6.4: Upper: Electron and muon counts of electron probabilities for the previous and new tuning. Lower: ROC curves for the previous calibration as well as the new calibration with different choices of CF combinations. This figure is for the whole detector and not just xenon straws in the barrel. See App. 18.A for ROC curves for the different parts and gases. The background efficiency reduction at 95% signal efficiency for the new calibration with all CFs compared to the old calibration is shown in the figure as percentage points and percentage.

nal efficiency in the ROC curves. The new calibration does not have this issue.

The calculation of  $p_{HT}$  (the fraction) is done by dividing all HT hits by all LT hits per bin. Another approach is to divide the HT hits by LT hits for each track, and then taking the average for each track in each bin. Performing this tuning on fractions derived per track shows very similar performance for gas/parts with great amount of statistics but leads to more noisy data when very little statistics is available. See App. 18.I for an in-depth explanation and figures.

## 6.4 Additional analysis

This section will summarize different concerns regarding the calibration and provide additional figures.

### 6.4.1 ROC curves for different occupancies

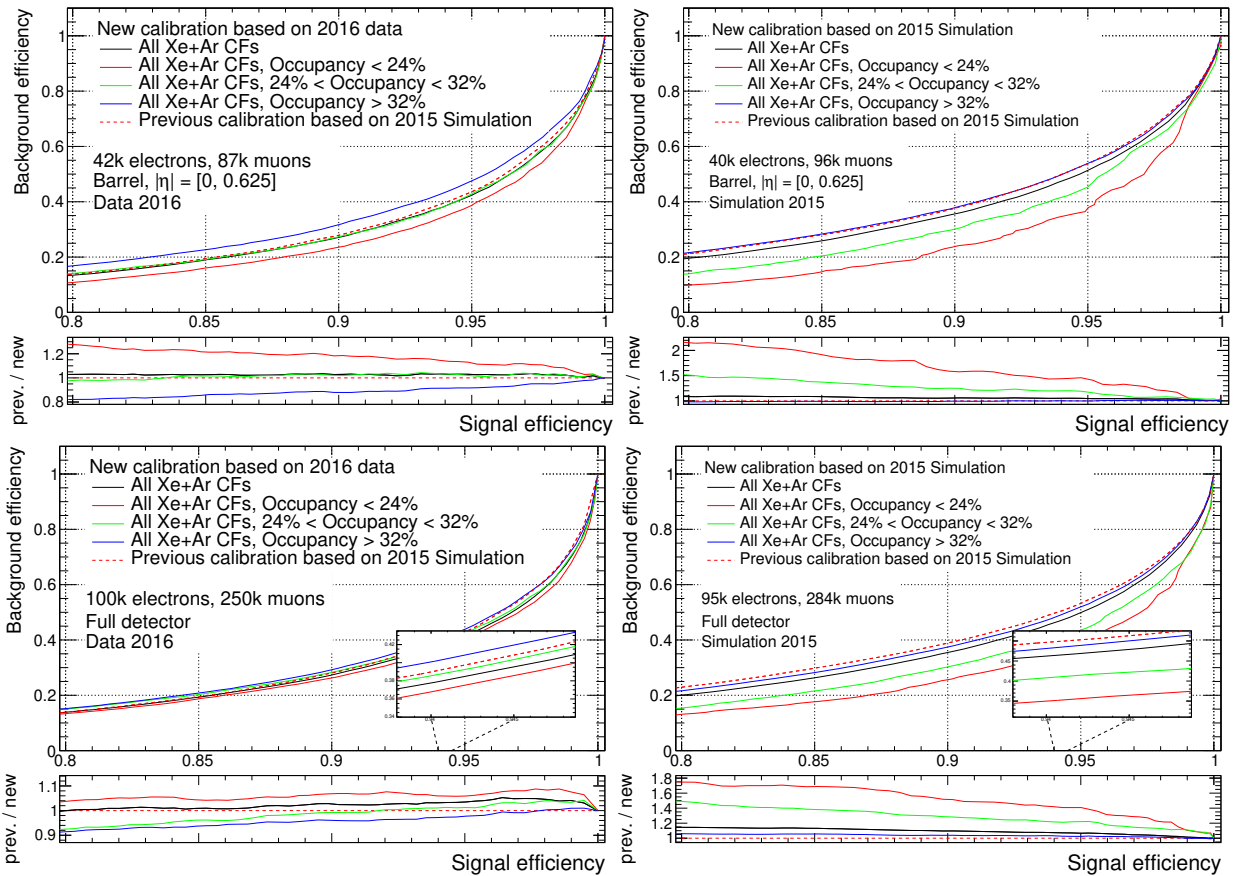
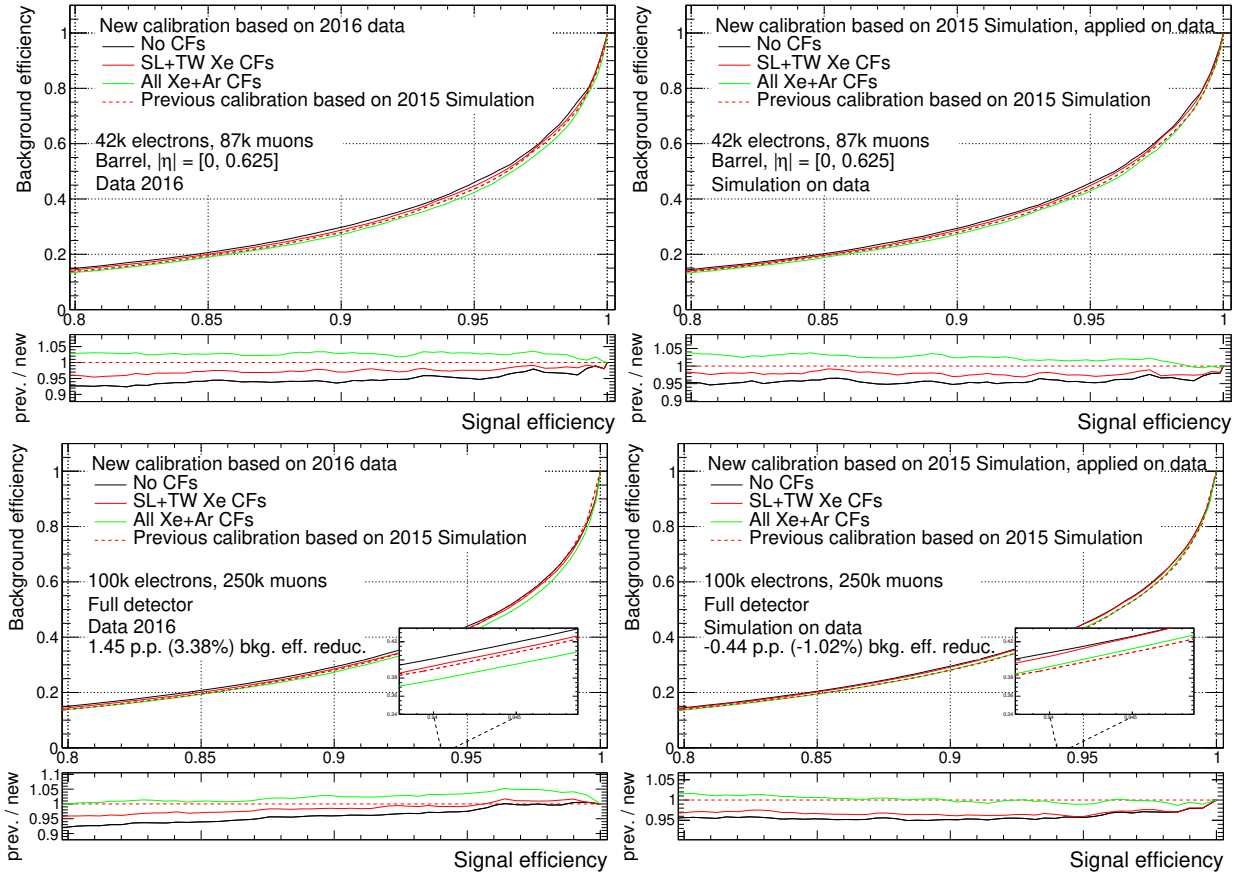


Figure 6.5: ROC curves for the previous calibration as well as the new calibration with all CFs. The new calibration is also shown in three approximately equal occupancy slices. As expected, lower occupancy leads to a greater performance. The upper sub-figure is for the barrel only, while the lower sub-figure is for the full detector.

The performance of the PID as shown in Fig. 6.4 is for all occupancies. It is known that higher occupancy gives a higher baseline HT fraction and thus lower performance. In Fig. 6.5, the calibrated PID is applied to three occupancy slices:  $occ < 24\%$ ,  $24 < occ < 32\%$ , and  $occ > 32\%$ . The three occupancy slices are chosen such that they each contain approximately one third of the entries in data. When

more statistics at higher pileup is available, these ranges can be increased. See Fig. 18.9 in App. 18.A for the reason behind the  $\eta$  slices used in the ROC curves. This analysis can be used to predict the PID performance as a function of increasing occupancy.

### 6.4.2 Applying simulation-tuned calibration on data



The previous calibration was made entirely in simulation and applied on both simulated and real data samples. To see the performance difference between tuning in simulation and applying on data against tuning in data and applying on data, the simulation-tuned calibration was applied on the data samples from which the ROC curves in Fig. 6.6 have been derived. See App. 18.C for ratios of the 2D histograms before and after fitting.

Figure 6.6: ROC curves for the new calibration tuned in data and applied on data (left, for reference) and tuned in simulation and applied on data (right). Even with the additional CFs, tuning in simulation leads to performance worse than the previous calibration and the data-tuned calibration.



*The calibration was successfully derived from simulation and for the first time data as well. The performance in data increased slightly, and we do not see the issues of rising lepton counts at low or high electron probabilities. Some issues that were stumbled upon during the calibration work were already mentioned throughout, but we will discuss all here.*

*Simulation inconsistencies* The consistently higher track occupancy per  $\langle\mu\rangle$  in simulation compared to data in Fig. 4.1 is a known yet unexplained issue. Understanding this discrepancy is not an issue for PID as its calibration is now data-driven, unless one wants a tool with identical calibration constants for data and simulation.

The jump in electron probability for muons in xenon in the barrel, pointed at in Fig. 6.2c, is also a known issue. Bear in mind, truth-matching was not applied. The issue might stem from a turn-on of TR from muons in simulation with no effect below the threshold of approximately 50 GeV. This jump also affects the ability of the model to fit the lower plateau. No effort has been made to better model this, as no electrons will be identified at such low momenta.

*Additional statistics is needed* Data taken during 2017 was not included in this work, as not enough statistics was ready in time. Furthermore, some gas/parts still have too little statistics with the available 2016 data. Finally, the datasets with real data have no events with track occupancy above 70%. When more real and simulated data is available, the calibration must be remade to better model higher occupancies as well as gas/parts now lacking the statistics.

*Additional simulation backgrounds* This calibration analysis introduces, for the first time, tag and probe in data for the calibration of the TRT's PID. As such, care should be taken that the data samples obtained through T&P are at purity levels sufficient for the tuning of the current model as well as for future PID efforts that may use machine learning. This may require using the tight "cut-based" PID without the TRT part to reach higher purity. To estimate the amount of background T&P picks up, simulation samples of  $W$  decaying to  $e\nu$  and  $\mu\nu$  as well as jet samples (e.g. the "any two-to-two dijet" samples JF17, JF35, JF50) should be used. Applying the signal T&P (used for electrons) on these samples will help estimate the amount of non-electron probes.

*More detailed comparison figures* Additional analysis of the PID performance for different occupancy slices (Sect. 6.4.1) shows, as expected, that the separation power decreases for higher occupancies. However, Fig. 6.5 does not compare the current calibration against the previous for the same occupancy slices; the previous calibration is used for all occupancies. A proper comparison between the previous and current calibration for the same occupancy slices should be made.

The first 9 straws of the barrel are so-called short straws. Instead of being terminated at  $\eta = 0$ , which normally separates the A and C side of the barrel, the short straws are terminated at some higher  $|\eta|$  value (only the last 20 cm of the wires at each end of the modules are active), rendering the middle part of the straws inoperational. Separating all the barrel figures into short and long straw parts will help visualize any possible differences between the current and the previous calibrations as well as the different responses between short and long straws.

*Adjusting selections and corrections* Some selections and corrections were not included because of the significant increase in xAOD size that they would bring; calorimeter cluster corrections on electrons and  $b$ -jets require adding new containers. Therefore, there is no veto on  $b$ -jets during selection nor any corrections to the electron clusters at the moment. A test file for simulated data should be generated to test the influence of adding these.

The  $\eta$  selection on electrons is currently from  $-2$  to  $2$ , including the crack. Excluding tags and probes in the crack may help select electrons of better quality.

The selection of electrons is quite tight. Only the  $p_T$  selection has been lowered to regain some efficiency (and even then, the invariant mass selection has an indirect  $p_T$  selection). Some selections could be loosened to increase efficiency. The final three selections for electrons in Tab. 5.3 (probe hits, loose "cut-based" ID, and isolation) are additional selections not used by the ATLAS Electron and Photon Performance Group in their tag and probe framework; removing these selections could gain back some electrons, especially at higher occupancies, hopefully without accepting too much background.

*Low  $p_T$  muons to fill lower plateaus* To better fit the lower plateaus of the onset curves (upper-left sub-figure of Fig. 6.2c and Fig. 18.2d), less energetic muons are needed. Pions might also be a possibility, if a pure enough sample is obtainable.

Single isolated, combined muons with tight ID are easily selected and come with high purity.

One could obtain single muons in the 5 to 15 GeV range, which are now lost due to the indirect momentum selection from requiring the invariant mass to be approximately the Z mass.

*Checking CF-momentum correlation* Calculating the CFs for low, medium, and high occupancies show mostly no differences in shape, with  $CF(TW) > 1.8$  for muons being the greatest exception. When calculating the CFs, an upper requirement of 80 GeV is put on the momentum. This is made to ensure that the  $p_{HT}$  is approximately constant in the momentum range. For higher momenta, the muons reach into the onset of the curve, and  $p_{HT}$  will quickly rise. Following the same procedure for CF-momentum as for CF-occupancy, one should show CFs for low (e.g.  $p < 40$  GeV), higher (e.g.  $40 < p < 80$  GeV), and very high ( $p > 80$  GeV) momenta to verify the low dependency on momentum for the correction factors.



## **Part IV**

# **Physics analysis: Off-alignment Higgs bosons search**



In this chapter, we will define several concepts that will be used throughout the analysis. Then we outline the analysis from the signal signature and objects used, through the event selection and background reduction, before entering the fit model and upper limits on the production cross-section as well as the 2HDM interpretation. By the end of this chapter, the reader will have an understanding of the workflow and overall process of the analysis. All details will, of course, be presented in the respective chapters.

## Contents

<b>8.1 Data and simulated samples</b> . . . . .	<b>82</b>
---	-----------

The motivation for searching for the  $A \rightarrow ZH$  signature stems from the need for a strong first-order phase transition in order to have electroweak baryogenesis in the early universe, and 2HDMs are able to explain the (level of) baryon asymmetry that exists today [14]. The choice of signal signature was motivated in Sect. 1.2 by examining Fig. 1.6a. A previous analysis [54] used data recorded by ATLAS from 2015 and 2016 to set exclusions on the models from Ref. [16]. Only the  $H \rightarrow bb$  channel was considered since this dominates very near alignment.

A second iteration of the analysis using the full Run 2 data has been done. In this analysis, models further away from alignment have been considered.  $H \rightarrow WW$  takes over as the dominant decay channel in this regime, as was also discussed in Sect. 1.2. As such, this analysis looks for the following signal signature:

- A hadronically decaying<sup>2</sup>  $WW$  pair (diagram in Fig. 8.1) that comes from an  $H$  boson decay where the  $H$  mass range covers<sup>3</sup>  $200 < m_H < 700$  GeV;
- an  $\ell\ell$  pair ( $\ell = e$  or  $\mu$ ) that comes from a  $Z$  boson decay; and
- the  $2\ell 4q$  system that comes from the  $A \rightarrow ZH$  decay where  $300 < m_A < 800$  GeV.

The notation used in this analysis to refer to the additional Higgs bosons is given in Tab. 8.1a. When referring to the theoretical or simulated particles or when defining selection windows, the capital letters are used for bosons; when referring to the reconstructed particle candidates, the particle systems (e.g.  $2\ell 4q$ ) are used.  $q$  will refer to both quarks and jets reconstructed from quark-initiated showers. Jargon (especially local to this analysis) is explained in Tab. 8.1b.

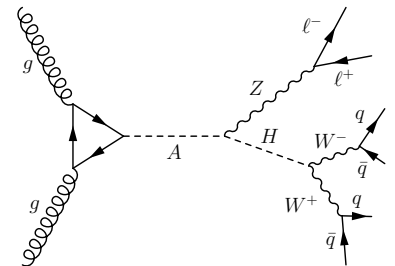


Figure 8.1: The Feynman diagram for the process and channel considered in this analysis. From our paper.

<sup>2</sup>Only the fully-hadronic  $WW$  decay is considered. The semi-leptonic  $WW$  decay was also part of this analysis in its early stages. Due to low personpower, the semi-leptonic channel fell through when the fully-hadronic was becoming mature.

<sup>3</sup>Although the mass of the  $H$  boson is assumed to be larger than that of the  $h$  boson and can therefore be, say, 130 GeV, the lower limit for the  $H$  mass is set to 200 GeV. Below this limit, effects from being near the kinematic limit of the  $W$  bosons would complicate the analysis, and especially moving below 160 GeV (which would mean one off-shell  $W$ ) would require careful analysis. This would lead to this phase space being treated separately at every point of the analysis chain. It was then decided to start at 200 GeV due to low personpower. A future analysis must consider moving the limit to 130 GeV.

Particle	Reconstructed	Note
$A$	$2\ell 4q$	Neutral, CP-odd, chosen to be heavier than $H$
$H$	$4q$	Neutral, CP-even, heavier than $h$
$H^\pm$	-	Charged, CP-even
$h$	-	Neutral, CP-even, assumed to be the SM Higgs boson
Lepton	$\ell$	Curly-l; electron or muon

(a) Particle names

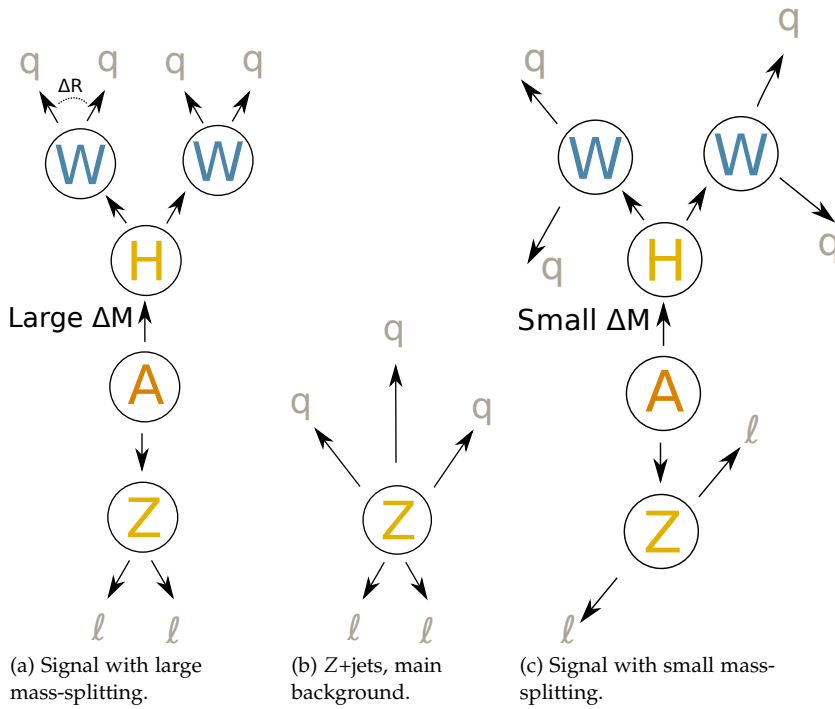
Phrase	Meaning
Fit	The act as well as the result of minimizing the (negative log-)likelihood.
Floating, constrained, and fixed parameters	Parameters in a model may be floating (free, unconstrained by any function), constrained (limited in range), or fixed (constant, possibly parameterized in other variables).
Simulated signal	Signal events generated by a Monte Carlo generator and passed through Geant4 and the ATLAS reconstruction.
Interpolated signal	Signal events generated from fits derived from the simulated signals.
Window	A selection on a variable with both lower and upper thresholds, ie. a window on $x$ is $a < x < b$ , where $a$ and $b$ are the lower and upper thresholds, respectively.
Simulated and real data	"Data" always refers to real data recorded by ATLAS but is prepended by "real" when simulation is mentioned in the same sentence.
(300, 200)	The masses, in GeV, of the simulated or reconstructed signal bosons, $A$ and $H$ , respectively.

(b) Jargon

Table 8.1: (a) The Standard Model and additional 2HDM Higgs particles along with names for their reconstructed objects. (b) Jargon that the reader will come across in reading this analysis.

The event is selected by identifying a pair of electrons or muons, for which the  $p_T$ -leading lepton has triggered the event, and at least four  $R = 0.4$  jets<sup>1</sup>, from which the  $H$  candidate will be formed. In the mass range considered, the jets initiated by the final state quarks do not merge until about or above the maximum mass of  $A$  considered. Therefore, the analysis does not include boosted objects reconstructed with large- $R$  jets.

The signal signature consists of a real  $Z$  boson and four jets.  $Z$ +jets will therefore be a significant irreducible background. Minor backgrounds include  $t\bar{t}$  and  $VV$ .



The signal topology is shown in Fig. 8.2. It depends on the mass-splitting  $\Delta M = m_A - m_H$ . For large mass-splittings, the momenta carried by the decay products of  $Z$  or  $H$  will be in the same direction as the decaying particle, meaning that the transverse momenta of the decaying particles will be close to the sum of the transverse momenta of the decay products. This is sketched in Fig. 8.3 for the variable  $H_2$ , which will be introduced in Sect. 10.2. As such, depending on the *reconstructed masses* of the  $4q$  or  $2\ell 4q$  systems, the signal can be selected from the expected  $H_2$  value.

Only the gluon–gluon fusion (normally shortened ggF, here shortened ggA) signal is considered for this channel. To cover the  $b$ -associated production ( $bbA$ ), yet another jet (or two) would have had to be selected. Considering the level of mismodeling with already 4 jets<sup>2</sup>,  $bbA$  will require its own dedicated study. New Sherpa  $V$ +jets samples are being produced by ATLAS, which might have improved modeling at large jet multiplicity<sup>3</sup>.

Since  $bbA$  is not considered, and ggA mostly produces central jets,

<sup>1</sup> Jets were defined in Sect. 3.4.

Figure 8.2: The topologies for large mass-splitting signals,  $Z$ +jets, and small mass-splitting signals, respectively. In the laboratory frame, the decay products of  $Z$  and  $H$  are "back to back" for signals with large mass-splittings (small  $\Delta R$  between quarks) and much less so for signals with low mass-splittings. The  $Z$  will recoil against its jets; the topology will be in-between the signals.

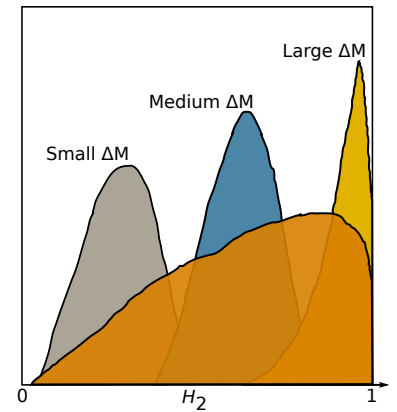


Figure 8.3: A drawing of  $H_2$  for signals with three different mass-splittings with the background overlaid in orange.

<sup>2</sup> The mismodeling will be covered in Chap. 11.

<sup>3</sup> Alternatively, it would be necessary to entirely switch generator.

forward jets are not included in this analysis.

All quark flavors are included, meaning that  $t\bar{t}$  will contribute less compared to the main background,  $Z$ +jets. If jets initiated by  $b$ -quarks were identified (to identify  $b\bar{b}A$ ),  $t\bar{t}$  would contribute more and therefore  $t\bar{t}$  specific selections could be employed. Conversely, since  $b\bar{b}A$  is not considered,  $b$ -quarks could be identified and suppressed as the signal would suffer little loss due to  $|V_{qb}| \approx 4\%$ . This was not done in order not to introduce systematic uncertainties from  $b$ -tagging.

The four jets in the final state present some issues regarding signal selection. The jet combinatorics is resolved by considering pairs of jets and whether they originate from  $W$  bosons.

After the initial event and signal selections, the background is reduced by applying a further selection, which considers the full signal topology. The background will generally have lower  $p_T$  but higher  $m_{2\ell 4q}$  due to the large angular separation. The signal, however, will have a higher  $p_T$  that correlates with the  $m_{2\ell 4q}$ . This can be exploited by the  $J$  variable<sup>1</sup>, which is defined as,

<sup>1</sup> Pronounced "Jvar".

$$J \equiv \frac{\sqrt{p_T^2(\ell_1) + p_T^2(\ell_2) + p_T^2(q_1) + p_T^2(q_2) + p_T^2(q_3) + p_T^2(q_4)}}{m_{2\ell 4q}},$$

where  $\ell$  and  $q$  are the selected leptons and jets, respectively. This variable was chosen because the signals, independent of their masses, produce very similar distributions that are separable from the background. This allows for a flat selection to be applied to any signal regardless of the  $A$  and  $H$  masses.

A final step of the selection is the  $m_{4q}$  window. A window moving in steps of 10 GeV along  $m_{4q}$  selects  $H$  candidates from compatible signal hypotheses, e.g. a (600, 300) signal will have a window around  $m_{4q} = 300$  GeV. The width of the window is optimized to maximize signal significance. The window is optimized for narrow-width  $H$  only, which is acceptable for large parts of the phase space as was mentioned by the end of Sect. 1.2.

After the selections, the reconstructed  $A$  mass,  $m_{2\ell 4q}^{\text{COR}}$ , is fitted for each signal hypothesis. The variable  $m_{2\ell 4q}^{\text{COR}}$  is defined as the mass of the  $2\ell 4q$  system, in which the  $\ell\ell$  and  $4q$  four-vectors are scaled such that they reproduce the mass of the  $Z$  and  $H$  bosons, respectively. This rescaling is not applied before the  $m_{4q}$  window because the  $H$  hypothesis is not yet decided before entering a window.

The signal region is defined at three levels with increasing signal significance. The levels are:

- Level 1: Initial event selection and resolved jet combinatorics
- Level 2: The  $J$  variable selection
- Level 3: A  $m_{4q}$  window

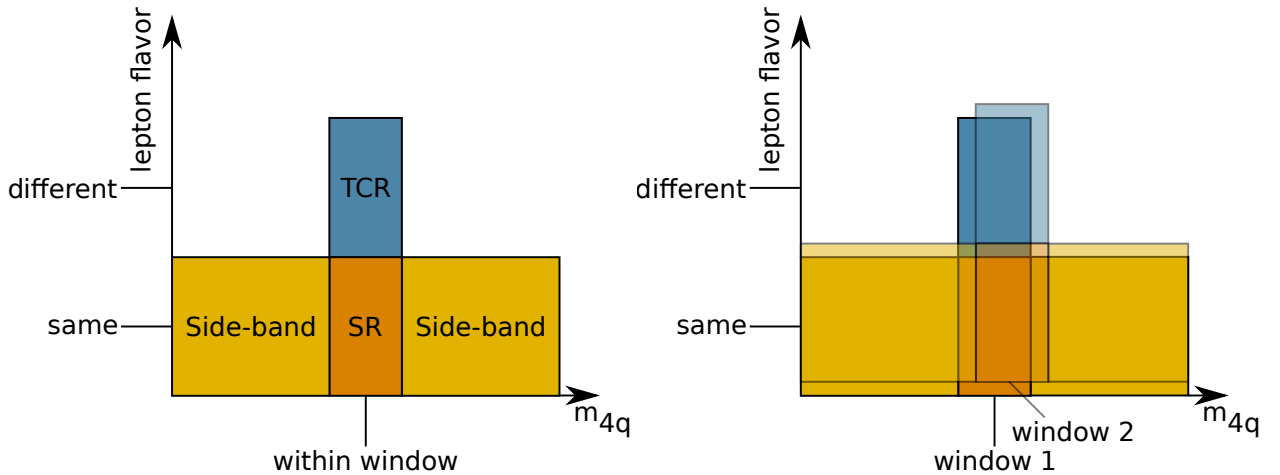
The signal regions are named "CRcutbased" at Level 1, "CRcutbased-Jvar" at Level 2, and "SRcutbasedJvarH300" at Level 3 for an  $m_{4q}$  window at 300 GeV.

At levels 1 and 2, the signal is considered diluted by the background, and the analysis is as such effectively blind. Therefore, the distributions before the  $m_{4q}$  windows are shown unblinded. After entering an  $m_{4q}$  window, the analysis is explicitly blinded.

Several regions are defined at Level 3. Apart from the signal regions, two regions enriched with their respective backgrounds are defined. The regions are discriminated as follows:

1. Signal regions (SRs): Same-flavor leptons
2. Side-bands: Same-flavor leptons with inverted  $m_{4q}$  window
3. Top control regions (TCRs): Different-flavor leptons

There is one SR, side-band, and TCR *per H hypothesis*. This is sketched in Fig. 8.4. The window will slide in steps of 10 GeV, and regions will therefore overlap. For the range  $200 < m_H < 700$  and  $m_H + 100 < m_A < 800$  GeV, this gives 1326 signal regions with accompanying control regions. The control regions will only be used to constrain the Z+jets and  $t\bar{t}$  normalizations, which will be left floating in the eventual likelihood fit. Since only normalization information is required, the bins of the control regions will be combined into 1 bin each during the fit.



This analysis is separated into the following chapters, whose contents are shortly listed as well:

**Object definitions and preselection:** Define leptons and jets used in analysis and apply preselection during the production of calibrated input samples.

**Object and event selection:** Apply event selections to identify signal signature; select signal jets; apply further selections using the  $J$  variable to reduce background; and enter the signal regions using the  $m_{4q}$  windows.

**Background modeling:** Show various variables for the simulated backgrounds and real data; evaluate the modeling accuracy of the simulated backgrounds; and apply corrections.

**Signal modeling:** Fit the simulated signals and interpolate the fit parameters; after this point, the simulated signals are replaced by

Figure 8.4: Left: A picture of the region definitions for one  $m_{4q}$  window. The SR and TCR are within the window but have same and different lepton flavors, respectively. The side-band covers all of  $m_{4q}$  outside the window. Right: A second window drawn on top of the first window (and slightly raised to help see the difference; the lepton flavors are unchanged). The SR of the first window is partly contained within the side-band and SR of the second window.

these interpolated fits, which can be made for any arbitrary mass point  $(m_A, m_H)$ .

**Systematic uncertainties:** List the systematic uncertainties stemming from the detector, reconstruction, and modeling.

**Fit model:** Introduce the likelihood function along with its nuisance parameters; evaluate the fit using the simulated background and test in real data outside the signal region; and evaluate the fit model in the signal region with unblinded data.

**Results:** Apply the fit model to real data; calculate limits for narrow-width and large-width signals; and interpret limits on large-width signals in 2HDM.

**Discussion:** Discuss several issues discovered during the analysis work.

## 8.1 Data and simulated samples

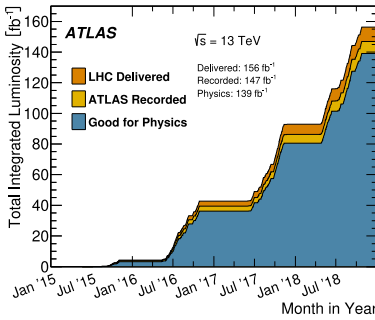


Figure 8.5: Instantaneous luminosity delivered by LHC, recorded by the ATLAS detector, and useful for physics analysis (passing the GRL). Adapted from [112].

<sup>1</sup> ATLFAST-II gains its speed improvement from having parameterized the response of ATLAS calorimeters without having to simulate every detail. Jet substructure, forward jets using the FCAL, among others, may be areas where ATLFAST-II is lacking, but these will not be necessary for this analysis.

The analysis uses LHC-delivered data from  $\sqrt{s} = 13$  TeV proton–proton collisions recorded by the ATLAS detector between 2015 and 2018 with a total of  $139 \text{ fb}^{-1}$  of usable integrated luminosity. Fig. 8.5 shows the LHC-delivered and ATLAS-recorded data as well as actual useful data selected by the GRL [112] where all parts of the detector were working.

Signal and background processes are simulated using various Monte Carlo generators with some generators only simulating the productions and then passing the event to others for fragmentation and hadronization simulations. The details for the specific processes will be given below. All background processes are passed through Geant 4 [115] to simulate the traversal of particles through the ATLAS detector [116] after the hadronization step. Signal samples are passed through the much faster ATLFAST-II [116], which has great accuracy and precision for the needs of the analysis<sup>1</sup>, in order to save time, so that more signal samples (more  $A$  and  $H$  hypotheses) could be produced. Simulated events undergo *digitization*, which converts the output into detector response digits, making the output of the Geant4 or ATLFAST-II identical to data in structure (with additional truth information). After this, simulated and collision events undergo the same reconstruction.

Signal, only produced from gluon–gluon fusion, is generated by MadGraph5\_aMC@NLO 2.3.3 [117, 118] at LO with parton showering handled by Pythia 8.210 [119] with the A14 tune [120] and NNPDF2.3 PDF set [121].

Z+jets decaying leptonically (including taus) is generated by Sherpa v.2.2.1 [122] using matrix elements (ME) at next-to-leading order (NLO) for up to two partons and LO for up to four partons with Sherpa’s own tune and the NNPDF3.0nnlo PDF set [123]. The ME are calculated by the Comix [124] and OpenLoops [125, 126] libraries. The ME are matched to the Sherpa parton shower [127] using the MEPS@NLO prescription [128–131]. The samples are normalized to a next-to-next-to-leading order (NNLO) prediction [132].

Dibosons decaying semi-leptonically ( $WW$ ,  $ZZ$ , and  $WZ$ ) are generated by the same generator as for  $Z$ +jets and with the same parameters.

$t\bar{t}$  is generated by PowhegBox v2 [133–136] at NLO with the NNPDF3.0nlo PDF set [123] and the parameter<sup>1</sup>  $h_{\text{damp}}$  set to  $1.5 m_{\text{top}}$  [137].<sup>1</sup>  $h_{\text{damp}}$  is one of the parameters that regulates the high- $p_{\text{T}}$  radiation, which the  $t\bar{t}$  system recoils against.

Top quark in association with a  $W$  ( $tW$ ) and single-top  $s$ -channel are generated by PowhegBox v2 [134–136, 139, 140] at NLO in  $\alpha_{\text{S}}$  using the five-flavor scheme and the NNPDF3.0nlo PDF set. Interference and overlap between  $t\bar{t}$  and  $tW$  are removed through diagram removal [141]. Parton showering is handled by Pythia 8.210 with the A14 tune and NNPDF2.3lo PDF set. Bottom and charm hadron decays are simulated by EvtGen v1.2.0.

Inelastic proton–proton collisions are generated by Pythia 8.186 with the A3 tune [142] and NNPDF2.3lo PDF set to simulate the pileup of the simulated samples. This pileup serves as the multiple interactions in the current bunch-crossing and bunch-crossings before and after. The pileup is normalized to the average number of interactions per bunch crossing  $\langle\mu\rangle$  observed in data and is overlaid the simulated samples at the digitization step.

The only background processes used in this analysis are  $Z$ +jets ( $> 88\%$  of total background depending on region),  $t\bar{t}$  +single-top (up to 7%), and semi-leptonic dibosons (up to 6%). Smaller backgrounds, such as  $W$ +jets,  $t\bar{t}V$ , and  $Vh^2$ , contributed less than 1.0% of the total background and have been pruned from the analysis.  $W$ +jets would be the most significant source of fake leptons but its contribution is negligible. Multi-jet contamination is presumed negligible since two loosely identified leptons with rather large  $p_{\text{T}}$  are required, and the leptons must lie in the range of the  $Z$  mass. This was specifically tested in the two-lepton channel of the  $Vh$  analysis [47], which has an event selection similar to this analysis but looser  $p_{\text{T}}$  requirements on the leptons. They found negligible contributions from multi-jets after the event selection.

<sup>2</sup> Remember, the lowercase  $h$  refers to the SM Higgs boson.



## 9 Object definitions and pre-selection

*This section will introduce the preselections that are applied during the creation of the calibrated samples. The preselection will be presented verbatim, including selections not relevant to this analysis, as the calibrated samples are used by multiple analyses and the selections that are applied affect which events are saved. Technical definitions of the object identifications, isolations, qualities, etc. were presented in Chap. 3.*

### Contents

---

<b>9.1 Leptons</b> . . . . .	<b>86</b>
<b>9.2 Jets</b> . . . . .	<b>86</b>
<b>9.3 Overlap removal</b> . . . . .	<b>87</b>
<b>9.4 Event preselection</b> . . . . .	<b>88</b>

---

As mentioned in Chap. 3, the data recorded by ATLAS and reconstructed into datasets contain a significant number of irrelevant events; a reduced dataset which includes light selections on leptons and selections on the number of these will heavily reduce the number of events without a significant loss of potential signal. The derived dataset used by this analysis, HIGG2D4, includes light selections on the kinematics of electrons, muons, and jets, and requires that at least two leptons and one jet pass these selections.

The analysis uses fully-calibrated samples ("CxAOD" samples) made from these derived datasets. During the production of the calibrated samples, several preselections are made on objects, and these objects are used for the event preselection. The object preselections and overlap removal will be presented in this chapter. The object preselections will define different classes of preselected objects, e.g. "loose" and "signal" leptons. Finally, selections on the number of preselected objects are applied. Most notably, the event is required to contain exactly two "loose" leptons, of which at least one is a "signal" lepton, and at least two "signal" jets.

"Forward" ( $|\eta| \geq 2.5$ ) jets, large-R jets ( $\Delta R = 1.0$ ), and tau leptons are not part of this analysis. Yet, they do affect overlap removal and event preselection and are mentioned for completeness but without further introduction or explanation.

## 9.1 Leptons

Basic selections are applied to all electrons and muons, including identification, kinematics, and isolation. These define the "loose" leptons. Loose leptons are then required to pass further kinematic selections to become "signal" leptons. All selections are listed in Tab. 9.1. Note that electrons in the calorimeter crack are not vetoed.

Cut	Electron selection	Muon selection
	<i>Loose electrons</i>	<i>Loose muons</i>
Identification	Pass LooseLH	Pass Loose
Pseudorapidity	$ \eta^{\text{BE}(2)}  < 2.47$ (in second layer of ECAL)	-
Transverse momentum	$p_T > 7 \text{ GeV}$	$p_T > 7 \text{ GeV}$
Impact significance	$ d_0^{\text{BL,sig}}  < 5$	$ d_0^{\text{BL,sig}}  < 3$
Track-vertex association	$ \Delta z_0 \sin \theta  < 0.5 \text{ mm}$	$ \Delta z_0 \sin \theta  < 0.5 \text{ mm}$
Shower shape quality	Pass OQ	-
Isolation	Any of: <ul style="list-style-type: none"> <li>• <math>p_T &gt; 100 \text{ GeV}</math></li> <li>• Pass Loose</li> <li>• Pass HighPtCaloOnly</li> </ul>	Any of: <ul style="list-style-type: none"> <li>• <math>p_T &gt; 100 \text{ GeV}</math></li> <li>• Pass Loose</li> <li>• Pass TightTrackOnly</li> </ul>
	<i>Signal electrons</i>	<i>Signal muons</i>
Loose lepton	Pass loose electron selections above	Pass loose muon selections above
Transverse momentum	$p_T > 25 \text{ GeV}$	$p_T > 25 \text{ GeV}$
Pseudorapidity	-	$ \eta  < 2.5$

Table 9.1: Lepton preselection cut-flow. Identification and isolation WPs were defined in Chap. 3.

## 9.2 Jets

Jets also undergo a number of kinematic and isolation selections. Central ( $|\eta| < 2.5$ ) and forward ( $|\eta| \geq 2.5$ ) jets are selected individually. Both jet types must then afterwards pass further selections to be considered "base" jets. Jets passing the first two base jet selections (without checking the third) are considered "preselected" jets and used in the coming overlap removal. Finally, "signal" jets are central jets that pass base jet selections. See the list of selections in Tab. 9.2.

Cut	Selection
	<i>Central jets</i>
Jet transverse momentum	$p_T > 20$ GeV
Jet pseudorapidity	$ \eta  < 2.5$
	<i>Forward jets</i>
Fwd. jet transverse momentum	$p_T^{\text{fwd}} > 30$ GeV
Fwd. jet pseudorapidity	$2.5 \leq  \eta^{\text{fwd}}  < 4.5$
	<i>Base jets</i>
Track-vertex association	Pass JVT Medium
Central or forward jet	Pass central or forward selections above
Bad jet cleaning	Pass LooseBad
	<i>Signal jets</i>
Central and base jet	Pass central and base jet selections above

Table 9.2: Jet preselection cut-flow. Note that forward jets always pass JVT, and no forward JVT selection is applied. Jets are "preselected" after passing the first two base jet selections.

### 9.3 Overlap removal

Objects are reconstructed by separate algorithms using the same detector information; tracks and clusters are **not** removed when an algorithm has reconstructed an object from these. Therefore, it is necessary to decide which two objects to use if they are reconstructed from the same tracks, clusters, or other information in the same direction. This process is known as *overlap removal*<sup>1</sup>. For the  $\Delta R$  calculation, rapidity is used. Only jets passing "preselection" and leptons passing "loose" are considered for overlap removal.

The procedure is summarized in Tab. 9.3. For steps that are not simple  $\Delta R$  selections, the details are laid out here. The removal process is done in the order given in the table; any object passing the criteria is tested at the next step.

If two electrons share the same GSF<sup>2</sup> track and either the first electron is ambiguous and the second is not<sup>3</sup> or the  $p_T$  of the first is lower than that of the second, the first electron is removed.

If a CT<sup>4</sup> muon shares its ID track with an electron, the muon is removed.

If an electron shares its original ID track with a muon, the electron is removed.

If a jet has fewer than three ghost-matched<sup>5</sup> tracks and either the muon ID track was ghost-matched to the jet or the  $\Delta R$  between them is less than 0.2, the jet is removed.

The official overlap removal contains more steps, but they are not relevant to this analysis (ie. rejecting photons).

<sup>1</sup> More information in this presentation internal to ATLAS, [https://indico.cern.ch/event/631313/contributions/2683959/attachments/1518878/2373377/Farrell\\_ORTools\\_ftagbbb.pdf](https://indico.cern.ch/event/631313/contributions/2683959/attachments/1518878/2373377/Farrell_ORTools_ftagbbb.pdf).

<sup>2</sup> See Sect. 3.2 for the definition.

<sup>3</sup> This criterion is not specified in any documentation but is applied in the code: <https://gitlab.cern.ch/atlas/athena/-/blob/21.2/PhysicsAnalysis/AnalysisCommon/AssociationUtils/Root/EleEleOverlapTool.cxx>, line 192.

<sup>4</sup> See Sect. 3.3 for the definition.

<sup>5</sup> Tracks are *ghost-matched* to jets, if the tracks are within the area of the jet when it is formed.

Table 9.3: Overlap removal steps. The steps are done from top to bottom.

Reject (first)	Against (second)	Criteria
electron	electron	Shared GSF track AND (first electron ambiguous while second not OR $p_T^{\text{first}} < p_T^{\text{second}}$ )
tau	electron	$\Delta R < 0.2$
tau	muon	$\Delta R < 0.2$
muon	electron	Muon is of type CT AND shared ID track
electron	muon	shared ID track
jet	electron	$\Delta R < 0.2$
electron	jet	$\Delta R < 0.4$
jet	muon	NumTrack $< 3$ AND (ghost-matched OR $\Delta R < 0.2$ )
muon	jet	$\Delta R < \min(0.4, 0.04 + 10 \text{ GeV} / p_T^{\text{muon}})$
jet	tau	$\Delta R < 0.2$
large-R jet	electron	$\Delta R < 1.0$

## 9.4 Event preselection

Objects have been preselected and overlaps have been removed. The event must pass the standard event quality selections and contain a number of leptons and jets as listed in Tab. 9.4 to pass the preselection.

Table 9.4: Event preselection cut-flow. The event quality selections were introduced in Sect. 3.5. Finally, the event must contain at least two leptons (mixed flavor is allowed) and a minimum number of jets (either two jets or one large-R jet).

Cut	Selection
Good Runs List	Pass GRL
Primary vertex	Has primary vertex
Event cleaning	Pass event cleaning
Bad jet veto	Veto event if a jet passes the selections in Sect. 3.5 but fails jet cleaning (LooseBad)
Lepton multiplicity	The event must contain exactly two loose leptons passing the overlap removal of which at least one is also a signal lepton
Jet multiplicity	The event must either contain at least two signal jets passing overlap removal or
Large-R jet multiplicity	at least one large-R jet passing $p_T > 200 \text{ GeV}$ and $ \eta  < 2.5$

The signal and backgrounds were introduced in Chap. 8, while Chap. 9 defined the objects that will be used in this analysis. In this chapter, we will look into how to properly select our signal and suppress background events. Since the signal decays to four quarks, which we reconstruct as four jets, we will discuss how to select the right four jets in events with at least four jets.

## Contents

<b>10.1 Initial event selection</b> . . . . .	<b>90</b>
<b>10.2 Resolving jet combinatorics</b> . . . . .	<b>91</b>
10.2.1 Deriving the selections . . . . .	92
10.2.2 Applying the selections . . . . .	94
<b>10.3 Optimization of the <math>J</math> variable</b> . . . . .	<b>97</b>
<b>10.4 <math>m_{4q}</math> window optimization</b> . . . . .	<b>99</b>
10.4.1 Window optimization in 2D . . . . .	100
<b>10.5 Final selection and summary</b> . . . . .	<b>101</b>
10.5.1 Cut-flow tables . . . . .	104

The final state of the  $H \rightarrow WW$  decay consists of four quarks. In the event, there will often be additional jets coming from the underlying event and pileup. This issue of combinatorics will shape the event selection.

Choosing between 5 jets gives  $\binom{N=5}{4} \times 3 = 15$  combinations to consider. For  $N = 6$ , this is already 45. The number of combinations are derived this way: Choosing 4 jets from a pool of  $N = 5$  jets yields the binomial coefficient. If the individual  $W$  bosons are reconstructed, there are 3 unique combinations due to the interchangeability of the  $W$  candidates.

One also needs to consider whether to perform selections on the final state objects themselves or on systems made of these objects; the four jets can therefore be selected in two different ways:

Case 1: The  $H$  boson from all four jets are identified without resolving which jets belong to which  $W$  boson, or

Case 2: The correct dijets<sup>2</sup> that make up the two  $W$  bosons are identified.

An example of the combinatorics issue is shown in Tab. 10.1 for the two above Cases. While Case 1 will have much fewer combinations to consider, Case 2 has the added benefit of being able to use the

Case 2		Case 1	
good	bad	good	bad
12 34	12 35	1234	1235
	12 45		1254
	13 24		1534
	13 25		5234
	13 45		
	14 23		
	14 25		
	14 35		
	15 23		
	15 24		
	15 34		
	23 45		
	24 35		
	25 34		

Table 10.1: Consider an event with 5 jets. One  $W$  boson decays to jets 1 and 2, and the other decays to jets 3 and 4. To reconstruct the individual  $W$  bosons, the two dijets must be identified. As seen in this table, for 5 jets, this leads to 15 combinations to consider compared to only 5 if the individual dijets are not identified.

<sup>2</sup> Dijet: An object made from a pair of jets.

reconstructed  $W$  candidates to suppress some bad combinations as well as reduce background to some extent.

Two approaches (selection strategies), based on Cases 1 and 2, to select the signal are realized in the following two ways:

1. "Hardest jets": The 4  $p_T$ -leading jets are selected (based on Case 1)
2. Resolving jet combinatorics: The 5  $p_T$ -leading jets are combined into two  $W$  boson candidates that are required to pass several selections (based on Case 2)

The analysis initially considered both approaches. However, during the maturation of the analysis, preliminary upper limits on the production cross-section of  $A$  were 1.4 to 4.1 times lower (=better) for the approach that resolves jet combinatorics, depending on the masses (see App. 19.A for the full table). The "hardest jets" approach was therefore discontinued in favor of the more advanced approach.

Due to the level of combinatorics, it is important for the selection to loosely reject bad combinations in order to keep a high signal efficiency. Therefore, when the approach that resolves jet combinatorics is derived and applied in the following sections, the selection windows will approximately cover the samples within their 95% error bars.

This chapter is structured as follows. Some initial selections are done in Sect. 10.1 to derive a set of candidate events. In Sect. 10.2, the approach that resolves jet combinatorics is introduced, derived, and applied. Sects. 10.3 and 10.4 will introduce additional background reductions that will finally be applied in Sect. 10.5, which also introduces the signal and control regions. The final section will show full cut-flow diagrams for the signal samples (Sect. 10.5.1).

## 10.1 Initial event selection

The events were preselected in Chap. 9. Now, at this stage, the actual event selection is applied. The event must pass the triggers, and the features mentioned in the beginning of the chapter are selected for.

The event must pass any of the unprescaled single lepton triggers with the lowest  $p_T$  thresholds<sup>1</sup>. The triggers are listed in Tab. 10.2. There are a few things to note regarding this list:

- As the instantaneous luminosity increased over the years, the thresholds were likewise increased in order to keep a constant event rate at the L1 trigger stage.
- The triggers with the lowest  $p_T$  thresholds require tight (medium for 2015) electrons or medium (loose for 2015) muons. The event will therefore often contain at least one tight electron.<sup>2</sup>
- The list does not contain dilepton triggers. The efficiency is already quite high for higher masses. For the lowest simulated signal, the trigger efficiency is about 80%. In this case, adding 2e17\_lhvloose\_nod0\_2EM15VHI [94] to the list could regain some lost events.

Trigger	year
electron channel	
e24_lhmedium_L1EM20VH	2015
e60_lhmedium	2015
e120_lhloose	2015
e26_lhtight_nod0_ivarloose	2016 - 2018
e60_lhmedium_nod0	2016 - 2018
e140_lhloose_nod0	2016 - 2018
e300_etcut	2016 - 2018
muon channel	
mu20_iloose_L1MU15	2015
mu50	2015 - 2018
mu26_ivarmedium	2016 - 2018

Table 10.2: The single lepton triggers that have been used in this analysis. See Chap. 3 for the naming convention.

<sup>1</sup> The electron triggers use calorimeter clusters and hence measure the (transverse) energy of electrons. The transverse energy is, however, colloquially called  $p_T$  for electrons.

<sup>2</sup> The reader may realize at this point that no ID requirement has nor will be applied to the leptons except for the initial loose requirement at the preselection stage. Since the leading lepton will be matched with the triggers of the event, there should be a corresponding ID selection on the lepton matching the ID in the trigger. This was not done.

The remaining selections are as follows. At least one of the two  $p_T$ -leading leptons must have  $p_T$  higher than the smallest trigger threshold for all years. The invariant mass of the two leptons,  $m_{\ell\ell}$ , must be compatible with the mass of the  $Z$  boson. Muon pairs must have opposite charge<sup>1</sup>. The event must contain at least 4 jets.

The precise selections applied are summarized in this list:

1. The event must pass the lowest un-prescaled triggers listed in Tab. 10.2,
2. The two  $p_T$ -leading leptons must have  $p_T > 30, 15$  GeV, respectively,
3. For compatibility with the  $Z$  boson,  $80 < m_{\ell\ell} < 100$  GeV,
4. For events with  $\mu\mu$  leptons, the muons must have opposite charge,
5. The event must contain at least 4 jets within  $|\eta| < 2.4$  and  $p_T > 20$  GeV, and
6. The  $p_T$  of the two  $p_T$ -leading jets must be 40 and 30 GeV, respectively.

The jet  $p_T$  selections were optimized such that no more than half the signal events for the lowest mass point  $(m_A, m_H) = (300, 200)$  GeV would be removed.

## 10.2 Resolving jet combinatorics

The approach makes use of the opening angles ( $\Delta R$ ) between the jets in each  $W$  candidate as well as measure of "back-to-backness" of the reconstructed objects.

The procedure for selecting the four signal jets, which are pairwise reconstructed as  $W_1$  and  $W_2$ , is as follows. Among the five  $p_T$ -leading jets, every combination, without double-counting, is considered. This gives 15 combinations per event. When the two  $W$  candidates are formed,  $W_1$  will be the  $p_T$ -leading  $W$  candidate. For every combination, the  $W$  candidates must pass four selections. When more than one combination remains after the selections, the combination with the  $W$  candidate masses most consistent with that of a  $W$  boson is chosen.

The variables for the four selections have been chosen due to their ability to discriminate between correctly and wrongly combined signals. The choice of these variable are based on the topological considerations that were presented in Chap. 8.

The four selections and the final determining selection are:

1. Window selection on  $\Delta R(q, q)$  of the  $p_T$ -leading  $W$ , named  $\Delta R(W_1)$ .
2. Window selection on  $\Delta R(q, q)$  of the  $p_T$ -sub-leading  $W$ , named  $\Delta R(W_2)$ .
3. Window selection on<sup>2</sup>  $H_2 = \frac{p_T^{\ell\ell} + p_T^{4q}}{p_T^{\ell_1} + p_T^{\ell_2} + p_T^{W_1} + p_T^{W_2}}$ .
4.  $\sqrt{(m_{W_1} - 80 \text{ GeV})^2 + (m_{W_2} - 80 \text{ GeV})^2} < 60 \text{ GeV}$ ;  $(m_{W_1}, m_{W_2})$  must be within a circle with center (80, 80) GeV and a radius<sup>3</sup> of 60 GeV.

<sup>1</sup> This requirement is not applied to electron pairs. Bremsstrahlung or the possibly resulting pair production might flip the measured charge, which would then lower the signal efficiency without appropriately lowering background as well. The main background is already real  $Z$  bosons, so little is gained from applying this selection to electrons.

<sup>2</sup> This variable is inspired by the  $H_{T2}^R$  variable presented in the internal note of Ref. [143]. A public paper is also available at Ref. [144].

<sup>3</sup> The  $W$  candidates of many bad combinations either have very asymmetrical or high masses, so they are still rejected with the wide radius.

5. When more than one combination is left after the above selections, the combination with lowest  $\chi^2 \propto (m_{W_1} - 80 \text{ GeV})^2 + (m_{W_2} - 80 \text{ GeV})^2$  is chosen (a constant uncertainty is chosen for the  $\chi^2$ ).

The following two subsections will

- in Sect. 10.2.1 derive the lower and upper thresholds on  $H_2$ ,  $\Delta R(W_1)$ , and  $\Delta R(W_2)$ , for each simulated signal individually, and
- in Sect. 10.2.2 interpolate between the thresholds of the simulated signals to make the windows.

### 10.2.1 Deriving the selections

In this section, the initial event selection introduced in Sect. 10.1 is applied with additional selections per simulated signal that use the simulated masses to identify the signal.

The right combinations are found using only the reconstructed objects with an iterative method. The basis of the method is the a priori knowledge of correctly-combined signals:

1. The reconstructed masses of  $m_{4q}$  and  $m_{2\ell 4q}$  must be close to the simulated masses  $m_H$  and  $m_A$ , respectively.
2. The reconstructed masses of  $W$  candidates,  $m_{W_1}$  and  $m_{W_2}$ , must both be close to 80 GeV.
3. For heavier  $A$  bosons, the  $\Delta R$ s between the jets in each  $W$  candidate are small; for (generally low energy) pileup to lead to large invariant masses, their  $\Delta R$  must be large.

The *base selection* used in this iterative method is therefore:

$$|m_{4q} - m_H| < 10 \text{ GeV} \quad (10.1)$$

$$|m_{2\ell 4q} - m_A| < 10 \text{ GeV} \quad (10.2)$$

$$\sqrt{(m_{W_1} - 80 \text{ GeV})^2 + (m_{W_2} - 80 \text{ GeV})^2} < 36 \text{ GeV} \quad (10.3)$$

$$\Delta R(W_1) < 2.5 \quad (10.4)$$

$$\Delta R(W_2) < 2.5 \quad (10.5)$$

This procedure is used on the simulated signals separately, using only signal samples produced for data taken during 2015 and 2016<sup>1</sup>. The requirements on the mass reconstruction are rather tight and will skew the distributions for signals that have radiated, which is more often the case for heavier signals if these radiated particles are not within the radius of the jet. The procedure will be detailed below; one can compare the steps taken with Fig. 10.1, which is shown at the end.

Using this base selection,  $H_2$  is plotted and the bell-like distribution is fitted with an asymmetric Gaussian from which the mean  $\mu_{H_2}$  of the distribution as well as the left-side width  $\sigma_L^{H_2}$  and right-side width  $\sigma_R^{H_2}$  are extracted. See the top-left plot in Fig. 10.1.

The asymmetric Gaussian with a constant term is of this form:

$$C_0 e^{-\frac{1}{2} \left( \frac{x - \mu}{\sigma} \right)^2} + C_1, \quad \text{where } \sigma = \sigma_R \text{ for } x > \mu \text{ else } \sigma = \sigma_L \quad (10.6)$$

<sup>1</sup> This procedure was done early in the analysis stage before signals for all years were combined.

These fit values are used to further constrain the combination selection by appending  $H_2 > \mu_{H_2} - 3\sigma_L^{H_2}$  and  $H_2 < \mu_{H_2} + 3\sigma_R^{H_2}$  to the base selection. Note that three times the width is used initially since these estimates still contain some wrong combinations.

After this step,  $\Delta R(W_1)$  is plotted and fitted, and the results of the fit is appended to the base selection in the same manner. See the top-middle plot in Fig. 10.1. Finally,  $\Delta R(W_2)$  is plotted and fitted, and the results are appended to the base selection. See the top-right plot in Fig. 10.1.

The base selection is then frozen. It contains the previous selections as well as:

$$\mu_{H_2} - 3\sigma_L^{H_2} < H_2 < \mu_{H_2} + 3\sigma_R^{H_2} \quad (10.7)$$

$$\mu_{\Delta R(W_1)} - 3\sigma_L^{\Delta R(W_1)} < \Delta R(W_1) < \mu_{\Delta R(W_1)} + 3\sigma_R^{\Delta R(W_1)} \quad (10.8)$$

$$\mu_{\Delta R(W_2)} - 3\sigma_L^{\Delta R(W_2)} < \Delta R(W_2) < \mu_{\Delta R(W_2)} + 3\sigma_R^{\Delta R(W_2)} \quad (10.9)$$

The three variables,  $H_2$ ,  $\Delta R(W_1)$ , and  $\Delta R(W_2)$ , will now each be fitted again, this time with the frozen base selection. The iterative method is not used at this stage. The fit function is the same asymmetric gaussian. The mean as well as the left and right widths will be saved. These are the bottom three plots in Fig. 10.1 in the respective order.

To summarize, the iterative method is done through these steps:

1. For the 5  $p_T$ -leading jets, perform every combination, leading to 15 signal candidates per event.
2. Apply the base selection on the combination and fit the  $H_2$  distribution.
3. Apply the base selection on the combination as well as  $H_2 > \mu_{H_2} - 3\sigma_L^{H_2}$  and  $H_2 < \mu_{H_2} + 3\sigma_R^{H_2}$ , and fit the  $\Delta R(W_1)$  distribution.
4. Apply the base selection on the combination as well as  $H_2 > \mu_{H_2} - 3\sigma_L^{H_2}$ ,  $H_2 < \mu_{H_2} + 3\sigma_R^{H_2}$ ,  $\Delta R(W_1) > \mu_{\Delta R(W_1)} - 3\sigma_L^{\Delta R(W_1)}$ , and  $\Delta R(W_1) < \mu_{\Delta R(W_1)} + 3\sigma_R^{\Delta R(W_1)}$ , and fit the  $\Delta R(W_2)$  distribution.
5. The final set of selections is: the base selection,  $H_2 > \mu_{H_2} - 3\sigma_L^{H_2}$ ,  $H_2 < \mu_{H_2} + 3\sigma_R^{H_2}$ ,  $\Delta R(W_1) > \mu_{\Delta R(W_1)} - 3\sigma_L^{\Delta R(W_1)}$ ,  $\Delta R(W_1) < \mu_{\Delta R(W_1)} + 3\sigma_R^{\Delta R(W_1)}$ ,  $\Delta R(W_2) > \mu_{\Delta R(W_2)} - 3\sigma_L^{\Delta R(W_2)}$ , and  $\Delta R(W_2) < \mu_{\Delta R(W_2)} + 3\sigma_R^{\Delta R(W_2)}$ .
6. There are now rough lower and upper thresholds for  $H_2$ ,  $\Delta R(W_1)$ , and  $\Delta R(W_2)$ , which will be used to derive the actual thresholds; the three variables will now be fitted again with the final set of selections, and their means and widths are saved.

The iterative method is applied to each simulated signal. From this, a set of thresholds is derived for each simulated signal. These thresholds will be interpolated in the next subsection.

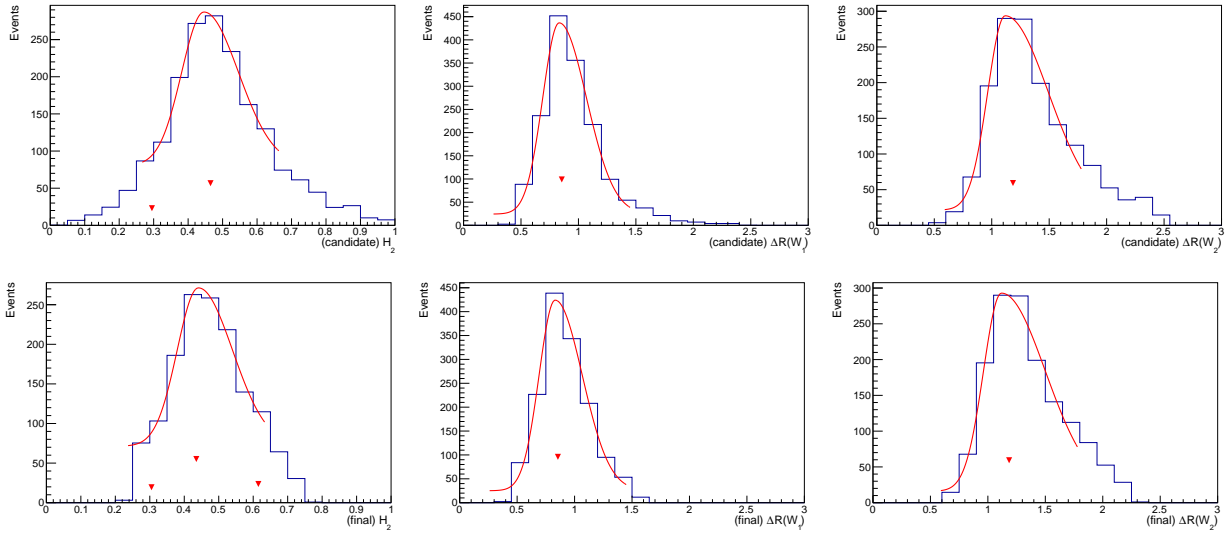


Figure 10.1: The iterative process of constructing the variable thresholds for the (500, 350) sample. The first row shows the  $H_2$ ,  $\Delta R(W_1)$ , and  $\Delta R(W_2)$  candidates after the selections in steps 2-4, respectively. The second row shows the final distributions of the variables after the final set of selections has been found. The red arrows show the peaks of the distributions, which define the initial mean before the fit is executed. Due to noise, some plots show multiple peaks; only the tallest peak is used.

## 10.2.2 Applying the selections

The three variables,  $H_2$ ,  $\Delta R(W_1)$ , and  $\Delta R(W_2)$  with windows applied are shown in Fig. 10.2.

All three variables, when plotted for all simulated signals, show a clear correlation with the mass-splitting ( $m_{2\ell 4q} - m_{4q}$ ). Therefore, the variables were plotted as a function of the mass-splitting, but they still showed some correlation with  $m_{2\ell 4q}$ . Due to this, the parametrization seen on the x-axis was manually adjusted until the samples were following a trend that could be contained by simple expressions. The parameterizations and derived windows are given in the following list where the windows are split into their lower and upper limits:

- $\Delta R(W_1)$ ;  $x = \left(m_{2\ell 4q} - m_{4q}\right)^{0.0047} - m_{2\ell 4q} \cdot 0.000048$  [arb. units];  $m_{2\ell 4q}, m_{4q}$  [GeV]:
  - Lower limit:  $0.18x^{17 \cdot 10^1} + 0.28$
  - Upper limit:  $0.89x^{12 \cdot 10^1} + 0.77$
- $\Delta R(W_2)$ ;  $x = \left(m_{2\ell 4q} - m_{4q}\right)^{0.0057} - m_{2\ell 4q} \cdot 0.000030$  [arb. units];  $m_{2\ell 4q}, m_{4q}$  [GeV]:
  - Lower limit:  $0.020x^{21 \cdot 10^1} + 0.28$
  - Upper limit:  $0.030x^{27 \cdot 10^1} + 1.0$
- $H_2$ ;  $x = \left(m_{2\ell 4q} - m_{4q}\right)^{0.01} - m_{2\ell 4q} \cdot 0.00001$  [arb. units];  $m_{2\ell 4q}, m_{4q}$  [GeV]:
  - Lower limit:  $234958.9 - 671743.2x + 640116.53x^2 - 203309.9x^3$
  - Upper limit:  $277186.2 - 794663.5x + 759336.8x^2 - 241837.7x^3$

The choice of functions and their values for the lower and upper limits for the three variables were decided on early in the analysis; the lower and upper limits were fitted with the above expressions against the tips of the error bars in Fig. 10.2.

The cut-flow table is listed in Tab. 10.3 for all simulated signals, backgrounds by group, and real data.

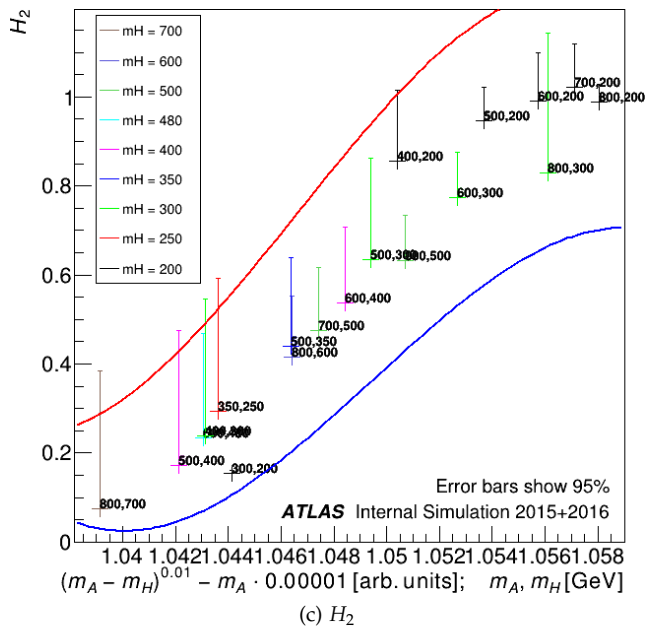
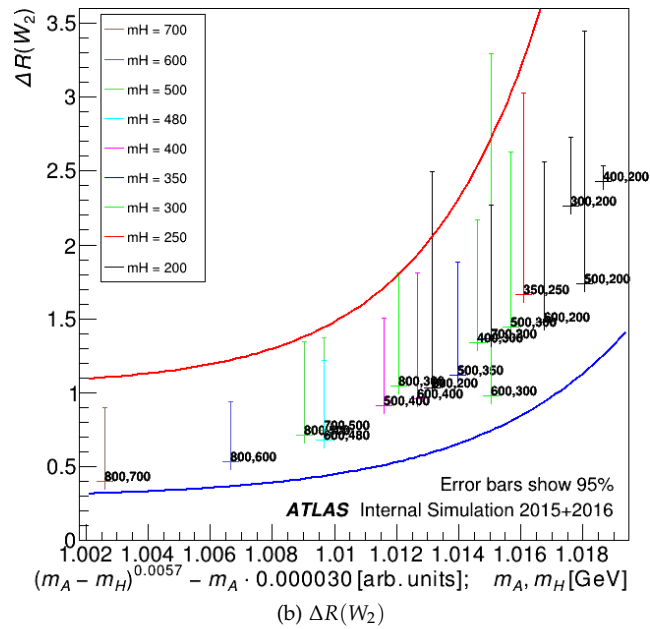
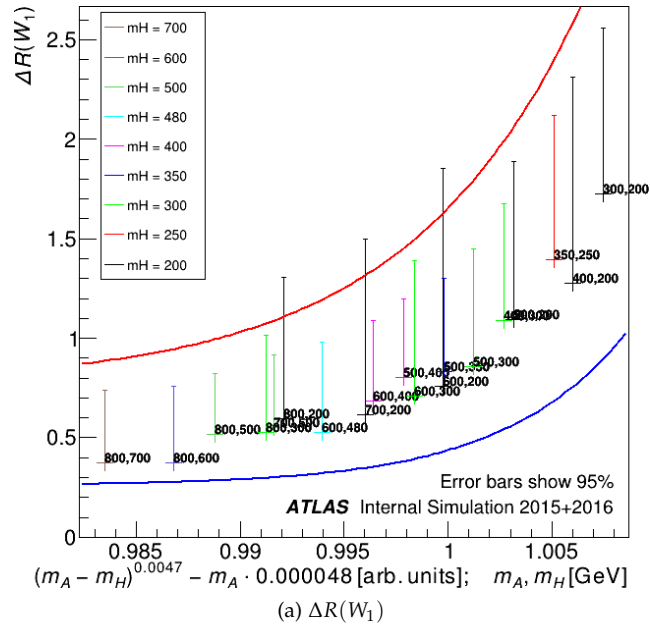
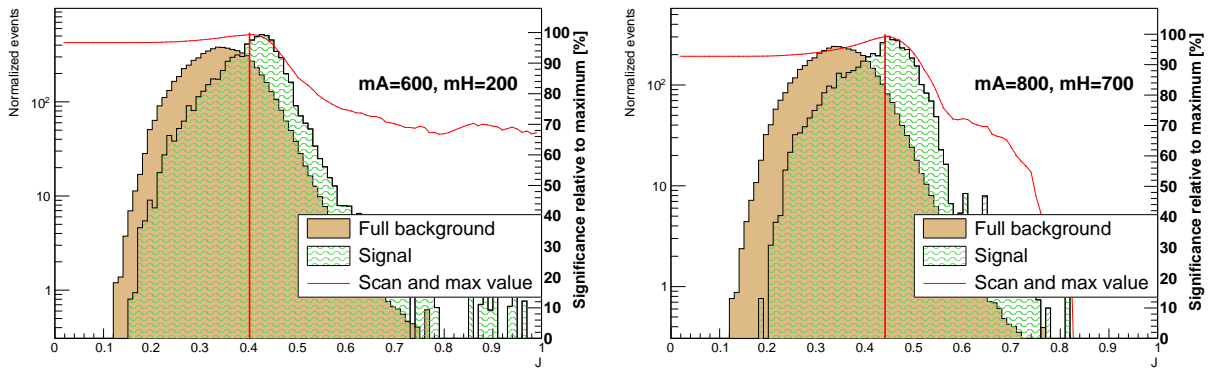


Figure 10.2: The windows for  $H_2$ ,  $\Delta R(W_1)$ , and  $\Delta R(W_2)$ . Each signal sample is represented by a point and parameterized by their simulated masses,  $m_A$  and  $m_H$ . The red and blue lines represent the windows used to select the correct combinations. Note that the error bars show two sigmas. See the text for details.

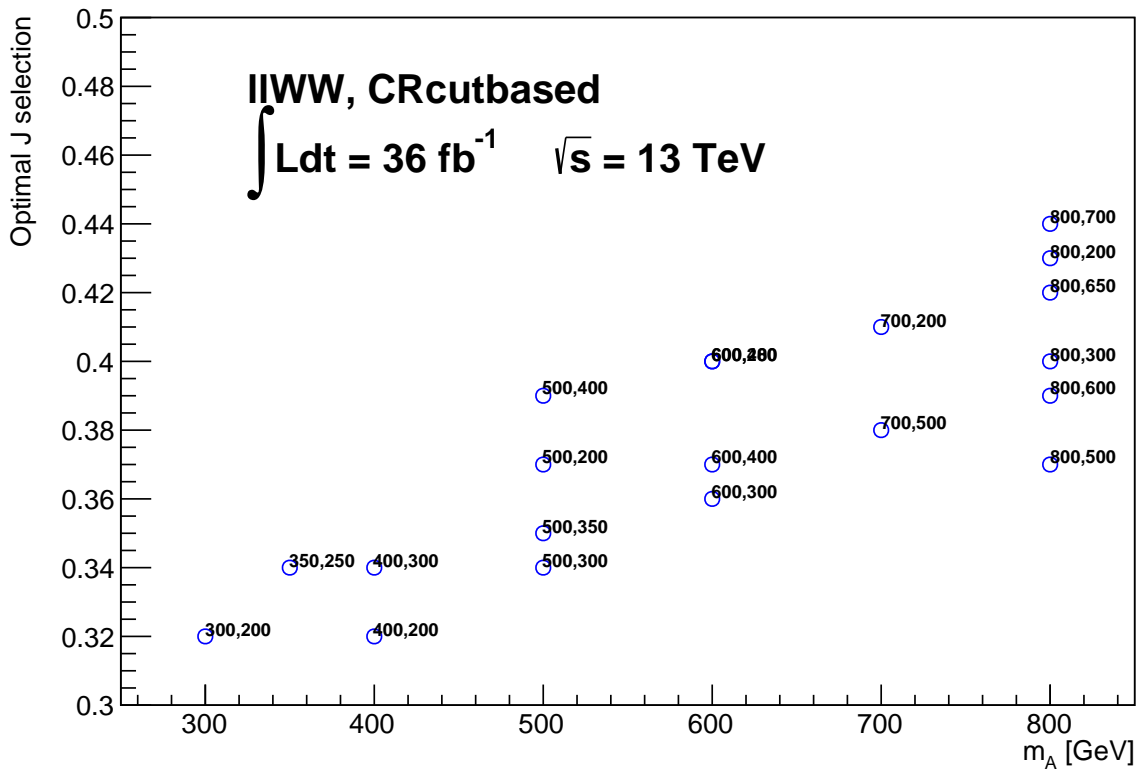
Sample	Values						Individual efficiency [%]					Accumulated eff. [%]				
	Initial	Preselection	$\Delta R(W_1)$	$\Delta R(W_2)$	$H_2$	$m_{W_1}, m_{W_2}$	Preselection	$\Delta R(W_1)$	$\Delta R(W_2)$	$H_2$	$m_{W_1}, m_{W_2}$	Preselection	$\Delta R(W_1)$	$\Delta R(W_2)$	$H_2$	$m_{W_1}, m_{W_2}$
(300,200)	21k	21k	18k	16k	15k	14k	100	87	89	90	97	100	87	78	70	68
(350,250)	25k	25k	22k	19k	17k	17k	100	88	87	89	97	100	88	77	69	66
(400,200)	30k	30k	27k	23k	22k	22k	100	89	85	97	97	100	89	76	74	71
(400,300)	28k	28k	25k	21k	18k	18k	100	88	83	89	97	100	88	73	65	63
(500,200)	35k	35k	31k	25k	25k	24k	100	89	82	98	97	100	89	73	71	69
(500,300)	38k	38k	33k	28k	27k	25k	100	88	83	96	95	100	88	73	70	66
(500,350)	37k	37k	32k	26k	24k	23k	100	88	80	92	97	100	88	71	65	63
(500,400)	32k	32k	28k	21k	19k	18k	100	88	77	88	98	100	88	68	60	58
(600,200)	39k	39k	35k	27k	27k	26k	100	90	78	98	96	100	90	70	69	66
(600,300)	42k	42k	37k	29k	28k	26k	100	88	78	96	95	100	88	69	66	63
(600,400)	41k	41k	36k	28k	26k	25k	100	88	77	94	97	100	88	68	64	62
(600,480)	36k	36k	32k	24k	22k	21k	100	88	76	90	98	100	88	67	60	59
(700,200)	41k	41k	37k	26k	25k	24k	100	89	70	98	96	100	89	63	61	59
(700,300)	46k	46k	40k	29k	28k	27k	100	88	71	96	96	100	88	63	60	58
(700,400)	45k	45k	40k	29k	27k	26k	100	87	73	94	97	100	87	64	60	58
(700,500)	42k	42k	37k	28k	26k	25k	100	88	74	93	97	100	88	66	61	60
(700,600)	34k	34k	30k	23k	19k	19k	100	88	76	84	98	100	88	66	56	54
(800,200)	42k	42k	38k	24k	23k	22k	100	89	63	98	94	100	89	56	54	51
(800,300)	47k	47k	40k	25k	25k	24k	100	85	64	97	96	100	85	54	53	51
(800,400)	47k	47k	41k	27k	26k	25k	100	86	67	93	97	100	86	58	54	52
(800,500)	47k	47k	40k	29k	26k	26k	100	86	72	92	97	100	86	62	56	55
(800,600)	43k	43k	37k	27k	25k	25k	100	86	73	93	97	100	86	63	59	57
(800,650)	40k	40k	35k	26k	23k	23k	100	86	74	90	97	100	86	64	58	56
(800,700)	35k	35k	30k	22k	18k	17k	100	86	73	81	97	100	86	62	51	49
All backgrounds	578k	578k	407k	273k	234k	219k	100	70	67	85	94	100	70	47	40	38
Z	1310k	1310k	944k	650k	559k	523k	100	72	69	86	94	100	72	50	43	40
Top	93k	93k	67k	47k	40k	37k	100	72	70	85	93	100	72	51	43	40
Diboson	19k	19k	15k	10k	9k	9k	100	75	72	89	95	100	75	54	48	45
Data	1197k	1197k	862k	592k	510k	477k	100	72	69	86	94	100	72	49	43	40

Table 10.3: The raw counts after the selections involved in resolving jet combinatorics for all signal samples, backgrounds by group, and data. The efficiencies show the ratio of events with at least one combination passing the respective selections (and not the efficiency to choose the right combination since this cannot be known). The individual efficiency is calculated for the given selection after passing the previous selections (and as such shows higher efficiencies for correlated selections). For data, the efficiency columns show the fraction of events surviving the selections.





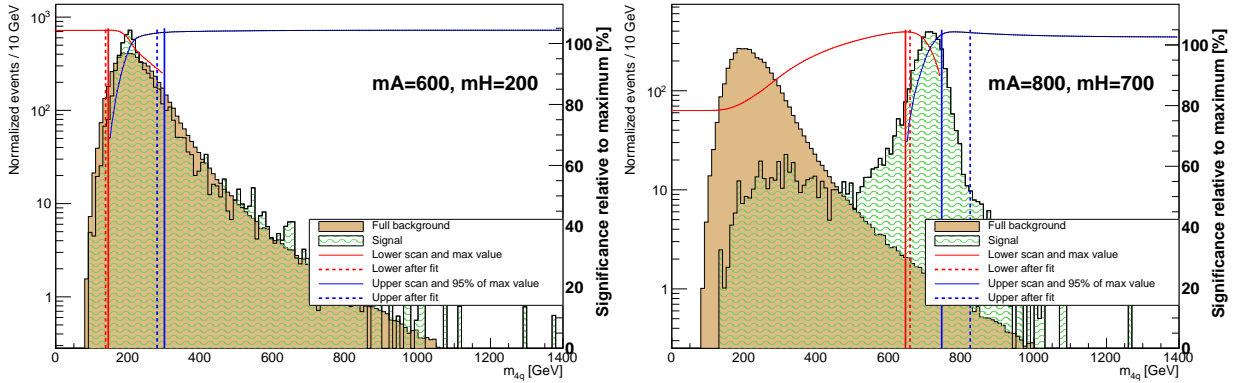
(a) Significance scan for  $J$  for two simulated signals. Left: (600,200). Right: (800,700).



(b) Optimal selection on  $J$  for all simulated signals.

Figure 10.4: (a) Two examples of a scan over the  $J$  variable to find the optimal threshold with (600,200) on the left and (800,700) on the right. The red curve represents the relative significance of the selections. The optimal selection is highlighted by the red, vertical line. Signal is normalized to the integral of the background. (b) The result of optimizing  $J$  for all simulated signals. Each point, annotated by the simulated signal, represents the optimal selection for the given simulated signal. A definite upwards trend in  $m_A$  can be seen, but no further correlation is obvious.

## 10.4 $m_{4q}$ window optimization



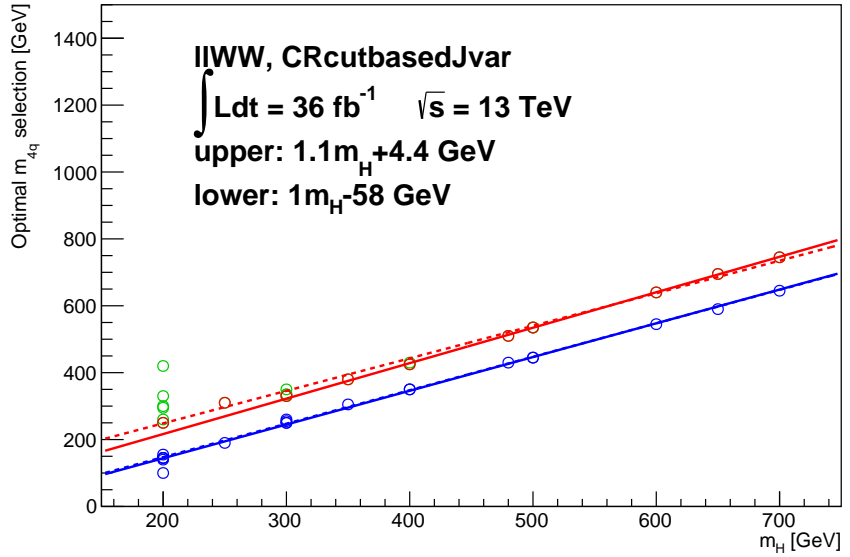
The  $m_{4q}$  windows are made by selecting on  $m_{4q}$  and examining the signal significances in the  $m_{4q}$ . A better approach is to select on  $m_{4q}$  and examine the significance in  $m_{2l4q}$ . This has also been done and the results are shown at the end. The windows in use were found early on before many of these considerations were taken; since the windows are very similar, the original windows are used.

For each simulated signal, the lower threshold is found by calculating the significance of a selection on  $m_{4q}$  from  $x$  to infinity with  $x$  increasing. The selection with the highest significance decides the lower threshold  $x$ . Logically, the upper threshold would then be found by selecting from the found  $x$  to  $y$  with  $y$  decreasing from infinity. However, because of the wide tails, the most significant selection is often at maximum  $y$ . Instead of using the point of maximum significance, the upper threshold is found by decreasing  $y$  until the significance reaches 95% of the maximum significance. This works well as a proxy for the correct upper threshold, had there been no excessive tail, but mostly for simulated signals with low mass-splitting.

The lower and upper thresholds are plotted as a function of  $m_{4q}$  and fitted with first order polynomials, excluding points with mass-splitting greater than 150 GeV. Two examples are shown in Fig. 10.5, and the results are shown in Fig. 10.6.

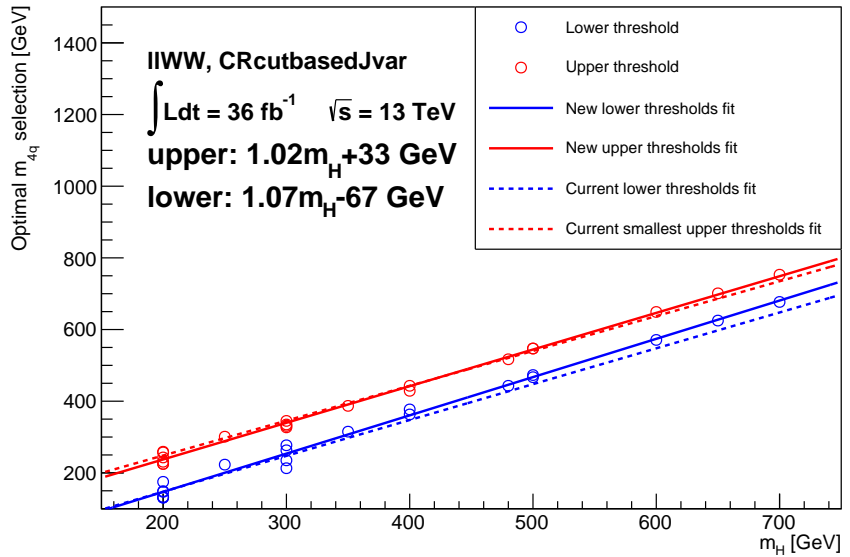
Figure 10.5: Two examples of a scan over the  $m_{4q}$  variable to find the optimal selection with (600, 200) on the left and (800, 700) on the right. The red and blue curves represent the relative significances of the selections for the lower and upper scans, respectively. The optimal selections are highlighted by the red or blue vertical lines. The pre-fit optimal points are drawn in solid lines while the post-fit points are shown with dashed lines. Signal is normalized to the integral of the background.

Figure 10.6: The obtained lower (blue circles) and upper (red and green circles) thresholds for the  $m_{4q}$  window. Samples with mass-splitting greater than 150 GeV (green circles) are not used in the fit. The window currently in use is shown in dashed line for reference.



### 10.4.1 Window optimization in 2D

Figure 10.7: The obtained lower (blue circles) and upper (red circles) thresholds for the 2D  $m_{4q}$  window optimization. Unlike in the previous optimization, all points are used in the fit to the upper threshold. The window currently in use is shown in dashed lines for reference.



To properly account for the correlations between  $m_{4q}$  and  $m_{2\ell 4q}$  and to also test directly on the  $m_{2\ell 4q}$  shape, the window optimization has been repeated in 2D.  $m_{4q}$  is finely binned along its axis to precisely find the optimal selection points, while  $m_{2\ell 4q}$  is roughly binned (24 GeV per bin) along its axis and only evaluated on the 3 middle bins when calculating the significances<sup>1</sup>. The mass-dependent width of the signal is not taken into account, meaning the bin width is the same for all signals.

The procedure is as follows. Like in the 1D case, for every simulated signal, a selection is applied on  $m_{4q}$  from  $x$  (increasing  $x$ ) to infinity. After each selection, the 2D histogram is projected onto the  $m_{2\ell 4q}$  axis, and the integral of the tallest bin and its two single

<sup>1</sup> This works as a proxy for the likelihood fit that will be introduced in Chap. 14 to set the upper limits on the production cross-section.

neighbors to either side is used for the signal yield. Likewise, the background yield is calculated for the same bins. From these yields, the significance is calculated.

For the upper selection scan,  $m_{4q}$  is scanned from  $x$  to  $y$ , with  $y$  starting at  $x$  and moving to infinity. This is opposed to the previous procedure where the point that gave 95% of the maximum significance when scanning from  $x$  to  $y$  ( $y$  decreasing) was used.

The results are shown in Fig. 10.7. Three things are important to note:

1. The 2D fit takes properly care of the tails for simulated signals with large  $\Delta M$  meaning no more large upper thresholds, and so all upper thresholds are used for the upper threshold fit.
2. The new thresholds are close to the previously found thresholds that are in use, validating the previous method.
3. The lower thresholds for some simulated signals with  $m_{4q} = 200$  GeV are very low; this is due to the significance curve being very flat at the beginning; this is not an issue since the fit for the lower threshold converges on the same value at low  $m_{4q}$ .

## 10.5 Final selection and summary

The event has been selected, the background has been reduced, and the  $m_{4q}$  window has been defined. The selections are summarized in Tab. 10.4. The number of events before and after the  $J$  variable selection is shown in Tab. 10.5 for the backgrounds and all signals. The  $m_{4q}$  window for compatibility with the  $H$  boson mass is found to be,

$$m_H - 53\text{GeV} < m_{4q} < 0.97 \times m_H + 54 \text{ GeV}.$$

Since the analysis does not consider  $m_A < 300$  GeV, an explicit requirement of  $m_{2\ell 4q} > 250$  GeV is applied. The range between the two numbers allows for wide signals and for some background in the side-band control region. The analysis is not optimized for masses below 250 GeV, and the modeling at this scale may require more aggressive corrections.

Scale factors derived from the ratio of simulated backgrounds to real data are separately calculated for the SR and TCR after Levels 1 and 2. The scale factors are derived for the total background in each region. The scale factors are only used for demonstration in the pre-fit plots, as the actual  $Z$ +jets normalizations are taken from the side-bands and  $t\bar{t}$  normalizations from the TCR in data during the fitting procedure.

Table 10.4: Summary of the event selection and region definitions. Leptons are defined as  $\ell = e, \mu$ .

	<ul style="list-style-type: none"> <li>• Single-electron or single-muon trigger</li> <li>• Exactly 2 leptons with <math>p_T &gt; 30, 15</math> GeV, respectively</li> <li>• <math>80 \text{ GeV} &lt; m_{\ell\ell, e\mu} &lt; 100 \text{ GeV}</math></li> <li>• Opposite electric charge for <math>\mu\mu</math> pairs</li> <li>• At least 4 jets with <math>p_T &gt; 40, 30, 20, 20</math> GeV for the 4 leading</li> <li>• Resolve jets (using <math>H_2</math> and <math>\Delta R</math> of the dijets)</li> <li>• <math>J &gt; 0.3</math></li> <li>• <math>m_{2\ell 4q} &gt; 250 \text{ GeV}</math></li> </ul>
Signal regions	$ee$ or $\mu\mu$ pair Within $m_{4q}$ window
Z+jets control regions	$ee$ or $\mu\mu$ pair Outside $m_{4q}$ window
Top control regions	$e\mu$ pair Within $m_{4q}$ window
$m_{4q}$ window	$m_H - 53 \text{ GeV} < m_{4q} < 0.97 \cdot m_H + 54 \text{ GeV}$

Sample	Signal region			Top control region	
	Level 1 (Before $J$ sel.)	Level 2 (After $J$ sel.)	Ratio	Level 1 (Before $J$ sel.)	Level 2 (After $J$ sel.)
All backgrounds	481979	343983	0.714	17722	14459
Z	447255	315083	0.704	131	87
Top	20870	17565	0.842	17394	14229
Diboson	13854	11334	0.818	197	143
Data	499110	348832	0.699	18962	15434
Scale factor	$1.036 \pm 0.002$	$1.014 \pm 0.002$		$1.070 \pm 0.004$	$1.067 \pm 0.004$
Signal	Level 1	Level 2	Ratio	Level 1	Level 2
(300,200)	13578	12380	0.91	< 1	< 1
(350,250)	16486	15284	0.92	< 1	< 1
(400,200)	21615	19750	0.91	< 1	< 1
(400,300)	17581	16554	0.94	< 1	< 1
(500,200)	24896	22721	0.91	< 1	< 1
(500,300)	26042	24442	0.93	< 1	< 1
(500,350)	24321	22810	0.93	< 1	< 1
(500,400)	18366	17327	0.94	< 1	< 1
(600,200)	25195	23004	0.91	< 1	< 1
(600,300)	26441	24826	0.93	< 1	< 1
(600,400)	25879	24548	0.94	< 1	< 1
(600,480)	22581	21285	0.94	< 1	< 1
(700,200)	24458	22220	0.90	< 1	< 1
(700,500)	25768	24444	0.94	< 1	< 1
(800,200)	22780	20714	0.90	< 1	< 1
(800,300)	23598	21979	0.93	< 1	< 1
(800,500)	25052	23922	0.95	< 1	< 1
(800,600)	24397	22985	0.94	< 1	< 1
(800,650)	22246	20864	0.93	< 1	< 1
(800,700)	16885	15795	0.93	< 1	< 1

Table 10.5: The number of data and background events as well as number of individual signal events after Levels 1 and 2, for both the signal region and the top control region, along with the scale factors between background and data. Only uncertainty due to the finite number of generated events in the simulated signals is shown.

### 10.5.1 Cut-flow tables

As described in Chap. 8, Level 3 is reached after applying all the selections in the previous sections and finally entering an  $m_{4q}$  window. The *relative* acceptance times efficiency for all selections, using raw event counts, is listed for all simulated signals in Tab. 10.6 and shown in Fig. 10.8 for three  $m_H$  slices. The raw event counts are used instead of the weighted yield since weights are not applied at the preselection stage. The absolute numbers for some signals are shown in Tab. 10.7.

$m_A, m_H$	Preselection			Initial event selection					SR	Level 1	Level 2	Level 3
	jet cleaning	lepton	jet	Trigger	LepPtCut	ZMass	MuOppSign	4Jet	LepSameFlavor	Resolve jets	J selection	$m_{4q}$ window
300, 200	0.995	0.426	0.408	0.357	0.332	0.287	0.287	0.146	0.146	0.096	0.088	0.063
350, 250	0.995	0.426	0.416	0.362	0.339	0.291	0.291	0.179	0.179	0.117	0.108	0.075
400, 200	0.995	0.500	0.486	0.455	0.435	0.392	0.392	0.235	0.235	0.168	0.154	0.109
400, 300	0.996	0.428	0.422	0.367	0.343	0.294	0.294	0.205	0.205	0.127	0.119	0.077
500, 200	0.995	0.530	0.520	0.495	0.479	0.426	0.426	0.276	0.276	0.191	0.175	0.119
500, 300	0.995	0.508	0.503	0.473	0.452	0.405	0.405	0.303	0.303	0.203	0.191	0.122
500, 400	0.996	0.429	0.425	0.371	0.345	0.296	0.296	0.229	0.229	0.131	0.124	0.077
600, 200	0.995	0.545	0.538	0.516	0.503	0.445	0.445	0.301	0.301	0.197	0.180	0.121
600, 400	0.995	0.507	0.505	0.474	0.455	0.408	0.408	0.329	0.329	0.206	0.196	0.115
600, 480	0.996	0.455	0.452	0.405	0.380	0.344	0.344	0.287	0.287	0.173	0.163	0.104
700, 200	0.996	0.558	0.554	0.534	0.523	0.462	0.462	0.328	0.328	0.193	0.176	0.119
700, 300	0.995	0.552	0.550	0.350	0.342	0.302	0.302	0.235	0.235	0.134	0.125	0.079
700, 500	0.996	0.511	0.509	0.478	0.459	0.411	0.411	0.344	0.344	0.208	0.198	0.116
800, 200	0.995	0.569	0.565	0.547	0.537	0.471	0.471	0.346	0.346	0.181	0.165	0.112
800, 300	0.995	0.564	0.562	0.542	0.532	0.469	0.469	0.371	0.371	0.188	0.175	0.112
800, 500	0.995	0.539	0.538	0.514	0.500	0.445	0.445	0.370	0.370	0.201	0.192	0.108
800, 650	0.995	0.480	0.478	0.440	0.418	0.376	0.376	0.321	0.321	0.181	0.170	0.099
800, 700	0.995	0.440	0.438	0.383	0.357	0.306	0.306	0.261	0.261	0.128	0.120	0.072

Table 10.6: The relative acceptance times efficiency of 120k events for all simulated signals. GRL, primary vertex check, and clean event check (not shown) always pass in simulation. Raw event counts from the simulated signals are used. LepSameFlavor is the same-flavor selection.

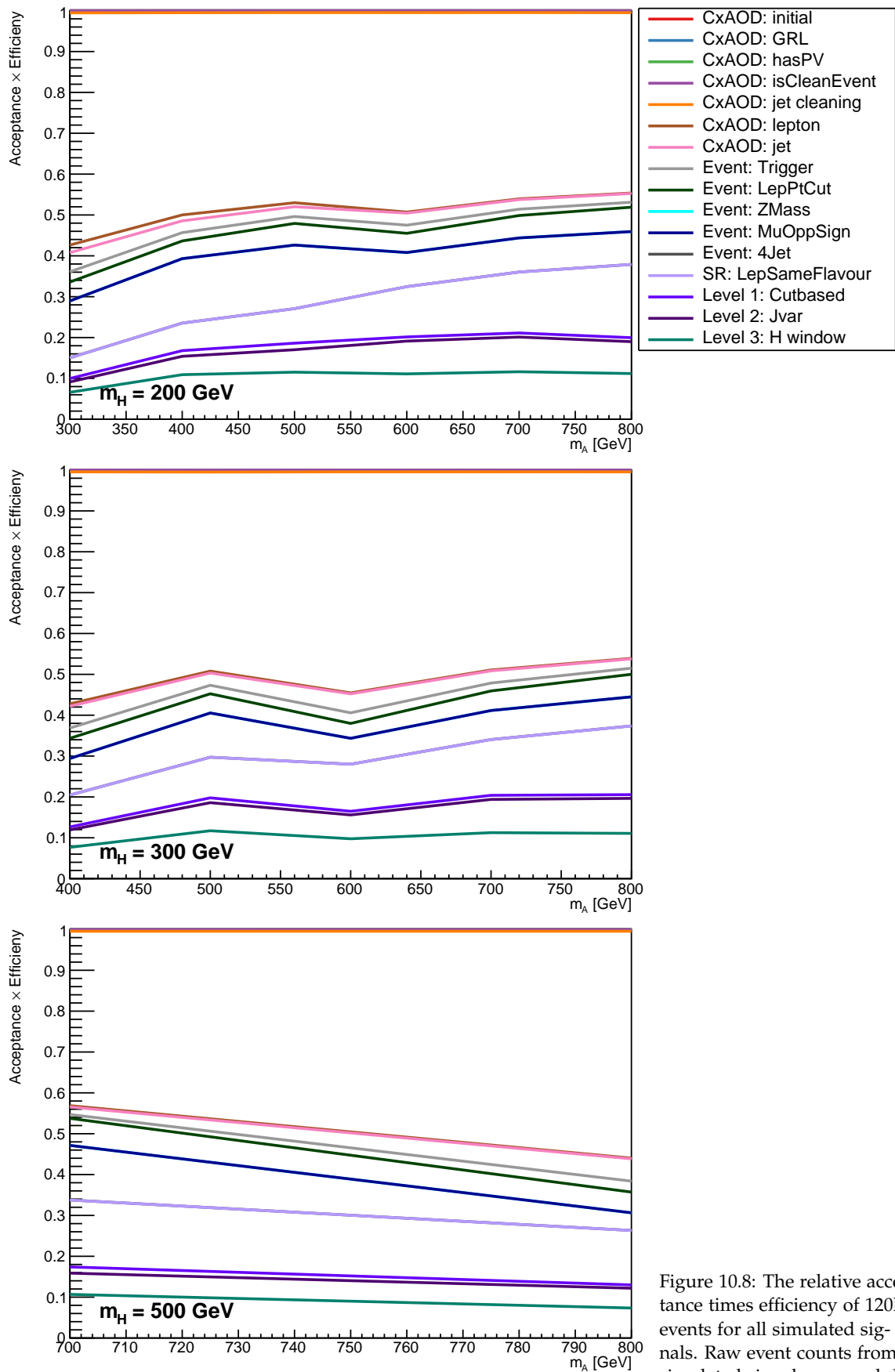


Figure 10.8: The relative acceptance times efficiency of 120k events for all simulated signals. Raw event counts from the simulated signals are used. Lep-SameFlavour is the same-flavor selection.

Cut	300,200	500,300	700,200	800,700
CxAOD: initial	120000	120000	120000	120000
CxAOD: GRL	120000	120000	120000	120000
CxAOD: hasPV	120000	120000	120000	120000
CxAOD: isCleanEvent	120000	120000	120000	120000
CxAOD: jet cleaning (LooseBad)	119356	119408	119403	119462
CxAOD: Exactly two loose leptons	51170	51137	60015	51341
CxAOD: At least one signal jet	48933	49892	58269	50622
Event: Trigger	42823	43474	54548	44073
Event: Lepton $p_T > 30, 15$ GeV	39891	40652	52159	41126
Event: $80 < m_{\ell\ell} < 100$ GeV	34406	34926	46991	35224
Event: Muons opposite charge	34406	34925	46990	35224
Event: 4+ jets, $p_T > 40, 30, 20, 20$ GeV, $ \eta  < 2.4$	17523	21518	28249	24556
SR: Same-flavor leptons ( $ee$ or $\mu\mu$ )	17522	21516	28246	24551
Level 1: Resolve jets	11516	13996	20152	15200
Level 2: $J > 0.3$	10527	13006	18488	14326
Level 3: $m_H - 53\text{GeV} < m_{4q} < 0.97 \times m_H + 54$ GeV	7562	9001	13098	9188

Table 10.7: The absolute number of events for some simulated signals leading into the SR. Raw event counts from the simulated signals are used.

# 11 Background modeling

Now that the event selection is finalized, we will want to consider the pre-fit figures. In this chapter, we will examine the accuracy of the simulated background processes and correct the mismodeling in the transverse momentum of the reconstructed  $Z$  boson as well as the transverse momentum of the leading jet.

## Contents

---

<b>11.1 Mismodeling</b> . . . . .	<b>112</b>
<b>11.2 <math>t\bar{t}</math> modeling</b> . . . . .	<b>115</b>

---

Figures of various variables will be shown at Levels 1 through 3 for the SR. The variables are either used in the likelihood fit later (ie. the reconstructed  $A$  and  $H$  masses), used to correct mismodeling, or part of the background reduction. The  $p_T$  of the  $\ell\ell$  system is shown to verify the modeling after the corrections applied later in Sect. 11.1. The modeling of  $J$  is shown as well, since this variable was used for background reduction. During the work on reducing the mismodeling, the masses of the  $W$  candidates as well as the  $p_T$  of the  $H$  candidate were examined but showed no modeling issues. The variable list is:

- $m_{2\ell 4q}$  mass of the  $A$  candidate before and after mass scaling
- $m_{4q}$  mass of the  $H$  candidate
- $p_T^{\ell\ell}$   $p_T$  of the  $Z$  candidate
- $J$  background-reducing variable
- $m_{W_1}, m_{W_2}$  masses of the  $W$  candidates
- $p_T^{4q}$   $p_T$  of the  $H$  candidate

For Levels 1 and 2, only the unscaled  $m_{2\ell 4q}$  is shown<sup>2</sup>.  $J$  is shown for Level 1 and replaced by  $p_T^{4q}$  in the Level 2 figure. For level 3, only blinded  $m_{2\ell 4q}$  is shown, unscaled and scaled.

Figs. 11.1–11.5 show logarithmically and linearly scaled histograms of the data and simulated background yield with the background components color-coded. The background components are ordered by yield<sup>3</sup> with the main background  $Z$ +jets shown on top and followed by  $t\bar{t}$ , dibosons, and an insignificant amount of single-top production. The relative differences between data and the sum of backgrounds are shown in the panel below. The systematic uncertainties entering this panel have been symmetrized through random sampling. The shape systematic is normalized to the nominal yield during the random sampling.

<sup>2</sup>Since there is no  $H$  hypothesis yet.

<sup>3</sup>This order is decided from these figures and fixed for all subsequent figures.

<sup>1</sup> Strictly speaking, the test is a measure of certainty for whether two histograms originate from a common distribution.

<sup>2</sup> Read also ROOT's own remarks on the matter at, <https://root.cern.ch/doc/master/classTH1.html#aeadc087afe6ba203bcde124cfabbee4>.

<sup>3</sup> For a back-of-the-envelope calculation, a  $\chi^2$  of 3 with 15 degrees of freedom gives  $p = 99.96\%$  which one would expect 0.04% of the time for data that fits the model.

The figures quote results for reduced  $\chi^2$  two-sample and binned Kolmogorov-Smirnov (KS) tests, which are produced by the plotting code. The reduced  $\chi^2$  is a poor metric for testing histogram compatibility<sup>1</sup>, and the KS test cannot be done reliably on binned data<sup>2</sup> [146]. Regardless, taking the quoted reduced  $\chi^2$  and KS at face-value, the agreement between data and background is poor when only taking statistical uncertainty into account, and the agreement becomes suspiciously good (reduced  $\chi^2 \ll 1$ , KS = 1) when systematics are taken into account. This is either due to overestimated uncertainties (to cover many analyses, ATLAS prefers conservative estimates for its uncertainties, which may then be constrained by the likelihood fit) or a happy coincidence<sup>3</sup>.

Additional figures for the signal leptons and jets are shown in App. 19.B at Levels 1 and 2.

The figures show great agreement between real and simulated data.  $m_{4q}$  in Fig. 11.1 shows a slightly growing disagreement towards lower values but is still within the systematic uncertainty at 10% disagreement.  $J$  in Fig. 11.2 shows actual disagreement at  $J > 0.6$ . This is, however, in a region of very little background and signal as was shown in Fig. 10.3.

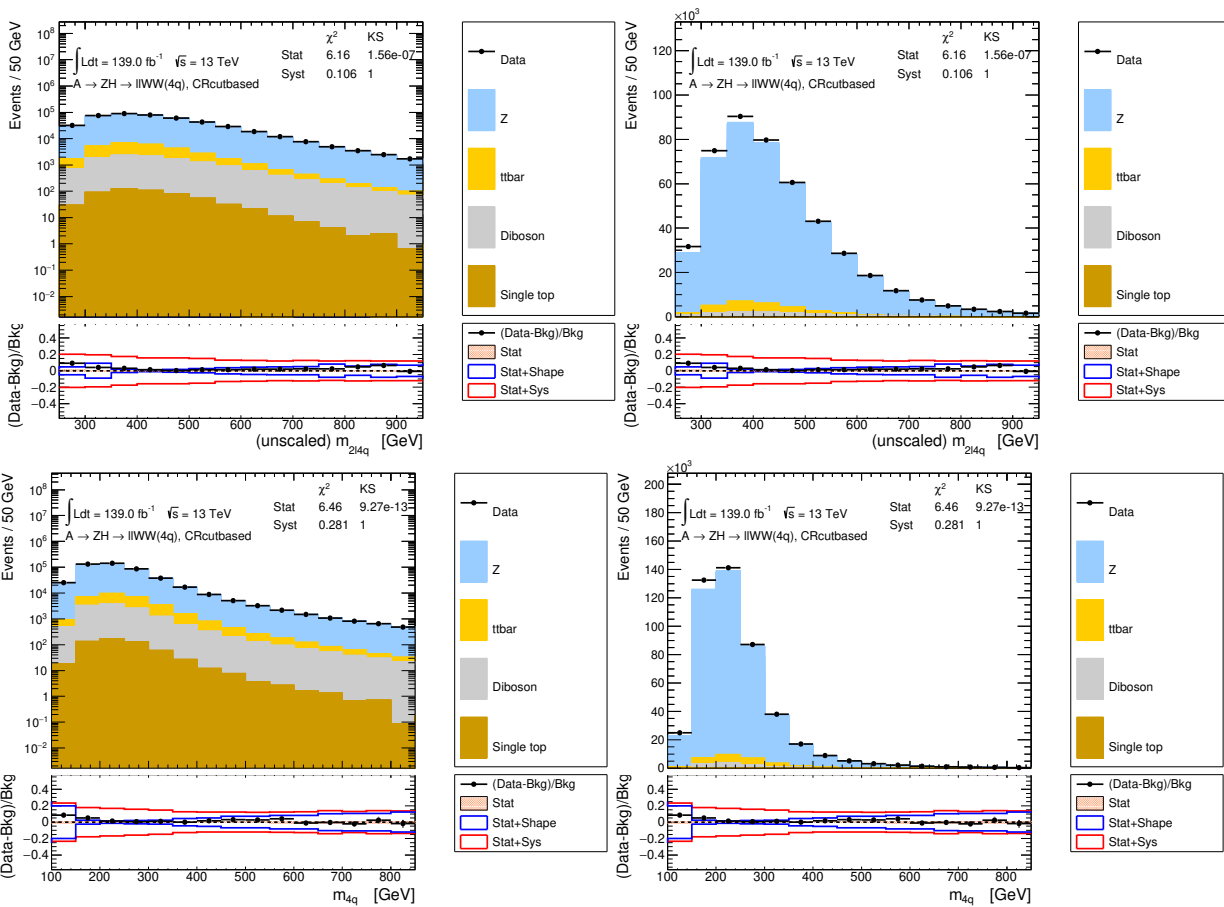


Figure 11.1: The  $m_{2l4q}$  and  $m_{4q}$  mass distributions at Level 1. Logarithmic scale on the left and linear scale on the right.

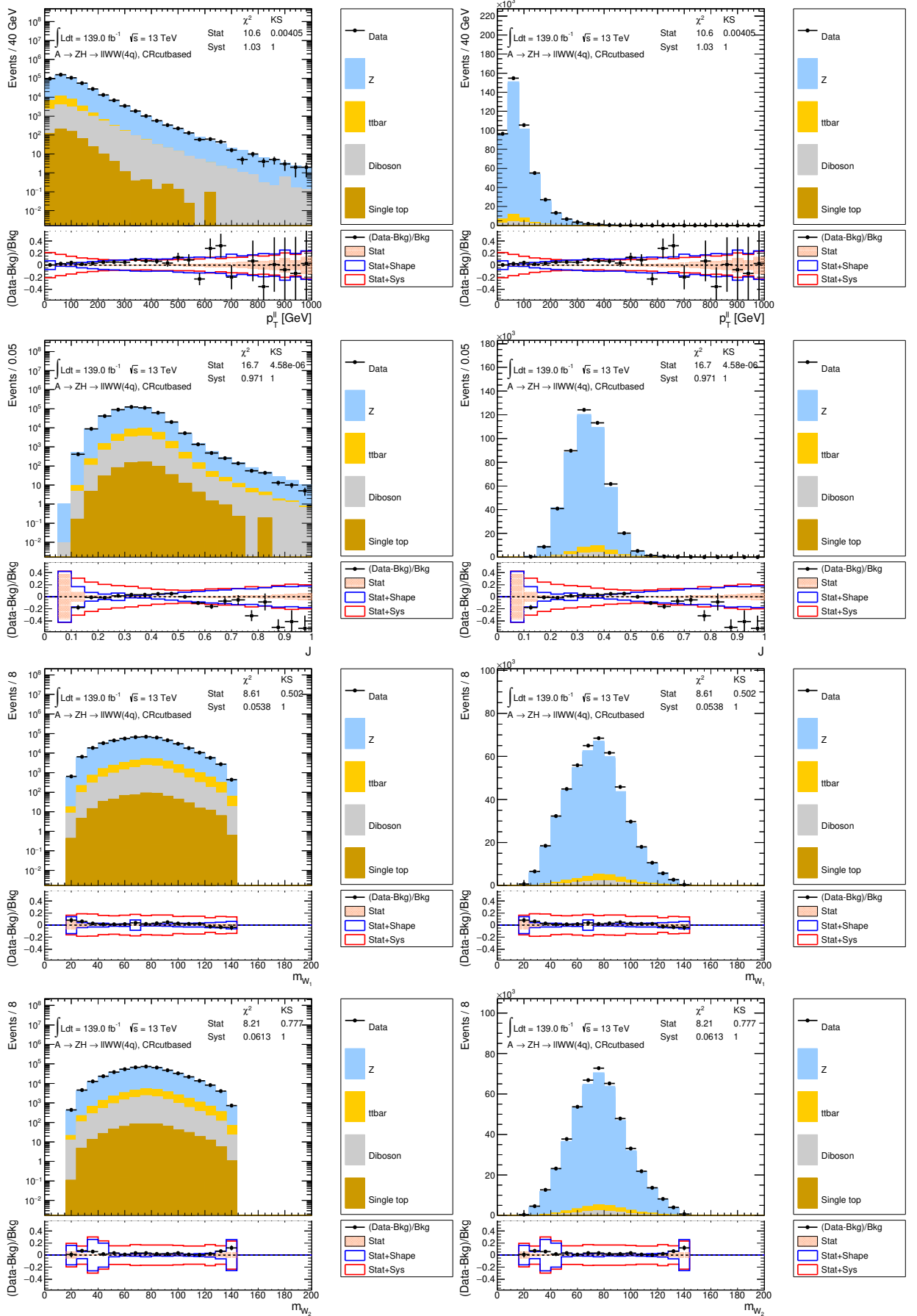


Figure 11.2: The distributions for  $p_T^{\ell\ell}$ ,  $J$  variable, and  $W$  candidate masses at Level 1. Logarithmic scale on the left and linear scale on the right.

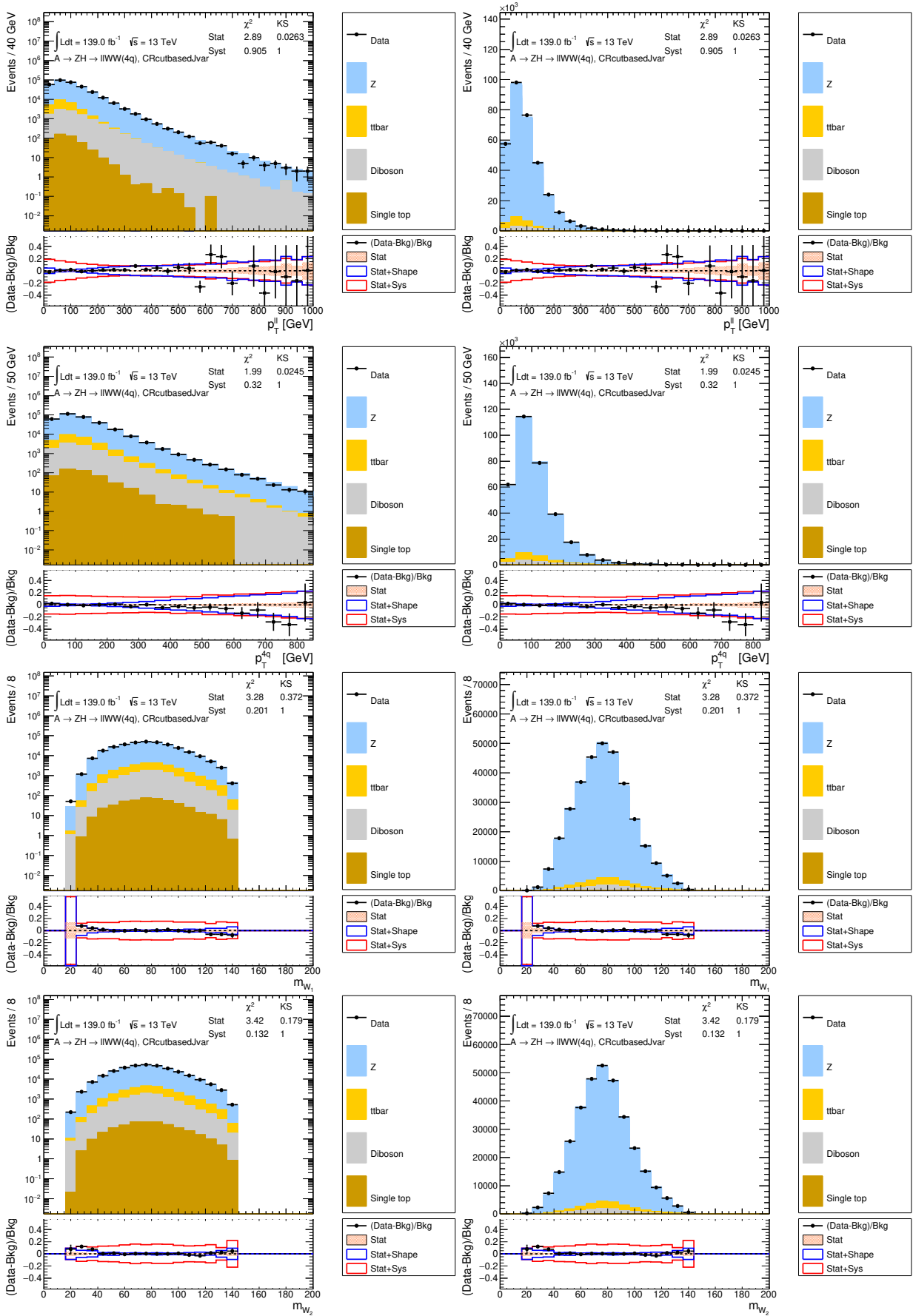


Figure 11.3: The distributions for  $p_T^{\ell\ell}$ ,  $p_T^{4q}$ , and  $W$  candidate masses at Level 2. Logarithmic scale on the left and linear scale on the right.

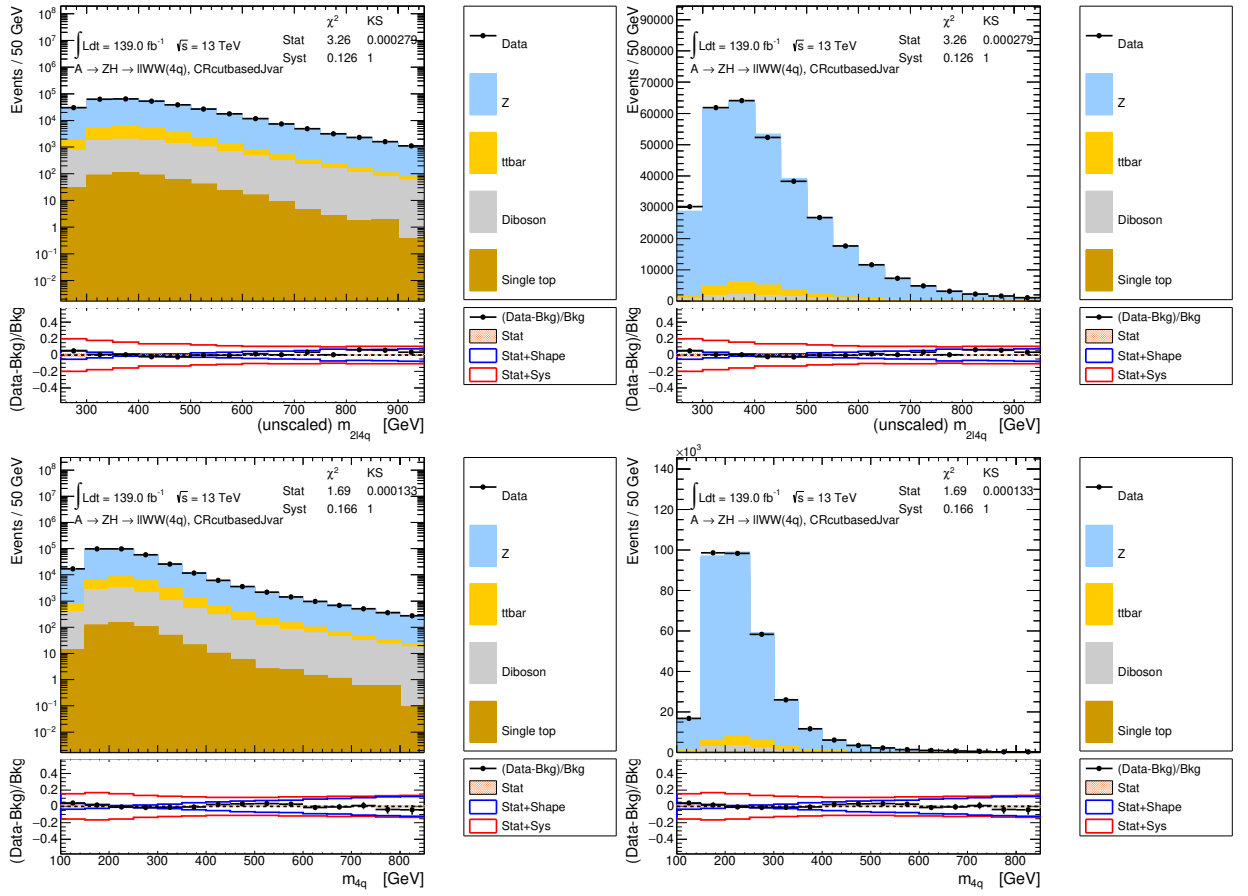
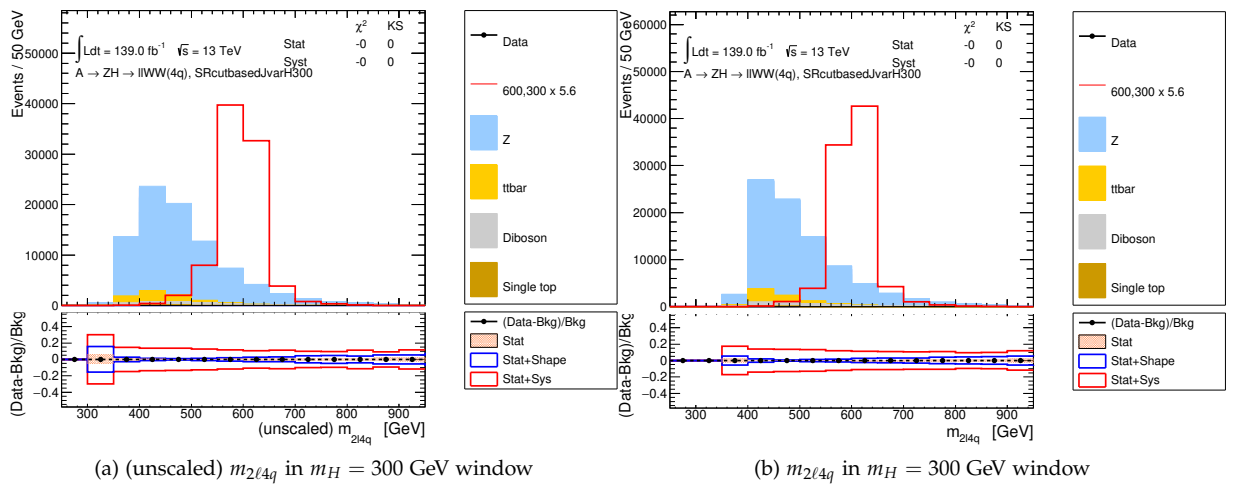


Figure 11.4: The  $m_{2l4q}$  and  $m_{4q}$  mass distributions at Level 2. Logarithmic scale on the left and linear scale on the right.



(a)  $(\text{unscaled}) m_{2l4q}$  in  $m_H = 300$  GeV window

(b)  $m_{2l4q}$  in  $m_H = 300$  GeV window

Figure 11.5: The  $m_{2l4q}$  distribution at Level 3. (b) The masses of the  $\ell\ell$  and  $4q$  systems are scaled to the masses of the Z and the H bosons, respectively. Linear scale plots are shown.

## 11.1 Mismodeling

<sup>1</sup> See Ref. [147] or the following internal presentation on the matter, [https://indico.cern.ch/event/796353/contributions/3309032/attachments/1791020/2917889/2019\\_02\\_05\\_WJetsModelling\\_ColinearVeto.pdf](https://indico.cern.ch/event/796353/contributions/3309032/attachments/1791020/2917889/2019_02_05_WJetsModelling_ColinearVeto.pdf).

The analysis suffers from mismodeling that is known<sup>1</sup> for some region of phase space in Sherpa's  $Z$ +jets samples. Fig. 11.6 shows the uncorrected  $p_T^{\ell\ell}$ ,  $p_T$  of the  $p_T$ -leading jet of the event,  $m_{4q}$ , and  $m_{2\ell 4q}$  with the corrected figures for comparison. The two transverse momenta are corrected by deriving a ratio between real and simulated data in a signal-poor control region and applying these corrections to the signal region. The corrections will be derived using the full set of backgrounds, as similar issues are seen for the  $t\bar{t}$  sample. The effects of the corrections on  $t\bar{t}$  will be covered in the next section. The effects on the diboson background cannot be examined in an isolated region, but given that the diboson samples have been generated using the same setup as for  $Z$ +jets, it is reasonable to assume a similar mismodeling. In any case, the dibosons (and  $t\bar{t}$  for that matter) are small compared to  $Z$ +jets and may not affect the likelihood fit with or without prior corrections.

It is possible to define an orthogonal control region to the SR with an inverted  $J$  selection, that is to say  $J < 0.3$ . The correction was derived using 2015+2016 data only. However, using data from all years shows little difference.

The correction procedure is as follows. The event is required to pass all event-level selections (like Level 1) after which the  $J < 0.3$  selection is applied. In this AntiJvar CR,  $p_T^{\ell\ell}$  is plotted with 50 bins from 0 to 500 GeV, which is rebinned such that each bin has at least 2000 events in data<sup>2</sup>. The ratio of real to simulated data is taken and the ratio is applied bin-by-bin as weight to the simulation. Afterwards, the  $p_T$  of the  $p_T$ -leading jet of the event is plotted from 40 to 1000 GeV with 960 bins<sup>3</sup> (1 GeV wide bins), and rebin in the same manner as before. The small bin width is due to the more complex shape at low values as opposed to  $p_T^{\ell\ell}$  that shows a monotonically increasing disagreement. The ratio is then like-wise multiplied bin-by-bin to the simulation weight.

The result of applying the corrections to the AntiJvar CR can be seen in Fig. 11.7a. The ratios are fitted with envelopes, and half of the fit values are applied as systematics for the mismodeling. The corrections and the fits can be seen in Fig. 11.7b, which also shows ratio for  $p_T^{\ell\ell}$  using data from all years. The fit expressions and their fitted parameters are listed in Tab. 11.1.

After applying the corrections derived in the AntiJvar CR, the mismodeling is greatly reduced in the corrected variables in the SR. For other variables, the disagreement in especially  $m_{2\ell 4q}$  in Fig. 11.6 is noticeably reduced to well within the systematic band.

<sup>2</sup> The number, 2000, is a compromise between having too few and too many bins but the exact value is arbitrarily chosen.

<sup>3</sup> Remember, the event selection requires the leading jet to have  $p_T > 40$  GeV.

Table 11.1: The fitted parameters for the ratio of real to simulated data for  $p_T^{\ell\ell}$  and  $p_T^{\text{lead jet, evt.}}$ .

Variable	Expression
$p_T^{\ell\ell}$	$\begin{cases} 0.065, & \text{if } p_T^{\ell\ell} < 90 \text{ GeV} \\ 0.0941176 - 0.0003235294 p_T^{\ell\ell}, & \text{otherwise} \end{cases}$
$p_T^{\text{lead jet, evt.}}$	$\exp(-1.6 - 1.5 \cdot 10^{-5} p_T^{\text{lead jet, evt.}}) + 0.024$

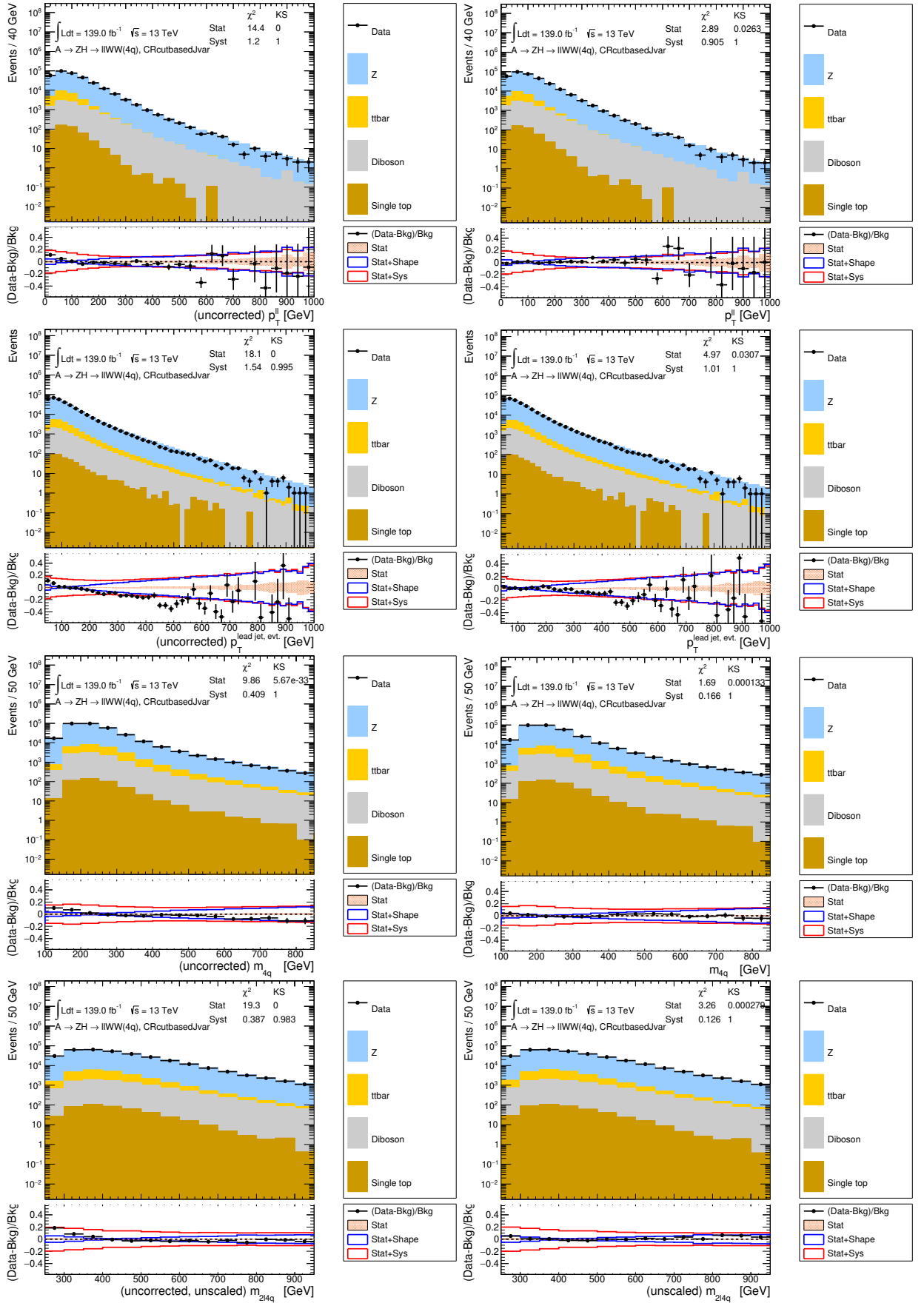


Figure 11.6: Uncorrected  $p_T^{\ell\ell}$ ,  $p_T$  of the leading jet of the event,  $m_{4q}$ , and  $m_{2l4q}$  at Level 2 on the left. On the right, the corrected figures are shown for comparison. Logarithmic scales are shown.

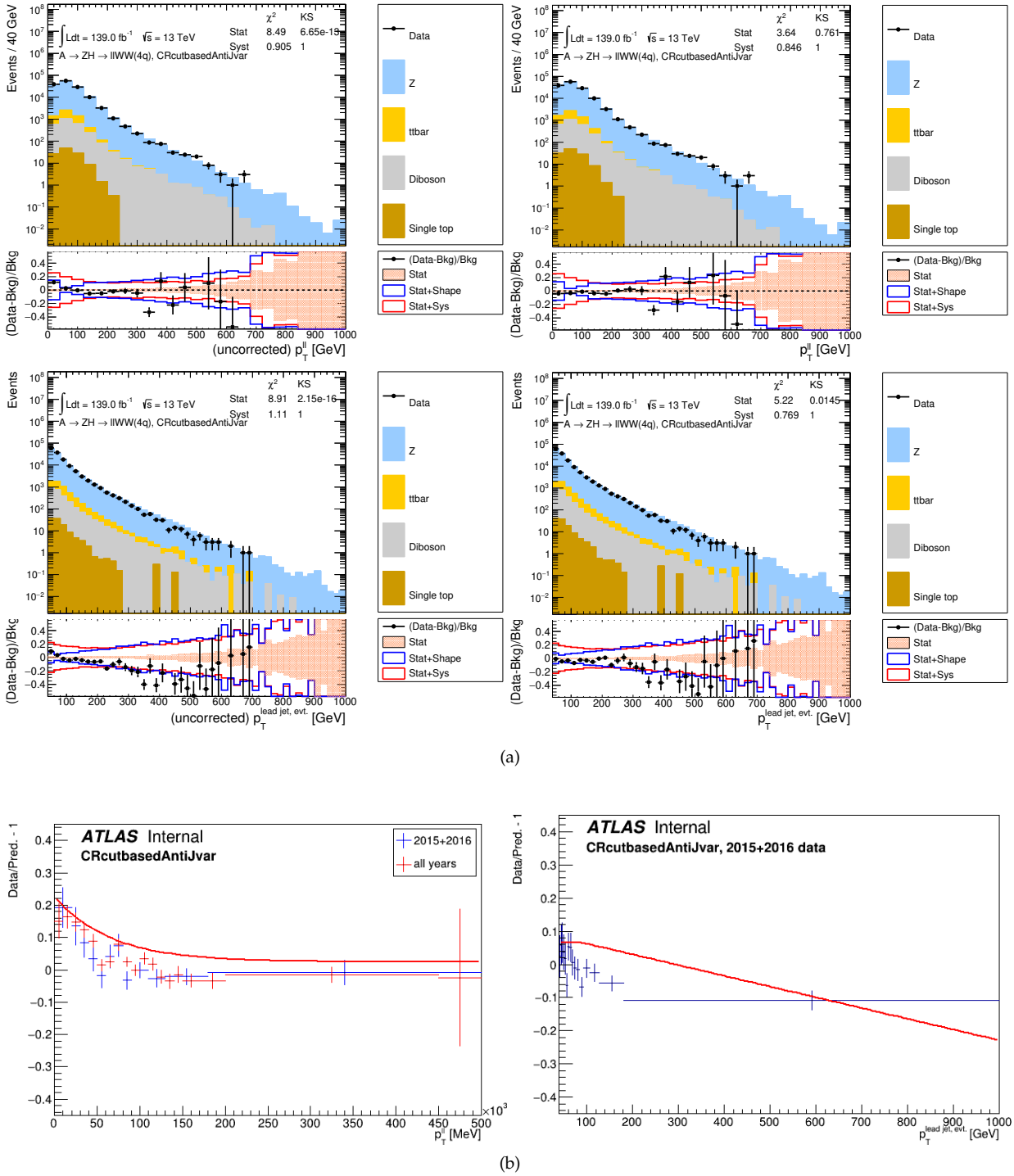


Figure 11.7: (a) The  $p_T^{\ell\ell}$  (top) and  $p_T$  of the  $p_T$ -leading jet of the event (bottom) in the AntiJvar CR before (left) and after (right) applying the corrections detailed in the text. Note, no scale factor has been derived for this region and hence the ratio is not centered about 0, and the ratio is not perfectly flat due to different binning. (b) The ratio of real to simulated data for  $p_T^{\ell\ell}$  and the  $p_T$  of the  $p_T$ -leading jet in the AntiJvar CR. The ratios are fitted with functions that envelope the points.

## 11.2 $t\bar{t}$ modeling

It is possible to define a region pure in  $t\bar{t}$ , in which the modeling of the  $t\bar{t}$  process can be examined. This region will also be used to correct the  $t\bar{t}$  normalization in the likelihood fit. Neither can be done for the dibosonic backgrounds. The TCR is defined in the same way as the signal region, with the difference that an  $e\mu$  pair is required instead of a same-flavor  $\ell\ell$  pair.

$J$  at Level 1 is plotted in Fig. 11.8.  $m_{e\mu 4q}$ ,  $m_{4q}$ ,  $p_T^{e\mu}$  at Level 2 are plotted in Figs. 11.9a–11.9c. The unscaled and scaled  $m_{e\mu 4q}$  at Level 3 are plotted in Figs. 11.9d and 11.9e. All figures contain the corrections derived in the previous section. All figures except for Fig. 11.9b show great agreement. The disagreement in Fig. 11.9b towards lower values was also seen in the uncorrected  $m_{4q}$  of Fig. 11.6, which suggests that the derived correction was not adequate for the  $t\bar{t}$  process, although the systematic uncertainty is slightly smaller in this regions compared to the SR.

The effects of the corrections can be examined in Fig. 11.10, which shows the two corrected momenta as well as the masses of the  $4q$  and  $e\mu 4q$  systems. While an inadequate correction is seen at about 100 GeV in  $p_T^{e\mu}$ , the two masses and especially  $m_{e\mu 4q}$  are somewhat corrected.

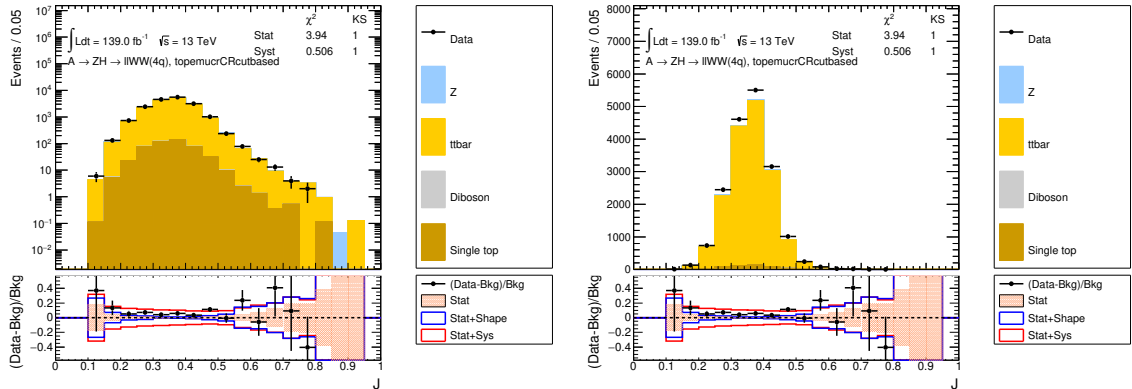
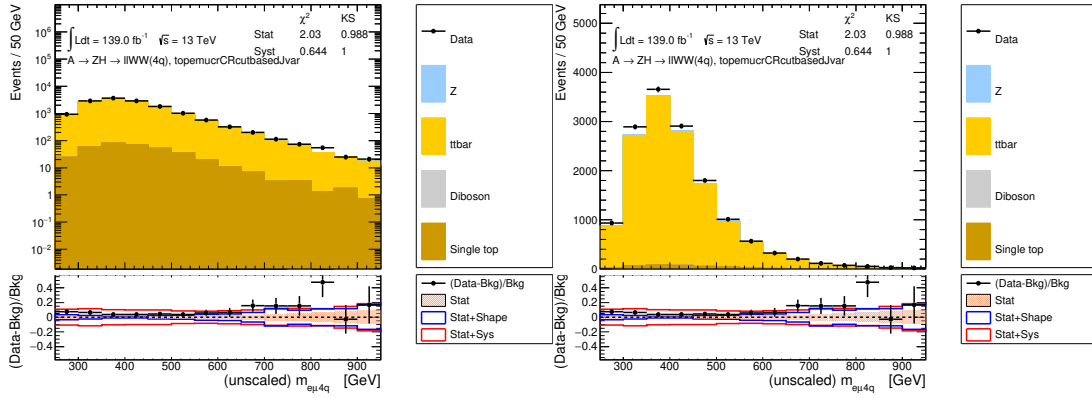
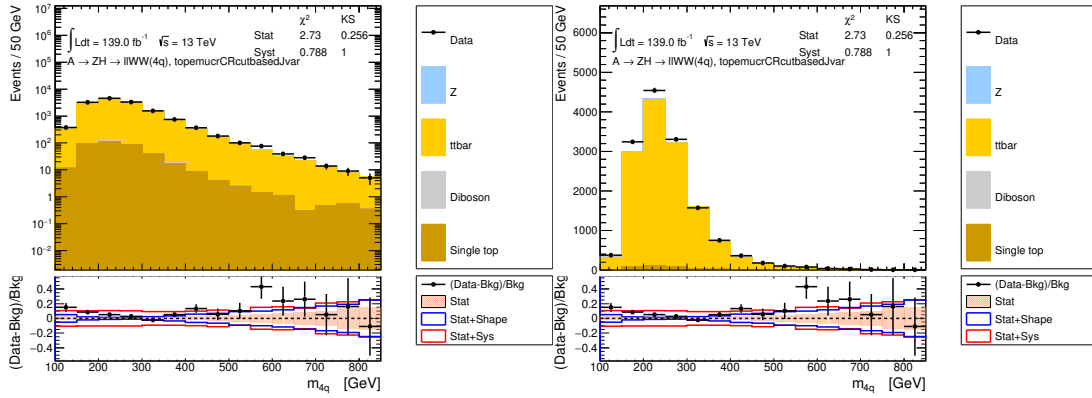
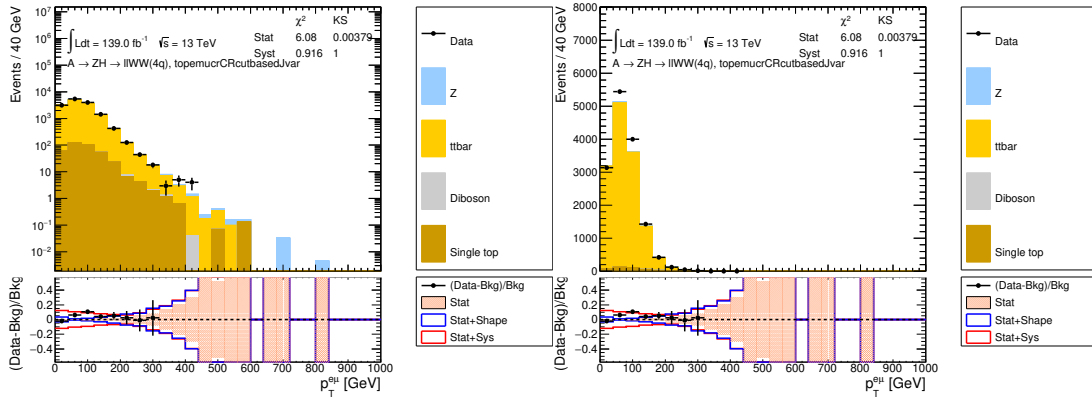
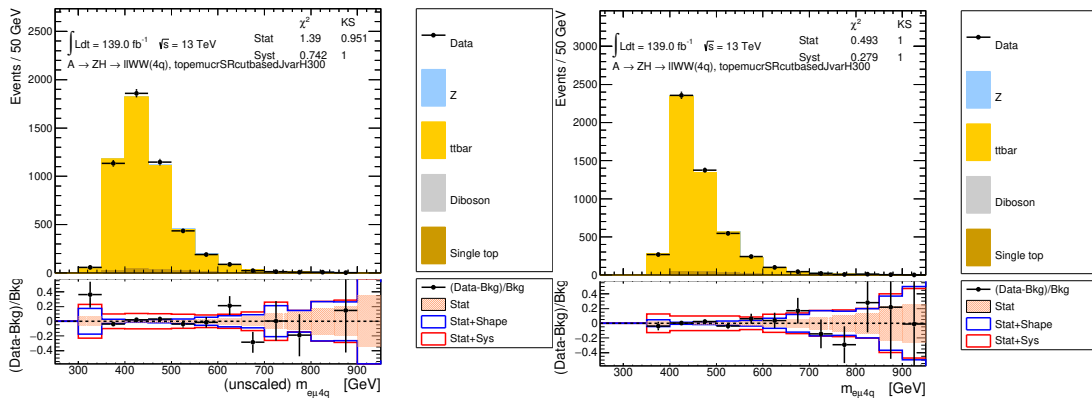


Figure 11.8: The TCR distribution for  $J$  at Level 1.


 (a) (unscaled)  $m_{\ell\mu 4q}$ 

 (b)  $m_{4q}$ 

 (c)  $p_T^{\ell\mu}$ 

 (d) (unscaled)  $m_{\ell\mu 4q}$  in  $m_H = 300$  GeV window

 (e)  $m_{\ell\mu 4q}$  in  $m_H = 300$  GeV window

Figure 11.9: (a-c) The TCR distributions for  $m_{2\ell 4q}$ ,  $m_{4q}$ , and  $p_T^{\ell\mu}$  at Level 2. (d-e)  $m_{2\ell 4q}$  at Level 3; on the right, the masses of the  $\ell\ell$  and  $4q$  systems are scaled to the masses of the  $Z$  and the  $H$  bosons, respectively. Logarithmic scale on the left and linear scale on the right.

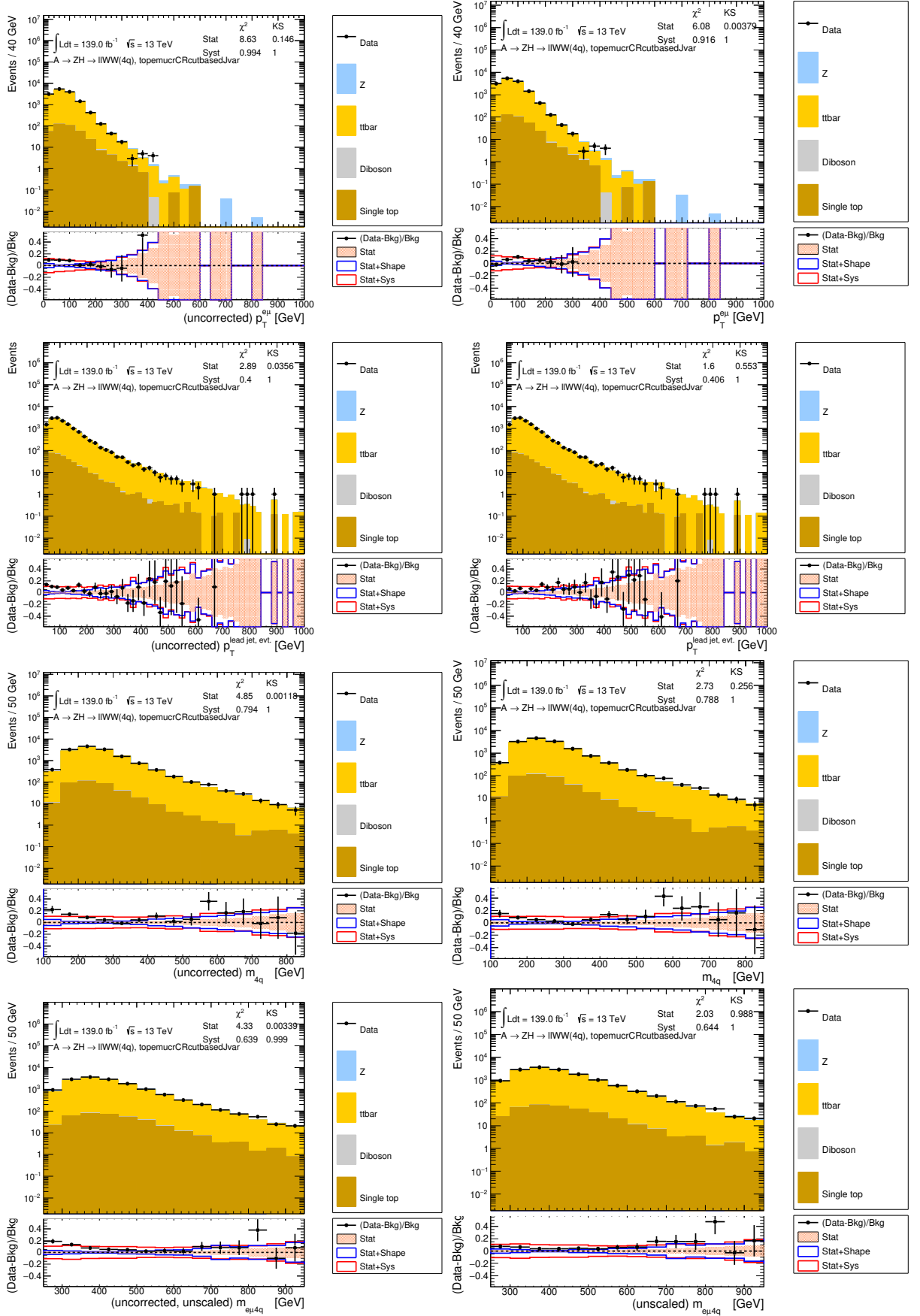


Figure 11.10: The TCR distributions for uncorrected  $p_T^{\ell\ell}$ ,  $p_T$  of the leading jet of the event,  $m_{4q}$ , and  $m_{2\ell 4q}$  at Level 2 on the left. On the right, the corrected figures are shown for comparison. Logarithmic scales are shown.



# 12 Signal modeling

The signal was selected in Chap. 10. The selection was derived from and applied to simulated signal samples at representative mass points in a range that covers the search scope of this analysis. From these simulated signals, we will now derive functional representations for both the shapes and normalizations/acceptances, which we will use to construct signals for arbitrary mass points.

"With four parameters I can fit an elephant, and with five I can make him wiggle his trunk."

- John von Neumann

## Contents

---

<b>12.1 Shape interpolation</b> . . . . .	<b>120</b>
12.1.1 Large-width signals . . . . .	125
<b>12.2 Acceptance interpolation</b> . . . . .	<b>126</b>

---

The shape interpolation is done by fitting the  $m_{2\ell 4q}$  distributions of each simulated signal with the double-sided crystal ball (DSCB) [148] that has the following expression:

$$\begin{aligned}
 f_{DSCB}(x; \mu, \sigma, n_1, a_1, n_2, a_2) &= \frac{e^{-\frac{1}{2}a_1^2}}{\left[ \frac{|a_1|}{n_1} \left( \frac{n_1}{|a_1|} - |a_1| - \frac{x-\mu}{\sigma} \right) \right]^{n_1}} && \text{for } \frac{x-\mu}{\sigma} < -a_1 \\
 &= e^{-\frac{1}{2}\left(\frac{x-\mu}{\sigma}\right)^2} && \text{for } -a_1 \leq \frac{x-\mu}{\sigma} < a_2 \\
 &= \frac{e^{-\frac{1}{2}a_2^2}}{\left[ \frac{|a_2|}{n_2} \left( \frac{n_2}{|a_2|} - |a_2| + \frac{x-\mu}{\sigma} \right) \right]^{n_2}} && \text{for } \frac{x-\mu}{\sigma} \geq a_2
 \end{aligned}$$

The DSCB has a Gaussian core (with the usual mean  $\mu$  and width  $\sigma$ ) with power-law tails (parameters  $a_1, a_2, n_1, n_2$ ). The points at which the Gaussian core joins the power-law tails are controlled by the  $a$  parameters, and the sizes of these tails are controlled by the  $n$  parameters. The parameters of this function (except for the mean  $\mu$ ) will be interpolated from the best-fit values obtained by individual fits to the simulated signals. After this, the interpolated shapes will be compared to the original shapes, and a shape uncertainty will be derived.

Large-width signals will be convoluted with a modified Breit-Wigner to properly account for the natural widths of these signals.

The yield interpolation will be done on the weighted number of signal events passing the selection<sup>2</sup> using thin-plate splines [149] in the plane spanned by  $m_A$  and  $m_H$ .

The detector systematics for the interpolated signals will be explained in the next chapter.

<sup>2</sup> The interpolation does not use the yield from the shape fits in order not to correlate the two.

## 12.1 Shape interpolation

The fitting procedure will be done in multiple steps, detailed in the list below. All simulated signals are fitted at each step. After each step, some tail parameters are fixed, and the simulated signals are fitted again. While any of the tail parameters are being fitted for, the mean of the fit is fixed to  $m_A$ . After the tail parameters have been found, the mean is left floating. The normalization is always left floating, and the width is left floating until the tail parameters have been fixed and the width itself has been interpolated<sup>1</sup>.

The fit procedure is as follows:

1. A fully floating fit with the DSCB is done on each simulated signal. The fitted distributions are shown in Fig. 12.1 and the tail parameters are shown in Fig. 12.2.
2.  $n_1$  shows a clear trend that is modeled by an exponential for mass-splittings greater than 100 GeV, while  $n_1$  for  $\Delta M = 100$  GeV and  $n_2$  are fixed to constants.
3. With  $n_1$  and  $n_2$  fixed, a second fit is done with the remaining parameters floating. The new tail parameters are shown in Fig. 12.3.
4.  $a_1$  is constant for  $\Delta M = 100$  GeV and otherwise follows a second-order polynomial in both  $\Delta M$  and  $m_H$ .  $a_2$  follows a first-order polynomial in both  $\Delta M$  and  $m_H$ .
5. With the tail parameters fixed (Fig. 12.4), the signal is fitted a final time, now leaving the mean floating.
6. The core parameters,  $\mu$  and  $\sigma$ , are shown in Fig. 12.5 as a function of the mass-splitting. The evolution of  $\sigma$  shows an additional dependency on  $m_H$ . This dependency has been fitted and shown in the figure for slices in  $m_H$  and listed in Tab. 12.2.

The expressions for the interpolated fit parameters are listed in Tab. 12.1. Since there are no simulated signals with  $\Delta M$  between 100 and 120 GeV, this region will be covered by the  $\Delta M = 100$  GeV parameters.

Table 12.1: Expressions for the interpolated parameters of the DSCB function.

Parameter	for $\Delta M < 120$ GeV	for $\Delta M \geq 120$ GeV
$\mu$	Floating	Floating
$\sigma$	Floating	Floating
$a_1$	4.61	$\max(0.5, -1.277 + 0.001856\Delta M - 0.0000001761\Delta M^2 + 0.007455m_{4q} - 0.000005514m_{4q}^2)$
$a_2$		$0.1917 + 0.0006275\Delta M + 0.001149m_{4q}$
$n_1$	100	$23.68 \exp(-0.01156\Delta M) + 1.752$
$n_2$	3.98	4.20

Table 12.2: The expression for the core parameter  $\sigma$  fitted with a second-order polynomial in  $m_A$  and  $m_H$  incl. a cross-term:  $\sigma(x) = p_0 + p_1m_{2\ell 4q} + p_2m_{4q} + p_3m_{2\ell 4q}^2 + p_4m_{4q}^2 + p_5m_{2\ell 4q}m_{4q}$ , in GeV.

$p_0$	$p_1$	$p_2$	$p_3$	$p_4$	$p_5$
-0.3746	0.0595	-0.0665	$-2.041 \times 10^{-5}$	$3.603 \times 10^{-5}$	$5.280 \times 10^{-6}$

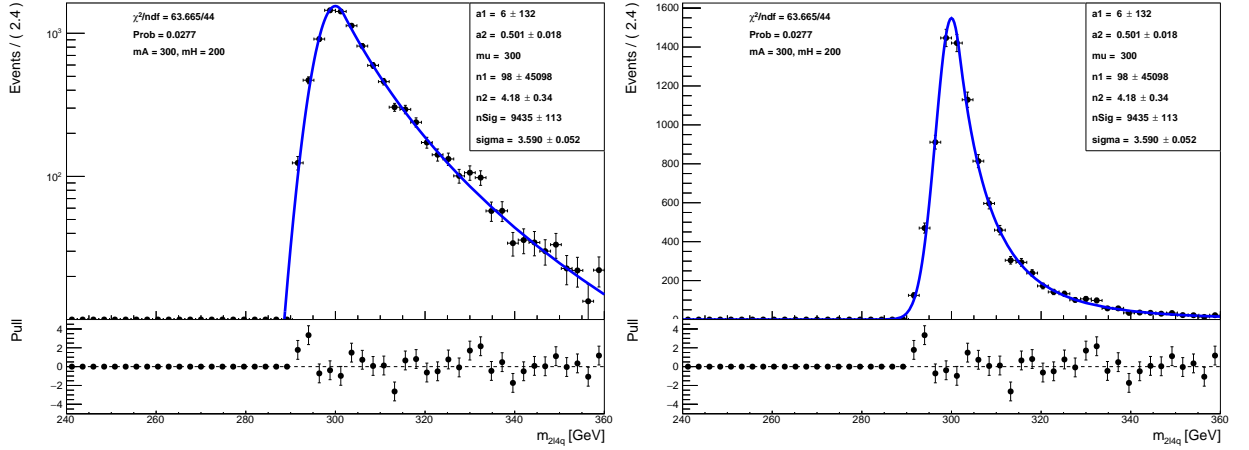
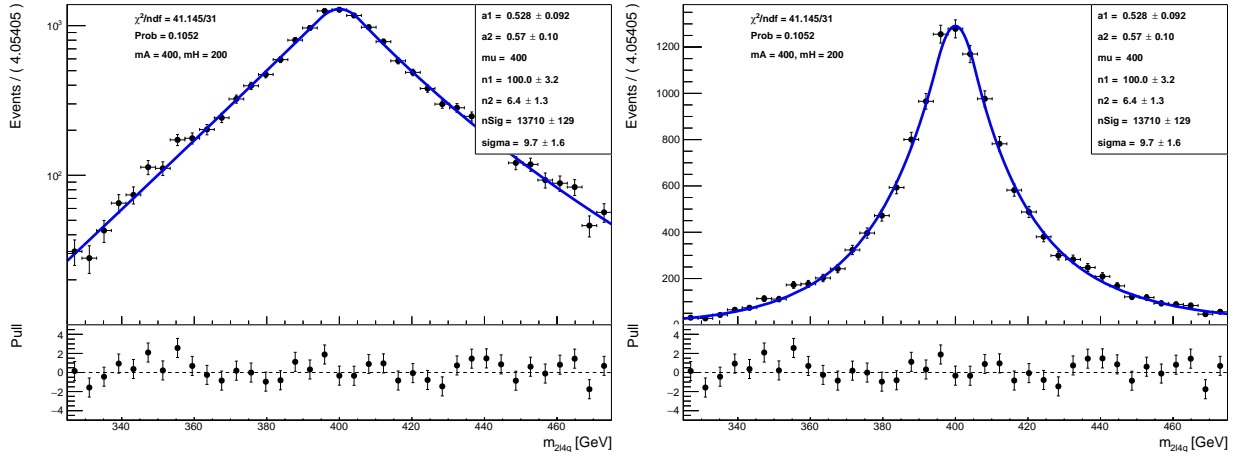
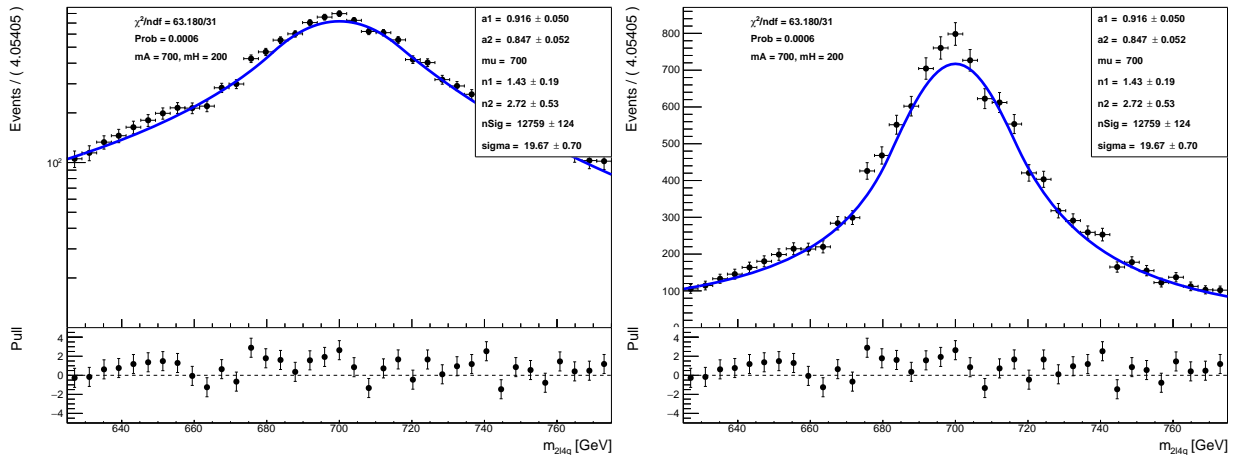

 (a)  $m_A = 300$  GeV,  $m_H = 200$  GeV

 (b)  $m_A = 400$  GeV,  $m_H = 200$  GeV

 (c)  $m_A = 700$  GeV,  $m_H = 200$  GeV

Figure 12.1: Fully-floating fits of  $m_{2l4q}$  using the DSCB for different simulated signals. Logarithmic scale on the left and linear scale on the right. The pull is defined as the fit subtracted by the simulated data divided by the uncertainty of the simulated data.

Figure 12.2: Best-fit values of  $a_1$ ,  $a_2$ ,  $n_1$ , and  $n_2$  for the DSCB fit to the simulated signals as a function of the mass-splitting when all parameters are allowed to float in the fit.

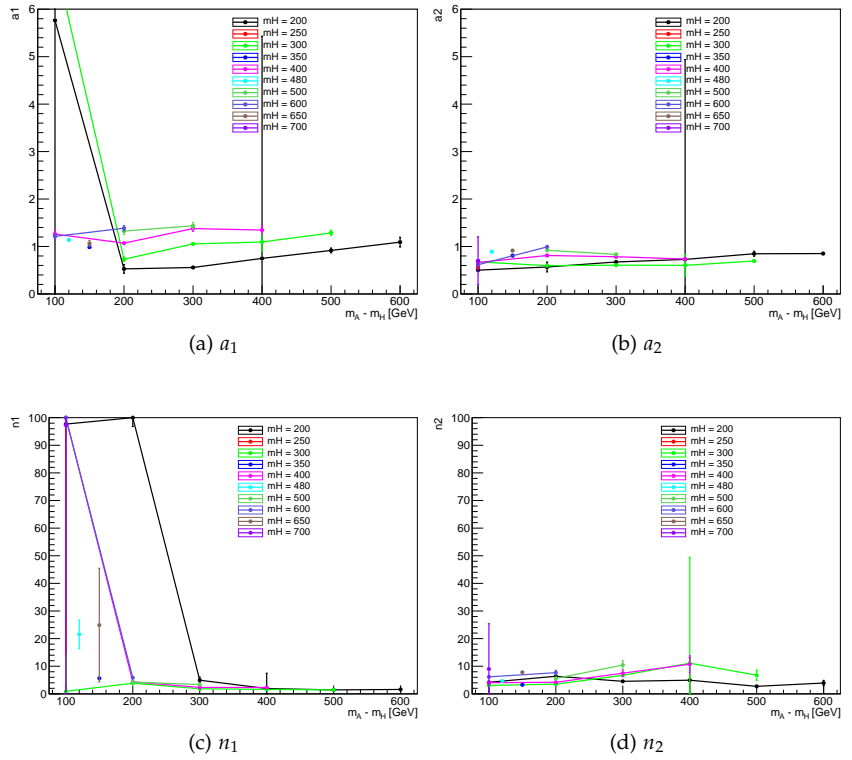
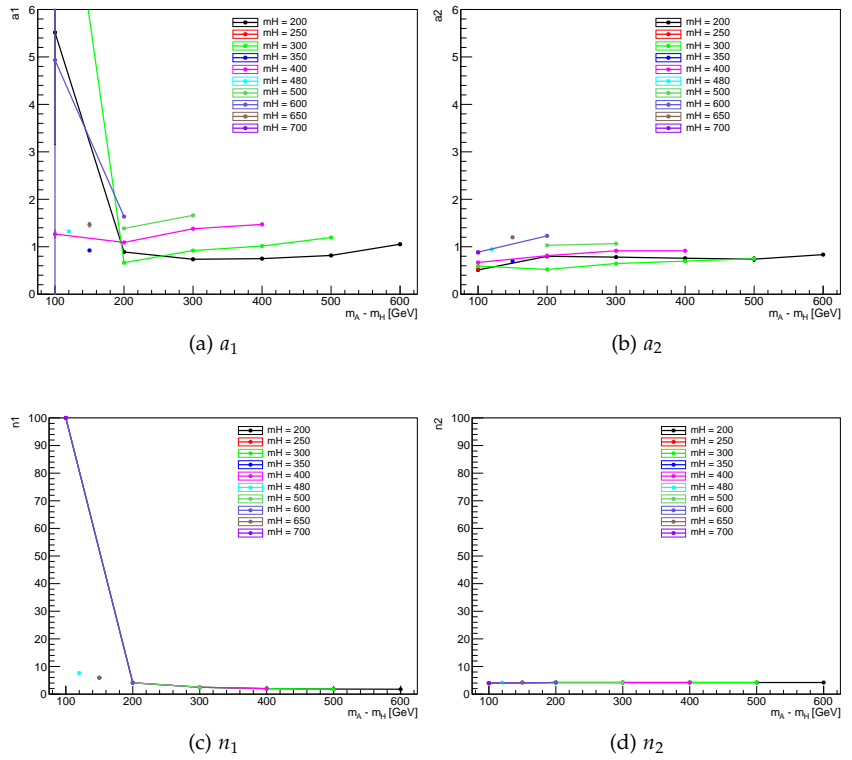


Figure 12.3: Best-fit values of  $a_1$  and  $a_2$  for the DSCB fit to the simulated signals as a function of the mass-splitting when  $n_1$  and  $n_2$  have been fixed.



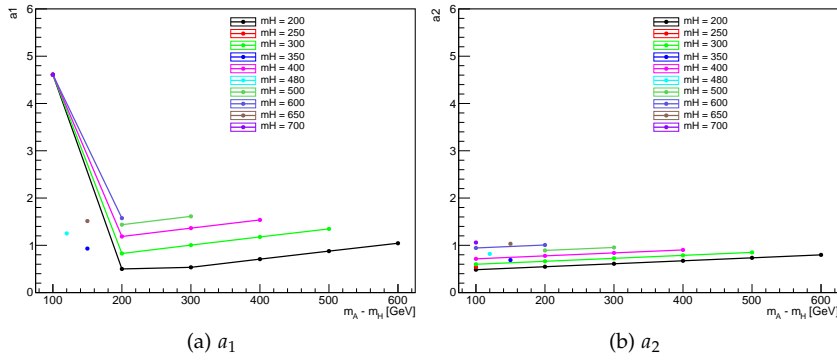


Figure 12.4: Fixed tail parameters for the DSCB fit to the simulated signals as a function of the mass-splitting.

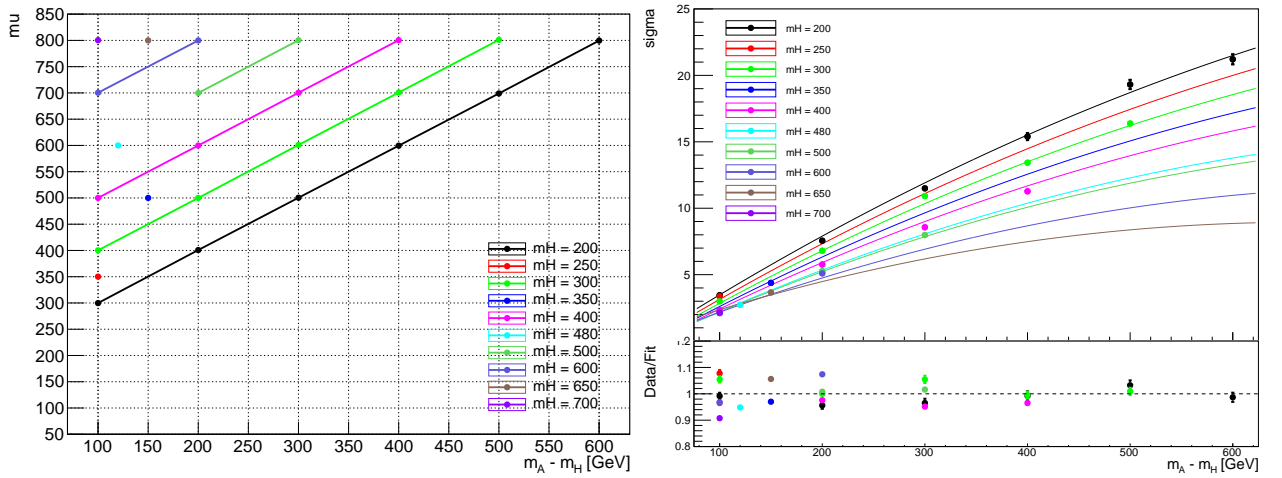
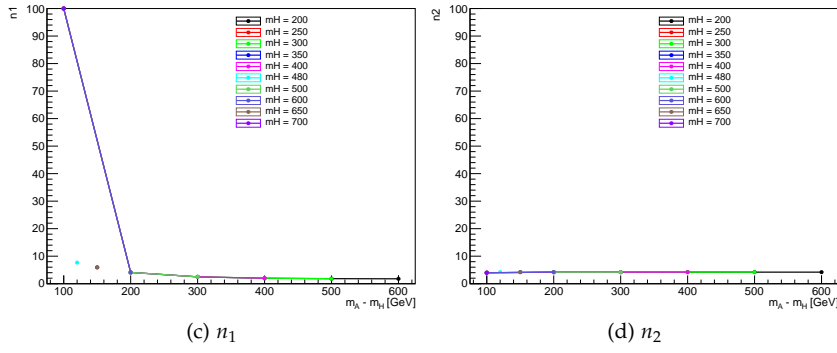


Figure 12.5: Left: The mean  $\mu$  with mass points of the same  $m_H$  connected by lines. Right: The width  $\sigma$  as a function of the mass-splitting. The fit to  $\sigma$  comes from Tab. 12.2.

The shape uncertainties are shown in Fig. 12.6 for some signals and in App. 19.C for the remaining. The procedure for deriving these uncertainties is as follows. The interpolated parameters ( $\sigma$ ,  $a_1$ ,  $a_2$ ,  $n_1$ , and  $n_2$ ) are varied randomly within 10% of their interpolated values for the particular mass points, each time producing a new curve. Then, from this set of curves, the largest and smallest variations per  $m_{2l4q}$  bin are chosen to define the up and down variations of the shape systematic. The variations enclose the cores well with some deviations in some  $\Delta M = 100$  GeV mass points and some deviations in the tails for several other mass points. Since the signal will be binned such that 68% of the core is in one bin during the likelihood fitting stage (more on this in Sect. 14.1), deviations in the tails matter little as Fig. 12.7 shows.

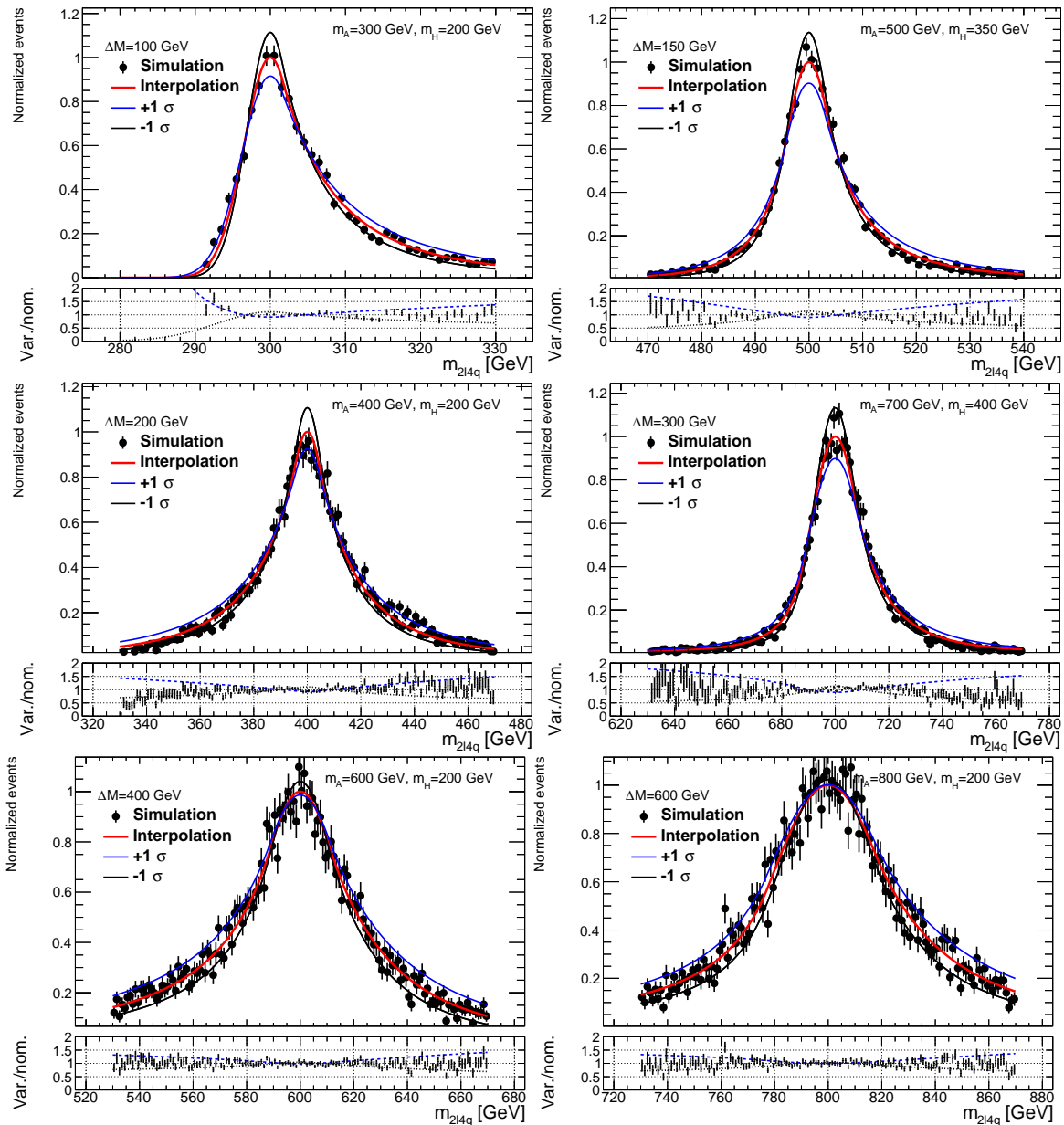


Figure 12.6: The simulated signals compared against interpolated signals along with their interpolation uncertainties.

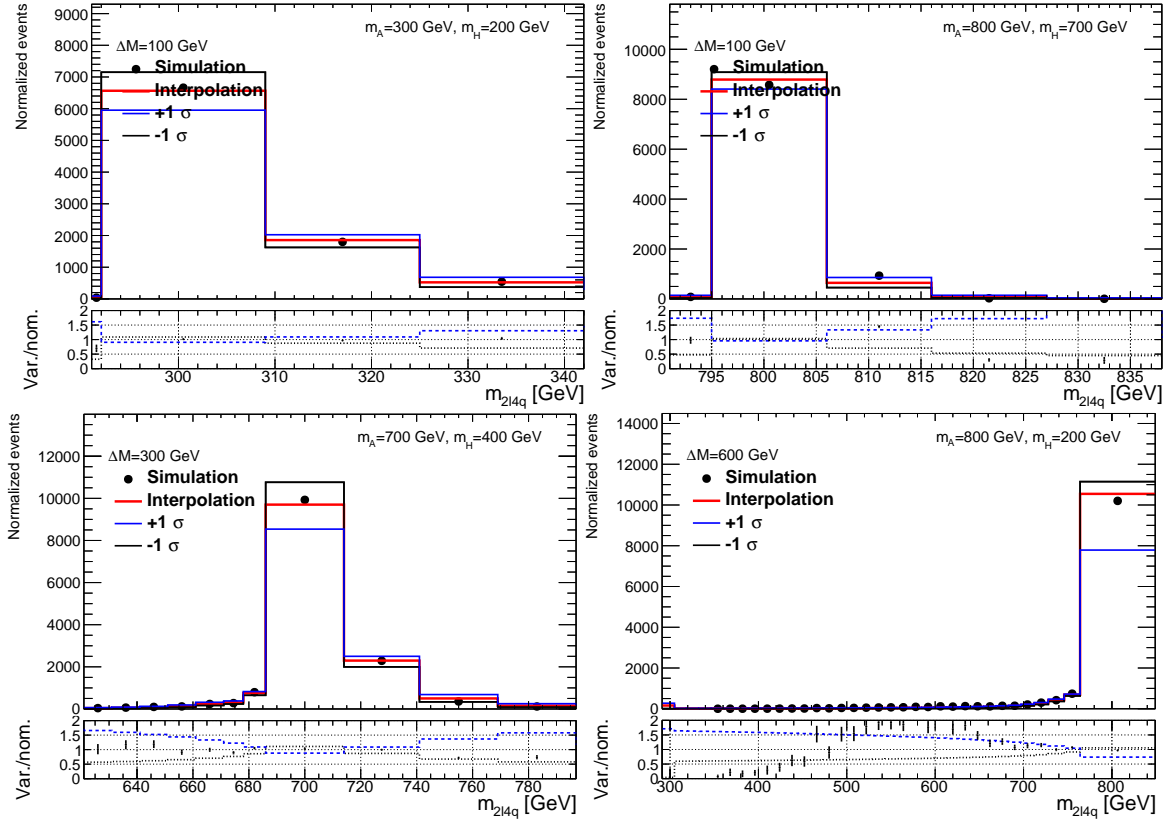


Figure 12.7: Some of the mass points from Fig. 12.6. The interpolated signals have been rebinned such that the core contains 68% of the signal following Sect. 14.1.

### 12.1.1 Large-width signals

For the 2HDM models, the natural width of the  $A$  boson can be as large as 35%, depending on the  $\alpha$  and  $\beta$  parameters of the models (cf. Sect. 1.2). The Gaussian cores (or the FWHM) of the narrow-width signals are on the order of a few percent<sup>1</sup>. It is therefore necessary to convolve the signal distributions with a Breit-Wigner distribution to properly model their natural widths.

Only the natural width of  $A$  is considered, since the analysis is searching for the  $A \rightarrow ZH$  decay. It would require additional optimization of the  $m_{4q}$  windows, if  $H \rightarrow ZA$  decay were to be considered as well in this large-width scenario.

The interpolated signals are convolved with a modified Breit-Wigner. This was shown to agree with simulated large-width signals in the previous iteration of this analysis (Ref. [54] for paper, Ref. [1] for internal note). The modified Breit-Wigner is defined as follows:

$$\text{BW}(m_{2l4q}) = \begin{cases} 0 & \text{if } m_{2l4q} \leq m_H - 20 \text{ GeV} \\ \frac{2}{\pi} \frac{\Gamma^2 m_A^2}{(m_{2l4q}^2 - m_A^2)^2 + \Gamma^2 m_A^2} \cdot \text{LogNormal}(m_{2l4q}; 0.88, m_H - 20 \text{ GeV}, m_A), & \text{otherwise} \end{cases}$$

where  $\Gamma = m_A w$  and  $w$  is the width. The  $\text{LogNormal}(x, \sigma, \theta, m)$  distribution is taken from ROOT<sup>2</sup> [150]. The reason for the LogNormal addition is that the shape changes when the mass-splitting nears the  $Z$  mass due to the constrained kinematic space. The log-normal shape can be seen in Fig. 12.8.

<sup>1</sup> Compare this to the naive standard deviation of the signal distributions that are up to 17%, for (580, 200) in this case, because of the long tails.

<sup>2</sup> Found in the ROOT documentation at <https://root.cern.ch/doc/master/namespaceTMath.html#a0503deae555bc6c0766801e4642365d2>.

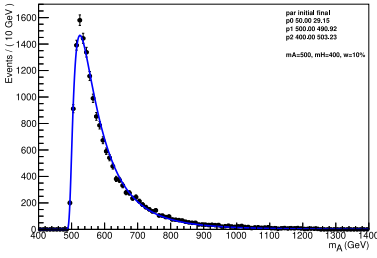


Figure 12.8:  $m_{\ell\ell b\bar{b}}$  using truth particles generated from  $A \rightarrow ZH \rightarrow \ell\ell b\bar{b}$  with masses (500, 400) and 10% width. The distribution has been fitted with the modified Breit-Wigner distribution where the fit parameters have been constrained to be within a factor of 1/2 and 2 of their initial values. The log-normal shape is apparent.

The interpolated shape uncertainty for the large-width signals should then derived from the set of convolutions as is the case for the narrow-width signals. However, it would require many CPU hours to compute the convolutions (thousands) per bin (20) per mass point (1326) per width (20) for each variation (2) of the large-width shape systematic. Instead, the narrow-width shape systematics are convolved with the modified Breit-Wigner. The results for three widths are shown in Fig. 12.9.

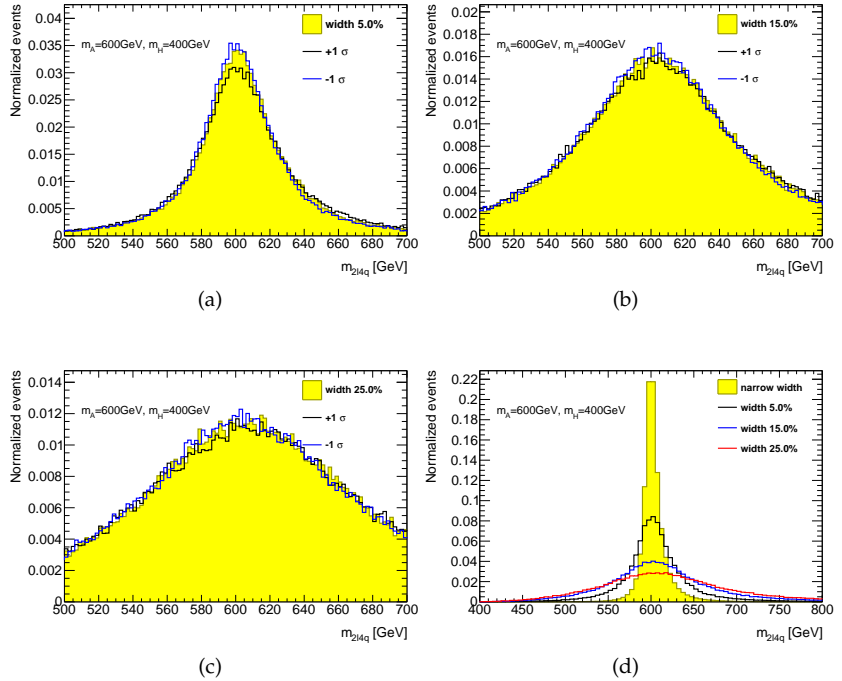


Figure 12.9: (a-c) Interpolated large-width signals with shape uncertainties. (d) The interpolated large-width signals compared to the interpolated narrow-width signal.

### 12.2 Acceptance interpolation

The yields in the SRs at Level 3 for all simulated signals will like-wise be interpolated to find normalizations for arbitrary mass points. The normalizations are interpolated using the thin-plate spline. The yields of the simulated signals are placed in a 2D grid as a function of their simulated masses and fit with the spline. However, fake points are added to aid the fit in order to suppress extrapolation errors at the boundaries. The fake points are made in the following way:

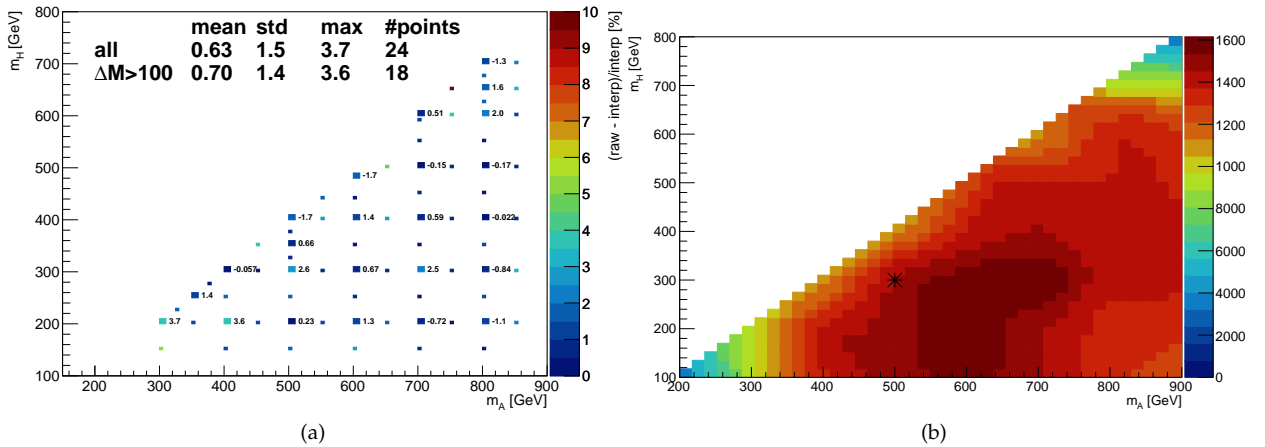
1. The bottom row signals (with the lowest  $m_H$ ) have their yields duplicated and inserted 50 GeV below
2. The right column signals (with the highest  $m_A$ ) have their yields duplicated and inserted 50 GeV to the right
3. To the left of the left-most and above the top-most points, yields are duplicated similar to the previous two bullets, unless these points give  $\Delta M < 100$  GeV
4. In-between every point, a new point is made that uses the average of its two closest neighbors; using the left and right points for

horizontal fakes as well as the lower and upper points for the vertical fakes

5. Lastly, in-between the points on the diagonal, a new point is made using the average of its two closest diagonal neighbors

The yields drop significantly for  $\Delta M \lesssim 150$  GeV. Therefore, extra care is taken such that points from further away do not copy their yields towards low  $\Delta M$ . The fake point to the left of (500, 350) is discarded as this would place a high yield at  $\Delta M = 100$  GeV where the yield drops off much too quickly for the fake point to fit in. The point (600, 480) is also used for the diagonal point interpolations, which is otherwise only done for  $\Delta M = 100$  GeV points.

After adding the fake points, the grid is fitted with the thin-plate spline. To estimate an uncertainty on this spline, the yield from one mass point is left out to make a spline of  $N-1$  points. The yield at the left-out mass point is then interpolated from the new spline and the relative uncertainty is calculated. This is repeated for all simulated signals. The differences between the "raw" and interpolated yields will show the power of the splines. The addition of the fake points in-between the real data points will yield very small differences in areas with little variation. For the final spline that is used later on in the analysis, all yields are used.



The uncertainties of the fits are shown in Fig. 12.10a. The spline-fit works very well for the bulk of the data. For low  $\Delta M$  and for low  $m_A, m_H$ , there are some significant differences. The points (300, 200) and (400, 200) are overestimated by 3.7% and 3.6%, respectively. The greatest difference, 3.7%, is taken as the uncertainty on the normalization interpolation for all mass points. This value is much larger than the standard deviation of differences in percent (at 1.5) and is conservative for most of the mass space.

Adding all the fake points to help the spline may make it less smooth. The spline for which the yield from the (500, 300) point was left out is shown in Fig. 12.10b. This spline is used to interpolate the whole grid. The interpolation is smooth.

Areas with low relative uncertainty in Fig. 12.10a (say, the middle parts of the triangle) correspond to areas of little color change in

Figure 12.10: (a) Results of the two-dimensional thin-plate spline signal yield interpolations. The z-axis gives the relative differences between the raw and interpolated yields for points that are left out of the spline. The real data points are drawn in bigger boxes and annotated with their differences. The sign is kept; negative values mean overestimated yields. The smaller boxes are the fake points explained in the text. (b) The result of applying the thin-plate spline that was made to interpolate the (500, 300) data point. There is very little variation between the different splines, so only this one is shown.

Fig. 12.10b, meaning relatively flat yields. Conversely, at the edges and corners of the triangle, larger relative uncertainties correspond to larger changes in the yield.

This shows that the spline is relatively stable, and the larger uncertainties are in areas where the yields change drastically. This was concluded using the spline that was made by leaving out the 500,300 point, but one could use any of the “N-1” splines to reach this conclusion since they will produce figures that are very similar to Fig. 12.10b.

# 13 Systematic uncertainties

Before building our fit model, we shall go through the list of systematics that will go into it. The list contains many sources of uncertainties coming from the detector, reconstruction, and theory. We categorize the systematics by whether they affect the normalization (rate) or shape of the final nominal distribution.

## Contents

---

<b>13.1 Detector uncertainties</b> . . . . .	<b>130</b>
13.1.1 Signal detector uncertainties interpolation . . . . .	133
<b>13.2 Modeling uncertainties on signal</b> . . . . .	<b>133</b>
13.2.1 Scale . . . . .	133
13.2.2 Tune (ISR/FSR/MPI) . . . . .	134
13.2.3 PDF . . . . .	136
<b>13.3 Background modeling uncertainties</b> . . . . .	<b>137</b>

---

The systematic uncertainties in this analysis can roughly be categorized by three types:

**detector/reconstruction (experimental):** Systematics from detector effects and reconstruction of physical objects and their identification, isolation, momentum scale factors, etc.

**interpolation (method):** Uncertainty on the interpolation itself as well as propagation of detector uncertainties to interpolated signals

**modeling (theoretical):** The Monte Carlo generator with uncertainties on theoretical and phenomenological parameters

The detector systematics will be covered in the next section, which ends with how to carry these into the interpolated signals. The narrow-width shape uncertainty has already been covered. The subsequent section covers the theoretical uncertainties on the signal only, as the modeling for the backgrounds have been derived directly from data in Sect. 11.1.

In ATLAS, many systematics are calculated by groups with specific responsibilities, e.g. the groups delivering electron identification also give  $\pm 1\sigma$  variations of the associated systematics. The systematics are propagated through an analysis by varying the calculated (e.g. electron probability) or measured value (jet  $p_T$ ) up or down by  $1\sigma$  and repeating the selections. Some variations affect either whether an event passes (e.g. a nominal medium electron becomes loose for one variation) or the event weight (scale factors which do not affect the

variables that are part of the selections) or both (jet  $p_T$  scaled down for one variation may lead to too few jets with  $p_T > 20$  GeV).

### 13.1 Detector uncertainties

The detector systematics include the integrated luminosity for 2015–2018 at 1.7% [82]; electron triggers [94]; electron reconstruction, energy scale and resolution, identification, and isolation [99]; muon triggers [93]; muon identification [102, 151]; muon reconstruction and isolation [102]; muon track to vertex association; and jet vertex tagging (JVT) as well as jet energy resolution (JER) and scale (JES) [152].

Since the analysis is not sensitive to the electron energy resolution or scale, a simplified list of systematics is used, which combines the electron trigger, reconstruction, identification, and isolation systematics into one systematic each. The JES and JER systematics are also from a reduced list as the analysis need not be combined with other analyses or experiments.

The full list of systematics is in Tab. 13.1. Electron-specific systematics start with "EL", muon with "MUON", E/gamma (electrons) with "EG", and jet with "JET". The type of systematic can be known by identifying "ID" as identification, "Reco" as reconstruction, "Iso" as isolation, "Trig" as trigger, "scale" as scale factor<sup>1</sup>, etc. A short explanation of the systematics used in this analysis is listed in Tab. 13.2.

<sup>1</sup> The ratio of simulated data to real data as a function of a variable, typically  $p_T$ .

EL_EFF_ID_TOTAL_1NPCOR_PLUS_UNCOR	✓	JET_CR_JET_Pileup_OffsetMu	✓
EL_EFF_Reco_TOTAL_1NPCOR_PLUS_UNCOR	✓	JET_CR_JET_Pileup_OffsetNPV	✓
EL_EFF_Iso_TOTAL_1NPCOR_PLUS_UNCOR	✓	JET_CR_JET_Pileup_PtTerm	✓
EL_EFF_Trigger_TOTAL_1NPCOR_PLUS_UNCOR	✓	JET_CR_JET_Pileup_RhoTopology	✓
MUON_EFF_RECO_SYS		JET_CR_JET_EffectiveNP_Mixed1	✓
MUON_EFF_RECO_STAT		JET_CR_JET_EffectiveNP_Mixed2	
MUON_EFF_RECO_SYS_LOWPT		JET_CR_JET_EffectiveNP_Mixed3	
MUON_EFF_RECO_STAT_LOWPT		JET_CR_JET_EffectiveNP_Modelling1	✓
MUON_EFF_TrigSystUncertainty		JET_CR_JET_EffectiveNP_Modelling2	✓
MUON_EFF_TrigStatUncertainty		JET_CR_JET_EffectiveNP_Modelling3	✓
MUON_EFF_ISO_STAT		JET_CR_JET_EffectiveNP_Modelling4	
MUON_EFF_ISO_SYS		JET_CR_JET_EffectiveNP_Statistical1	
MUON_TTVA_STAT		JET_CR_JET_EffectiveNP_Statistical2	✓
MUON_TTVA_SYS		JET_CR_JET_EffectiveNP_Statistical3	
EG_SCALE_ALL	✓	JET_CR_JET_EffectiveNP_Statistical4	
EG_RESOLUTION_ALL	✓	JET_CR_JET_EffectiveNP_Statistical5	
MUON_ID	✓	JET_CR_JET_EffectiveNP_Statistical6	
MUON_MS		JET_CR_JET_EffectiveNP_Detector1	
MUON_SCALE		JET_CR_JET_EffectiveNP_Detector2	
MUON_SAGITTA_RHO		JET_CR_JET_EtaIntercalibration_TotalStat	✓
MUON_SAGITTA_RESBIAS	✓	JET_CR_JET_EtaIntercalibration_NonClosure_highE	
JET_JvtEfficiency	✓	JET_CR_JET_EtaIntercalibration_NonClosure_negEta	
JET_CR_JET_JER_EffectiveNP_1	✓	JET_CR_JET_EtaIntercalibration_NonClosure_posEta	
JET_CR_JET_JER_EffectiveNP_2		JET_CR_JET_EtaIntercalibration_Modelling	✓
JET_CR_JET_JER_EffectiveNP_3		JET_CR_JET_BJES_Response	✓
JET_CR_JET_JER_EffectiveNP_4		JET_CR_JET_Flavor_Response	✓
JET_CR_JET_JER_EffectiveNP_5	✓	JET_CR_JET_Flavor_Composition	✓
JET_CR_JET_JER_EffectiveNP_6	✓	JET_CR_JET_SingleParticle_HighPt	
JET_CR_JET_JER_EffectiveNP_7restTerm	✓	JET_CR_JET_PunchThrough_MC16	
JET_CR_JET_JER_DataVsMC_MC16	✓		

Table 13.1: The full list of systematics from detector systematics. The checkmarks indicate systematics that are kept after an evaluation in Sect. 14.2.1. The remaining systematics will be pruned away, as they turn out to be insignificant.

NP	Group	Description
EL_EFF_ID_TOTAL_1NPCOR_PLUS_UNCOR	Electron efficiency	Identification
EL_EFF_Reco_TOTAL_1NPCOR_PLUS_UNCOR		Reconstruction
EL_EFF_Iso_TOTAL_1NPCOR_PLUS_UNCOR		Isolation
EL_EFF_Trigger_TOTAL_1NPCOR_PLUS_UNCOR		Trigger
EG_SCALE_ALL	Electron calibration	Energy scale
EG_RESOLUTION_ALL		Energy resolution
MUON_ID	Muons	Smearing of Inner Detector tracks
MUON_SAGITTA_RESBIAS		Remaining charge-dependency after a charge-dependent scale correction
JET_JvtEfficiency	JVT	JVT efficiency
JET_CR_JET_JER_EffectiveNP_1,	JER	Combination of measurements from in-situ dijet asymmetry measurements as well as random cones in minimum bias
JET_CR_JET_JER_EffectiveNP_5,		
JET_CR_JET_JER_EffectiveNP_6, and		
JET_CR_JET_JER_EffectiveNP_7restTerm		
JET_CR_JET_JER_DataVsMC_MC16		
JET_CR_JET_Pileup_OffsetMu	JES	Uncertainty on jet response from varying jet selections
JET_CR_JET_Pileup_OffsetNPV		Uncertainty on modeling the average interactions per crossing
JET_CR_JET_Pileup_PtTerm		Uncertainty on modeling the number of primary vertices
JET_CR_JET_Pileup_RhoTopology		Uncertainty on modeling the per-event $p_T$ distribution
JET_CR_JET_EffectiveNP_Mixed1		Uncertainty on the residual $p_T$ dependence
JET_CR_JET_EffectiveNP_Modelling1,		In-situ measurements of jets in $Z$ -jets, $\gamma$ -jet, and multijet; Category with detector and modeling components
JET_CR_JET_EffectiveNP_Modelling2, and		
JET_CR_JET_EffectiveNP_Modelling3		
JET_CR_JET_EffectiveNP_Statistical2		
JET_CR_JET_EtaIntercalibration_TotalStat		Above and category with physics modeling components
JET_CR_JET_EtaIntercalibration_Modelling		Above and category with statistics and method components
JET_CR_JET_BJES_Response		Statistical uncertainties in jets with $ \eta  > 0.8$
JET_CR_JET_Flavor_Response		Physics mismodeling in jets with $ \eta  > 0.8$
JET_CR_JET_Flavor_Composition		Jet response uncertainty specifically for jets initiated by $b$ -quarks
		Differences in the jet response for jets initiated by light quarks, $b$ -quarks, and gluons
		Uncertainty from assuming a 50% quark and 50% gluon composition in the sample

Table 13.2: Explanations of the kept systematics. The jet response is defined as  $E^{\text{reco}}/E^{\text{truth}}$ . From [108, 153, 154]. Additional JER information in [https://indico.cern.ch/event/752759/contributions/3119136/attachments/1706979/2750689/JetETmiss\\_JERRecommendation\\_20180829.pdf](https://indico.cern.ch/event/752759/contributions/3119136/attachments/1706979/2750689/JetETmiss_JERRecommendation_20180829.pdf).

### 13.1.1 Signal detector uncertainties interpolation

The signals are modeled by the DSCB. The systematic variations of the simulated signals are fitted with the DSCB with fixed tail parameters and floating mean and  $\sigma$ . The fitted means are close to the original values, while  $\sigma$  has shown significant variations. For each systematic variation, the largest difference in  $\sigma$  across all simulated signals will be used for all interpolated signals. The values used are shown in Tab. 13.3.

Systematic	up [%]	down [%]
MUON_SAGITTA_RESBIAS	2.1	-1.9
MUON_ID	-0.9	1.3
JET_JvtEfficiency	-0.1	3.5
JET_CR_JET_Pileup_RhoTopology	-2.7	7.1
JET_CR_JET_Pileup_PtTerm	1.3	-1.5
JET_CR_JET_Pileup_OffsetNPV	2.5	-2.2
JET_CR_JET_Pileup_OffsetMu	-1.6	2.8
JET_CR_JET_JER_EffectiveNP_7restTerm	3.7	-0.9
JET_CR_JET_JER_EffectiveNP_6	2.3	-0.7
JET_CR_JET_JER_EffectiveNP_5	3.3	-0.8
JET_CR_JET_JER_EffectiveNP_4	2.6	-0.6
JET_CR_JET_JER_EffectiveNP_3	4.8	-1.2
JET_CR_JET_JER_EffectiveNP_2	5.1	0.3
JET_CR_JET_JER_EffectiveNP_1	5.4	0.8
JET_CR_JET_Flavor_Response	3.0	-3.8
JET_CR_JET_Flavor_Composition	-5.4	8.2
JET_CR_JET_EtaIntercalibration_Modelling	-1.5	1.9
JET_CR_JET_EffectiveNP_Modelling1	-3.6	5.9
JET_CR_JET_EffectiveNP_Mixed1	1.4	-0.5
JET_CR_JET_BJES_Response	-1.0	2.8
EL_EFF_ID_TOTAL_1NPCOR_PLUS_UNCOR	-0.1	2.5
EG_SCALE_ALL	1.1	-0.6
EG_RESOLUTION_ALL	2.3	-0.5
Total in quadrature	14.2	14.9

Table 13.3: Detector systematics and the variation of  $\sigma$  of the DSCB.

## 13.2 Modeling uncertainties on signal

The modeling of simulated backgrounds was covered by a data-driven method introduced in Sect. 11.1. However, theoretical uncertainties will need to be derived for signal. These are split into three parts: scale, tune, and PDF.

### 13.2.1 Scale

The re-normalization ( $\mu_R$ ) and factorization ( $\mu_F$ ) scales are separately varied up and down by a factor of two. The largest difference with respect to the nominal values is taken as an estimate of the uncertainty due to the choice of scale.

Sample	$\mu_R$	$\mu_F$
r0f0	$\mu_R$	$\mu_F$
r0fD	$\mu_R$	$\frac{1}{2}\mu_F$
r0fU	$\mu_R$	$2\mu_F$
rDf0	$\frac{1}{2}\mu_R$	$\mu_F$
rDfD	$\frac{1}{2}\mu_R$	$\frac{1}{2}\mu_F$
rUf0	$2\mu_R$	$\mu_F$
rUfU	$2\mu_R$	$2\mu_F$

Table 13.4: List of  $\mu_R$  and  $\mu_F$  samples. (r0f0) is the nominal sample.

Table 13.5: Truth level events selections.

The studied samples contain truth level signal events. The following mass points have been generated with 100 000 events each: (300, 200), (400, 250), (500, 200), (550, 450), (600, 400), (700, 200), and (800, 500). The naming convention of the samples is shown in Tab. 13.4.

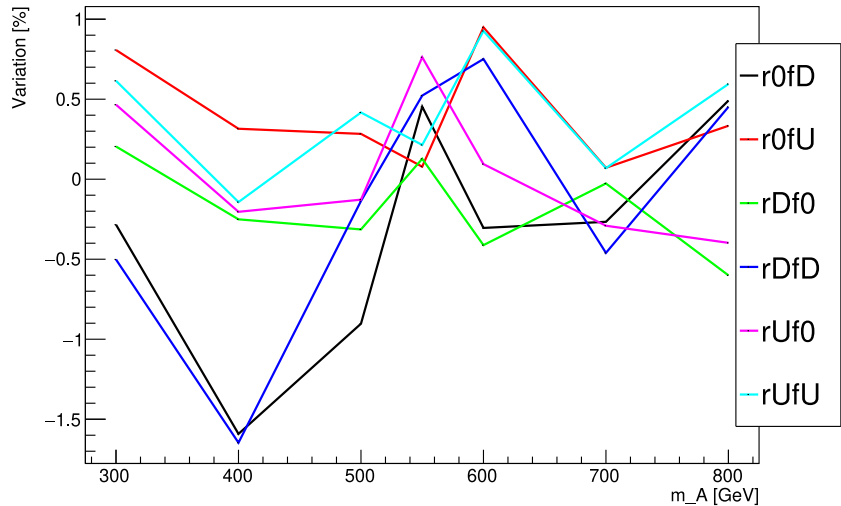
A truth level event selection that imitates the reconstruction level event selection is done. The selection does not include efficiencies from lepton identification and isolation requirements. The selections before the  $J$  variable selection are applied are shown in Tab. 13.5.

Cut	Selection
$A$ boson	Event contains exactly one $A$ boson
Jet multiplicity	Event contains at least 4 jets
Lepton $p_T$	$p_T > 30, 15$ GeV for leading and sub-leading
Pseudorapidity	$ \eta  < 2.47$ (electrons), $ \eta  < 2.5$ (muons)
$Z$ boson mass	$80 < m_{\ell\ell} < 100$ GeV
Jet kinematics	$p_T > 40, 30, 20, 20$ GeV and $ \eta  < 2.4$ for the four leading jets

The signal acceptance is defined as  $\varepsilon = N_{\text{after selection}} / N_{\text{before any selection}}$ , where  $N_{\text{before any selection}}$  counts events passing the second cut.

The variation in signal efficiency between the nominal and a varied sample is defined as  $(\varepsilon_{\text{Var}} - \varepsilon_{\text{Nom}}) / \varepsilon_{\text{Nom}}$ , where  $\varepsilon_{\text{Var}}$  and  $\varepsilon_{\text{Nom}}$  are the efficiencies of varied and nominal samples, respectively. Fig. 13.1 shows the variations as a function of  $m_A$  for all varied samples. The overall uncertainty is taken as the absolute envelope of the curves, which comes out as  $\pm 1.5\%$ . No clear shape dependence is found.

Figure 13.1: Scale variation as a function of  $m_A$ . The naming scheme in the legend was explained in Tab. 13.4.



### 13.2.2 Tune (ISR/FSR/MPI)

Monte Carlo generators use sets of parameters, named *tunes*, to adjust showering, hadronization, etc. The effects on the signal acceptance

by varying the parameters responsible for ISR, FSR, and MPI will be used to derive systematic uncertainties on signals' sensitivity to these variations. There are many parameters to vary, so a subset has been derived, which still covers the observables [120]. These variations are sensitive to the following:

- Var1: The underlying event
- Var2: Jet shapes and substructure
- Var3a-c: Extra jets (ISR/FSR)

Samples with same number of events and for the same mass points are generated for this as was generated for the scale study. The same truth selection is applied. The variations of Var1, Var2, Var3a, Var3b, and Var3c as well as the quadratic sum of positive and negative variations are given in Fig. 13.2 as a function of  $m_A$ .

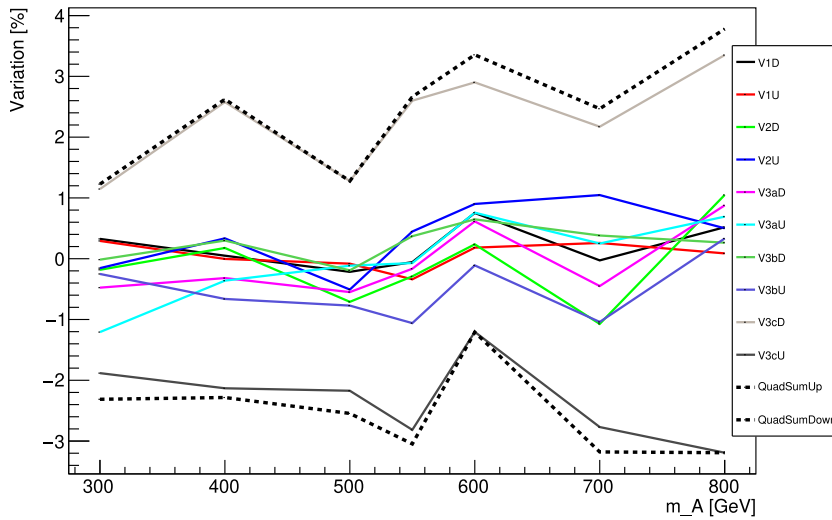


Figure 13.2: Tune variation in percent as a function of  $m_A$ . The black, dashed lines represent the quadratic sum of positive and negative variations.

Var3c varies  $\alpha_s$  for ISR jets in a large range of 0.115 – 0.140. This has a relatively large effect on the signal acceptance. The fall in efficiency happens during the jet selection stage ("ResolveJetsdRW2" in Tab. 13.6), because the signal jets are not among the 5  $p_T$ -leading jets.

The tune uncertainties are the quadratic sum of the positive and the negative variations, yielding  $\pm 3\%$ .

Table 13.6: The number of events passing the truth selection for the (800,500) mass point for the nominal setup and for the Var3c up variation. The relative difference is defined as  $(n_{Nom} - n_{Var})/n_{Var}$ .

Cut	Nom	Var3cU	Rel. diff. [%]
beforeTruthAZHCheck	100000.000	100000.000	0
beforeLeptonPt	97825.000	97833.000	-0.0081772
beforeLeptonEta	86450.000	86280.000	0.197033
beforeZMass	81802.000	81681.000	0.148137
before1stJetMul	73294.000	73298.000	-0.00545717
beforeJetPreSel	72197.000	72368.000	-0.236292
before2ndJetMul	72197.000	72368.000	-0.236292
beforeJetPt	71565.000	71813.000	-0.345341
beforeResolvingJets	71559.000	71805.000	-0.342595
ResolveJetsPreSel	71559.000	71805.000	-0.342595
ResolveJetsdRW1	63083.000	62918.000	0.262246
ResolveJetsdRW2	44526.000	43495.000	2.37039
ResolveJetsH2	38815.000	37812.000	2.6526
ResolveJetsW1W2mass	37085.000	35981.000	3.06829
Before Jvar	37085.000	35981.000	3.06829

### 13.2.3 PDF

The systematic uncertainty due to the choice of PDF can be estimated by use of alternative PDF sets when generating Monte Carlo events. However, the central values for the nominal PDF set already fit data well for gluon fusion<sup>1</sup>.

The uncertainties on the central values within the PDF due to the fitting method (or training in the case of NNPDF) can be estimated from alternative *eigensets*, which carry variations of the fit parameters. The standard deviation of 100 eigensets added in quadrature for the nominal PDF set, NNPDF23\_lo\_as\_0130\_qed, using LHAPDF [155] in following the recommendations by Ref. [156] will be the PDF uncertainty. The ratio of this uncertainty to the re-weighting factor of the nominal PDF set will be applied on an event-to-event basis during the event selection on the reconstructed data.

The re-weighting is applied to the following samples: (300,200), (350,250), (400,200), (500,200), (600,400), (700,200), and (800,500). The effect on the acceptance is shown in Fig. 13.3, which shows the acceptance uncertainty due to the PDF variation as a function of  $m_A$ . The upper and lower variations are found to be symmetric and hence the absolute value is shown only. The following function is superimposed on the figure:

$$\text{PDF uncertainty}[\%] = 2.1 + 0.70 \times \frac{m_A}{100 \text{ GeV}}. \quad (13.1)$$

The expression fits the values well and is used as the PDF uncertainty.

<sup>1</sup> According to internal documentation, [https://twiki.cern.ch/twiki/bin/viewauth/AtlasProtected/PdfRecommendations#Computing\\_PDF\\_uncertainties](https://twiki.cern.ch/twiki/bin/viewauth/AtlasProtected/PdfRecommendations#Computing_PDF_uncertainties).

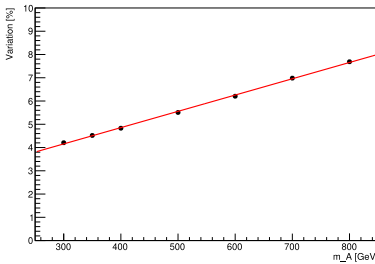


Figure 13.3: The relative difference on signal acceptance as a function of  $m_A$  due to the re-weighting variation using NNPDF23\_lo\_as\_0130\_qed.

### 13.3 Background modeling uncertainties

The corrections of the mismodeling have been covered in Sect. 11.1. For the corrections, two systematic uncertainties were derived using half of the fit to the corrections.

The remaining modeling uncertainty for  $m_{4q}$  is derived using 2015+2016 data. The disagreement between data and simulation is plotted and fitted for  $m_{4q}$  in Fig. 13.4, where the simulation is scaled to match data before-hand. The ratio is fitted with a linear expression:

$$-0.04181 + 0.00016m_{4q}$$

The fit expression will be applied as a weight to the analysis and its full value used as a systematic for the limit setting, similar to the previous two mismodeling systematics that used half the value as uncertainty (Sect. 11.1).

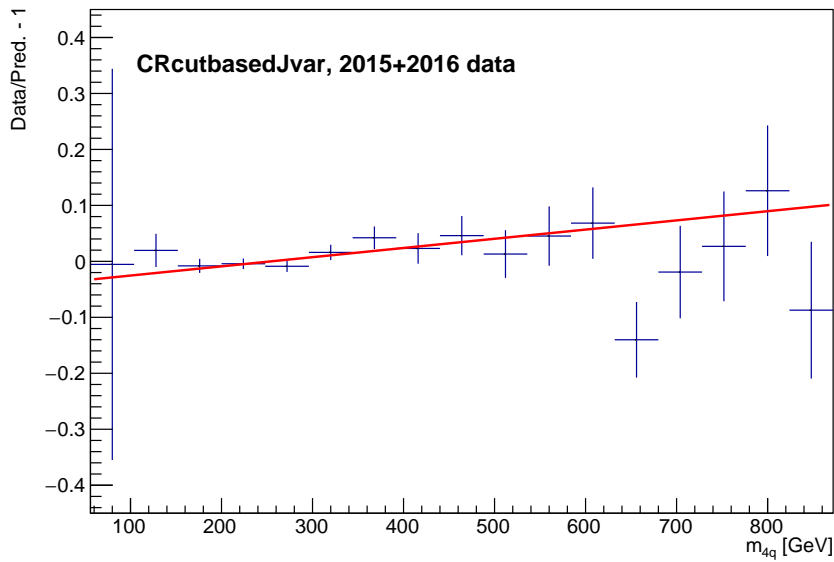


Figure 13.4: Ratio of data to background events for  $m_{4q}$ .



# 14 Fit model

*In this chapter, we will build our fit model, which we will fit to real data. We start by introducing the likelihood function with its statistical and systematic uncertainties. We will then first apply this fit model to the simulated data as well as real, blinded data to validate our model. With satisfactory results, we then apply the fit model to real, unblinded data and examine the model one last time. Actual results from the fit will be shown in the next chapter.*

## Contents

---

<b>14.1 The likelihood function . . . . .</b>	<b>141</b>
<b>14.2 Model inspection with Asimov . . . . .</b>	<b>143</b>
14.2.1 NP reduction campaign . . . . .	146
<b>14.3 Blinded model inspection with real data . . . . .</b>	<b>147</b>
<b>14.4 Model inspection with real data . . . . .</b>	<b>148</b>

---

The nominal, simulated backgrounds were shown against real data in Chap. 11. At that point, the expected sum of backgrounds was merely compared with data. In order to give proper expected upper limits on the production cross-section, the normalizations and shapes need to be estimated from data. These estimations are for instance  $Z$ +jets and  $t\bar{t}$  normalization factors derived from their control regions, which have been combined into one bin each; additionally, one sigma up and down variations of systematics (from detector, reconstruction, or theory) provide alternative shapes which can correct the simulated background towards data.

This is accomplished by the use of a fit model that encompasses all nominal as well as systematic information and has the flexibility to fit the simulated background to data within the boundaries given by the statistical and systematic variations.

The expected number of signal or background events is modeled by the Poisson distribution,

$$P(N|B) = \frac{e^{-B} B^N}{N!},$$

which gives the probability of observing  $N$  events given  $B$  expected background events.

To take normalization and shape systematics into account, each bin<sup>2</sup> must also be modeled by a probability density function (pdf). One can multiply the independent pdfs to form a pdf for the ensem-

<sup>2</sup>Or each event for unbinned fits.

ble. In general terms, the pdf will be of the form [157],

$$\text{PDF}(B|\theta) = \text{Poisson}(N|B) \prod_{i=\text{bins}} f(B_i|\theta),$$

where  $f(B_i|\theta)$  is a pdf for the expected background in bin  $i$  given the vector of systematic uncertainties  $\theta$ .

The observed number of events  $N$  is fixed to the real data recorded. Instead, the expected background events is varied until the probability calculated from the PDF is maximized. This is the maximum likelihood estimation. One constructs the *likelihood function* from the pdfs,

$$L(\mu|\theta) = \prod_{i=\text{bins}} \text{Poisson}[N_i | \mu S_i + B_i(\theta)] \cdot G(\theta),$$

where  $\mu$  is a parameter of interest apart from the systematics in  $\theta$  that scales the expected signal events  $S_i$ , and pdfs constraining the systematic uncertainties are multiplied on as  $G(\theta)$ .  $\mu = 1$  corresponds to the expected signal strength, and  $\mu = 0$  means no signal (ie. background-only) following the definitions in Tab. 14.1.

When the likelihood function has been maximized, the best *unconditional* estimate of  $\theta$  becomes  $\hat{\theta}$ . The *conditional* estimate is denoted  $\hat{\hat{\theta}}$  and is found by maximizing the likelihood with one or more parameters fixed ( $\mu$  in this case).

The likelihood value on its own has no meaning, but one can create a *test statistic* that is a quantification of the hypothesis testing using Wilks' theorem [158]. From aforementioned estimates, one can calculate the *profile likelihood ratio*<sup>1</sup> [157],

$$\lambda(\mu) = \frac{L(\mu|\hat{\hat{\theta}})}{L(\hat{\mu}|\hat{\hat{\theta}})},$$

where  $\lambda(\mu)$  has the property  $0 < \lambda(\mu) < 1$ . If the alternative hypothesis agrees with the null hypothesis, the value becomes 1.

This ratio is used to form the test statistic,

$$q_\mu = -2 \ln \lambda(\mu),$$

for values  $\mu \geq \hat{\mu}$ . This test statistic can be converted to a  $p$ -value:

$$p_\mu = \int_{q_{\mu,\text{obs}}}^{\infty} \text{PDF}(q_\mu|\mu, \hat{\hat{\theta}}) dq_\mu. \quad (14.1)$$

This test statistic is used to establish an upper limit on  $\mu$ , ie. by finding  $\mu$  for which  $p < 0.05$ . Since "inferior" experiments (large backgrounds, large uncertainties) can more easily reject a signal (see Fig. 14.1), a more robust measure is the modified frequentist confidence method,  $CL_s$  [159], which scales the signal+background probability by the background-only rejection,

$$CL_s = \frac{p_\mu}{p_0},$$

where  $1 - p_0$  is the  $p$ -value of the background-only hypothesis.  $p_0$  is calculated by setting  $\mu = 0$  in Eq. (14.1).

Hypo.	PDF
Null	$\text{Poisson}[N_i   B_i(\theta)]$
Alt.	$\text{Poisson}[N_i   \mu S_i + B_i(\theta)]$

Table 14.1: The null hypothesis assumes background only. The alternative hypothesis includes signal  $S$  with fitted strength  $\mu$ .

<sup>1</sup> Since  $\hat{\mu}$  can become negative, the denominator sets  $\hat{\mu} = 0$  for negative  $\hat{\mu}$ .

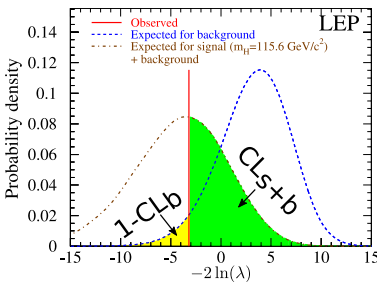


Figure 14.1: The pdfs for the signal+background (brown dot-dashed lines) and background-only (blue dashed lines). The observed value (vertical red line) in the middle of the signal+background distribution has excluded  $CL_b$  but not  $1 - CL_b$  (yellow area). If the two distributions overlap further, the experiment is less sensitive to new signals. Adapted from [159].

The  $p$ -value can be converted to a  $Z$  significance by reversing the one-sided  $p$ -value calculation of a unit Gaussian at  $Z$  standard deviations [160]:

$$Z = \Phi^{-1}(1 - p_0).$$

## 14.1 The likelihood function

The fit model is implemented in a custom framework built upon RooStats [161] and RooFit [162] that are included in the ROOT framework [150]. Minuit2 [163, 164] is used for the minimization of the likelihood function.

Uncertainties are added to the fit model as nuisance parameters (NPs). Shape and normalization systematics are constrained by either unit Gaussian or log-normal distributions. Statistical uncertainties are constrained by Poisson distributions. The floating normalizations for the  $Z$ +jets (named `norm_Z`) and  $t\bar{t}$  (`norm_tthbar`) backgrounds are constrained by their single-bin control regions. Note that the list of NPs have been reduced from the initial full list (cf. Sect. 14.2.1).

The likelihood function is a product of Poisson distributions in each bin with additional constraints from nuisance parameters:

$$L(\mu, \alpha, \theta \mid m_A, m_H) = \prod_{r=\text{regions}} \prod_{i=\text{bins}} \text{Poisson} \left[ N_{r,i} \mid \mu \times S_{r,i}(m_A, m_H, \theta) + B_{r,i}(\alpha, \theta) \right] \cdot G(\theta),$$

where

- $\mu$ , the parameter of interest, is a factor to the expected signal rate,
- $\alpha$  is a vector of floating scale factors for the  $Z$ +jets and  $t\bar{t}$  normalizations,
- $\theta$  is a vector of all NPs,
- $N_{r,i}$  is the number of observed events in bin  $i$  in region  $r$ ,
- $S_{r,i}$  is the number of expected signal events in bin  $i$  in region  $r$  for the mass hypothesis  $(m_A, m_H)$ ,
- $B_{r,i}$  is the number of expected background events (for all processes) in bin  $i$  in region  $r$ , and
- $G(\theta)$  is a product of the unit Gaussians that each constrain an NP.

$S_{r,i}$  is scaled to the integrated luminosity, cross-section times branching ratio and selection efficiency times acceptance.  $B_{r,i}$  is the sum of all simulated backgrounds but includes the scale factors for  $Z$ +jets and  $t\bar{t}$ .

The expected signal and background events in each bin are affected by the normalization and shape NPs. The process-specific normalizations naturally only affect the expected background. The product over the regions represents the signal region and the two single-bin control regions that aid in constraining the floating background normalizations.

The NPs additional to the experimental systematics are listed in Tab. 14.2. The data-driven uncertainties for the background modeling were made for the sum of all backgrounds and covered in Sects. 11.1 and 13.3.

<sup>1</sup>This reference is an internal document.

<sup>2</sup>This method has been used in previous analyses to extrapolate estimations to additional jets.

The diboson uncertainties are derived in Ref.<sup>1</sup> [165] under similar kinematic conditions. They find an uncertainty of approximately 20%. To account for the two additional jets of this analysis, the uncertainties are increased by adding 25% in quadrature for each additional jet<sup>2</sup>. With the two additional jets, the diboson systematic uncertainties are about 50% uncertainty. The uncertainty for single-top cross-section is 20% based on Ref. [166]. However, these backgrounds are very small, so the precise sizes of the uncertainties matter little.

The fit model is rather complex and includes a fair number of bins and a large number of NPs. To speed up and stabilize the fitting procedure, NPs that contribute very little are automatically pruned away before the minimization step. The level of contribution is quantified by requiring that at least one systematic bin deviates from the nominal by 1%, among others. "One-sided" NPs only have one variation. These are symmetrized to have equal but opposite up and down variations before the minimization step.

Some NPs, though especially JER and JES, can have large statistical fluctuations due to a limited number of simulated events, and that can lead to non-parabolic shapes near the likelihood extremum. This can be partly mitigated by the act of *smoothing*. The default smoothing algorithm works on the ratio between the nominal histogram and each systematic histogram and will combine the extremum bin with the smallest  $\chi^2$  between the nominal and systematic values in that bin with its right neighbor iteratively until 3 extrema remain. The signal systematics (e.g. shape and normalization systematics from the interpolation), the four EL\_EFF systematics, and the mismodeling systematics are never smoothed.

To maximize signal significance, a custom automatic rebinning method is employed as follows. The peak of the interpolated signal is identified and its bin value is saved; bins for the sum of the simulated backgrounds are likewise saved. The bins to the side of the peak, starting on the left and switching side at every step, are then added to the sum until all of the following criteria are met:

- the sum reaches at least 68.3% of the total signal yield,
- the error on the sum of background bins in the same interval is less than 30%, and
- the summed bins span at least 10 GeV.

Starting with the first non-zero background bin from the left, bins are combined until the error on the combined bins is less than a tolerance level and span at least 10 GeV. The tolerance is defined as 7 times the relative error on the full background (though max. 20%). This is repeated until the bin contained in the combined signal peak is reached. The same is done for bins starting at the first non-zero background bin from the right. Finally, bins, starting at the first bin, with 0 background are removed, until a bin with a non-zero value is met. The same is done for bins starting at the last bin.

Process	Parameter name	Description	Value	Effect
All	PtV	$p_T^{\ell\ell}$ shape correction	-	Shape
	Jet0pt	$p_T^{\text{lead jet}}$ shape correction	-	Shape
	Mqqqq	$m_{4q}$ shape correction	-	Shape
Z	norm_Z	Z+jets normalization	Floating	Norm
Top	norm_ttbar	$t\bar{t}$ normalization	Floating	Norm
	stopWtNorm	$tW$ normalization	20%	Norm
	stopsNorm	single top $s$ -channel normalization	20%	Norm
Diboson	WWNorm	WW normalization	50%	Norm
	ZZNorm	ZZ normalization	50%	Norm
	WZNorm	WZ normalization	50%	Norm
Signal	TheoryScaleAcc_signal	QCD scale variation	1.5%	Norm
	TheoryTuneAcc_signal	Tune variation	3%	Norm
	TheoryPDFAcc_signal	PDF variation	$2.1 + 0.70 \times \frac{m_A}{100 \text{ GeV}} [\%]$	Norm

Table 14.2: Nuisance parameters in addition to the experimental systematics, which were provided in the previous chapter (ie. Tab. 13.2).

## 14.2 Model inspection with Asimov

The Asimov dataset, first formalized in Ref. [160], is created from the simulated background. Instead of performing many Monte Carlo simulations to estimate the fit model's uncertainty when applied to the simulation, the model can be fit on the Asimov dataset, which is created from the sum of the nominal simulated backgrounds. The uncertainties on the model parameters can be estimated from this fit in the asymptotic limit, although the assumption is found to be valid even for somewhat small datasets [160].

Pull<sup>1</sup> plots for the NPs entering the fit are shown in Fig. 14.2 for three representative mass points and App. 19.D for the remaining mass points. The boxes in the pull figures show the significance of each pull. Due to lack of numerical accuracy, pulls that constrain extremely little might have large uncertainties, leading to fake large significances.

NPs are ranked by fixing them at their positive or negative one-sigma values one at a time and noting the difference on  $\mu$ . Fits leading to large  $\Delta\mu$  show large *impact* on the fit. Fig. 14.3 shows the impact (blue bars; upper horizontal axis) for the 25 impact-leading NPs as well as their pulls (black points; lower horizontal axis), which were shown in the previous figure. The yellow band shows the "pre-fit" impact by scaling the post-fit impact with the inverse of the pull. The NPs are ordered by the sizes of their post-fit impacts.

The rank plots shows the absolute change on the signal strengths. Tab. 14.3 shows the relative uncertainties on  $\hat{\mu}$  from the leading sources of systematic uncertainty for two mass points. Uncertainties having the largest impact depend on the choice of  $(m_A, m_H)$ . However, the jet energy scale and resolution clearly dominate the uncertainty. They are followed by simulation statistics and the systematic uncertainties derived for the background mismodeling.

<sup>1</sup> Defined as the fitted value subtracted from the initial value and divided by the uncertainty on the fitted value.



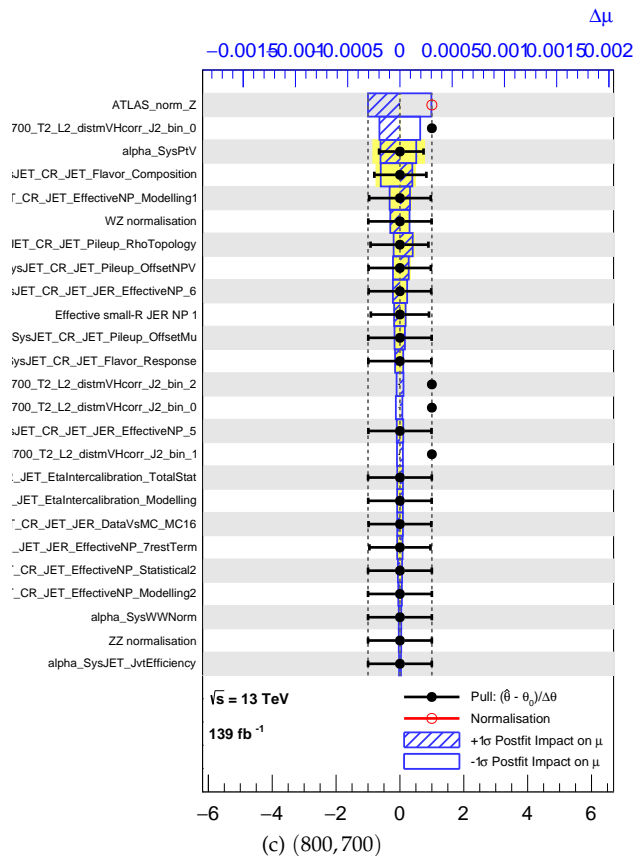
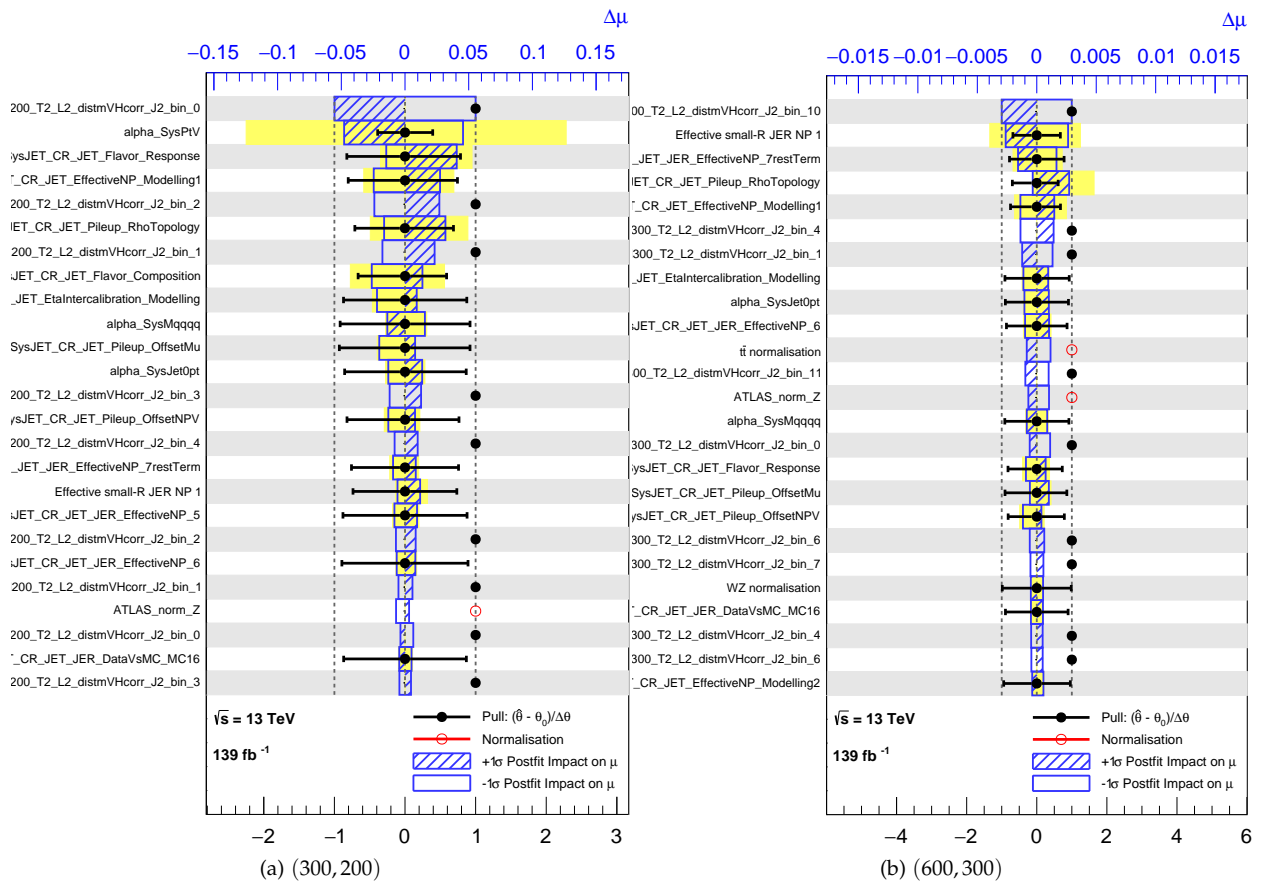


Figure 14.3: The post-fit ranking of the nuisance parameters used in the Asimov fits for the signals (a) (300,200), (b) (600,300), and (c) (800,700).

Table 14.3: The effect of the most important sources of uncertainty on  $\hat{\mu}$  at two mass points, (500,300) and (700,200). The signal cross-sections are taken to be the expected median upper limits and they correspond to values that are shown on the table next to the indicated mass points. "Sim. stat." stands for simulation statistics, "Sig. interp." for signal interpolation, and "Bkg. model." for the background modeling. "Theory" refers to the theoretical uncertainties on signal due to scales, tune, and PDF.

(500,300), 0.70 pb		(700,200), 0.38 pb	
Source	$\Delta\hat{\mu}/\hat{\mu}$ [%]	Source	$\Delta\hat{\mu}/\hat{\mu}$ [%]
Data stat.	32	Data stat.	33
Total syst.	42	Total stat.	38
Sim. stat.	24	Sim. stat.	19
Sig. interp.	14	Sig. interp.	12
Bkg. model.	14	Bkg. model.	16
JES/JER	30	JES/JER	23
Theory	6.5	Theory	7.6

### 14.2.1 NP reduction campaign

The production of the final histograms using all relevant systematics (including all years and all backgrounds) took initially  $\mathcal{O}(\text{weeks})$ . To reduce the production time, a single production was made using only real and simulated data from 2015+2016 including all systematics. The systematics were ranked according to their impact on the final limit for all simulated signals. Then a number of leading systematics for each simulated signal were selected, and a union of these was chosen as the set of systematics that will be used for future productions. An important criterion for selection process was that the final limit would be insignificantly affected. It was decided that a change of  $\mathcal{O}(1\%)$  in the limit, much less than the statistical uncertainty, would be tolerable.

During this campaign, a different number of leading systematics were tested. In the end, it was decided to use the union of the 15 leading systematics of each simulated signal<sup>1</sup>. The pruned list gives a difference of approximately 1 percent (or much less) in the final limit for most signals. The final list of systematics chosen was check-marked in Tab. 13.1, and the impact of this reduction is shown in Tab. 14.4.

With the pruned systematics, reduced number of backgrounds (cf. Sect. 8.1), and optimizations in the code, the full production was reduced to  $\mathcal{O}(\text{days})$ .

<sup>1</sup> The size of this final set is larger than 15.

$m_A$	$m_H$	All	Pruned	Rel. diff.	Stat. only
300	200	0.2163	0.2134	1.35%	0.0808
350	250	0.1119	0.1103	1.43%	0.0580
400	200	0.1028	0.1019	0.93%	0.0579
400	300	0.0560	0.0560	0.02%	0.0360
500	200	0.0693	0.0684	1.27%	0.0375
500	300	0.0473	0.0473	0.02%	0.0349
500	350	0.0421	0.0420	0.10%	0.0317
500	400	0.0209	0.0208	0.33%	0.0181
600	200	0.0324	0.0317	2.36%	0.0234
600	300	0.0308	0.0307	0.41%	0.0243
600	400	0.0186	0.0186	0.13%	0.0159
600	480	0.0128	0.0127	0.75%	0.0105
700	200	0.0166	0.0165	0.61%	0.0140
700	500	0.0097	0.0097	0.11%	0.0086
800	200	0.0113	0.0113	0.18%	0.0102
800	300	0.0129	0.0129	0.03%	0.0115
800	500	0.0073	0.0073	0.02%	0.0067
800	600	0.0061	0.0061	0.05%	0.0056
800	700	0.0052	0.0052	< 0.01%	0.0047

Table 14.4: The final limits for the fit model including all or a reduced list of systematics. "All" contains all systematics except for the modeling systematics, which were finalized later in the analysis. "Pruned" contains the NPs with checkmarks in Tab. 13.1. Limits with no systematics at all (stat. only) are shown for comparison.

### 14.3 Blinded model inspection with real data

To get a better understanding of the NPs, real data in the SR at Level 2 (before any  $m_{4q}$  window) has been fitted using a background-only assumption. The calculated limits and significances will not be observed. The fits are made using different lower bounds for  $m_A$  to show the stability of the fits for higher masses; for a choice of  $m_H$ , the lower bound of  $m_A$  is set to  $m_H + 90$  GeV. These lower bounds are also used in the final fits. The pull plots can be found in Fig. 14.4.

In making these fits, two major changes to the analysis have been made:

- An alternative smoothing algorithm is used because the standard smoothing algorithm was not effective or aggressive enough in smoothing fluctuations in the smaller NPs
- A number of NPs have had their variations symmetrized by averaging up and down because they were pulled or constrained strongly (even after switching smoothing algorithm):
  - MUON\_SAGITTA\_RESBIAS
  - JET\_CR\_JET\_Pileup\_RhoTopology
  - JET\_CR\_JET\_Pileup\_OffsetNPV
  - JET\_CR\_JET\_Pileup\_PtTerm
  - JET\_CR\_JET\_Pileup\_OffsetMu
  - JET\_CR\_JET\_EffectiveNP\_Mixed1
  - JET\_CR\_JET\_EffectiveNP\_Modelling1
  - JET\_CR\_JET\_EtaIntercalibration\_Modelling
  - JET\_CR\_JET\_BJES\_Response

- JET\_CR\_JET\_Flavor\_Composition
- JET\_CR\_JET\_Flavor\_Response

The alternative smoothing algorithm is based on the Nadaraya–Watson kernel regression estimate [167, 168] and applied on the ratio between each systematic histogram and the nominal histogram. Before applying the smoothing algorithm, the bins of each systematic histogram is combined so as to have at most 5% uncertainty each. The "box" kernel is used. The kernel bandwidth parameter is estimated from the average of the bandwidth parameters that, after smoothing, give the smallest  $\chi^2$  difference per bin, where the bin itself has been interpolated by the kernel.

#### 14.4 Model inspection with real data

The signal has been interpolated in 10 GeV steps in the range  $200 < m_H < 700$  and  $m_H + 100 < m_A < 800$  GeV. This gives 1326 signal regions.

See Figs. 14.5 and 14.6 for the pull plots and NP ranks of four representative mass points. App. 19.E contains post-fits, pull plots, and ranks for the remaining mass points. The NPs are not much pulled overall, and they also show little bias. The data-driven background modeling systematics do show rather large pull in several cases.



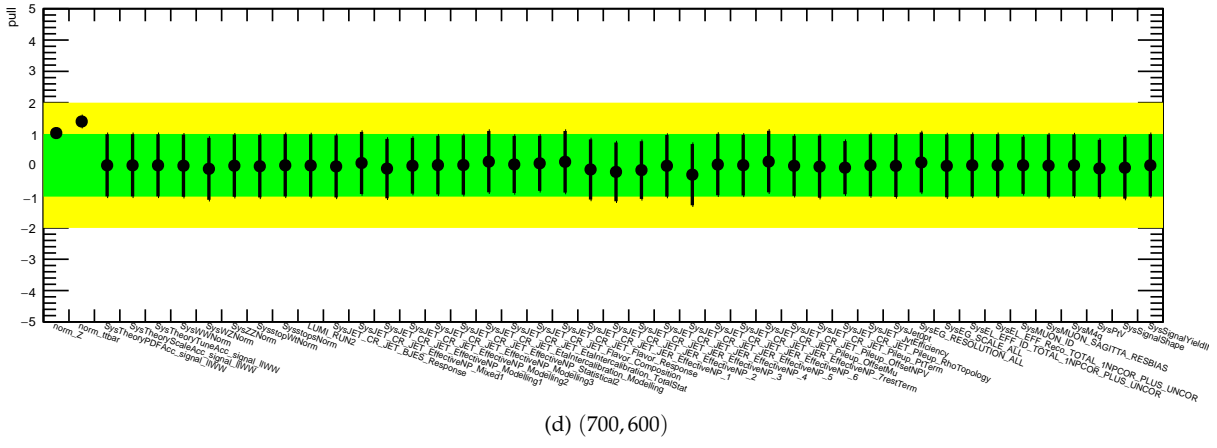
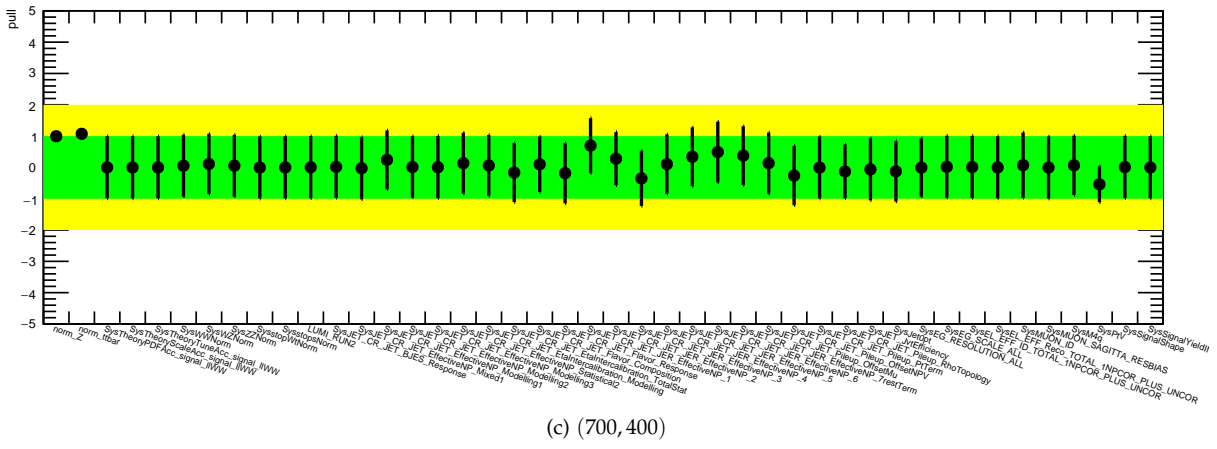
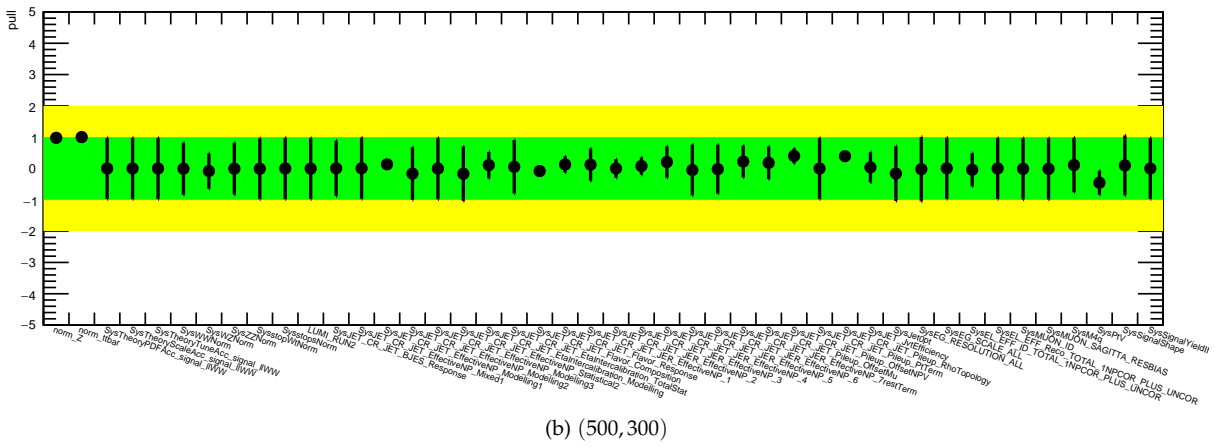
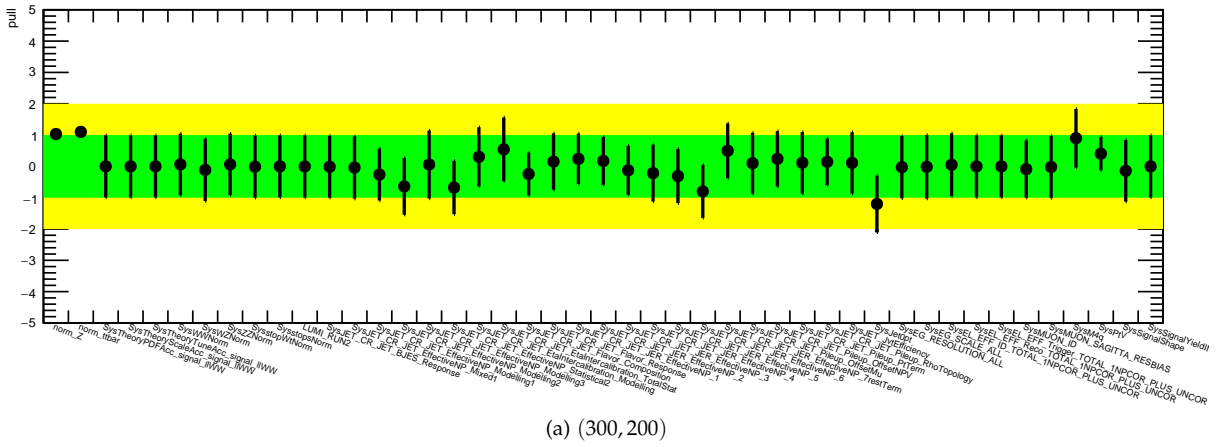


Figure 14.5: The unblinded pull plots.





# 15 Results

The fit model was examined in the previous chapter, and the NPs were found to be mostly reasonable, that is to say we saw few cases of very biased or very constrained or pulled NPs. We can now with confidence examine the post-fit plots of the mass distribution and derive upper limits on the production cross-section of our theoretical particles in the case of no discovery. This chapter will show these results in the narrow-width and large-width cases separately and finally set exclusions on parts of the phase space of the 2HDM type-I introduced in Sect. 1.2, given that we know the theoretical cross-sections and branching ratios.

## Contents

---

<b>15.1 Large-width and 2HDM limits . . . . .</b>	<b>157</b>
---	------------

---

As mentioned in Sect. 14.4, the signal was interpolated in 10 GeV steps in the range  $200 < m_H < 700$  and  $m_H + 100 < m_A < 800$  GeV yielding 1326 SRs in 51  $m_{4q}$  windows. The limits, given as

$$\sigma^{AZH} = \sigma(gg \rightarrow A) \times \text{BR}(A \rightarrow ZH) \times \text{BR}(H \rightarrow WW)$$

in picobarn, and their  $p$ -values, given by Eq. (14.1), have been calculated and will be shown in 2D as a function of the  $H$  and  $A$  masses for the signal hypotheses. The limits will also be shown in 1D in slices of  $m_H$ . Signals shown in this chapter are scaled such that  $\sigma^{AZH} = 1$  pb.

Before showing the final results, some intermediate background-only post-fit figures for  $m_{4q}$ ,  $J$ ,  $p_T$  of leading jet, and  $p_T^{\ell\ell}$  will be shown for the SR at Level 2 (after the  $J$  selection but before any  $m_{4q}$  window), except  $J$  that will be shown at Level 1. The fits have been done in the same way except the side-band region is not (ie. cannot be) included. The post-fit of  $m_{4q}$  must agree well with data so as not to introduce any bias for some signal hypotheses. Fig. 15.1a shows extremely good agreement.  $J$  was used to remove background, and its pre-fit modeling at high values did show some disagreement. As can be seen in Fig. 15.1b, the post-fit shows good agreement. The two momenta in Figs. 15.1c and 15.1d were used to correct some of the pre-fit mismodeling and introduce systematic uncertainties that the likelihood fit could use to correct the remaining mismodeling.

Background-only fits to data in the SR at Level 3 using both control regions are shown in Figs. 15.2a–15.2d for four representative signal hypotheses. Fig. 15.2e shows the most significant (defined in a moment) signal hypothesis. The figures contain the post-fit expected

background and the observed data with each a signal hypothesis. App. 19.E contains post-fits, pull plots, and ranks for the remaining mass points for which signal was simulated.

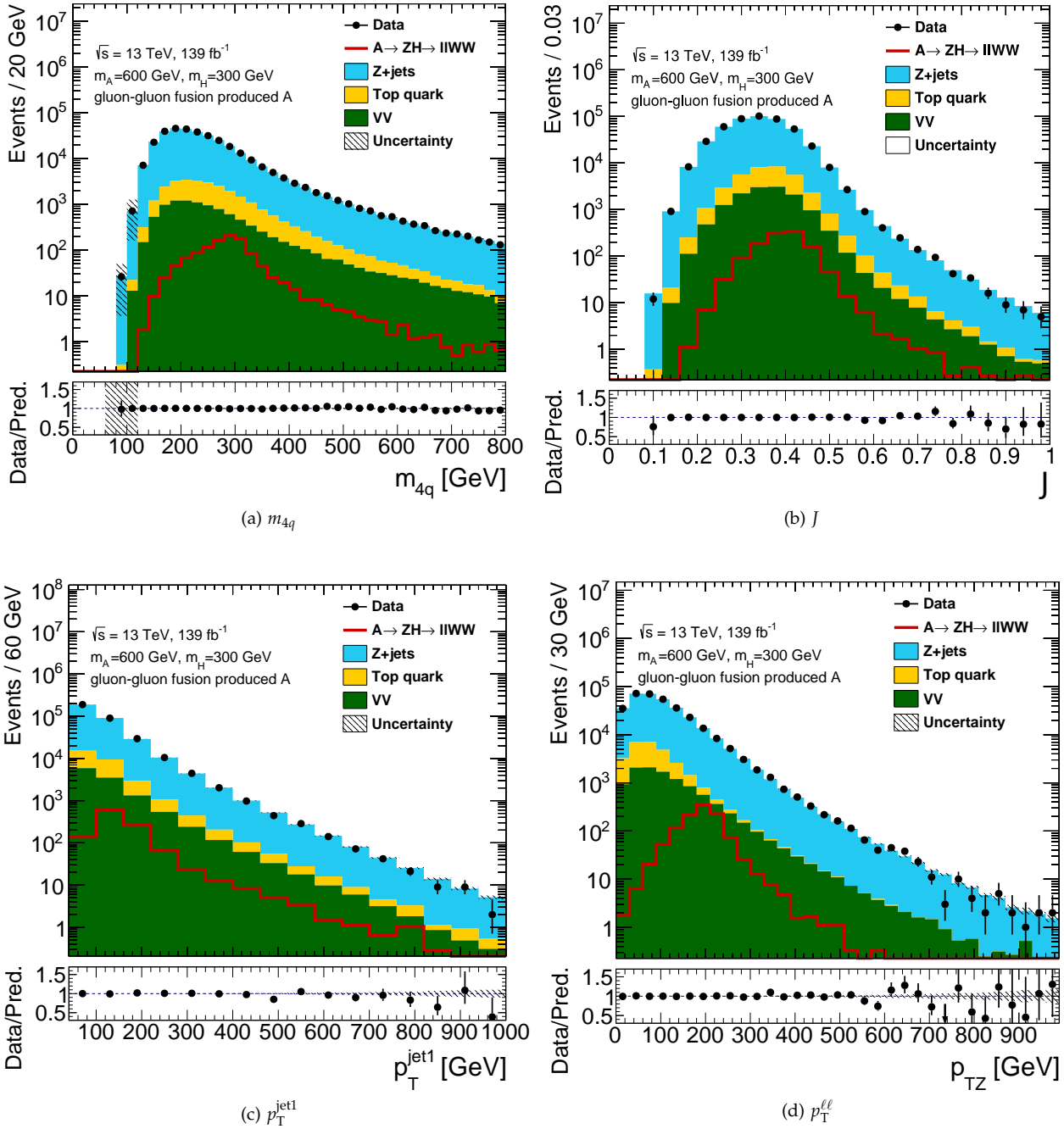


Figure 15.1: Post-fit plots in the SR at Level 2 (except for (b) that is at Level 1) of (a) the mass  $m_{4q}$  of the  $H$  candidate, (b) the  $J$  variable, (c) the  $p_T$  of the leading jet, and (d) the  $p_T$  of the  $Z$  candidate.

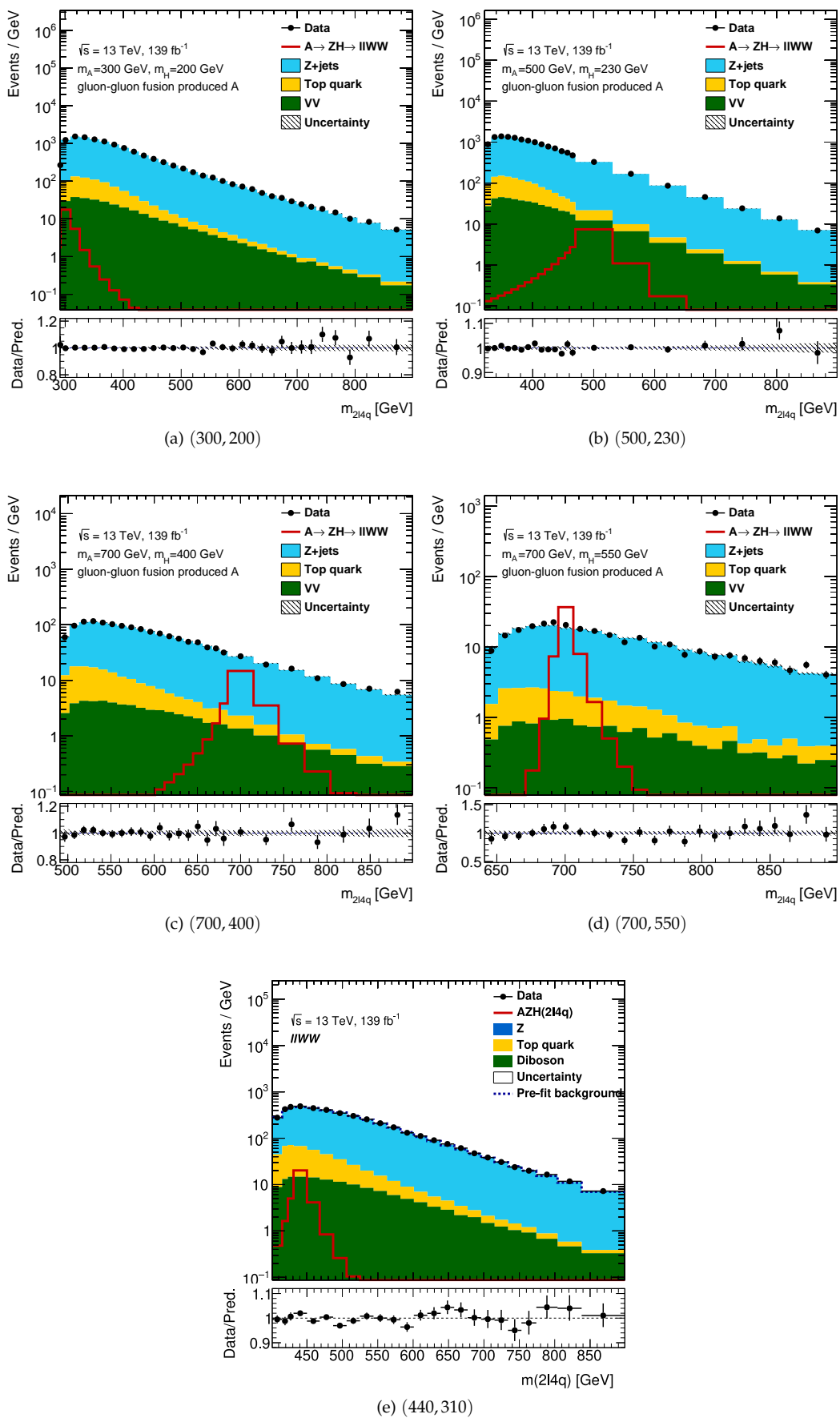


Figure 15.2: (a-d) The post-fit plots for four representative signal hypotheses. (e) The post-fit plot for the (440,310) signal hypothesis with local significance at 2.9 sigma.

The fits have then been done on the combined signal and background. No excess above 3 sigma has been observed; the largest local (global) deviation is 2.9 (0.82) sigma at (440, 310). The global significance has been calculated from the largest up-crossing [169] of 15 at  $m_A = 750$  GeV in Fig. 15.4d. The upper limit varies from 8.9 pb (3.6 pb expected) for the (340, 220) signal hypothesis down to 0.023 pb (0.041 pb expected) for the (770, 660) signal hypothesis.

The limits are shown in slices of  $m_H$  in Fig. 15.3 in the usual "Brazil bands" for the narrow-width signals. The large-width signals without error bands are shown as well, and they will be further discussed in the next section. See Fig. 15.3c for the 1D limit slice hosting the mass point, whose post-fit mass was shown in Fig. 15.2e. See App. 19.F for the remaining slices. For low  $m_H$  ( $m_H < 300$ ), the observed narrow-width limits dip below the expected at around  $m_A = 430$  GeV and then consistently overshoot after  $m_A = 560$  GeV. This overshooting disappears for slices  $m_H = 250$  GeV and higher. However, the dip is visible in some fashion relative to the original position up to  $m_H = 370$  GeV.

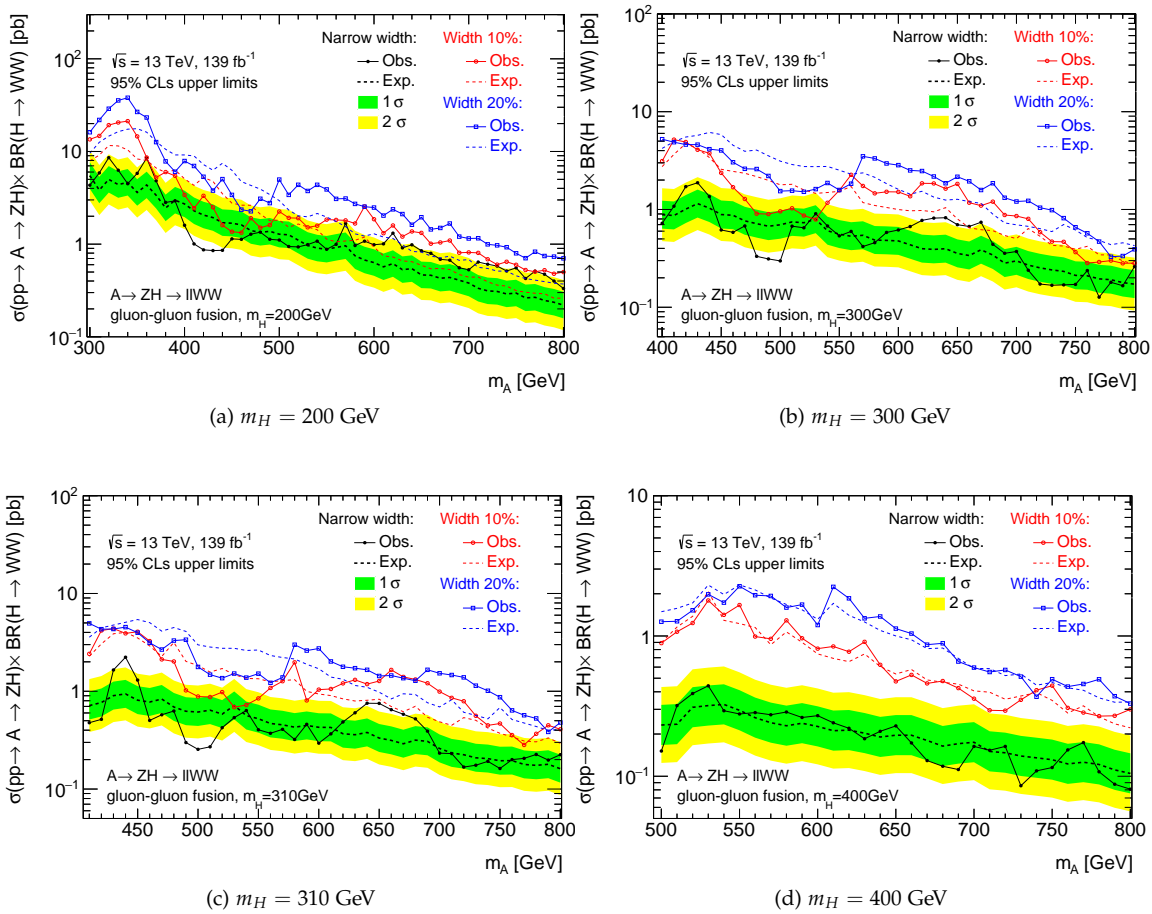


Figure 15.3: The limits on the production cross-section times branching ratios for  $A$  in  $m_H$  slices of 200, 300, 310, and 400 GeV, respectively. The  $m_H = 310$  GeV slice hosts the largest deviation at  $m_A = 440$  GeV.

The limits for all 1326 signal hypotheses are drawn in a 2D histogram (each bin representing an SR) in Fig. 15.4, which includes the significances of these limits. Figs. 15.4a and 15.4b respectively show

the expected and observed 95% upper limits. The uncertainties on the limits are not shown in the 2D figures, and the reader may refer to the previous 1D slices or the  $p$ -values in Fig. 15.4c. As noted earlier, no excess above 3 sigma is observed, and the observed data can be considered consistent with the background-only hypothesis.

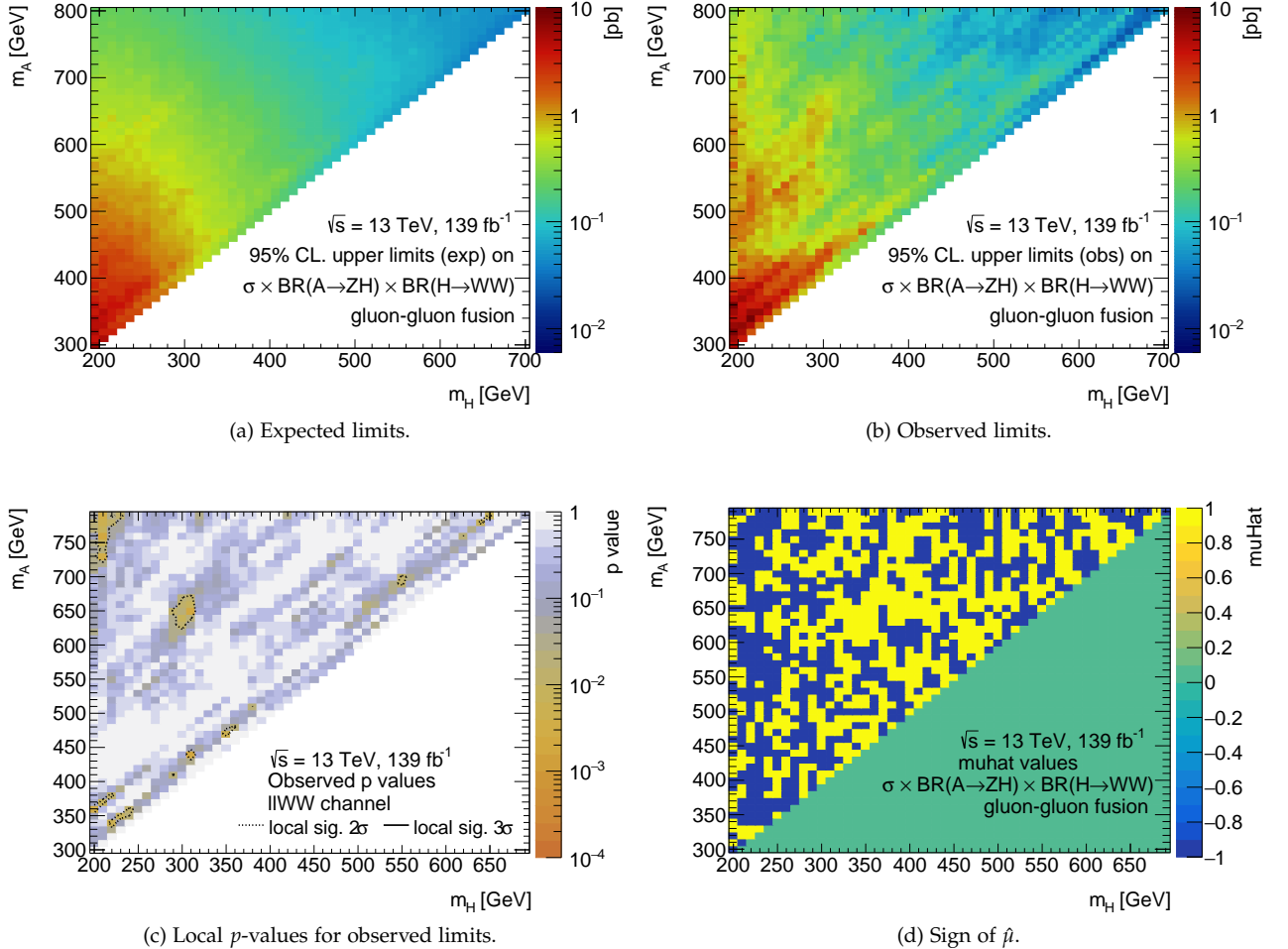


Figure 15.4: (a) The expected limits for  $A$  and  $H$ . (b) Observed limits. (c) The local significances of the observed limits. (d) The sign of  $\hat{\mu}$  for every signal hypothesis, which is used to calculate the number of up-crossings.

## 15.1 Large-width and 2HDM limits

Before showing results in the 2HDM interpretation, a benchmark with fixed large widths is made. The limits for signals with 10% and 20% widths are shown in Fig. 15.5 in 2D and was shown in Fig. 15.3 for different  $m_H$  slices. The dip and overshoot seen for narrow-width signals are also visible for the large-width signals. As the width of  $A$  increases, a decrease in the signal significance is to be expected, which can be seen as higher upper limits for the large width signals. The local deviations are 0.68 sigma and 0.74 sigma at (440, 310) for 10% and 20% width signals, respectively.

The observed data is now interpreted in the type-I 2HDM model using the setup and settings described in Sect. 1.2 to derive the theoretical production cross-sections, branching ratios, and  $A$  widths. Due

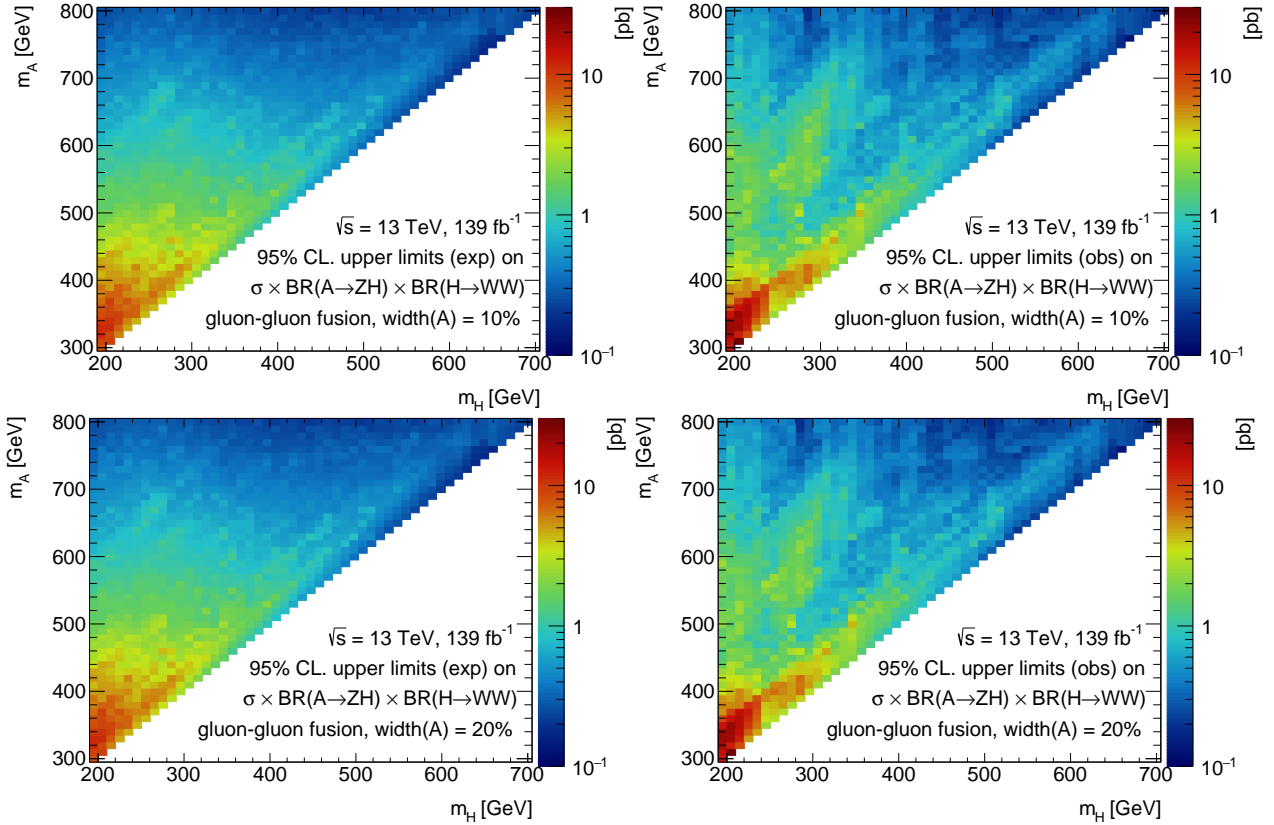


Figure 15.5: Left column: The expected limits for  $A$  and  $H$ . Right column: Observed limits. Top row: Signals of 10% width. Bottom row: Signals of 20% width.

to the analysis searching for off-alignment signals, the at-alignment constrain  $\cos(\beta - \alpha) = 0$  cannot be applied. Instead, the results will be shown as a function of  $\cos(\beta - \alpha)$  and  $m_A$  in slices of  $\tan \beta$  and  $m_H$  in Fig. 15.6. The dip and overshoot are visible in the exclusion figures, especially for  $\tan \beta = 0.5$ , as respective observed exclusions around 430 GeV in the about 2 sigma band of the expected exclusions and no observed exclusions for higher  $m_A$  where there was expected exclusion. The majority of the parameter space that the analysis is sensitive to is already excluded by previous ATLAS analyses [25] (cf. Fig. 1.8b). Since the lepton-specific type is identical to type-I in the quark sector, these results apply to the former model as well for the given  $\tan \beta$  slices<sup>1</sup>. As this analysis has not included  $b$ -associated production, which is important to type-II and the flipped type, no exclusions are provided for these models.

<sup>1</sup> For larger values,  $H \rightarrow \tau\tau$  takes over.

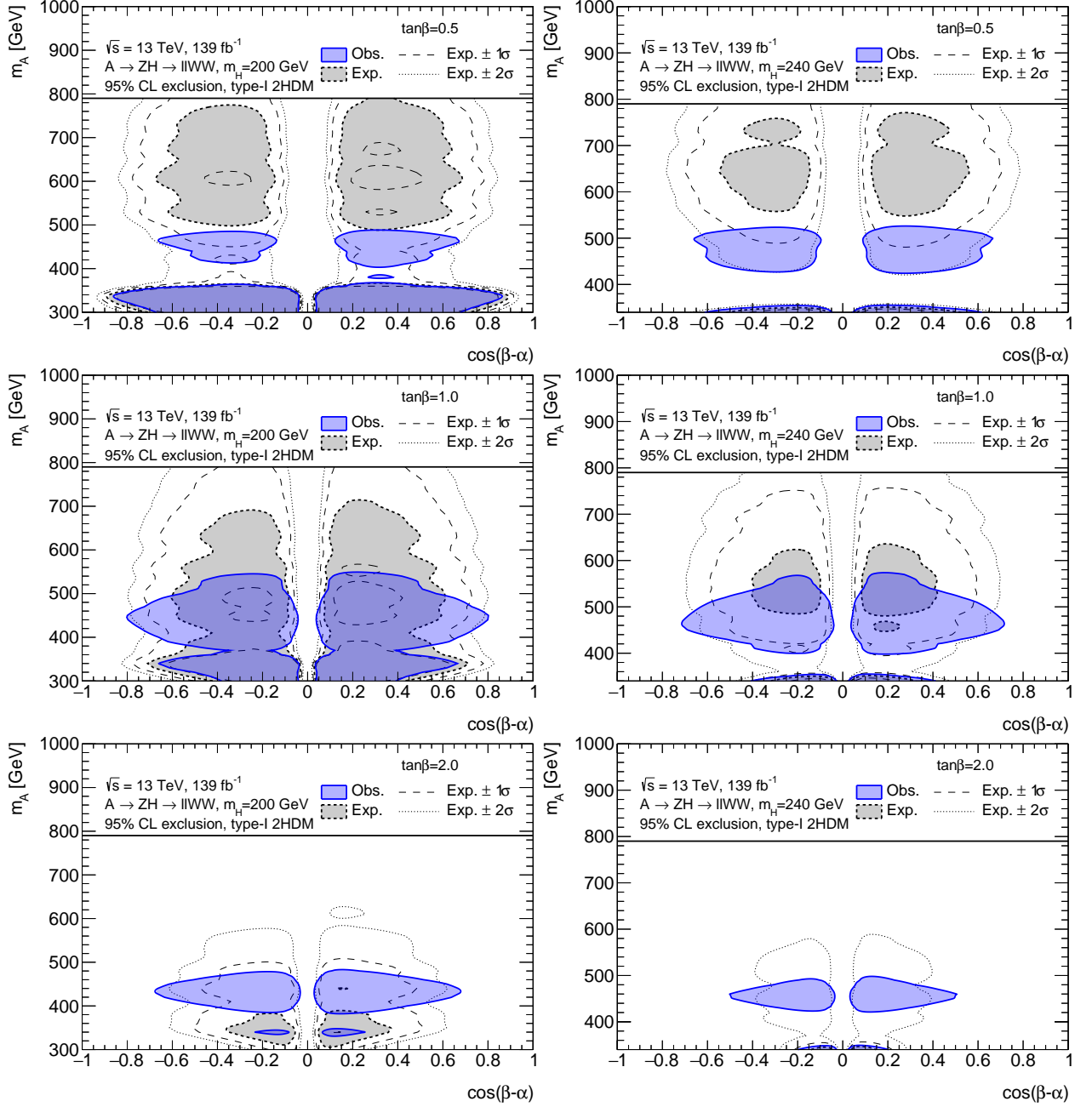


Figure 15.6: The expected and observed exclusion limits for  $m_A$  as a function of  $\cos(\beta - \alpha)$  for three  $\tan\beta$  slices (values 0.5, 1.0, and 2.0 for the rows from top to bottom) for  $m_H = 200$  (left column) and 240 GeV (right column). Only type-I is shown, since the analysis has insignificant sensitivity to other types.



## 16 Discussion

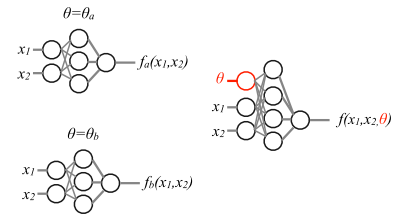
The analysis has been completed, and we have set exclusions on the type-I 2HDM model. We will discuss some issues that were stumbled upon during the analysis work.

The analysis is a second iteration that now uses the full Run 2 data as well as a second channel that covers 2HDM models away from alignment. The  $\ell\ell b\bar{b}$  channel has no further sub-channels and therefore selects directly the two leptons and  $b$ -tagged jets. The  $\ell\ell WW$  channel presented in this analysis has to reconstruct the  $W$  bosons from their decay products. The branching ratios are about one-third to leptons and two-thirds to hadrons [73]. Therefore, fully leptonic  $WW$  decays happen in about 10 percent of decays, while branching ratios for fully-hadronic and semi-leptonic are about 45 percent each. At the start of the analysis, the  $\ell\ell WW$  channel originally contained both the fully-hadronic and the semi-leptonic sub-channels in order to cover the about 90 percent of the branching ratios. While the sensitivity of the fully-hadronic channel is affected by the size of the hadronic background, the semi-leptonic decay loses sensitivity due to the one neutrino. The lost sensitivities would be somewhat regained by employing the parameterized neural network (pNN) [170] that has been implemented by other analyses [171, 172].

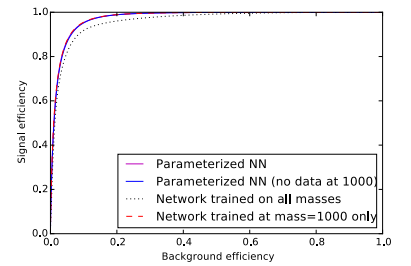
Possible improvements considered but not used in the analysis in this iteration are listed below. These can also be seen as suggested alleys of improvement for future analyses.

*Use of machine learning to remove background* Actually, a working pNN model has been trained and evaluated on nominal simulated data for this analysis, mostly in the  $\ell\ell b\bar{b}$  channel. A pNN is a neural network (NN) that incorporates the context into its feature set; in this case, the network is parameterized by the signal masses  $m_A$  and  $m_H$ , which are added along side the input features as shown in Fig. 16.1a. The masses of all the input signal samples are added to a histogram from which random values are sampled and added to the background in order to remove any false discriminatory power on the signal masses themselves. The end result is a single network with the same power as NNs trained on individual mass points with the additional powerful ability to interpolate to unseen mass points. An example of the power of interpolation is shown in Fig. 16.1b.

For the architecture of the pNN in this analysis, the network is



(a) Neural network with contextual features

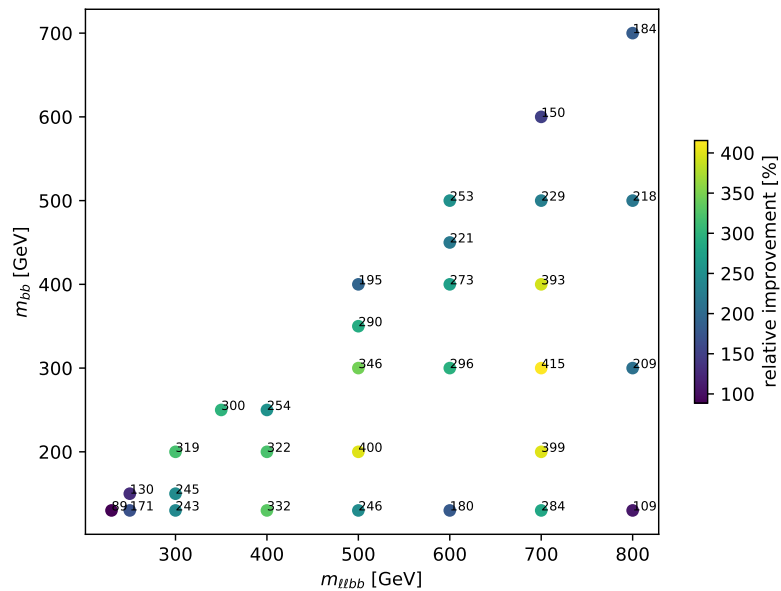


(b) Performance of pNN vs regular NN

Figure 16.1: (a) Individual regular NNs that are separately trained on sets of data with  $\theta = \theta_a$  and  $\theta = \theta_b$  can be combined into a single NN trained on the full set with  $\theta$  as an input feature. (b) The ROC curves for a regular NN trained only on a single mass point and pNNs that are trained on either the full set or the full set except for the single mass point, thereby forcing it to interpolate. The performance is identical between all three cases. Both from [170].

constructed by 5 layers of 800 nodes each with the ReLU activation function and 20 percent dropout after each layer. The output layer is one node with a sigmoid function. The binary cross-entropy is used to calculate the loss, and the model is optimized by use of the stochastic gradient descent. The model has been trained with a batch size of 128 for 30 epochs. The input features are the kinematic variables  $p_T$ ,  $\eta$ , and  $\phi$  for the two leptons and three leading jets as well as the reconstructed  $m_{bb}$ ,  $m_{\ell\ell bb}$ , and  $m_{\ell\ell bb}^{\text{COR}}$  and the simulated masses  $m_A$  and  $m_H$ . The performance of the pNN model is evaluated by the significance (cf. Eq. (10.10)) calculated using wide bins of signal and background to emulate the binning mechanism presented in Sect. 14.1. For each simulated signal, the selection on the pNN score that yields the largest significance is used. Fig. 16.2 shows the relative improvement in the significance after applying the most significant selections on the simulated  $\ell\ell bb$  signals; the expected significance would be at least about 2 times higher compared to the combined  $J$  selection and  $m_{bb}$  window.

Figure 16.2: The relative improvement in significance when selecting signal events using the pNN compared to the combined  $J$  selection and  $m_{bb}$  window in the  $\ell\ell bb$  channel.



Unfortunately, due to time constraints, the pNN could not be included in later stages of the analysis, and so the actual improvements remain to be seen<sup>1</sup>.

<sup>1</sup> However, several analyses reported similarly positive results with pNNs at the ATLAS Exotics + HDDBS Workshop 2019, which ATLAS members can find at <https://indico.cern.ch/event/801402/>.

*Issues with jet combinatorics* The fully-hadronic  $\ell\ell WW$  sub-channel has four jets in the final state, which need to be selected correctly among the pileup jets. The simplest signal selection would be to choose the 4  $p_T$ -leading jets in the event. The more advanced technique presented in this analysis deals with the combinatorics of selecting jet pairs from each  $W$  boson. As stated in Chap. 10, the advanced technique is better for every mass point. However, the solution is not elegant and suffers from several issues, some of which

were mentioned in Sect. 10.2.2. The "correct combinations" were determined using the "base selection" in the iterative method in Sect. 10.2.1 instead of using proper truth-matching. This is in part due to the lack of the necessary truth particles in the CxAOD files, insufficient truth information saved on the reconstructed objects (ie. only the absolute value of the PDG ID is saved!), and finally because truth-matching (using the available information) for the lower masses proved difficult. Instead of parameterizing the three variables  $\Delta R(W_1)$ ,  $\Delta R(W_2)$ , and  $H_2$  in  $f(m_A, m_H)$ , their windows could be derived from fits to errors bars drawn in 2D histograms. The methodology itself could also be changed from making windows from the 95% error bars to windows that are optimized by use of selections that maximize significance as was done for the  $J$  and  $m_{\ell\ell}$  optimizations. The analysis considered only the 5  $p_T$ -leading jets in the event, and more careful combinatorics resolutions could include more jets.

Actually, before the  $\ell\ell WW$  signal samples used in this analysis were generated, three representative samples had been made to gauge the efficacy of the channel. These three samples were included in a simple boosted decision tree (BDT), which used correct combinations as signal and wrong combinations as background. The BDT was not included in the analysis, as it was difficult to evaluate its performance. With the full list of datasets available, a proper machine learning algorithm that deals with combinatorics must be considered, possibly even as part of the pNN.

*Background modeling* The issues of background modeling have been covered well. Here follows additional thoughts. The  $p_T$  mismodeling seen for the  $Z$ +jets samples depends strongly on the number of jets in the event. For fewer than 4 jets with  $p_T > 20$  GeV, little mismodeling is seen. Events with 5 jets show significantly greater mismodeling compared to events with 4 jets, and this mismodeling worsens for higher multiplicity. The correction applied to the  $p_T^Z$  distribution has been inclusive in the number of jets. While the new generation of  $V$ +jets samples will likely show better modeling, the mismodeling can be better corrected if the correction is done exclusively per number of jets. The modeling of the  $J$  variable was not corrected, even as higher values showed mismodeling outside the systematics band. The variable was corrected in the  $\ell\ell bb$  channel. After the fit to data, post-fit figures of  $p_T^Z$  and  $J$  did show little disagreement between real data and simulation, but finding and correcting the mismodeling in these variables before fitting would be preferable.

*Limited scope* The  $\ell\ell WW$  channel unfortunately only contained the ggA production. Had there been additional personpower available for the channel, the bbA production mechanism could have been included, and the results could have been interpreted in the type-II as well.

The fully-hadronic channel for  $H \rightarrow ZZ$  was not included even though this would likely not add much work given the similarity

to  $WW$ . Actually, the  $H \rightarrow WW$  signal efficiency could have been adjusted by examining the contamination from a few representative  $H \rightarrow ZZ$  without running the full analysis on many  $H \rightarrow ZZ$  samples. The exclusions are therefore slightly conservative in this regard.

*Summary* To summarize the experiences with the  $\ell\ell WW$  channel, a future iteration on this analysis should:

- Include the semi-leptonic channel,
- lower minimum  $H$  mass from the current 200 GeV,
- use the pNN for selection,
- as well as, following Tab. 14.3 in descending order of importance,
  - use particle flow jets to decrease the JES/JER systematics<sup>1</sup>,
  - simulate more events per sample, and
  - use newer Z+jets samples with less mismodeling at high jet multiplicity.

<sup>1</sup>This is already required in ATLAS. Also, if memory serves, one can expect about half the JES/JER uncertainty at low  $p_T$  using the PFlow jets.

The expected sensitivity for the type-I 2HDM model was presented in Sect. 1.2. The exclusions on the production cross-section times the branching ratios presented in Sect. 15.1 are in agreement with expectations. To increase sensitivity for off-alignment searches, the proposed improvements might not even be sufficient to cover heavier  $m_H$  bosons, if the branching ratios for  $A \rightarrow t\bar{t}$  and possibly  $H \rightarrow hh$  become so dominating after  $m_H = 250$  GeV. However, the expected parameter space covers relatively low  $m_H$  (cf. Fig. 1.6b), and the improved sensitivity may still exclude higher  $m_A$  and  $\tan\beta$ , which these results only moderate exclude.

Run 3 of the LHC has so far been delayed to around 2022 due to the current world situation, but will never-the-less eventually deliver about  $300 \text{ fb}^{-1}$  of integrated luminosity with 14 TeV of center-of-mass energy. The high-luminosity LHC will some day deliver ten times as much integrated luminosity. The suggested improvements and the additional integrated luminosity open the door for new rare processes, but the  $A \rightarrow ZH$  channel of the 2HDM models remains a strong contestant for finding new Higgs bosons, whose existence may be used to explain that the observed baryon asymmetry is due to the electroweak phase transition in the early universe.

## **Part V**

# **Conclusion and bibliography**



## 17 Conclusion

In this thesis, both performance and physics analyses have been presented. The performance analysis focused on the TRT electron identification (PID) using real data for calibration. In the physics analysis, a search for new heavy Higgs bosons has been done.

*Performance analysis* The PID has been calibrated by  $Z \rightarrow ee$  and  $Z \rightarrow \mu\mu$  events obtained using the tag and probe method applied to simulated data as well as 2016 data recorded by the ATLAS experiment at the LHC.

In both simulation and data, electron (muon) counts now correctly fall off for decreasing (increasing) electron probability. Correction factors (CFs) have been tested for possible dependence on occupancy. The CFs have shown to have little dependency except for  $CF(TW)$  for muons past  $TW = 1.8$  mm. A track-based  $p_{HT}$  method was investigated but showed no improvement in calibration.

Overall, the improvement in PID performance in both data and simulation compared to the previous calibration has been shown. Using the full set of CFs has also improved the performance of the tool in data. The new calibration reduces the background efficiency by 1.45 percentage points in data and 3.31 p.p. in simulation at 95% signal efficiency compared to the calibration from 2015.

*Physics analysis* Data has been recorded by the ATLAS experiment at the LHC during the years 2015–2018, corresponding to an integrated luminosity of  $139 \text{ fb}^{-1}$  from proton–proton collisions at 13 TeV of center-of-mass energy.

In the search of new Higgs bosons, the analysis has focused on the  $A \rightarrow ZH$  signature with  $A$  produced by gluon–gluon fusion,  $Z$  decaying to leptons, and  $H$  decaying to  $WW$  that further decay hadronically. The mass range of  $300 < m_A < 800$  GeV and  $200 < m_H < 700$  GeV with  $m_A - m_H \geq 100$  GeV, relevant for electroweak baryogenesis, has been covered.

No significant excess above the Standard Model prediction has been observed. Upper limits at the 95% confidence level are set to  $0.023\text{--}8.9$  pb for  $\sigma(gg \rightarrow A) \times \text{BR}(A \rightarrow ZH) \times \text{BR}(H \rightarrow WW)$ . Exclusions have been placed on type-I 2HDM models in the  $(\cos(\beta - \alpha), m_A)$  plane for different  $m_H$  and  $\tan\beta$  values.

The  $H \rightarrow WW$  channel is a novel addition to the  $A \rightarrow ZH$  search and presents new possibilities for constraining 2HDM parameters

away from the alignment limit. As the LHC enters Run 3 and is eventually upgraded to the high-luminosity LHC, this channel remains a viable option for finding new physics beyond the Standard Model.

# Bibliography

- [1] Xiaohu Sun et al. *Search for a heavy CP-odd Higgs Boson decaying to a Z boson and a heavy CP-even Higgs boson H with A to ZH to llbb produced in 13 TeV Collisions with the ATLAS Detector*. Tech. rep. ATL-COM-PHYS-2016-1737. NOTE: Internal document. Geneva: CERN, 2016. URL: <https://cds.cern.ch/record/2235744> (cit. on pp. 9, 125).
- [2] A. D. Sakharov. "Violation of CP in variance, C asymmetry, and baryon asymmetry of the universe". In: *Phys. Usp.* 34.5 (1991). Note: This is the English translation and republication of the original article from 1967., pp. 392–393. DOI: 10.1070/PU1991v034n05ABEH002497. URL: <https://ufn.ru/en/articles/1991/5/h/> (cit. on p. 10).
- [3] Wikimedia Commons. *File:Standard Model of Elementary Particles.svg* — *Wikimedia Commons, the free media repository*. [Online; accessed 7-August-2020]. 2020. URL: <https://commons.wikimedia.org/w/index.php?title=File:Standard%5C%5FModel%5C%5Fof%5C%5FElementary%5C%5FParticles.svg&oldid=430960007> (cit. on p. 16).
- [4] M. Thomson. *Modern Particle Physics*. Cambridge University Press, 2013. ISBN: 9781107034266 (cit. on pp. 16–20, 27–29, 31).
- [5] Belle Collaboration. "Observation of a Narrow Charmonium-like State in Exclusive  $B^\pm \rightarrow K^\pm \pi^+ \pi^- J/\psi$  Decays". In: *Phys. Rev. Lett.* 91 (2003), p. 262001. DOI: 10.1103/PhysRevLett.91.262001. arXiv: [hep-ex/0309032](https://arxiv.org/abs/hep-ex/0309032) (cit. on p. 17).
- [6] LHCb Collaboration. "Observation of  $J/\psi p$  Resonances Consistent with Pentaquark States in  $\Lambda_b^0 \rightarrow J/\psi K^- p$  Decays". In: *Phys. Rev. Lett.* 115 (2015), p. 072001. DOI: 10.1103/PhysRevLett.115.072001. arXiv: 1507.03414 [hep-ex]. URL: <https://link.aps.org/doi/10.1103/PhysRevLett.115.072001> (cit. on p. 17).
- [7] LHCb Collaboration. "Observation of structure in the  $J/\psi$ -pair mass spectrum". In: (June 2020). arXiv: 2006.16957 [hep-ex] (cit. on p. 17).
- [8] Fred Bellaïche. *What's this Higgs boson anyway ?* 2012. URL: <https://www.quantum-bits.org/?p=233> (cit. on p. 19).

- [9] Jørgen Beck Hansen. “Particle detectors and accelerators”. Lecture notes in Particle Physics at the Energy Frontier. 2015 (cit. on pp. 20, 28–30).
- [10] Kari Enqvist et al. “Standard Model with a real singlet scalar and inflation”. In: *Journal of Cosmology and Astroparticle Physics* 2014 (2014). DOI: [10.1088/1475-7516/2014/08/035](https://doi.org/10.1088/1475-7516/2014/08/035) (cit. on p. 20).
- [11] Tania Robens, Tim Stefaniak, and Jonas Wittbrodt. “Two-real-scalar-singlet extension of the SM: LHC phenomenology and benchmark scenarios”. In: *The European Physical Journal C* 80 (2020). DOI: [10.1140/epjc/s10052-020-7655-x](https://doi.org/10.1140/epjc/s10052-020-7655-x) (cit. on p. 20).
- [12] S. Dawson and M. Sullivan. “Enhanced di-Higgs Production in the Complex Higgs Singlet Model”. In: *Phys. Rev. D* 97 (2017). DOI: [10.1103/PhysRevD.97.015022](https://doi.org/10.1103/PhysRevD.97.015022) (cit. on p. 20).
- [13] T. D. Lee. “A Theory of Spontaneous T Violation”. In: *Phys. Rev. D* 8 (1973), pp. 1226–1239. DOI: [10.1103/PhysRevD.8.1226](https://doi.org/10.1103/PhysRevD.8.1226) (cit. on p. 20).
- [14] G. Branco et al. “Theory and phenomenology of two-Higgs-doublet models”. In: *Physics Reports* 516 (2011). DOI: [10.1016/j.physrep.2012.02.002](https://doi.org/10.1016/j.physrep.2012.02.002). arXiv: [1106.0034](https://arxiv.org/abs/1106.0034) [hep-ph] (cit. on pp. 20–23, 77).
- [15] Abdelhak Djouadi. “The Anatomy of electroweak symmetry breaking Tome II: The Higgs bosons in the Minimal Supersymmetric Model”. In: *Phys. Rept.* 459 (2008), pp. 1–241. DOI: [10.1016/j.physrep.2007.10.005](https://doi.org/10.1016/j.physrep.2007.10.005). arXiv: [hep-ph/0503173](https://arxiv.org/abs/hep-ph/0503173) (cit. on p. 20).
- [16] G.C. Dorsch et al. “Echoes of the Electroweak Phase Transition: Discovering a second Higgs doublet through  $A_0 \rightarrow ZH_0$ ”. In: *Phys. Rev. Lett.* 113.21 (2014), p. 211802. DOI: [10.1103/PhysRevLett.113.211802](https://doi.org/10.1103/PhysRevLett.113.211802). arXiv: [1405.5537](https://arxiv.org/abs/1405.5537) [hep-ph] (cit. on pp. 20–23, 77).
- [17] Neil Turok and John Zadrozny. “Electroweak baryogenesis in the two-doublet model”. In: *Nucl. Phys. B* 358 (1991), pp. 471–493. DOI: [10.1016/0550-3213\(91\)90356-3](https://doi.org/10.1016/0550-3213(91)90356-3) (cit. on p. 20).
- [18] Lars Fromme, Stephan J. Huber, and Michael Seniuch. “Baryogenesis in the two-Higgs doublet model”. In: *JHEP* 11 (2006), p. 038. DOI: [10.1088/1126-6708/2006/11/038](https://doi.org/10.1088/1126-6708/2006/11/038). arXiv: [hep-ph/0605242](https://arxiv.org/abs/hep-ph/0605242) (cit. on p. 20).
- [19] P. Basler et al. “Strong first order electroweak phase transition in the CP-Conserving 2HDM revisited”. In: *JHEP* 02 (2017), p. 121. DOI: [10.1007/JHEP02\(2017\)121](https://doi.org/10.1007/JHEP02(2017)121). arXiv: [1612.04086](https://arxiv.org/abs/1612.04086) [hep-ph] (cit. on p. 20).
- [20] Andrew G. Cohen, D. B. Kaplan, and A. E. Nelson. “Progress in Electroweak Baryogenesis”. In: *Ann. Rev. Nucl. Part. Sci.* 43 (1993), pp. 27–70. DOI: [10.1146/annurev.ns.43.120193.000331](https://doi.org/10.1146/annurev.ns.43.120193.000331). arXiv: [hep-ph/9302210](https://arxiv.org/abs/hep-ph/9302210) (cit. on p. 20).

- [21] Jalal Abdallah et al. “Simplified models for dark matter searches at the LHC”. In: *Phys. Dark Univ.* 9-10 (2015), pp. 8–23. DOI: [10.1016/j.dark.2015.08.001](https://doi.org/10.1016/j.dark.2015.08.001). arXiv: [1506.03116](https://arxiv.org/abs/1506.03116) [hep-ph] (cit. on p. 20).
- [22] S. F. King. “Neutrino mass models”. In: *Rept. Prog. Phys.* 67 (2004), pp. 107–158. DOI: [10.1088/0034-4885/67/2/R01](https://doi.org/10.1088/0034-4885/67/2/R01). arXiv: [hep-ph/0310204](https://arxiv.org/abs/hep-ph/0310204) (cit. on p. 20).
- [23] ATLAS Collaboration. “Observation of a new particle in the search for the Standard Model Higgs boson with the ATLAS detector at the LHC”. In: *Phys. Lett. B* 716 (2012), p. 1. DOI: [10.1016/j.physletb.2012.08.020](https://doi.org/10.1016/j.physletb.2012.08.020). arXiv: [1207.7214](https://arxiv.org/abs/1207.7214) [hep-ex] (cit. on p. 20).
- [24] CMS Collaboration. “Observation of a new boson at a mass of 125 GeV with the CMS experiment at the LHC”. In: *Phys. Lett. B* 716 (2012), p. 30. DOI: [10.1016/j.physletb.2012.08.021](https://doi.org/10.1016/j.physletb.2012.08.021). arXiv: [1207.7235](https://arxiv.org/abs/1207.7235) [hep-ex] (cit. on p. 20).
- [25] ATLAS Collaboration. “Combined measurements of Higgs boson production and decay using up to  $80\text{ fb}^{-1}$  of proton–proton collision data at  $\sqrt{s} = 13\text{ TeV}$  collected with the ATLAS experiment”. In: *Phys. Rev. D* 101 (2020), p. 012002. DOI: [10.1103/PhysRevD.101.012002](https://doi.org/10.1103/PhysRevD.101.012002). arXiv: [1909.02845](https://arxiv.org/abs/1909.02845) [hep-ex] (cit. on pp. 20, 23, 158).
- [26] ATLAS Collaboration. “CP Properties of Higgs Boson Interactions with Top Quarks in the  $t\bar{t}H$  and  $tH$  Processes Using  $H \rightarrow \gamma\gamma$  with the ATLAS Detector”. In: *Phys. Rev. Lett.* 125 (2020), p. 061802. DOI: [10.1103/PhysRevLett.125.061802](https://doi.org/10.1103/PhysRevLett.125.061802). arXiv: [2004.04545](https://arxiv.org/abs/2004.04545) [hep-ex] (cit. on p. 20).
- [27] ATLAS Collaboration. “Test of CP invariance in vector-boson fusion production of the Higgs boson in the  $H \rightarrow \tau\tau$  channel in proton–proton collisions at  $\sqrt{s} = 13\text{ TeV}$  with the ATLAS detector”. In: *Phys. Lett. B* 805 (2020), p. 135426. DOI: [10.1016/j.physletb.2020.135426](https://doi.org/10.1016/j.physletb.2020.135426). arXiv: [2002.05315](https://arxiv.org/abs/2002.05315) [hep-ex] (cit. on p. 20).
- [28] ATLAS Collaboration. “Study of the spin and parity of the Higgs boson in diboson decays with the ATLAS detector”. In: *Eur. Phys. J. C* 75 (2015), p. 476. DOI: [10.1140/epjc/s10052-015-3685-1](https://doi.org/10.1140/epjc/s10052-015-3685-1). arXiv: [1506.05669](https://arxiv.org/abs/1506.05669) [hep-ex] (cit. on p. 20). Erratum: in: *Eur. Phys. J. C* 76 (2016), p. 152. DOI: [10.1140/epjc/s10052-016-3934-y](https://doi.org/10.1140/epjc/s10052-016-3934-y).
- [29] CMS Collaboration. “Measurement and interpretation of differential cross sections for Higgs boson production at  $\sqrt{s} = 13\text{ TeV}$ ”. In: *Phys. Lett. B* 792 (2019), pp. 369–396. DOI: [10.1016/j.physletb.2019.03.059](https://doi.org/10.1016/j.physletb.2019.03.059). arXiv: [1812.06504](https://arxiv.org/abs/1812.06504) [hep-ex] (cit. on p. 20).

- [30] CMS Collaboration. “Combined measurements of Higgs boson couplings in proton–proton collisions at  $\sqrt{s} = 13$  TeV”. In: *Eur. Phys. J. C* 79.5 (2019), p. 421. DOI: [10.1140/epjc/s10052-019-6909-y](https://doi.org/10.1140/epjc/s10052-019-6909-y). arXiv: [1809.10733](https://arxiv.org/abs/1809.10733) [hep-ex] (cit. on p. 20).
- [31] CMS Collaboration. “Measurements of  $t\bar{t}H$  production and the CP structure of the Yukawa interaction between the Higgs boson and top quark in the diphoton decay channel”. In: *Phys. Rev. Lett.* 125.6 (2020), p. 061801. DOI: [10.1103/PhysRevLett.125.061801](https://doi.org/10.1103/PhysRevLett.125.061801). arXiv: [2003.10866](https://arxiv.org/abs/2003.10866) [hep-ex] (cit. on p. 20).
- [32] ATLAS and CMS Collaborations. “Measurements of the Higgs boson production and decay rates and constraints on its couplings from a combined ATLAS and CMS analysis of the LHC pp collision data at  $\sqrt{s} = 7$  and 8 TeV”. In: *JHEP* 08 (2016), p. 045. DOI: [10.1007/JHEP08\(2016\)045](https://doi.org/10.1007/JHEP08(2016)045). arXiv: [1606.02266](https://arxiv.org/abs/1606.02266) [hep-ex] (cit. on p. 20).
- [33] F. Englert and R. Brout. “Broken Symmetry and the Mass of Gauge Vector Mesons”. In: *Phys. Rev. Lett.* 13 (1964), pp. 321–323. DOI: [10.1103/PhysRevLett.13.321](https://doi.org/10.1103/PhysRevLett.13.321) (cit. on p. 20).
- [34] Peter W. Higgs. “Broken symmetries, massless particles and gauge fields”. In: *Phys. Lett.* 12.2 (1964), pp. 132–133. ISSN: 0031-9163. DOI: [10.1016/0031-9163\(64\)91136-9](https://doi.org/10.1016/0031-9163(64)91136-9) (cit. on p. 20).
- [35] Peter W. Higgs. “Broken Symmetries and the Masses of Gauge Bosons”. In: *Phys. Rev. Lett.* 13 (1964), pp. 508–509. DOI: [10.1103/PhysRevLett.13.508](https://doi.org/10.1103/PhysRevLett.13.508) (cit. on p. 20).
- [36] G. S. Guralnik, C. R. Hagen, and T. W. B. Kibble. “Global Conservation Laws and Massless Particles”. In: *Phys. Rev. Lett.* 13 (1964), pp. 585–587. DOI: [10.1103/PhysRevLett.13.585](https://doi.org/10.1103/PhysRevLett.13.585) (cit. on p. 20).
- [37] Peter W. Higgs. “Spontaneous Symmetry Breakdown without Massless Bosons”. In: *Phys. Rev.* 145 (1966), pp. 1156–1163. DOI: [10.1103/PhysRev.145.1156](https://doi.org/10.1103/PhysRev.145.1156) (cit. on p. 20).
- [38] T. W. B. Kibble. “Symmetry Breaking in Non-Abelian Gauge Theories”. In: *Phys. Rev.* 155 (1967), pp. 1554–1561. DOI: [10.1103/PhysRev.155.1554](https://doi.org/10.1103/PhysRev.155.1554) (cit. on p. 20).
- [39] ATLAS Collaboration. “Searches for heavy ZZ and ZW resonances in the  $\ell\ell qq$  and  $\nu\nu qq$  final states in pp collisions at  $\sqrt{s} = 13$  TeV with the ATLAS detector”. In: *JHEP* 03 (2018), p. 009. DOI: [10.1007/JHEP03\(2018\)009](https://doi.org/10.1007/JHEP03(2018)009). arXiv: [1708.09638](https://arxiv.org/abs/1708.09638) [hep-ex] (cit. on p. 20).
- [40] ATLAS Collaboration. “Search for WW/WZ resonance production in  $\ell\nu qq$  final states in pp collisions at  $\sqrt{s} = 13$  TeV with the ATLAS detector”. In: *JHEP* 03 (2018), p. 042. DOI: [10.1007/JHEP03\(2018\)042](https://doi.org/10.1007/JHEP03(2018)042). arXiv: [1710.07235](https://arxiv.org/abs/1710.07235) [hep-ex] (cit. on p. 20).

- [41] ATLAS Collaboration. “Search for heavy diboson resonances in semileptonic final states in  $pp$  collisions at  $\sqrt{s} = 13$  TeV with the ATLAS detector”. In: (2020). arXiv: [2004.14636 \[hep-ex\]](#) (cit. on p. 20).
- [42] ATLAS Collaboration. “Search for diboson resonances in hadronic final states in  $139 \text{ fb}^{-1}$  of  $pp$  collisions at  $\sqrt{s} = 13$  TeV with the ATLAS detector”. In: *JHEP* 09 (2019), p. 091. DOI: [10.1007/JHEP09\(2019\)091](#). arXiv: [1906.08589 \[hep-ex\]](#) (cit. on p. 20).
- [43] CMS Collaboration. “Search for a heavy Higgs boson decaying to a pair of  $W$  bosons in proton–proton collisions at  $\sqrt{s} = 13$  TeV”. In: *JHEP* 03 (2020), p. 034. DOI: [10.1007/JHEP03\(2020\)034](#). arXiv: [1912.01594 \[hep-ex\]](#) (cit. on p. 20).
- [44] CMS Collaboration. “Search for a new scalar resonance decaying to a pair of  $Z$  bosons in proton–proton collisions at  $\sqrt{s} = 13$  TeV”. In: *JHEP* 06 (2018), p. 127. DOI: [10.1007/JHEP06\(2018\)127](#). arXiv: [1804.01939 \[hep-ex\]](#) (cit. on p. 20).
- [45] ATLAS Collaboration. “Combination of searches for Higgs boson pairs in  $pp$  collisions at  $\sqrt{s} = 13$  TeV with the ATLAS detector”. In: *Phys. Lett. B* 800 (2020), p. 135103. DOI: [10.1016/j.physletb.2019.135103](#). arXiv: [1906.02025 \[hep-ex\]](#) (cit. on p. 20).
- [46] CMS Collaboration. “Combination of Searches for Higgs Boson Pair Production in Proton–Proton Collisions at  $\sqrt{s} = 13$  TeV”. In: *Phys. Rev. Lett.* 122 (2019), p. 121803. DOI: [10.1103/PhysRevLett.122.121803](#). arXiv: [1811.09689 \[hep-ex\]](#) (cit. on p. 20).
- [47] ATLAS Collaboration. “Search for heavy resonances decaying into a  $W$  or  $Z$  boson and a Higgs boson in final states with leptons and  $b$ -jets in  $36 \text{ fb}^{-1}$  of  $\sqrt{s} = 13$  TeV  $pp$  collisions with the ATLAS detector”. In: *JHEP* 03 (2018), p. 174. DOI: [10.1007/JHEP03\(2018\)174](#). arXiv: [1712.06518 \[hep-ex\]](#) (cit. on pp. 20, 83). Erratum: in: *JHEP* 11 (2018), p. 051. DOI: [10.1007/JHEP11\(2018\)051](#).
- [48] CMS Collaboration. “Search for a heavy pseudoscalar Higgs boson decaying into a 125 GeV Higgs boson and a  $Z$  boson in final states with two tau and two light leptons at  $\sqrt{s} = 13$  TeV”. In: *JHEP* 03 (2020), p. 065. DOI: [10.1007/JHEP03\(2020\)065](#). arXiv: [1910.11634 \[hep-ex\]](#) (cit. on p. 20).
- [49] ATLAS Collaboration. “Search for heavy Higgs bosons decaying into two tau leptons with the ATLAS detector using  $pp$  collisions at  $\sqrt{s} = 13$  TeV”. In: *Phys. Rev. Lett.* 125.5 (2020), p. 051801. DOI: [10.1103/PhysRevLett.125.051801](#). arXiv: [2002.12223 \[hep-ex\]](#) (cit. on p. 20).

- [50] CMS Collaboration. “Search for beyond the standard model Higgs bosons decaying into a  $b\bar{b}$  pair in  $pp$  collisions at  $\sqrt{s} = 13$  TeV”. In: *JHEP* 08 (2018), p. 113. DOI: [10.1007/JHEP08\(2018\)113](https://doi.org/10.1007/JHEP08(2018)113). arXiv: [1805.12191](https://arxiv.org/abs/1805.12191) [hep-ex] (cit. on p. 20).
- [51] CMS Collaboration. “Search for additional neutral MSSM Higgs bosons in the  $\tau\tau$  final state in proton–proton collisions at  $\sqrt{s} = 13$  TeV”. In: *JHEP* 09 (2018), p. 007. DOI: [10.1007/JHEP09\(2018\)007](https://doi.org/10.1007/JHEP09(2018)007). arXiv: [1803.06553](https://arxiv.org/abs/1803.06553) [hep-ex] (cit. on p. 20).
- [52] CMS Collaboration. “Search for neutral resonances decaying into a Z boson and a pair of  $b$  jets or  $\tau$  leptons”. In: *Phys. Lett. B* 759 (2016), p. 369. DOI: [10.1016/j.physletb.2016.05.087](https://doi.org/10.1016/j.physletb.2016.05.087). arXiv: [1603.02991](https://arxiv.org/abs/1603.02991) [hep-ex] (cit. on p. 20).
- [53] CMS Collaboration. “Search for new neutral Higgs bosons through the  $H \rightarrow ZA \rightarrow \ell^+ \ell^- b\bar{b}$  process in  $pp$  collisions at  $\sqrt{s} = 13$  TeV”. In: *JHEP* 03 (2020), p. 055. DOI: [10.1007/JHEP03\(2020\)055](https://doi.org/10.1007/JHEP03(2020)055). arXiv: [1911.03781](https://arxiv.org/abs/1911.03781) [hep-ex] (cit. on p. 20).
- [54] ATLAS Collaboration. “Search for a heavy Higgs boson decaying into a Z boson and another heavy Higgs boson in the  $\ell\ell b\bar{b}$  final state in  $pp$  collisions at  $\sqrt{s} = 13$  TeV with the ATLAS detector”. In: *Phys. Lett. B* 783 (2018), pp. 392–414. DOI: [10.1016/j.physletb.2018.07.006](https://doi.org/10.1016/j.physletb.2018.07.006). arXiv: [1804.01126](https://arxiv.org/abs/1804.01126) [hep-ex] (cit. on pp. 20, 23, 77, 125).
- [55] John F. Gunion and Howard E. Haber. “CP-conserving two-Higgs-doublet model: The approach to the decoupling limit”. In: *Phys. Rev. D* 67 (2003), p. 075019. DOI: [10.1103/PhysRevD.67.075019](https://doi.org/10.1103/PhysRevD.67.075019). URL: <https://link.aps.org/doi/10.1103/PhysRevD.67.075019> (cit. on p. 21).
- [56] Dimitris Komminis. “The Phenomenology of the CP odd scalar in two doublet models”. In: *Nucl. Phys. B* 427 (1994), pp. 575–613. DOI: [10.1016/0550-3213\(94\)90641-6](https://doi.org/10.1016/0550-3213(94)90641-6). arXiv: [hep-ph/9402339](https://arxiv.org/abs/hep-ph/9402339) (cit. on p. 22).
- [57] G. Dorsch, S. Huber, and J. No. “A strong electroweak phase transition in the 2HDM after LHC8”. In: *Journal of High Energy Physics* 2013 (2013). DOI: [10.1007/JHEP10\(2013\)029](https://doi.org/10.1007/JHEP10(2013)029). arXiv: [1305.6610](https://arxiv.org/abs/1305.6610) [hep-ph] (cit. on p. 22).
- [58] ATLAS Collaboration. “Search for Heavy Higgs Bosons  $A/H$  Decaying to a Top Quark Pair in  $pp$  Collisions at  $\sqrt{s} = 8$  TeV with the ATLAS Detector”. In: *Phys. Rev. Lett.* 119 (19 2017), p. 191803. DOI: [10.1103/PhysRevLett.119.191803](https://doi.org/10.1103/PhysRevLett.119.191803). arXiv: [1707.06025](https://arxiv.org/abs/1707.06025) [hep-ex] (cit. on p. 22).
- [59] Robert V. Harlander, Stefan Liebler, and Hendrik Mantler. “SusHi: A program for the calculation of Higgs production in gluon fusion and bottom-quark annihilation in the Standard Model and the MSSM”. In: *Comput. Phys. Commun.* 184 (2013), pp. 1605–1617. DOI: [10.1016/j.cpc.2013.02.006](https://doi.org/10.1016/j.cpc.2013.02.006). arXiv: [1212.3249](https://arxiv.org/abs/1212.3249) [hep-ph] (cit. on p. 22).

- [60] Robert Harlander, Stefan Liebler, and Hendrik Mantler. “SusHi Bento: Beyond NNLO and the heavy-top limit”. In: *Computer Physics Communications* 212 (2016). DOI: [10.1016/j.cpc.2016.10.015](https://doi.org/10.1016/j.cpc.2016.10.015). arXiv: [1605.03190](https://arxiv.org/abs/1605.03190) (cit. on p. 22).
- [61] Robert V. Harlander and William B. Kilgore. “Next-to-Next-to-Leading Order Higgs Production at Hadron Colliders”. In: *Phys. Rev. Lett.* 88 (2002), p. 201801. DOI: [10.1103/PhysRevLett.88.201801](https://doi.org/10.1103/PhysRevLett.88.201801). arXiv: [hep-ph/0201206](https://arxiv.org/abs/hep-ph/0201206) (cit. on p. 22).
- [62] Robert V. Harlander and William B. Kilgore. “Higgs boson production in bottom quark fusion at next-to-next-to-leading order”. In: *Phys. Rev. D* 68 (2003), p. 013001. DOI: [10.1103/PhysRevD.68.013001](https://doi.org/10.1103/PhysRevD.68.013001). arXiv: [hep-ph/0304035](https://arxiv.org/abs/hep-ph/0304035) (cit. on p. 22).
- [63] U. Aglietti et al. “Two-loop light fermion contribution to Higgs production and decays”. In: *Phys. Lett. B* 595 (2004), pp. 432–441. DOI: [10.1016/j.physletb.2004.06.063](https://doi.org/10.1016/j.physletb.2004.06.063). arXiv: [hep-ph/0404071](https://arxiv.org/abs/hep-ph/0404071) (cit. on p. 22).
- [64] R. Bonciani, G. Degrossi, and A. Vicini. “On the Generalized Harmonic Polylogarithms of One Complex Variable”. In: *Comput. Phys. Commun.* 182 (2011), p. 1253. DOI: [10.1016/j.cpc.2011.02.011](https://doi.org/10.1016/j.cpc.2011.02.011). arXiv: [1007.1891](https://arxiv.org/abs/1007.1891) [[hep-ph](#)] (cit. on p. 22).
- [65] Robert Harlander and Philipp Kant. “Higgs production and decay: analytic results at next-to-leading order QCD”. In: *JHEP* 12 (2005), p. 015. DOI: [10.1088/1126-6708/2005/12/015](https://doi.org/10.1088/1126-6708/2005/12/015). arXiv: [hep-ph/0509189](https://arxiv.org/abs/hep-ph/0509189) (cit. on p. 22).
- [66] Andy Buckley et al. “LHAPDF6: parton density access in the LHC precision era”. In: *The European Physical Journal C* 75 (2014). DOI: [10.1140/epjc/s10052-015-3318-8](https://doi.org/10.1140/epjc/s10052-015-3318-8) (cit. on p. 22).
- [67] David Eriksson, Johan Rathsman, and Oscar Stål. “2HDMC — two-Higgs-doublet model calculator”. In: *Computer Physics Communications* 181 (2009). DOI: [10.1016/j.cpc.2009.09.011](https://doi.org/10.1016/j.cpc.2009.09.011) (cit. on p. 22).
- [68] Baradhwaj Coleppa, Felix Kling, and Shufang Su. “Exotic decays of a heavy neutral Higgs through HZ/AZ channel”. In: *JHEP* 09 (2014), p. 161. DOI: [10.1007/JHEP09\(2014\)161](https://doi.org/10.1007/JHEP09(2014)161). arXiv: [1404.1922](https://arxiv.org/abs/1404.1922) [[hep-ph](#)] (cit. on p. 22).
- [69] Johannes Haller et al. “Update of the global electroweak fit and constraints on two-Higgs-doublet models”. In: *Eur. Phys. J. C* 78.8 (2018), p. 675. DOI: [10.1140/epjc/s10052-018-6131-3](https://doi.org/10.1140/epjc/s10052-018-6131-3). arXiv: [1803.01853](https://arxiv.org/abs/1803.01853) [[hep-ph](#)] (cit. on p. 23).
- [70] Peter Hansen. “Particle detectors and accelerators”. Lecture notes in Particle detectors and accelerators. 2016. URL: <https://www.nbi.dk/~phanzen/lecturenote.pdf> (cit. on pp. 27, 31, 36, 45).
- [71] Wikipedia. *Breit-Wigner*. [Online; accessed 2020-09-25]. 2006. URL: <https://commons.wikimedia.org/w/index.php?title=File:Breit-Wigner.svg&oldid=178019923> (cit. on p. 27).

- [72] Daniel S. Nielsen. “An alternative analysis of semi-leptonic diboson final states in the boosted regime”. MA thesis. University of Copenhagen, 2016 (cit. on pp. 27, 29).
- [73] K. A. Olive et al. “Review of Particle Physics”. In: *Chin. Phys. C* 38 (2014), p. 090001. DOI: 10.1088/1674-1137/38/9/090001 (cit. on pp. 28, 31, 161).
- [74] R. C et al. “Parton Distributions for the LHC”. In: *The European Physical Journal C* 63 (2007). DOI: 10.1140/epjc/s10052-009-1072-5. arXiv: 0901.0002 (cit. on p. 28).
- [75] Andy Buckley et al. “MCnet-11-01 General-purpose event generators for LHC physics”. In: *Physics Reports* 504 (2011), pp. 145–233. DOI: 10.1016/j.physrep.2011.03.005. arXiv: 1101.2599 [hep-ph] (cit. on p. 28).
- [76] W.J. Stirling. *Cross section plots*. URL: <https://www.hep.ph.ic.ac.uk/~wstirling/plots/plots.html> (cit. on p. 28).
- [77] ATLAS Collaboration. “The ATLAS Experiment at the CERN Large Hadron Collider”. In: *JINST* 3 (2008), S08003. 437 p. DOI: 10.1088/1748-0221/3/08/S08003. URL: <https://cds.cern.ch/record/1129811> (cit. on pp. 29, 35–41).
- [78] Dieter Zeppenfeld. *Parton shower*. [Online; accessed 7-August-2020]. 2005. URL: <https://web.archive.org/web/20141122034843/http://www.quantumdiaries.org/wp-content/uploads/2010/12/partonshower.png> (cit. on p. 30).
- [79] Richard D. Field and Stephen Wolfram. “A QCD Model for  $e^+e^-$  Annihilation”. In: *Nucl. Phys. B* 213 (1983), pp. 65–84. DOI: 10.1016/0550-3213(83)90175-X (cit. on p. 29).
- [80] Bo Andersson et al. “Parton Fragmentation and String Dynamics”. In: *Phys. Rept.* 97 (1983), pp. 31–145. DOI: 10.1016/0370-1573(83)90080-7 (cit. on p. 29).
- [81] Torbjorn Sjostrand, Stephen Mrenna, and Peter Z. Skands. “A Brief Introduction to PYTHIA 8.1”. In: *Comput.Phys.Commun.* 178 (2008), pp. 852–867. DOI: 10.1016/j.cpc.2008.01.036. arXiv: 0710.3820 [hep-ph] (cit. on p. 29).
- [82] ATLAS Collaboration. *Luminosity determination in pp collisions at  $\sqrt{s} = 13$  TeV using the ATLAS detector at the LHC*. ATLAS-CONF-2019-021. 2019. URL: <https://cds.cern.ch/record/2677054> (cit. on pp. 30, 36, 130).
- [83] Esmā Mobs. “The CERN accelerator complex - 2019. Complexe des accélérateurs du CERN - 2019”. In: (2019). General Photo. URL: <https://cds.cern.ch/record/2684277> (cit. on p. 35).
- [84] ATLAS Collaboration. “Operation of the ATLAS trigger system in Run 2”. In: (2020). arXiv: 2007.12539 [physics.ins-det] (cit. on pp. 35, 42).

- [85] Joany Manjarres Ramos et al. *TRT performance results from 13 TeV collision data (2015/2016)*. Tech. rep. ATL-COM-INDET-2016-049. Geneva: CERN, 2016. URL: <https://cds.cern.ch/record/2202124> (cit. on p. 38).
- [86] E. Abat et al. “The ATLAS Transition Radiation Tracker (TRT) proportional drift tube: Design and performance”. In: *Journal of Instrumentation* 3 (2008), P02013. DOI: 10.1088/1748-0221/3/02/P02013 (cit. on p. 38).
- [87] ATLAS Collaboration. “Performance of the ATLAS Transition Radiation Tracker in Run 1 of the LHC: tracker properties”. In: *JINST* 12.05 (2017), P05002. DOI: 10.1088/1748-0221/12/05/P05002. arXiv: 1702.06473 [hep-ex] (cit. on p. 38).
- [88] Esben Bryndt Klinkby. “W mass measurement and simulation of the transition radiation tracker at the ATLAS experiment”. Presented on 02 Jul 2008. 2008. URL: <https://cds.cern.ch/record/1123367> (cit. on p. 38).
- [89] Bartosz Mindur. *ATLAS Transition Radiation Tracker (TRT): Straw tubes for tracking and particle identification at the Large Hadron Collider*. Tech. rep. ATL-INDET-PROC-2016-001. Geneva: CERN, 2016. DOI: 10.1016/j.nima.2016.04.026. URL: <https://cds.cern.ch/record/2139567> (cit. on p. 38).
- [90] Daniel Stefaniak Nielsen. *2017 TRT PID calibration with data*. Tech. rep. ATL-COM-INDET-2018-034. qualification task note. Geneva: CERN, 1991. URL: <https://cds.cern.ch/record/2318461> (cit. on p. 39).
- [91] Arif Bayirli. *Particle Identification with Machine Learning in Transition Radiation Tracker (TRT) at ATLAS*. Tech. rep. ATL-COM-INDET-2020-001. Geneva: CERN, 2020. URL: <https://cds.cern.ch/record/2705706> (cit. on p. 39).
- [92] ATLAS Collaboration. “Resolution of the ATLAS muon spectrometer monitored drift tubes in LHC Run 2”. In: *JINST* 14.09 (2019), P09011. 36 p. DOI: 10.1088/1748-0221/14/09/p09011. arXiv: 1906.12226 [hep-ex] (cit. on p. 41).
- [93] ATLAS Collaboration. “Performance of the ATLAS muon triggers in Run 2”. In: *JINST* 15.09 (2020), P09015. 58 p. DOI: 10.1088/1748-0221/15/09/p09015. arXiv: 2004.13447 (cit. on pp. 42, 130).
- [94] Georges Aad et al. “Performance of electron and photon triggers in ATLAS during LHC Run 2”. In: *Eur. Phys. J. C* 80.1 (2020), p. 47. DOI: 10.1140/epjc/s10052-019-7500-2. arXiv: 1909.00761 [hep-ex] (cit. on pp. 42–44, 90, 130).
- [95] Morad Aaboud et al. “Electron reconstruction and identification in the ATLAS experiment using the 2015 and 2016 LHC proton-proton collision data at  $\sqrt{s} = 13$  TeV”. In: *Eur. Phys. J. C* 79.8 (2019), p. 639. DOI: 10.1140/epjc/s10052-019-7140-6. arXiv: 1902.04655 [physics.ins-det] (cit. on pp. 44, 45).

- [96] T. Cornelissen et al. “Concepts, Design and Implementation of the ATLAS New Tracking (NEWT)”. In: (2007). Ed. by A. Salzburger (cit. on pp. 44, 45).
- [97] R. Fruhwirth. “Application of Kalman filtering to track and vertex fitting”. In: *Nucl. Instrum. Meth. A* 262 (1987), pp. 444–450. DOI: [10.1016/0168-9002\(87\)90887-4](https://doi.org/10.1016/0168-9002(87)90887-4) (cit. on p. 45).
- [98] ATLAS Collaboration. *Vertex Reconstruction Performance of the ATLAS Detector at  $\sqrt{s} = 13$  TeV*. ATL-PHYS-PUB-2015-026. 2015. URL: <https://cds.cern.ch/record/2037717> (cit. on p. 45).
- [99] ATLAS Collaboration. “Electron and photon performance measurements with the ATLAS detector using the 2015–2017 LHC proton-proton collision data”. In: *JINST* 14.12 (2019), P12006. DOI: [10.1088/1748-0221/14/12/P12006](https://doi.org/10.1088/1748-0221/14/12/P12006). arXiv: [1908.00005](https://arxiv.org/abs/1908.00005) [hep-ex] (cit. on pp. 46, 47, 130).
- [100] ATLAS Collaboration. “Topological cell clustering in the ATLAS calorimeters and its performance in LHC Run 1”. In: *The European Physical Journal C* 77.7 (2017), p. 490. ISSN: 1434-6052. DOI: [10.1140/epjc/s10052-017-5004-5](https://doi.org/10.1140/epjc/s10052-017-5004-5). arXiv: [1603.02934](https://arxiv.org/abs/1603.02934) [hep-ex] (cit. on pp. 46, 48).
- [101] ATLAS Collaboration. *Improved electron reconstruction in ATLAS using the Gaussian Sum Filter-based model for bremsstrahlung*. Tech. rep. ATLAS-CONF-2012-047. Geneva: CERN, 2012. URL: <https://cds.cern.ch/record/1449796> (cit. on p. 46).
- [102] ATLAS Collaboration. “Muon reconstruction performance of the ATLAS detector in proton–proton collision data at  $\sqrt{s}=13$  TeV”. In: *Eur. Phys. J. C* 76.5 (2016), p. 292. DOI: [10.1140/epjc/s10052-016-4120-y](https://doi.org/10.1140/epjc/s10052-016-4120-y). arXiv: [1603.05598](https://arxiv.org/abs/1603.05598) [hep-ex] (cit. on pp. 47, 48, 130).
- [103] W Lampl et al. *Calorimeter Clustering Algorithms: Description and Performance*. Tech. rep. ATL-LARG-PUB-2008-002. ATL-COM-LARG-2008-003. Geneva: CERN, 2008. URL: <https://cds.cern.ch/record/1099735> (cit. on p. 48).
- [104] Matteo Cacciari, Gavin P Salam, and Gregory Soyez. “The anti-ktjet clustering algorithm”. In: *Journal of High Energy Physics* 2008.04 (2008), pp. 063–063. DOI: [10.1088/1126-6708/2008/04/063](https://doi.org/10.1088/1126-6708/2008/04/063). arXiv: [0802.1189](https://arxiv.org/abs/0802.1189) [hep-ph] (cit. on pp. 48, 49).
- [105] Matteo Cacciari, Gavin P. Salam, and Gregory Soyez. “FastJet User Manual”. In: *Eur. Phys. J. C* 72 (2012), p. 1896. DOI: [10.1140/epjc/s10052-012-1896-2](https://doi.org/10.1140/epjc/s10052-012-1896-2). arXiv: [1111.6097](https://arxiv.org/abs/1111.6097) [hep-ph] (cit. on p. 48).
- [106] Stephen D. Ellis and Davison E. Soper. “Successive combination jet algorithm for hadron collisions”. In: *Phys. Rev. D* 48 (1993), pp. 3160–3166. DOI: [10.1103/PhysRevD.48.3160](https://doi.org/10.1103/PhysRevD.48.3160). arXiv: [hep-ph/9305266](https://arxiv.org/abs/hep-ph/9305266) (cit. on p. 48).

- [107] Yuri Dokshitzer et al. “Better Jet Clustering Algorithms”. In: *Journal of High Energy Physics* 1997 (1997). DOI: [10.1088/1126-6708/1997/08/001](https://doi.org/10.1088/1126-6708/1997/08/001). arXiv: [hep-ph/9707323](https://arxiv.org/abs/hep-ph/9707323) (cit. on p. 48).
- [108] ATLAS Collaboration. “Jet energy scale measurements and their systematic uncertainties in proton-proton collisions at  $\sqrt{s} = 13$  TeV with the ATLAS detector.” In: *Phys. Rev. D* 96 (2017), p. 072002. DOI: [10.1103/PhysRevD.96.072002](https://doi.org/10.1103/PhysRevD.96.072002). arXiv: [1703.09665](https://arxiv.org/abs/1703.09665) [[hep-ex](#)] (cit. on pp. 49, 132).
- [109] ATLAS Collaboration. *Tagging and suppression of pileup jets with the ATLAS detector*. Tech. rep. ATLAS-CONF-2014-018. Geneva: CERN, 2014. URL: <https://cds.cern.ch/record/1700870> (cit. on p. 49).
- [110] Philippe Gras et al. “Systematics of quark/gluon tagging”. In: (2017). DOI: [10.1007/JHEP07\(2017\)091](https://doi.org/10.1007/JHEP07(2017)091). arXiv: [1704.03878](https://arxiv.org/abs/1704.03878) [[hep-ex](#)] (cit. on p. 49).
- [111] Julia Gonski. *Jet Cleaning in 2016 and the Event Level Cleaning Tool*. Tech. rep. ATL-COM-PHYS-2017-982. Geneva: CERN, 2017. URL: <https://cds.cern.ch/record/2272136> (cit. on pp. 49, 50).
- [112] ATLAS Collaboration. “ATLAS data quality operations and performance for 2015–2018 data-taking”. In: *JINST* 15 (2020), P04003. DOI: [10.1088/1748-0221/15/04/P04003](https://doi.org/10.1088/1748-0221/15/04/P04003). arXiv: [1911.04632](https://arxiv.org/abs/1911.04632) [[physics.ins-det](#)] (cit. on pp. 50, 82).
- [113] Jared Gregory Vasquez. *Occupancy Calibration of the TRT PID Tool*. Tech. rep. ATL-COM-INDET-2015-090. Geneva: CERN, 2015. URL: <https://cds.cern.ch/record/2104319> (cit. on p. 53).
- [114] Leigh Schaefer. *TRT Local Occupancy Studies*. Tech. rep. ATL-COM-INDET-2016-008. Geneva: CERN, 2016. URL: <https://cds.cern.ch/record/2128630> (cit. on p. 54).
- [115] S. Agostinelli et al. “GEANT4: A simulation toolkit”. In: *Nucl. Instrum. Meth. A* 506 (2003), pp. 250–303. DOI: [10.1016/S0168-9002\(03\)01368-8](https://doi.org/10.1016/S0168-9002(03)01368-8) (cit. on p. 82).
- [116] ATLAS Collaboration. “The ATLAS Simulation Infrastructure”. In: *Eur. Phys. J. C* 70 (2010), p. 823. DOI: [10.1140/epjc/s10052-010-1429-9](https://doi.org/10.1140/epjc/s10052-010-1429-9). arXiv: [1005.4568](https://arxiv.org/abs/1005.4568) [[hep-ex](#)] (cit. on p. 82).
- [117] Johan Alwall et al. “MadGraph 5: going beyond”. In: *JHEP* 06 (2011), p. 128. DOI: [10.1007/JHEP06\(2011\)128](https://doi.org/10.1007/JHEP06(2011)128). arXiv: [1106.0522](https://arxiv.org/abs/1106.0522) [[hep-ph](#)] (cit. on p. 82).
- [118] J. Alwall et al. “The automated computation of tree-level and next-to-leading order differential cross sections, and their matching to parton shower simulations”. In: *JHEP* 07 (2014), p. 079. DOI: [10.1007/JHEP07\(2014\)079](https://doi.org/10.1007/JHEP07(2014)079). arXiv: [1405.0301](https://arxiv.org/abs/1405.0301) [[hep-ph](#)] (cit. on p. 82).

- [119] Torbjörn Sjöstrand et al. “An introduction to PYTHIA 8.2”. In: *Comput. Phys. Commun.* 191 (2015), pp. 159–177. DOI: [10.1016/j.cpc.2015.01.024](https://doi.org/10.1016/j.cpc.2015.01.024). arXiv: [1410.3012](https://arxiv.org/abs/1410.3012) [hep-ph] (cit. on p. 82).
- [120] ATLAS Collaboration. *ATLAS Run 1 Pythia8 tunes*. ATL-PHYS-PUB-2014-021. 2014. URL: <http://cdsweb.cern.ch/record/1966419> (cit. on pp. 82, 135).
- [121] Richard D. Ball et al. “Parton distributions with LHC data”. In: *Nucl. Phys. B* 867 (2013), pp. 244–289. DOI: [10.1016/j.nuclphysb.2012.10.003](https://doi.org/10.1016/j.nuclphysb.2012.10.003). arXiv: [1207.1303](https://arxiv.org/abs/1207.1303) [hep-ph] (cit. on p. 82).
- [122] Enrico Bothmann et al. “Event generation with Sherpa 2.2”. In: *SciPost Phys.* 7.3 (2019), p. 034. DOI: [10.21468/SciPostPhys.7.3.034](https://doi.org/10.21468/SciPostPhys.7.3.034). arXiv: [1905.09127](https://arxiv.org/abs/1905.09127) [hep-ph] (cit. on p. 82).
- [123] Richard D. Ball et al. “Parton distributions for the LHC Run II”. In: *JHEP* 04 (2015), p. 040. DOI: [10.1007/JHEP04\(2015\)040](https://doi.org/10.1007/JHEP04(2015)040). arXiv: [1410.8849](https://arxiv.org/abs/1410.8849) [hep-ph] (cit. on pp. 82, 83).
- [124] Tanju Gleisberg and Stefan Höche. “Comix, a new matrix element generator”. In: *JHEP* 12 (2008), p. 039. DOI: [10.1088/1126-6708/2008/12/039](https://doi.org/10.1088/1126-6708/2008/12/039). arXiv: [0808.3674](https://arxiv.org/abs/0808.3674) [hep-ph] (cit. on p. 82).
- [125] Fabio Cascioli, Philipp Maierhöfer, and Stefano Pozzorini. “Scattering Amplitudes with Open Loops”. In: *Phys. Rev. Lett.* 108 (2012), p. 111601. DOI: [10.1103/PhysRevLett.108.111601](https://doi.org/10.1103/PhysRevLett.108.111601). arXiv: [1111.5206](https://arxiv.org/abs/1111.5206) [hep-ph] (cit. on p. 82).
- [126] Ansgar Denner, Stefan Dittmaier, and Lars Hofer. “Collier: A fortran-based complex one-loop library in extended regularizations”. In: *Comput. Phys. Commun.* 212 (2017), pp. 220–238. DOI: [10.1016/j.cpc.2016.10.013](https://doi.org/10.1016/j.cpc.2016.10.013). arXiv: [1604.06792](https://arxiv.org/abs/1604.06792) [hep-ph] (cit. on p. 82).
- [127] Steffen Schumann and Frank Krauss. “A parton shower algorithm based on Catani-Seymour dipole factorisation”. In: *JHEP* 03 (2008), p. 038. DOI: [10.1088/1126-6708/2008/03/038](https://doi.org/10.1088/1126-6708/2008/03/038). arXiv: [0709.1027](https://arxiv.org/abs/0709.1027) [hep-ph] (cit. on p. 82).
- [128] Stefan Höche et al. “A critical appraisal of NLO+PS matching methods”. In: *JHEP* 09 (2012), p. 049. DOI: [10.1007/JHEP09\(2012\)049](https://doi.org/10.1007/JHEP09(2012)049). arXiv: [1111.1220](https://arxiv.org/abs/1111.1220) [hep-ph] (cit. on p. 82).
- [129] Stefan Höche et al. “QCD matrix elements + parton showers. The NLO case”. In: *JHEP* 04 (2013), p. 027. DOI: [10.1007/JHEP04\(2013\)027](https://doi.org/10.1007/JHEP04(2013)027). arXiv: [1207.5030](https://arxiv.org/abs/1207.5030) [hep-ph] (cit. on p. 82).
- [130] S. Catani et al. “QCD Matrix Elements + Parton Showers”. In: *JHEP* 11 (2001), p. 063. DOI: [10.1088/1126-6708/2001/11/063](https://doi.org/10.1088/1126-6708/2001/11/063). arXiv: [hep-ph/0109231](https://arxiv.org/abs/hep-ph/0109231) (cit. on p. 82).
- [131] Stefan Höche et al. “QCD matrix elements and truncated showers”. In: *JHEP* 05 (2009), p. 053. DOI: [10.1088/1126-6708/2009/05/053](https://doi.org/10.1088/1126-6708/2009/05/053). arXiv: [0903.1219](https://arxiv.org/abs/0903.1219) [hep-ph] (cit. on p. 82).

- [132] Charalampos Anastasiou et al. “High-precision QCD at hadron colliders: Electroweak gauge boson rapidity distributions at next-to-next-to leading order”. In: *Phys. Rev. D* 69 (2004), p. 094008. DOI: [10.1103/PhysRevD.69.094008](https://doi.org/10.1103/PhysRevD.69.094008). arXiv: [hep-ph/0312266](https://arxiv.org/abs/hep-ph/0312266) (cit. on p. 82).
- [133] Stefano Frixione, Paolo Nason, and Giovanni Ridolfi. “A positive-weight next-to-leading-order Monte Carlo for heavy flavour hadroproduction”. In: *JHEP* 09 (2007), p. 126. DOI: [10.1088/1126-6708/2007/09/126](https://doi.org/10.1088/1126-6708/2007/09/126). arXiv: [0707.3088](https://arxiv.org/abs/0707.3088) [[hep-ph](https://arxiv.org/abs/0707.3088)] (cit. on p. 83).
- [134] Paolo Nason. “A New method for combining NLO QCD with shower Monte Carlo algorithms”. In: *JHEP* 11 (2004), p. 040. DOI: [10.1088/1126-6708/2004/11/040](https://doi.org/10.1088/1126-6708/2004/11/040). arXiv: [hep-ph/0409146](https://arxiv.org/abs/hep-ph/0409146) (cit. on p. 83).
- [135] Stefano Frixione, Paolo Nason, and Carlo Oleari. “Matching NLO QCD computations with Parton Shower simulations: the POWHEG method”. In: *JHEP* 11 (2007), p. 070. DOI: [10.1088/1126-6708/2007/11/070](https://doi.org/10.1088/1126-6708/2007/11/070). arXiv: [0709.2092](https://arxiv.org/abs/0709.2092) [[hep-ph](https://arxiv.org/abs/0709.2092)] (cit. on p. 83).
- [136] Simone Alioli et al. “A general framework for implementing NLO calculations in shower Monte Carlo programs: the POWHEG BOX”. In: *JHEP* 06 (2010), p. 043. DOI: [10.1007/JHEP06\(2010\)043](https://doi.org/10.1007/JHEP06(2010)043). arXiv: [1002.2581](https://arxiv.org/abs/1002.2581) [[hep-ph](https://arxiv.org/abs/1002.2581)] (cit. on p. 83).
- [137] ATLAS Collaboration. *Studies on top-quark Monte Carlo modelling for Top2016*. ATL-PHYS-PUB-2016-020. 2016. URL: <https://cds.cern.ch/record/2216168> (cit. on p. 83).
- [138] D. J. Lange. “The EvtGen particle decay simulation package”. In: *Nucl. Instrum. Meth. A* 462 (2001), p. 152. DOI: [10.1016/S0168-9002\(01\)00089-4](https://doi.org/10.1016/S0168-9002(01)00089-4) (cit. on p. 83).
- [139] Emanuele Re. “Single-top Wt-channel production matched with parton showers using the POWHEG method”. In: *Eur. Phys. J. C* 71 (2011), p. 1547. DOI: [10.1140/epjc/s10052-011-1547-z](https://doi.org/10.1140/epjc/s10052-011-1547-z). arXiv: [1009.2450](https://arxiv.org/abs/1009.2450) [[hep-ph](https://arxiv.org/abs/1009.2450)] (cit. on p. 83).
- [140] Simone Alioli et al. “NLO single-top production matched with shower in POWHEG: s- and t-channel contributions”. In: *JHEP* 09 (2009). [Erratum: *JHEP* 02, 011 (2010)], p. 111. DOI: [10.1088/1126-6708/2009/09/111](https://doi.org/10.1088/1126-6708/2009/09/111). arXiv: [0907.4076](https://arxiv.org/abs/0907.4076) [[hep-ph](https://arxiv.org/abs/0907.4076)] (cit. on p. 83).
- [141] Stefano Frixione et al. “Single-top hadroproduction in association with a W boson”. In: *JHEP* 07 (2008), p. 029. DOI: [10.1088/1126-6708/2008/07/029](https://doi.org/10.1088/1126-6708/2008/07/029). arXiv: [0805.3067](https://arxiv.org/abs/0805.3067) [[hep-ph](https://arxiv.org/abs/0805.3067)] (cit. on p. 83).
- [142] ATLAS Collaboration. *The Pythia 8 A3 tune description of ATLAS minimum bias and inelastic measurements incorporating the Donnachie-Landshoff diffractive model*. ATL-PHYS-PUB-2016-017. 2016. URL: <https://cds.cern.ch/record/2206965> (cit. on p. 83).

- [143] Daniel Joseph Antrim et al. *Search for Higgs boson pair production in the dileptonic  $WWbb$  channel in  $pp$  collisions at  $\sqrt{s} = 13$  TeV*. Tech. rep. ATL-COM-PHYS-2018-1491. Geneva: CERN, 2018. URL: <https://cds.cern.ch/record/2644924> (cit. on p. 91).
- [144] ATLAS Collaboration. “Search for non-resonant Higgs boson pair production in the  $b\bar{b}l\nu l\nu$  final state with the ATLAS detector in  $pp$  collisions at  $s=13$  TeV”. In: *Phys. Lett. B* 801 (2020), p. 135145. ISSN: 0370-2693. DOI: 10.1016/j.physletb.2019.135145. URL: <http://www.sciencedirect.com/science/article/pii/S0370269319308676> (cit. on p. 91).
- [145] William Buttinger and Michel Lefebvre. *Formulae for Estimating Significance*. Tech. rep. ATL-COM-GEN-2018-026. Geneva: CERN, 2018. URL: <https://cds.cern.ch/record/2643488> (cit. on p. 97).
- [146] G. Cowan. *Statistical data analysis*. Oxford science publications. 1998 (cit. on p. 108).
- [147] ATLAS Collaboration. “Measurement of the cross-section for electroweak production of dijets in association with a Z boson in  $pp$  collisions at  $\sqrt{s} = 13$  TeV with the ATLAS detector”. In: (2017). DOI: 10.1016/j.physletb.2017.10.040. arXiv: 1709.10264 [hep-ex] (cit. on p. 112).
- [148] M. Oreglia. “A Study of the Reactions  $\psi' \rightarrow \gamma\gamma\psi$ ”. PhD thesis. SLAC, 1980. URL: <https://www.slac.stanford.edu/cgi-bin/getdoc/slac-r-236.pdf> (cit. on p. 119).
- [149] Jean Duchon. “Interpolation des fonctions de deux variables suivant le principe de la flexion des plaques minces”. fre. In: *ESAIM: Mathematical Modelling and Numerical Analysis - Modélisation Mathématique et Analyse Numérique* 10.R3 (1976), pp. 5–12. URL: <http://eudml.org/doc/193284> (cit. on p. 119).
- [150] R. Brun and F. Rademakers. “ROOT: An object oriented data analysis framework”. In: *Nucl. Instrum. Meth. A* 389 (1997). Ed. by M. Werlen and D. Perret-Gallix, pp. 81–86. DOI: 10.1016/S0168-9002(97)00048-X (cit. on pp. 125, 141).
- [151] ATLAS Collaboration. *Muon reconstruction and identification efficiency in ATLAS using the full Run 2  $pp$  collision data set at  $\sqrt{s}=13$  TeV*. Tech. rep. ATLAS-CONF-2020-030. Geneva: CERN, 2020. URL: <https://cds.cern.ch/record/2725736> (cit. on p. 130).
- [152] ATLAS Collaboration. “Jet energy scale and resolution measured in proton-proton collisions at  $\sqrt{s} = 13$  TeV with the ATLAS detector”. In: (2020). DOI: 10.3204/PUBDB-2020-02665. arXiv: 2007.02645 [hep-ex] (cit. on p. 130).
- [153] Carsten Bittrich. “Evidence for Scattering of Electroweak Gauge Bosons in the  $W^\pm Z$  Channel with the ATLAS Detector at the Large Hadron Collider”. Presented 14 Jul 2020. 2020. URL: <https://cds.cern.ch/record/2719126> (cit. on p. 132).

- [154] ATLAS Collaboration. “Jet energy measurement and its systematic uncertainty in proton-proton collisions at  $\sqrt{s}=7$  TeV with the ATLAS detector”. In: *Eur. Phys. J. C* 75 (2014), p. 17. DOI: [10.1140/epjc/s10052-014-3190-y](https://doi.org/10.1140/epjc/s10052-014-3190-y) (cit. on p. 132).
- [155] M.R. Whalley, D. Bourilkov, and R.C. Group. “The Les Houches accord PDFs (LHAPDF) and LHAGLUE”. In: *HERA and the LHC: A Workshop on the Implications of HERA and LHC Physics (Startup Meeting, CERN, 26-27 March 2004; Midterm Meeting, CERN, 11-13 October 2004)*. 2005, pp. 575–581. arXiv: [hep-ph/0508110](https://arxiv.org/abs/hep-ph/0508110) (cit. on p. 136).
- [156] Jon Butterworth et al. “PDF4LHC recommendations for LHC Run II”. In: *J. Phys. G* 43 (2016), p. 023001. DOI: [10.1088/0954-3899/43/2/023001](https://doi.org/10.1088/0954-3899/43/2/023001). arXiv: [1510.03865](https://arxiv.org/abs/1510.03865) [[hep-ph](https://arxiv.org/archive/hep)] (cit. on p. 136).
- [157] Kyle Cranmer. “Practical Statistics for the LHC”. In: *2011 European School of High-Energy Physics*. 2014, pp. 267–308. DOI: [10.5170/CERN-2014-003.267](https://doi.org/10.5170/CERN-2014-003.267). arXiv: [1503.07622](https://arxiv.org/abs/1503.07622) [[physics.data-an](https://arxiv.org/archive/physics)] (cit. on p. 140).
- [158] S. S. Wilks. “The Large-Sample Distribution of the Likelihood Ratio for Testing Composite Hypotheses”. In: *Ann. Math. Statist.* 9.1 (1938), pp. 60–62. DOI: [10.1214/aoms/1177732360](https://doi.org/10.1214/aoms/1177732360) (cit. on p. 140).
- [159] Alexander L. Read. “Presentation of search results: The CLs technique”. In: *J. Phys. G* 28.10 (2002), pp. 2693–2704. DOI: [10.1088/0954-3899/28/10/313](https://doi.org/10.1088/0954-3899/28/10/313) (cit. on p. 140).
- [160] Glen Cowan et al. “Asymptotic formulae for likelihood-based tests of new physics”. In: *Eur. Phys. J. C* 71 (2011). [Erratum: *Eur.Phys.J.C* 73, 2501 (2013)], p. 1554. DOI: [10.1140/epjc/s10052-011-1554-0](https://doi.org/10.1140/epjc/s10052-011-1554-0). arXiv: [1007.1727](https://arxiv.org/abs/1007.1727) [[physics.data-an](https://arxiv.org/archive/physics)] (cit. on pp. 141, 143).
- [161] Lorenzo Moneta et al. “The RooStats Project”. In: *PoS ACAT2010* (2010). Ed. by T. Speer et al., p. 057. DOI: [10.22323/1.093.0057](https://doi.org/10.22323/1.093.0057). arXiv: [1009.1003](https://arxiv.org/abs/1009.1003) [[physics.data-an](https://arxiv.org/archive/physics)] (cit. on p. 141).
- [162] Wouter Verkerke and David Kirkby. “The RooFit toolkit for data modeling”. In: (2003). DOI: [10.1142/9781860948985\\_0039](https://doi.org/10.1142/9781860948985_0039) (cit. on p. 141).
- [163] *Minuit2*. (accessed 2020-09-07). URL: <https://root.cern.ch/doc/master/Minuit2Page.html> (cit. on p. 141).
- [164] F. James and M. Roos. “Minuit - a system for function minimization and analysis of the parameter errors and correlations”. In: *Computer Physics Communications* 10.6 (1975), pp. 343–367. ISSN: 0010-4655. DOI: [10.1016/0010-4655\(75\)90039-9](https://doi.org/10.1016/0010-4655(75)90039-9). URL: <http://www.sciencedirect.com/science/article/pii/0010465575900399> (cit. on p. 141).

- [165] Andrey Ryzhov et al. *Study of electroweak WW/WZ/ZZ production in the semileptonic final states in association with a high-mass dijet system and limits on anomalous quartic gauge couplings with 13 TeV ATLAS data*. Tech. rep. ATL-COM-PHYS-2018-270. Geneva: CERN, 2018. URL: <https://cds.cern.ch/record/2310214> (cit. on p. 142).
- [166] M. Aaboud et al. “Measurement of the cross-section for producing a W boson in association with a single top quark in pp collisions at  $\sqrt{s} = 13$  TeV with ATLAS”. In: *Journal of High Energy Physics* 2018 (2018). DOI: [10.1007/JHEP01\(2018\)063](https://doi.org/10.1007/JHEP01(2018)063) (cit. on p. 142).
- [167] E. A. Nadaraya. “On Estimating Regression”. In: *Theory of Probability & Its Applications* 9.1 (1964), pp. 141–142. DOI: [10.1137/1109020](https://doi.org/10.1137/1109020) (cit. on p. 148).
- [168] Geoffrey S. Watson. “Smooth Regression Analysis”. In: *Sankhyā: The Indian Journal of Statistics, Series A (1961-2002)* 26.4 (1964), pp. 359–372. JSTOR: [25049340](https://www.jstor.org/stable/25049340) (cit. on p. 148).
- [169] Ofer Vitells and Eilam Gross. “Estimating the significance of a signal in a multi-dimensional search”. In: *Astropart. Phys.* 35 (2011), pp. 230–234. DOI: [10.1016/j.astropartphys.2011.08.005](https://doi.org/10.1016/j.astropartphys.2011.08.005). arXiv: [1105.4355](https://arxiv.org/abs/1105.4355) [astro-ph.IM] (cit. on p. 156).
- [170] Pierre Baldi et al. “Parameterized neural networks for high-energy physics”. In: *Eur. Phys. J. C* 76.5 (2016), p. 235. DOI: [10.1140/epjc/s10052-016-4099-4](https://doi.org/10.1140/epjc/s10052-016-4099-4). arXiv: [1601.07913](https://arxiv.org/abs/1601.07913) [hep-ex] (cit. on p. 161).
- [171] ATLAS Collaboration. *Search for charged Higgs bosons decaying into a top-quark and a bottom-quark at  $\sqrt{s} = 13$  TeV with the ATLAS detector*. Tech. rep. ATLAS-CONF-2020-039. Geneva: CERN, 2020. URL: <https://cds.cern.ch/record/2727860> (cit. on p. 161).
- [172] CMS Collaboration. *Search for resonant and non-resonant Higgs boson pair production in the  $b\bar{b}l\nu l\nu$  final state at  $\sqrt{s} = 13$  TeV*. Tech. rep. CMS-PAS-HIG-17-006. Geneva: CERN, 2017. URL: <https://cds.cern.ch/record/2257068> (cit. on p. 161).

**Part VI**

**Appendix**



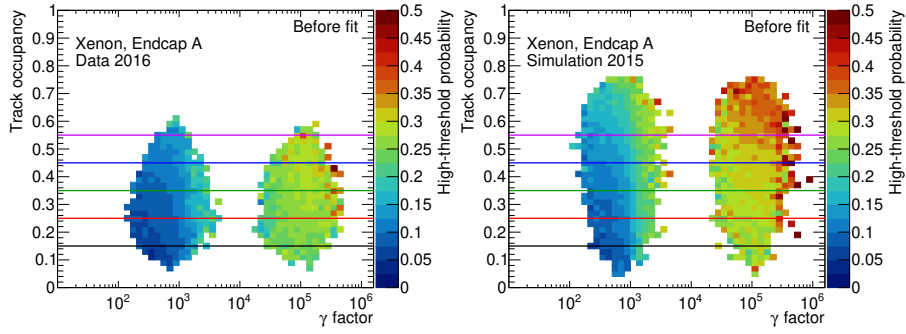
**Contents**

---

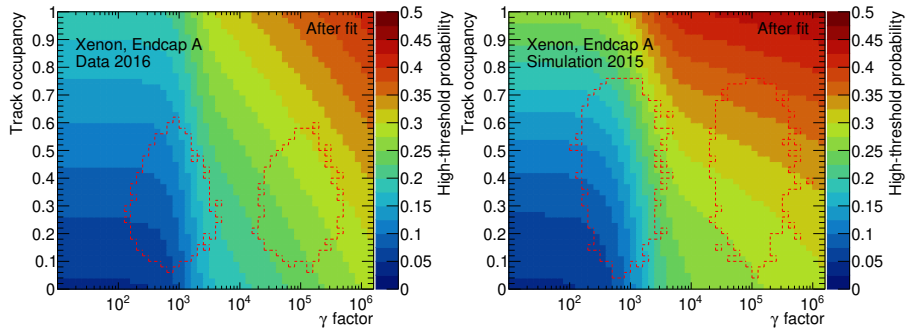
18.A Calibration results for all gases and TRT parts . . .	188
18.B z-scores between raw and fitted $p_{HT}$ . . . . .	198
18.C Probability ratio on data before and after simulation- tuned fit . . . . .	200
18.D Correction factors (CFs) . . . . .	202
18.E Probabilities for all CF configurations . . . . .	205
18.F CFs for different occupancy intervals . . . . .	206
18.G Performance for different CF configurations . . . . .	211
18.H Momentum to $\gamma$ factor . . . . .	213
18.I Track-based $p_{HT}$ method . . . . .	214

---

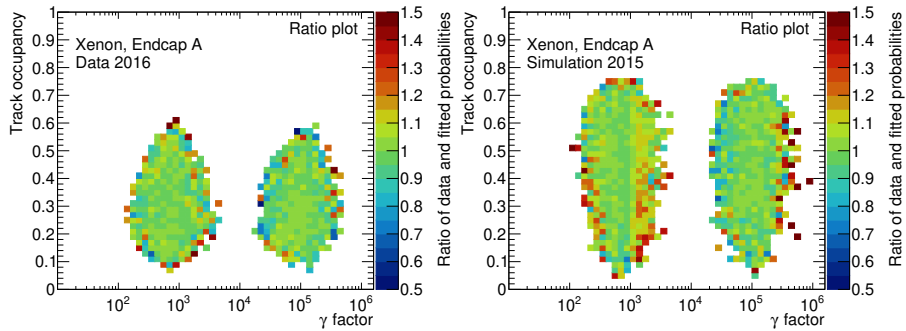
**18.A** Calibration results for all gases and TRT parts



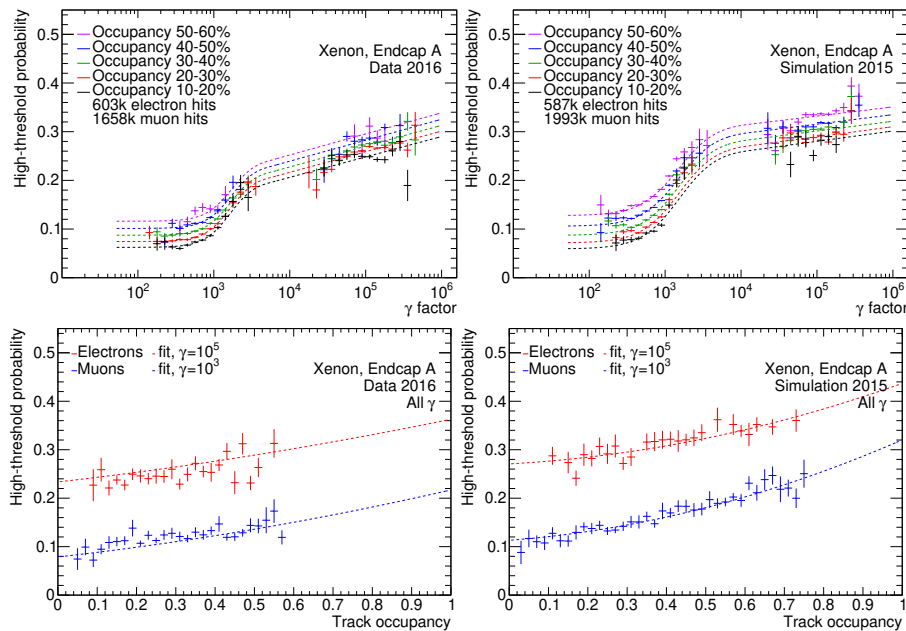
(a) The high-threshold fraction plotted as a function of the track occupancy and the  $\gamma$  factor with muons on the left and electrons on the right. This figure is only for xenon straws in the barrel. The colored lines correspond to the colored points on the upper sub-figures of the onset figures.



(b) The high-threshold fraction plotted as a function of the track occupancy and the  $\gamma$  factor after fitting. Muons are on the left and electrons are on the right.

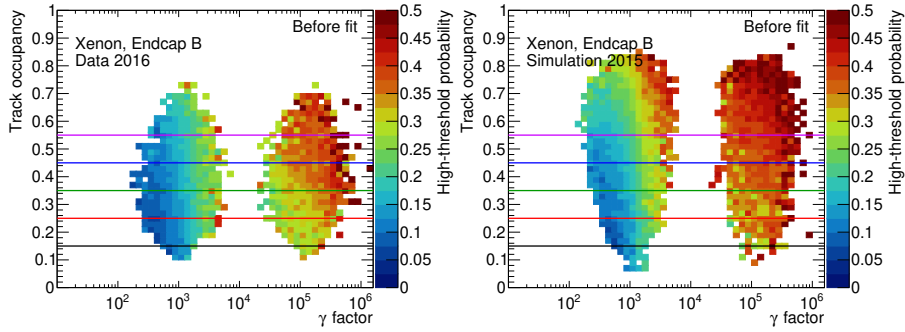


(c) Ratio of high-threshold fractions before and after the fit.

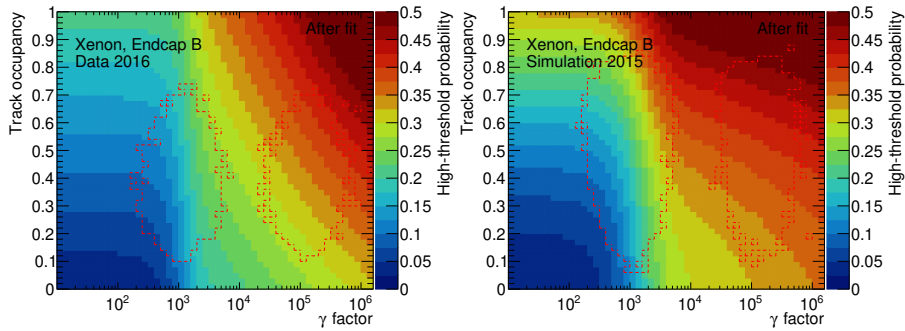


(d) Onset curves after fitting in slices of occupancy.

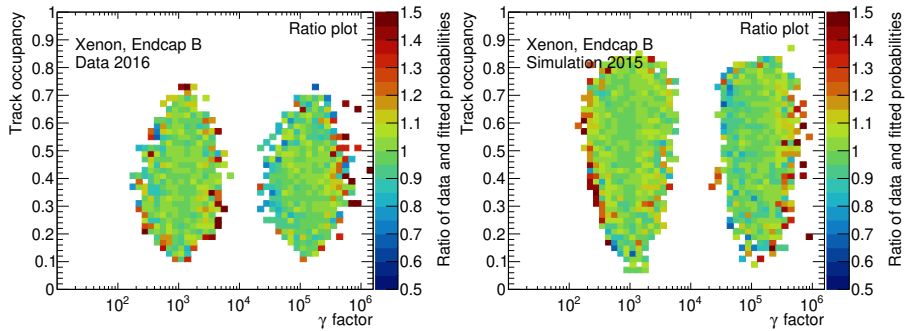
Figure 18.1: Calibrations results for all gases and TRT parts.



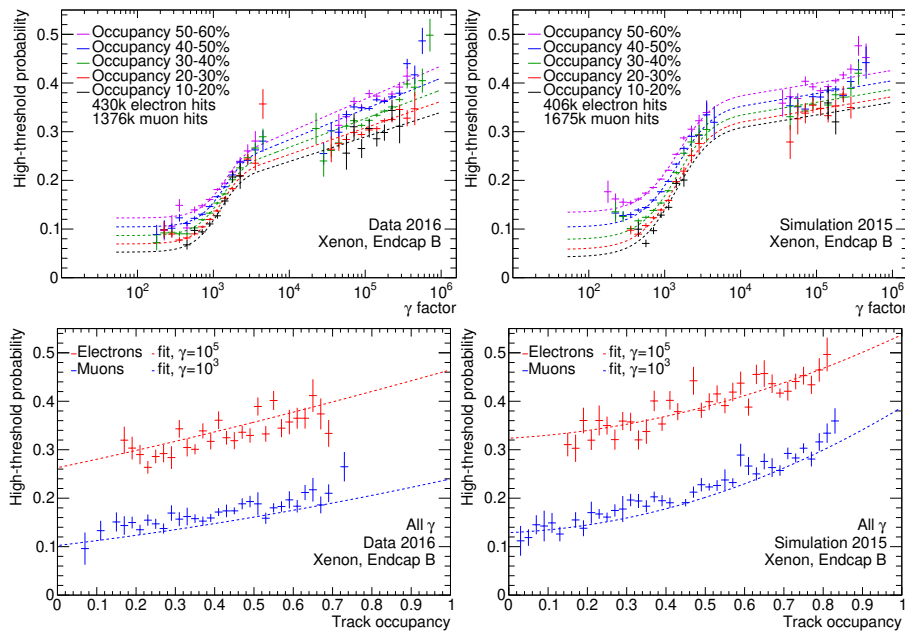
(a) The high-threshold fraction plotted as a function of the track occupancy and the  $\gamma$  factor with muons on the left and electrons on the right. This figure is only for xenon straws in the barrel. The colored lines correspond to the colored points on the upper sub-figures of the onset figures.



(b) The high-threshold fraction plotted as a function of the track occupancy and the  $\gamma$  factor after fitting. Muons are on the left and electrons are on the right.

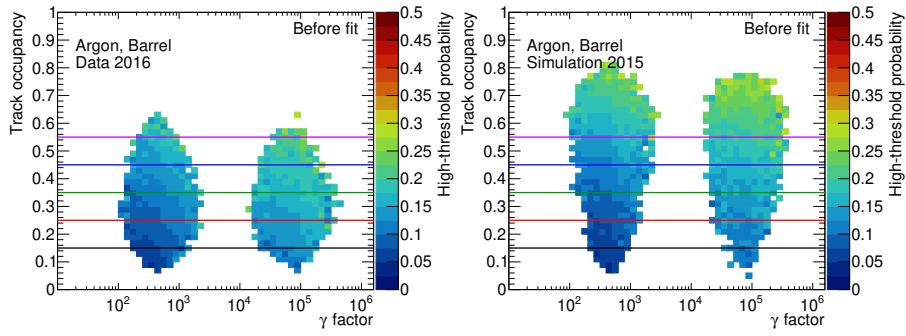


(c) Ratio of high-threshold fractions before and after the fit.

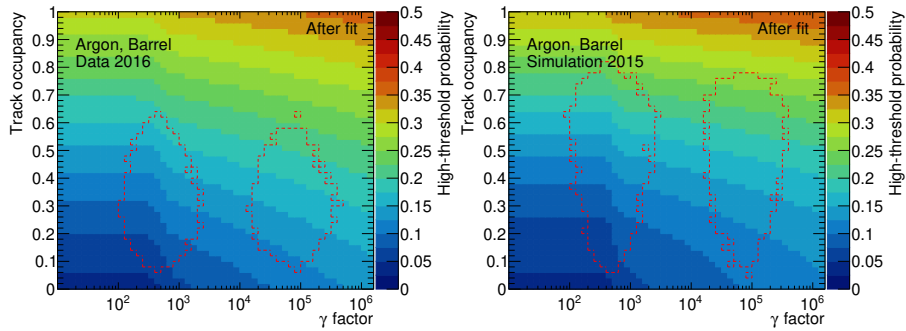


(d) Onset curves after fitting in slices of occupancy.

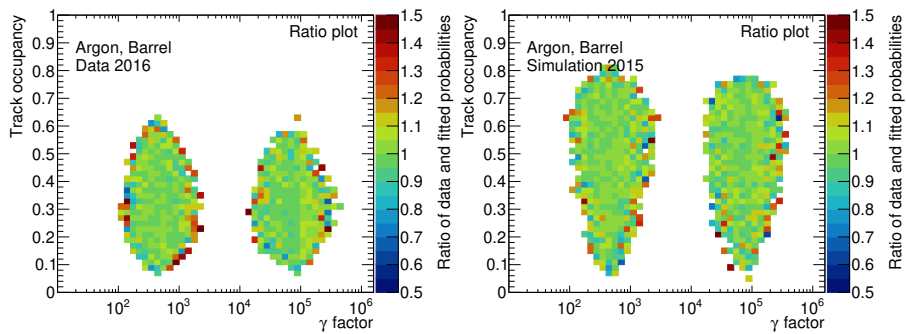
Figure 18.2: Calibrations results for all gases and TRT parts.



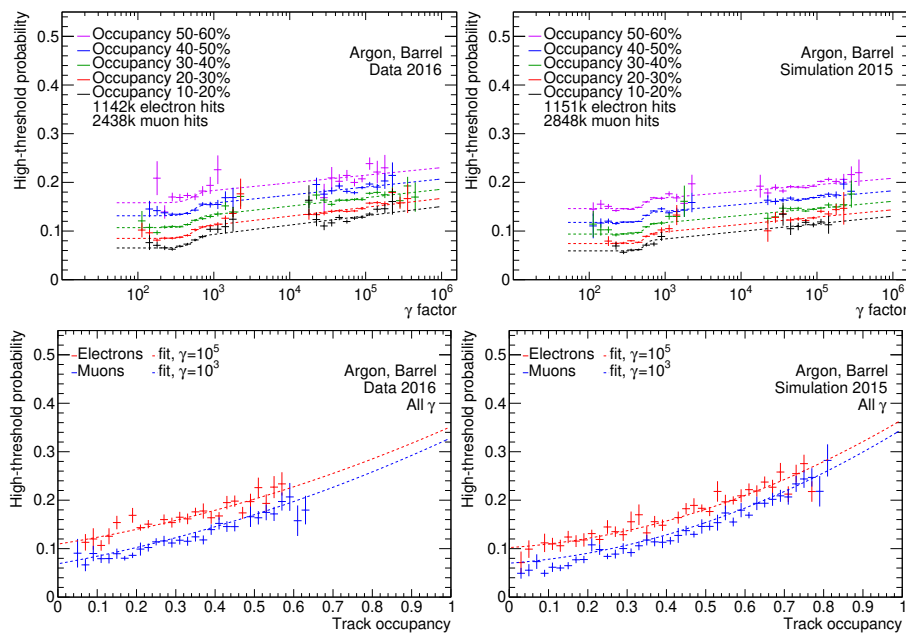
(a) The high-threshold fraction plotted as a function of the track occupancy and the  $\gamma$  factor with muons on the left and electrons on the right. This figure is only for xenon straws in the barrel. The colored lines correspond to the colored points on the upper sub-figures of the onset figures.



(b) The high-threshold fraction plotted as a function of the track occupancy and the  $\gamma$  factor after fitting. Muons are on the left and electrons are on the right.

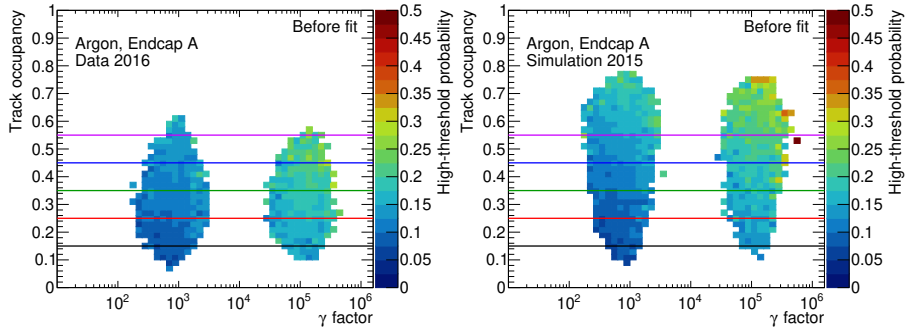


(c) Ratio of high-threshold fractions before and after the fit.

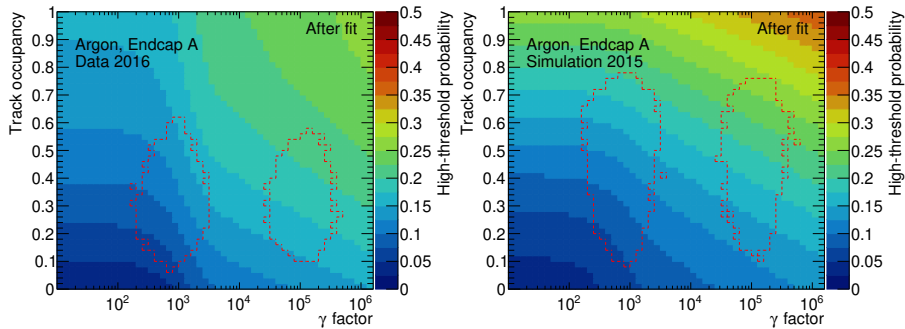


(d) Onset curves after fitting in slices of occupancy.

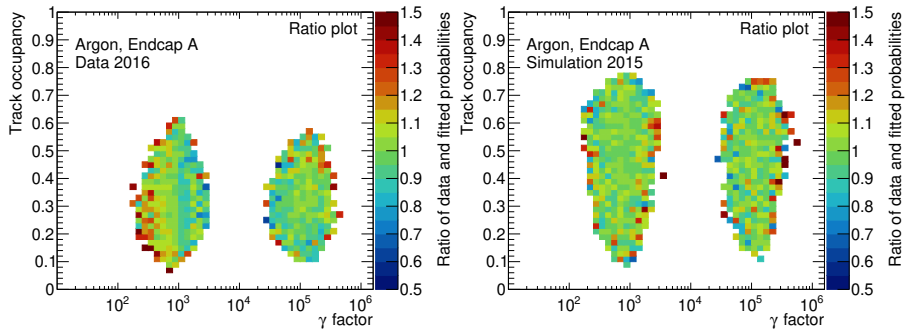
Figure 18.3: Calibrations results for all gases and TRT parts.



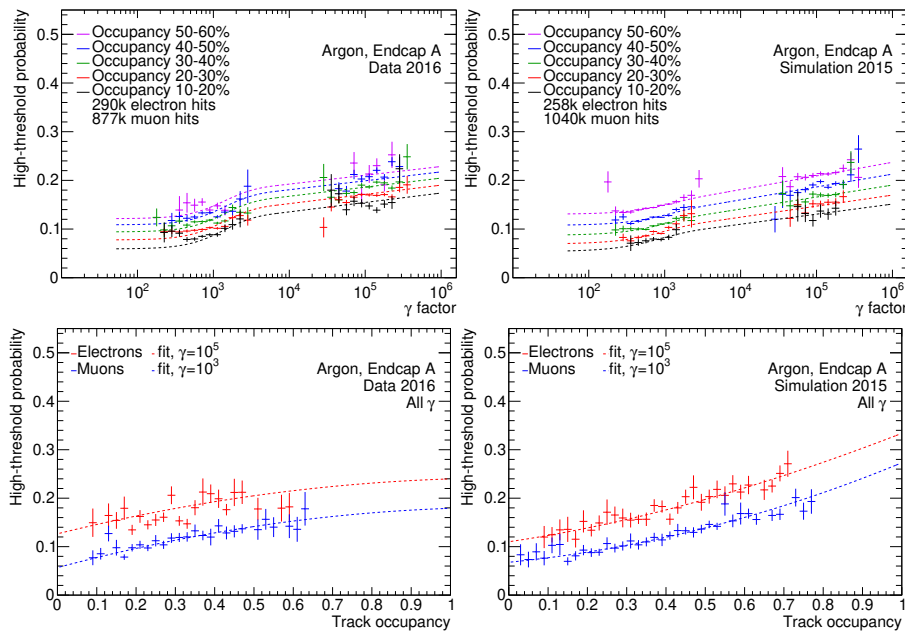
(a) The high-threshold fraction plotted as a function of the track occupancy and the  $\gamma$  factor with muons on the left and electrons on the right. This figure is only for xenon straws in the barrel. The colored lines correspond to the colored points on the upper sub-figures of the onset figures.



(b) The high-threshold fraction plotted as a function of the track occupancy and the  $\gamma$  factor after fitting. Muons are on the left and electrons are on the right.

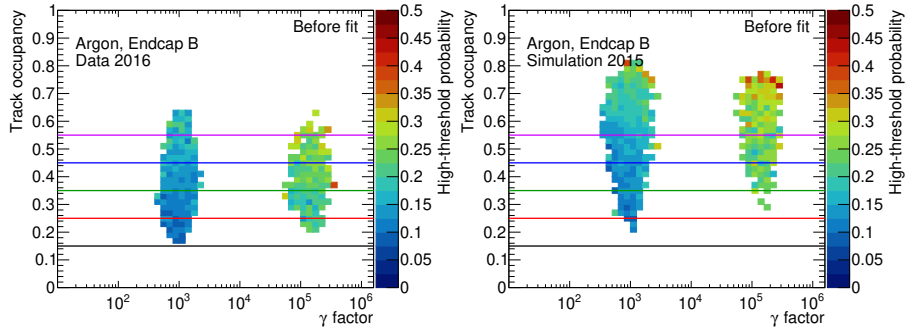


(c) Ratio of high-threshold fractions before and after the fit.

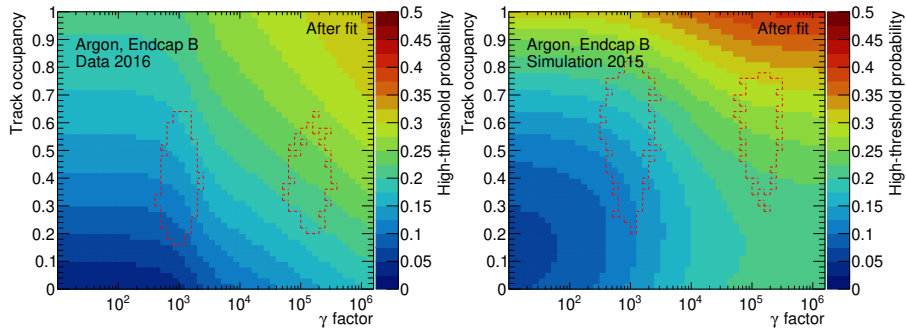


(d) Onset curves after fitting in slices of occupancy.

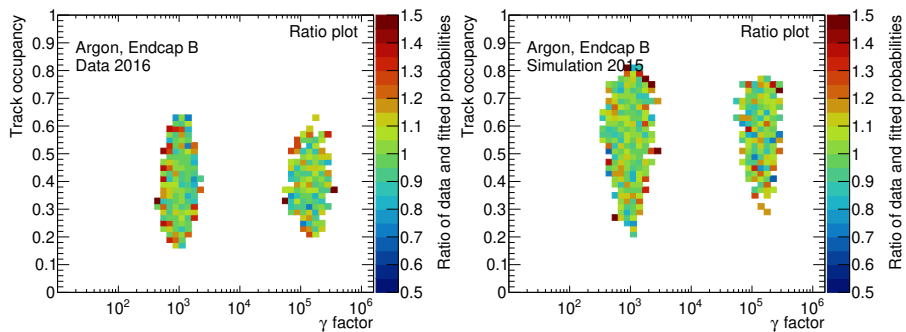
Figure 18.4: Calibrations results for all gases and TRT parts.



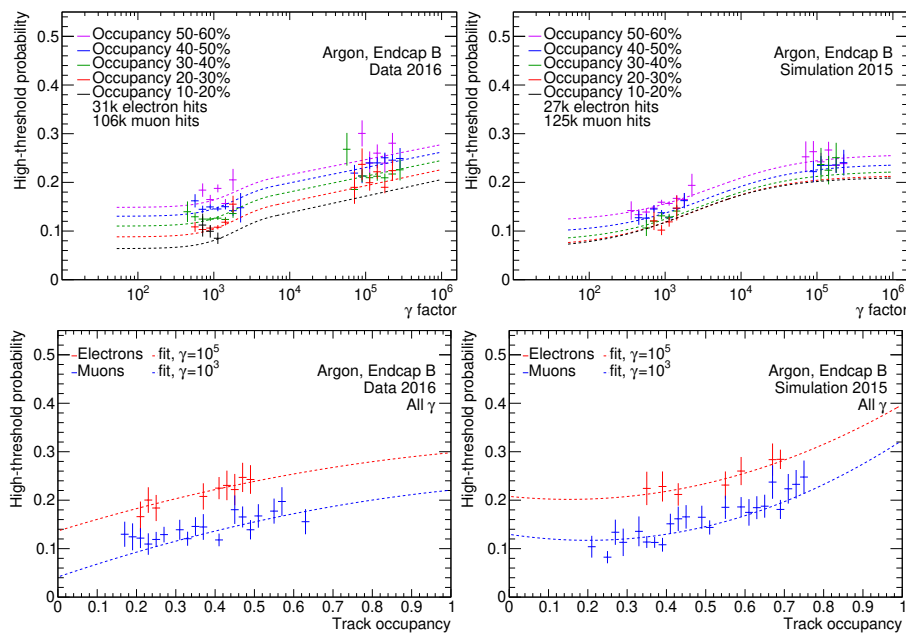
(a) The high-threshold fraction plotted as a function of the track occupancy and the  $\gamma$  factor with muons on the left and electrons on the right. This figure is only for xenon straws in the barrel. The colored lines correspond to the colored points on the upper sub-figures of the onset figures.



(b) The high-threshold fraction plotted as a function of the track occupancy and the  $\gamma$  factor after fitting. Muons are on the left and electrons are on the right.



(c) Ratio of high-threshold fractions before and after the fit.



(d) Onset curves after fitting in slices of occupancy.

Figure 18.5: Calibrations results for all gases and TRT parts.

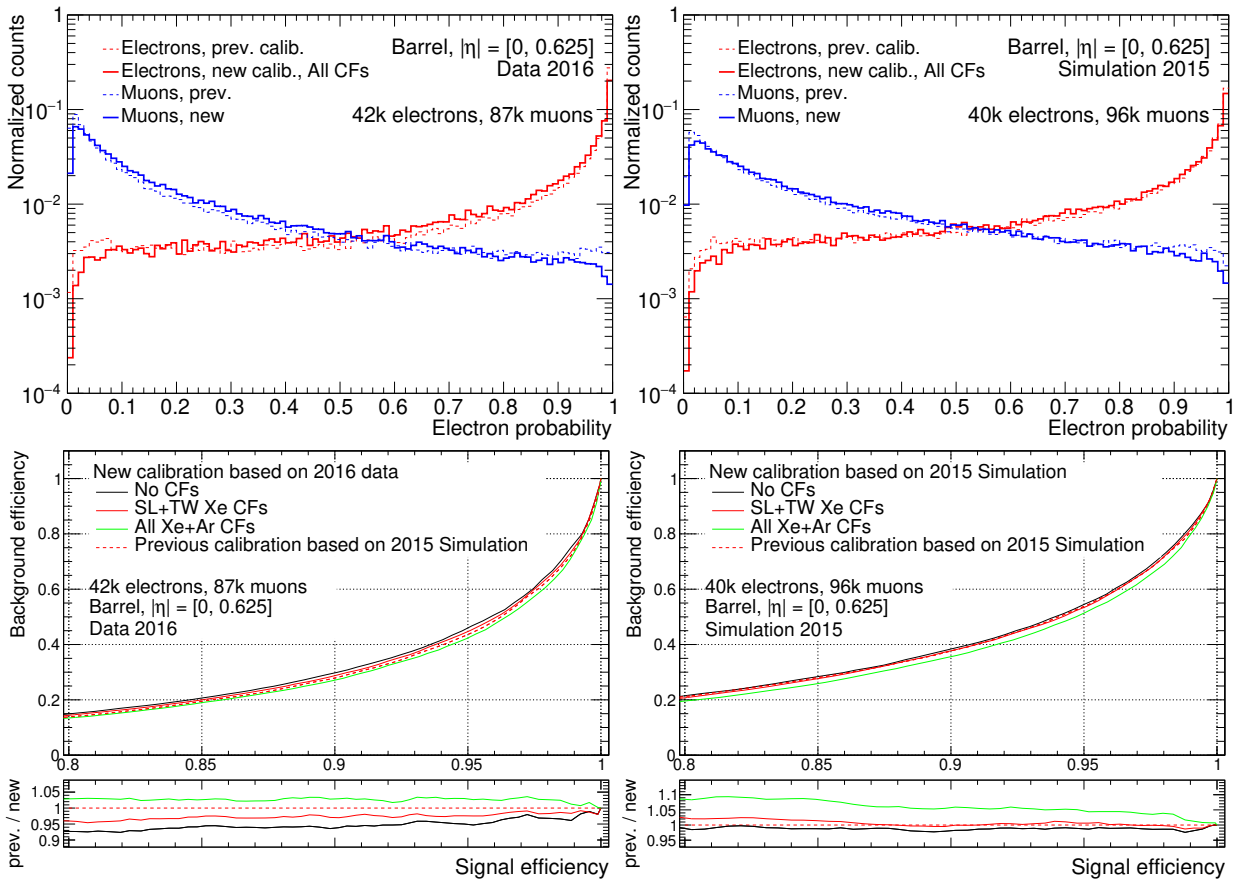


Figure 18.6: Upper: Electron and muon counts of electron probabilities for the previous and new tuning. Lower: ROC curves for the previous calibration as well as the new calibration with different choices of CF combinations. This figure is for an  $\eta$  range where hits will mostly be within the detector part given in the figure. See Fig. 18.9 for an explanation.

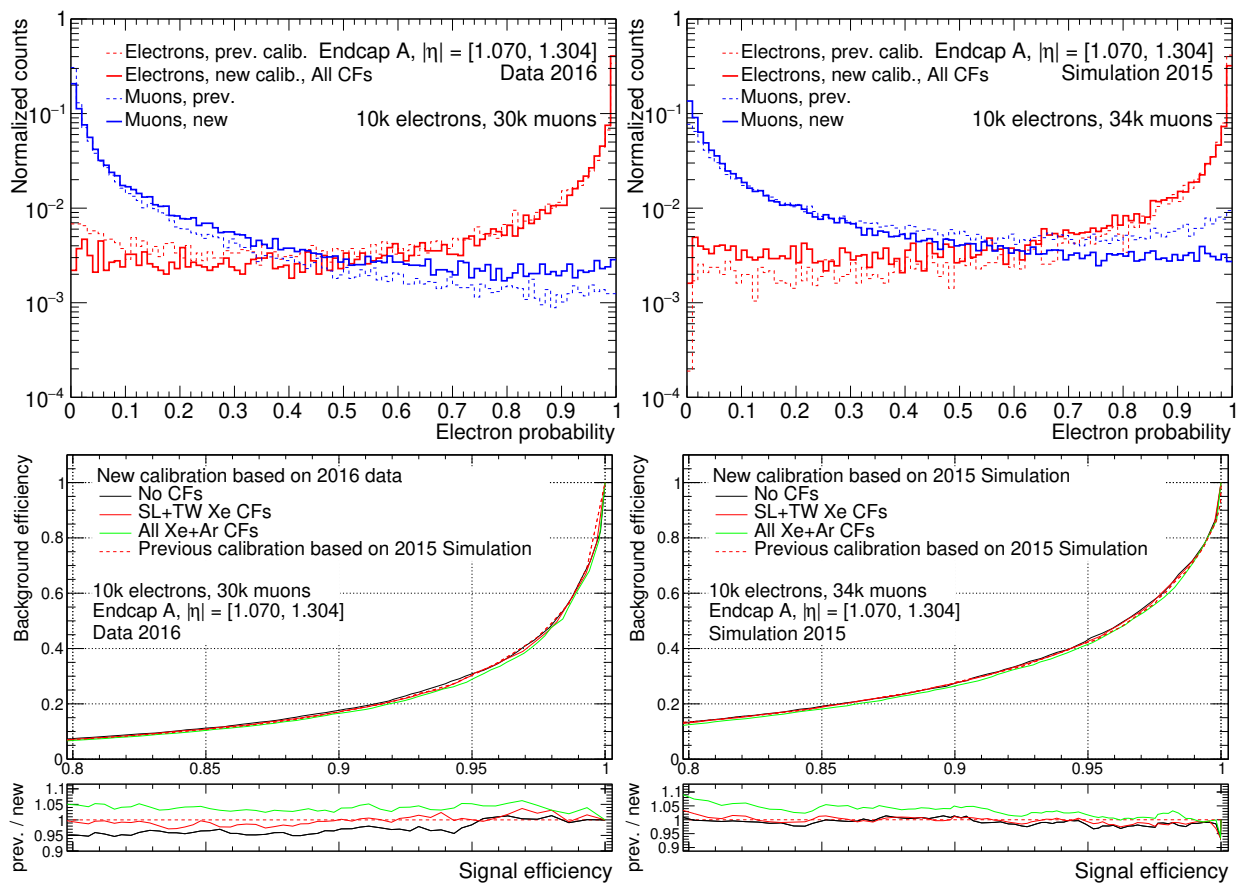


Figure 18.7: Upper: Electron and muon counts of electron probabilities for the previous and new tuning. Lower: ROC curves for the previous calibration as well as the new calibration with different choices of CF combinations. This figure is for an  $\eta$  range where hits will mostly be within the detector part given in the figure. See Fig. 18.9 for an explanation.

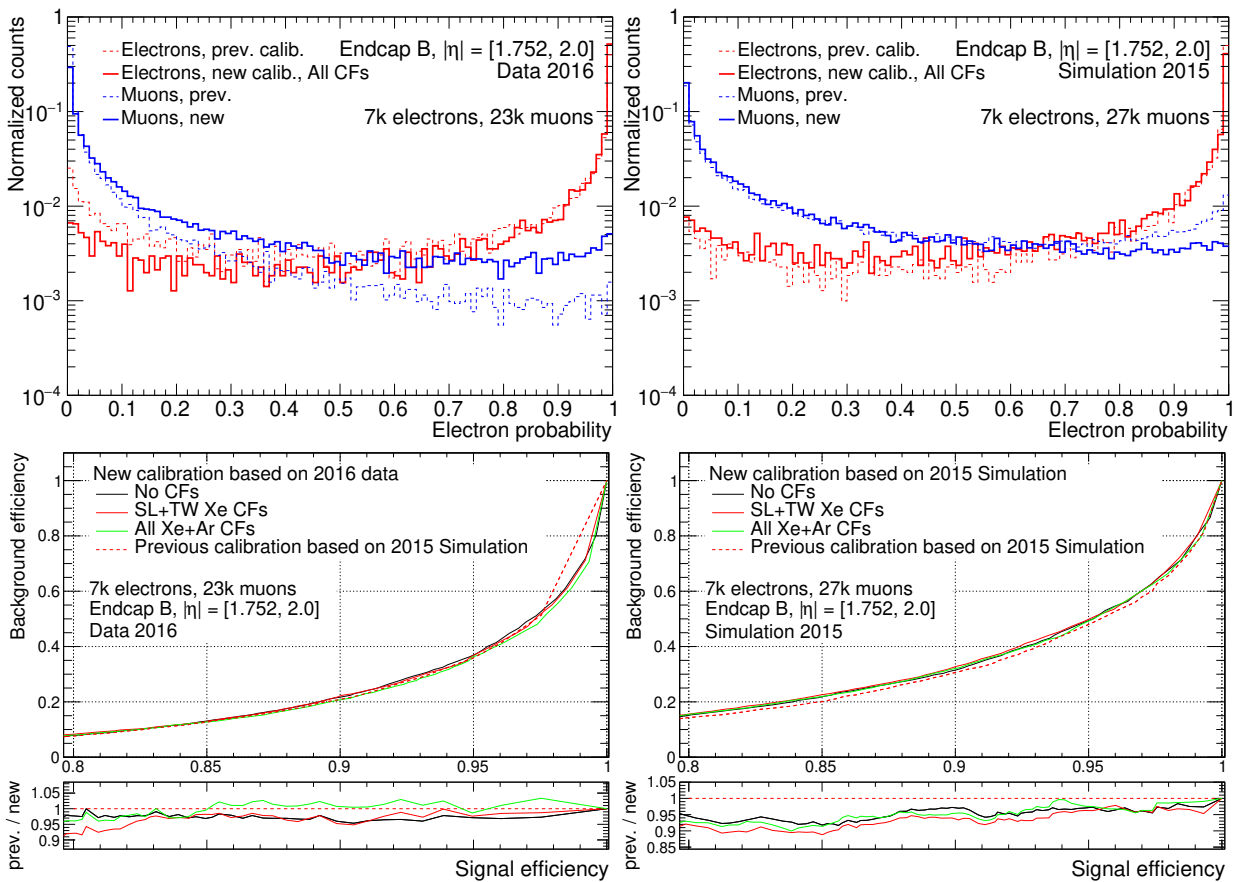


Figure 18.8: Upper: Electron and muon counts of electron probabilities for the previous and new tuning. Lower: ROC curves for the previous calibration as well as the new calibration with different choices of CF combinations. This figure is for an  $\eta$  range where hits will mostly be within the detector part given in the figure. See Fig. 18.9 for an explanation.

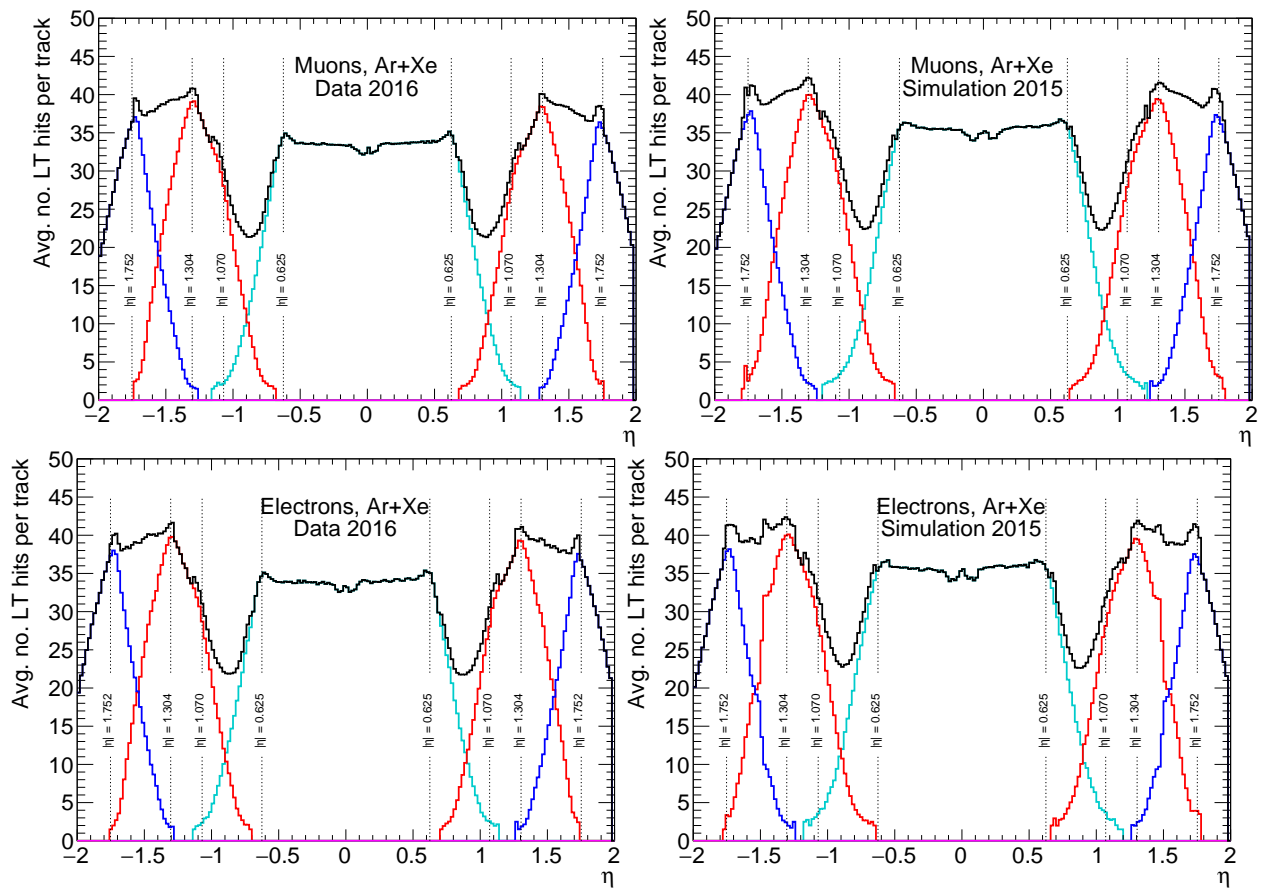


Figure 18.9: The ROC curves in this appendix are shown for three  $\eta$  regions of the detector corresponding to the barrel and the endcaps in which tracks will almost exclusively hit, according to this figure.

**18.B z-scores between raw and fitted  $p_{HT}$**

Fig. 6.2b in Sect. 6.1 shows the ratio between the raw high-threshold probabilities and those predicted by the fit. The ratio does not take uncertainties into account, hence the more noisy borders with lower statistics appearing red.

Instead, the z-score (significance) can be calculated, taking the uncertainties into account:

$$|z| = \frac{|p_{\text{raw}} - p_{\text{fit}}|}{\sqrt{\sigma_{\text{raw}}^2 + \sigma_{\text{fit}}^2}}. \tag{18.1}$$

The discrepancy between simulation and data in Fig. 18.10 is still visible, however, the edges now no longer show any deviation.

Figure 18.10: Absolute z-score between high-threshold fractions before and after fitting.

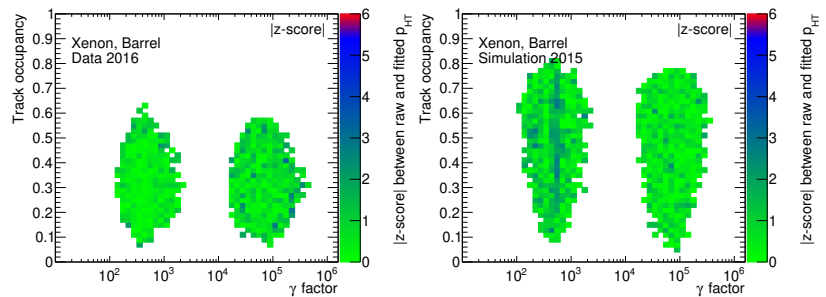


Figure 18.11: Absolute z-score between high-threshold fractions before and after fitting.

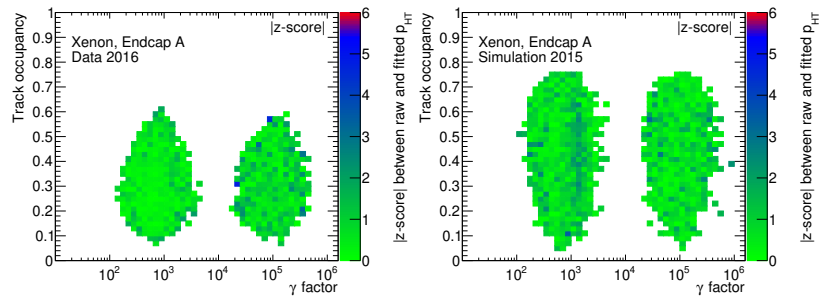
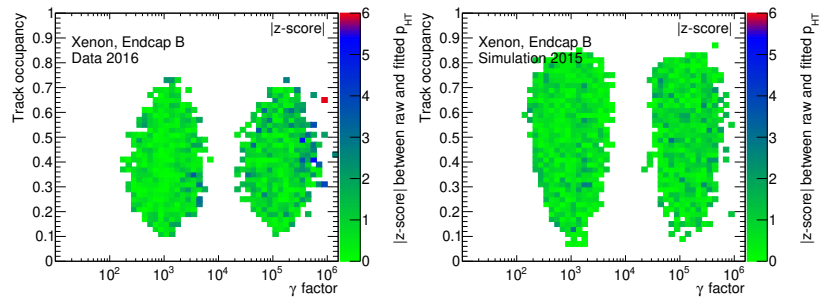


Figure 18.12: Absolute z-score between high-threshold fractions before and after fitting.



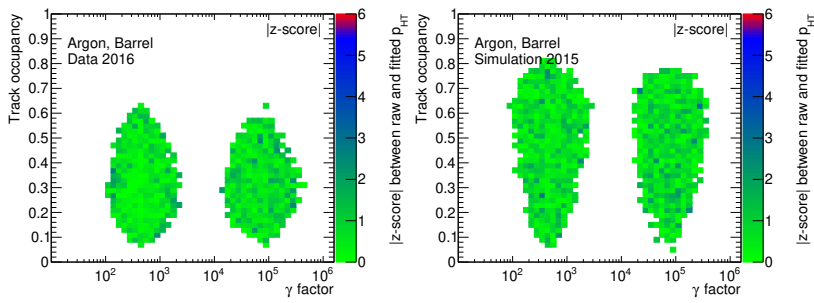


Figure 18.13: Absolute z-score between high-threshold fractions before and after fitting.

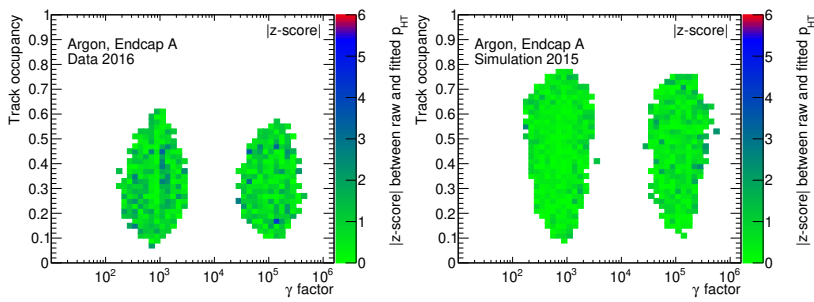


Figure 18.14: Absolute z-score between high-threshold fractions before and after fitting.

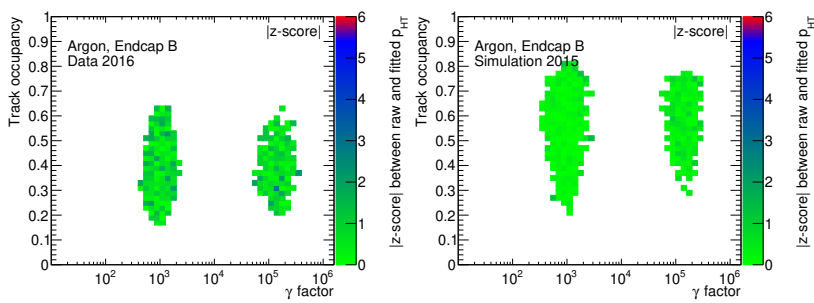


Figure 18.15: Absolute z-score between high-threshold fractions before and after fitting.

**18.C** Probability ratio on data before and after simulation-tuned fit

These are the ratio plots for Sect. 6.4.2 on simulation-tuned calibration used on data. The ratio plots show great differences. The simulation tuned calibration applied on data is shown on the right. For reference, the data on data plots are shown in the left.

Figure 18.16: The 2D fraction plot in data has been divided by the prediction from a simulation-tuned calibration. For reference, the data-tuned calibration applied on data is shown on the left.

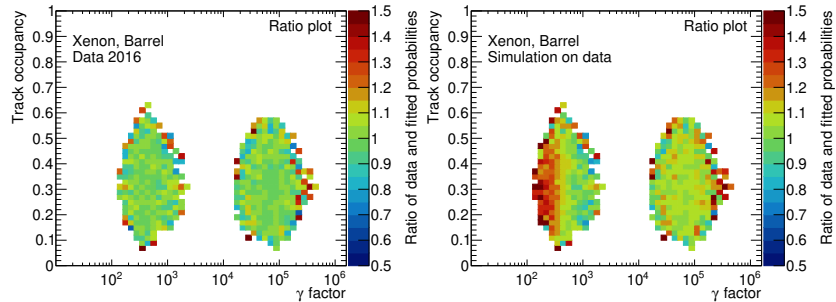


Figure 18.17: The 2D fraction plot in data has been divided by the prediction from a simulation-tuned calibration. For reference, the data-tuned calibration applied on data is shown on the left.

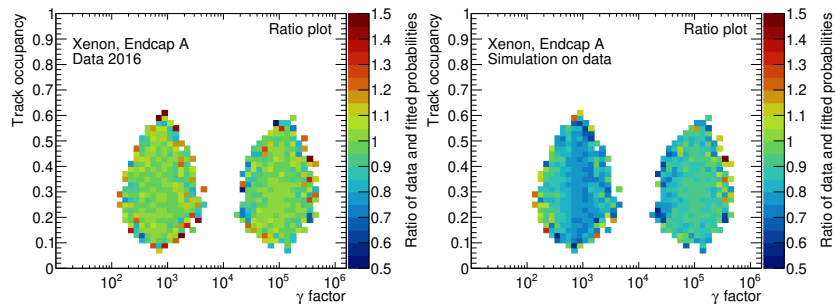
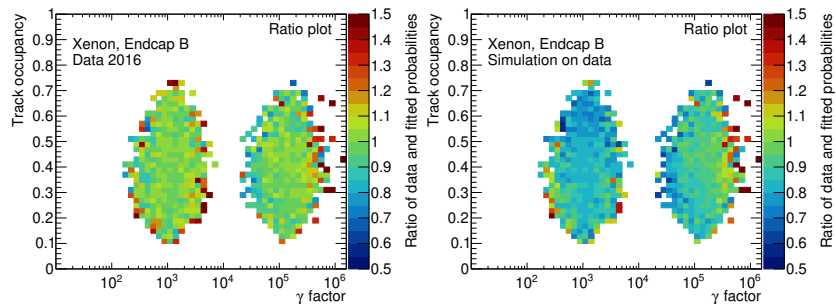


Figure 18.18: The 2D fraction plot in data has been divided by the prediction from a simulation-tuned calibration. For reference, the data-tuned calibration applied on data is shown on the left.



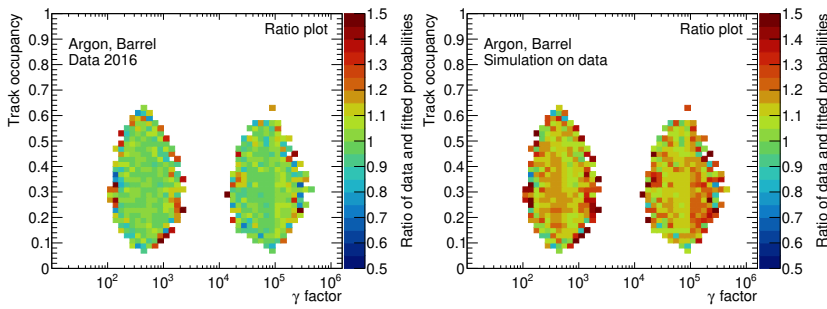


Figure 18.19: The 2D fraction plot in data has been divided by the prediction from a simulation-tuned calibration. For reference, the data-tuned calibration applied on data is shown on the left.

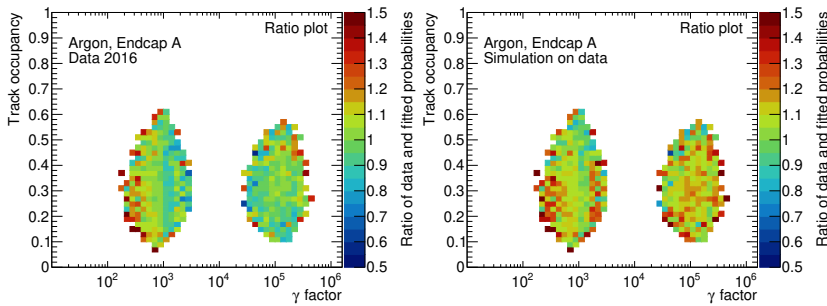


Figure 18.20: The 2D fraction plot in data has been divided by the prediction from a simulation-tuned calibration. For reference, the data-tuned calibration applied on data is shown on the left.

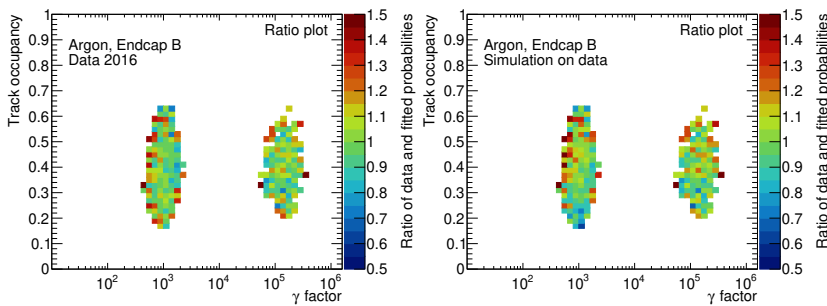


Figure 18.21: The 2D fraction plot in data has been divided by the prediction from a simulation-tuned calibration. For reference, the data-tuned calibration applied on data is shown on the left.

**18.D Correction factors (CFs)**

In this section, all three CFs (SL, ZR, TW) are plotted for electrons (top sub-figures) and muons (bottom sub-figures) with the usual data on the left and simulation on the right. The CFs are separated into barrel (main text) as well as endcap A and endcap B (this appendix) hits. The track-to-wire (TW) correction factor was capped at to 1.0 for  $TW \geq 2.0$  mm in the previous calibration. The reason for this has been uncertainty regarding the behavior in data, seeing as the radius of a TRT tube is 2.0 mm. The rising CF for  $TW > 2.0$  mm is also seen in data, and the main text (also App. 18.G) has shown that not capping at 2.0 mm improves performance.

Figure 18.22: Correction factor (SL, TW, or ZR) for the endcap A or endcap B. Electrons are on the top sub-figures, while muons are on the bottom sub-figures.

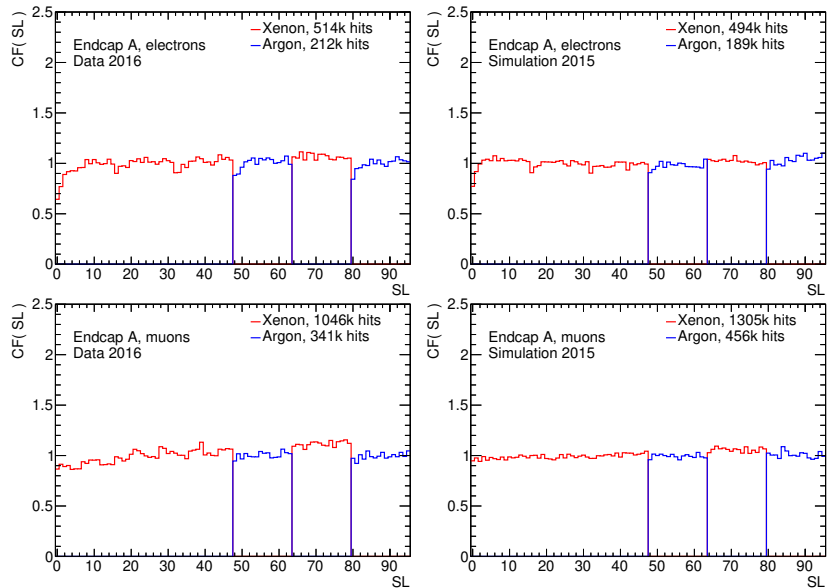
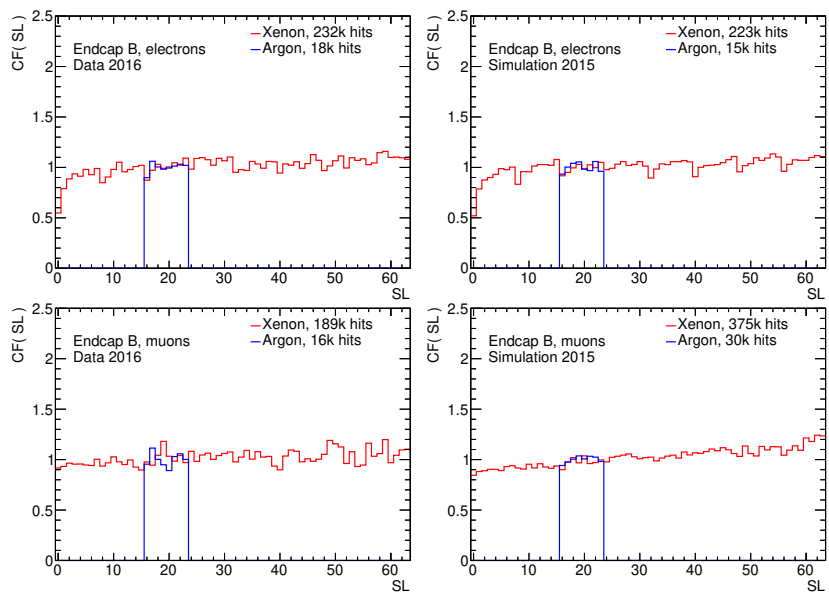


Figure 18.23: Correction factor (SL, TW, or ZR) for the endcap A or endcap B. Electrons are on the top sub-figures, while muons are on the bottom sub-figures.



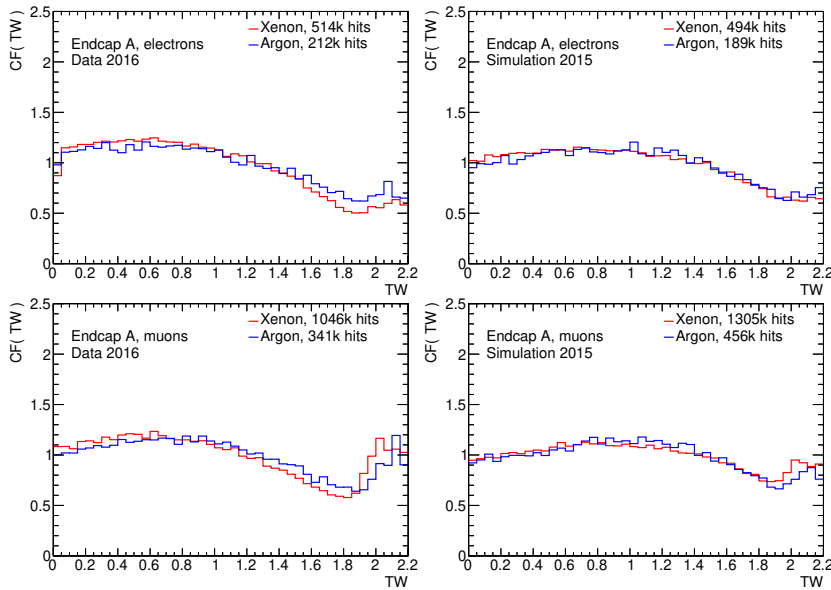


Figure 18.24: Correction factor (SL, TW, or ZR) for the endcap A or endcap B. Electrons are on the top sub-figures, while muons are on the bottom sub-figures.

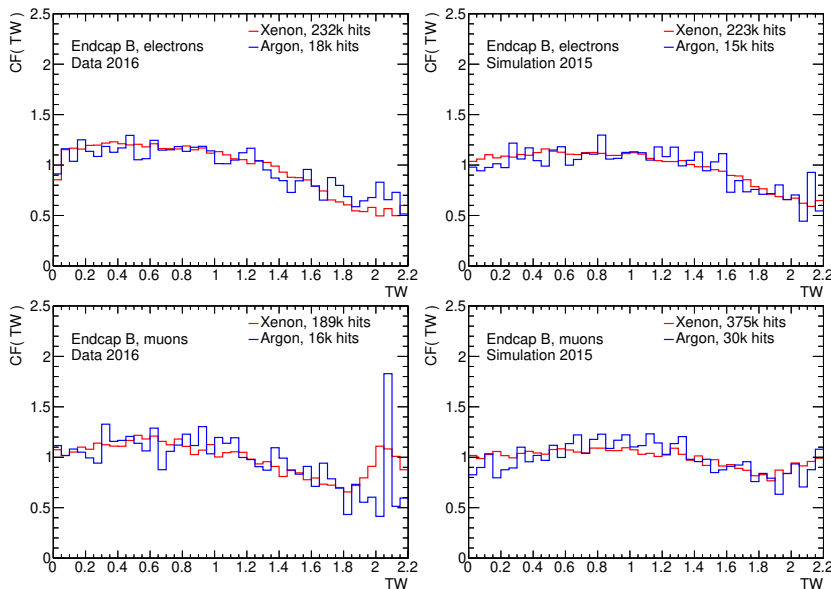


Figure 18.25: Correction factor (SL, TW, or ZR) for the endcap A or endcap B. Electrons are on the top sub-figures, while muons are on the bottom sub-figures.

Figure 18.26: Correction factor (SL, TW, or ZR) for the endcap A or endcap B. Electrons are on the top sub-figures, while muons are on the bottom sub-figures.

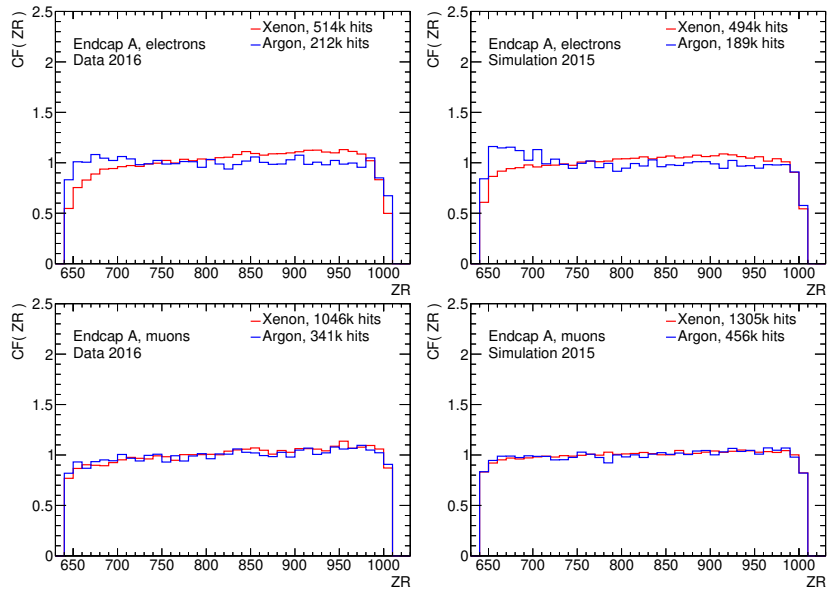
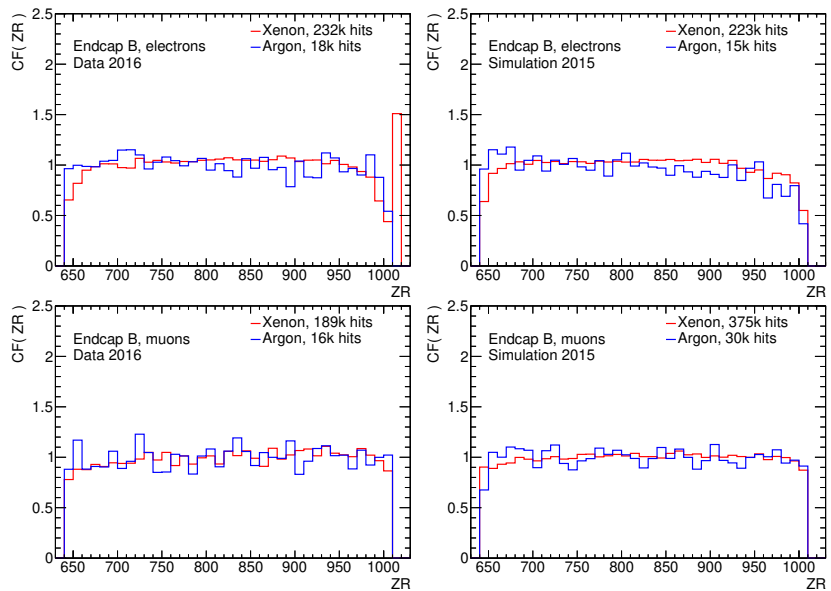


Figure 18.27: Correction factor (SL, TW, or ZR) for the endcap A or endcap B. Electrons are on the top sub-figures, while muons are on the bottom sub-figures.



## 18.E Probabilities for all CF configurations

Fig. 6.4 in simulation shows a significant increase in performance, due to the muon count now correctly falling for increasing electron probability. In data, an increase in electron count for *decreasing* electron probability was also seen using the previous calibration.

The electron probability figures only compare the previous calibration against the new calibration with all CFs. To show that the change in performance is not due to the additional CFs, the probabilities for all CF configurations are plotted in Fig. 18.28. Now, electrons and muons are shown in the same color, and the different colors denote the different CF configurations.

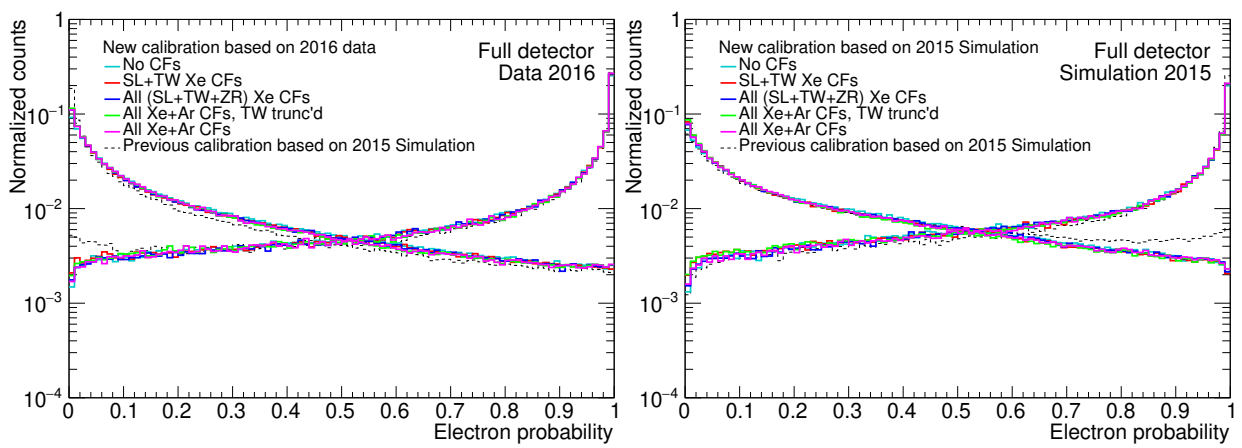


Figure 18.28: Probabilities with different sets of and no CFs with muons and electrons in the same color. The black, dashed line is the previous calibration for electrons. The change in performance is not due to the CFs.

## 18.F CFs for different occupancy intervals

To verify the claim that the correction factors indeed are not correlated with the occupancy, the CFs are computed for different intervals of occupancy. They are calculated for 3 slices of occupancy with each slice containing 1/3 of all entries from a 2D histogram of each variable against occupancy. The bin at which select is computed for each variable in each gas.

Figure 18.29: Correction factor (SL, TW, or ZR) for the barrel, endcap A, or endcap B. Electrons are on the top sub-figures, while muons are on the bottom sub-figures. The lighter colors show higher occupancy slices. Argon is only present in one wheel in endcap B, leading to very low statistics.

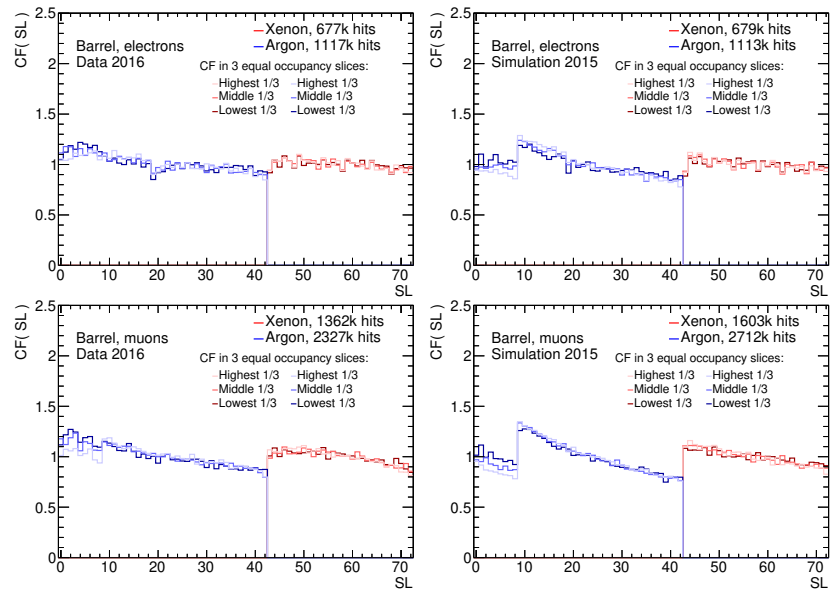
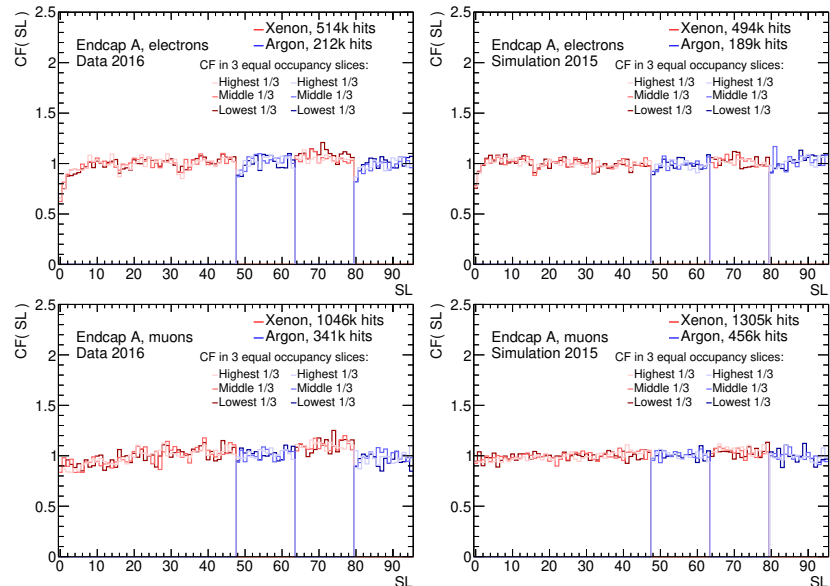


Figure 18.30: Correction factor (SL, TW, or ZR) for the barrel, endcap A, or endcap B. Electrons are on the top sub-figures, while muons are on the bottom sub-figures. The lighter colors show higher occupancy slices. Argon is only present in one wheel in endcap B, leading to very low statistics.



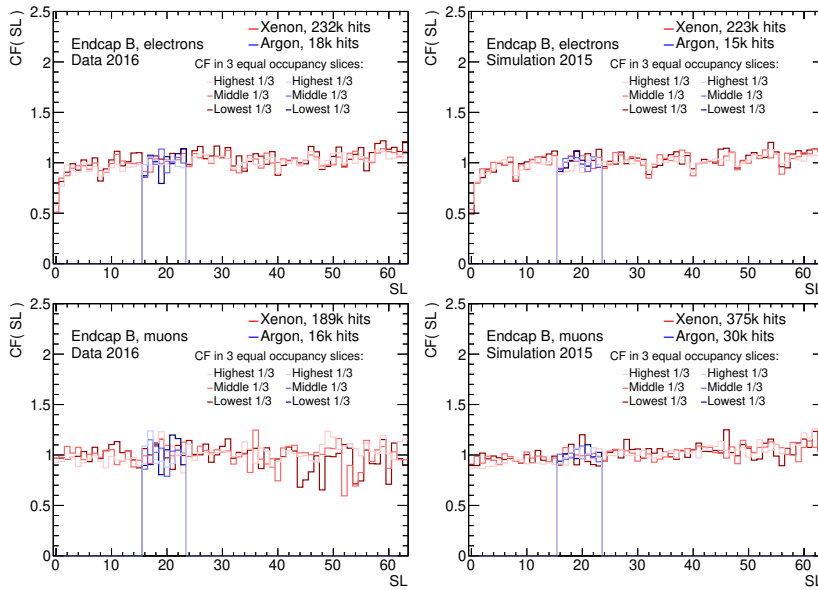


Figure 18.31: Correction factor (SL, TW, or ZR) for the barrel, endcap A, or endcap B. Electrons are on the top sub-figures, while muons are on the bottom sub-figures. The lighter colors show higher occupancy slices. Argon is only present in one wheel in endcap B, leading to very low statistics.

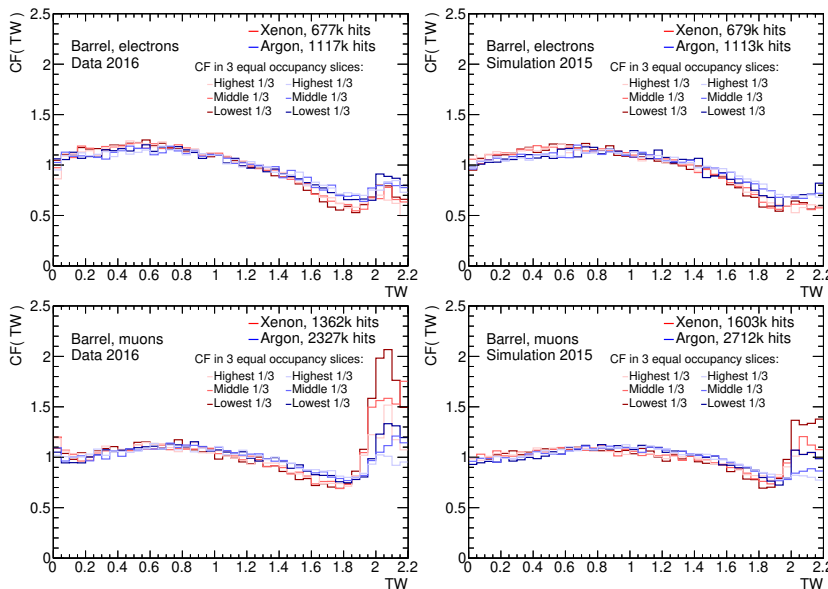


Figure 18.32: Correction factor (SL, TW, or ZR) for the barrel, endcap A, or endcap B. Electrons are on the top sub-figures, while muons are on the bottom sub-figures. The lighter colors show higher occupancy slices. Argon is only present in one wheel in endcap B, leading to very low statistics.

Figure 18.33: Correction factor (SL, TW, or ZR) for the barrel, endcap A, or endcap B. Electrons are on the top sub-figures, while muons are on the bottom sub-figures. The lighter colors show higher occupancy slices. Argon is only present in one wheel in endcap B, leading to very low statistics.

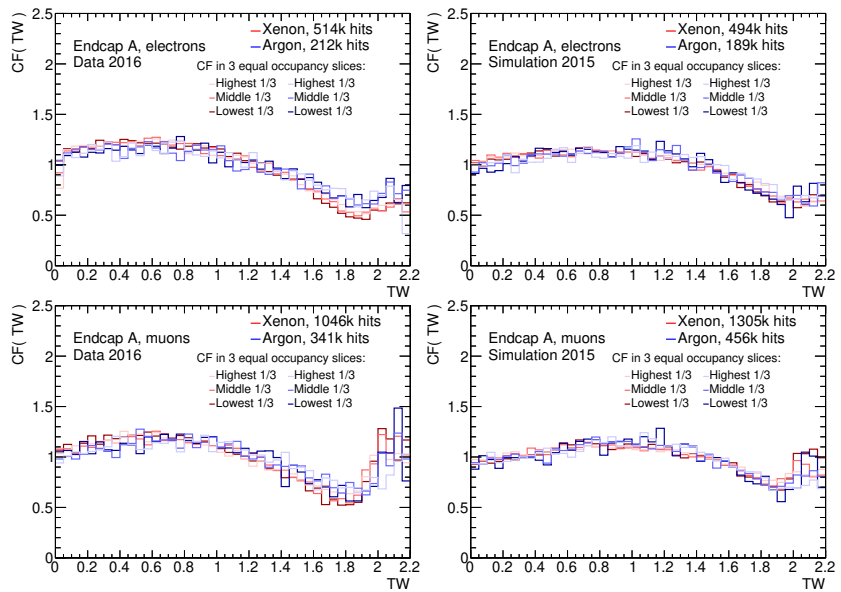
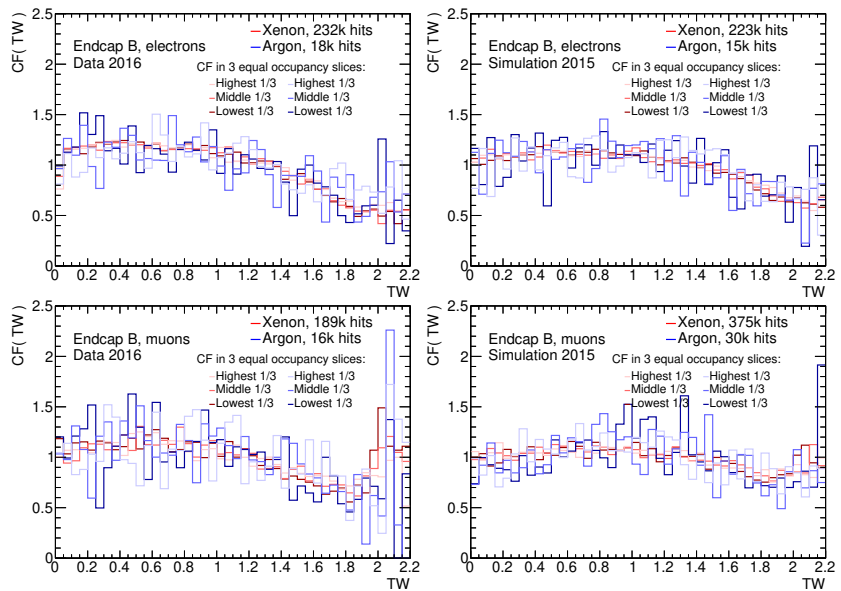


Figure 18.34: Correction factor (SL, TW, or ZR) for the barrel, endcap A, or endcap B. Electrons are on the top sub-figures, while muons are on the bottom sub-figures. The lighter colors show higher occupancy slices. Argon is only present in one wheel in endcap B, leading to very low statistics.



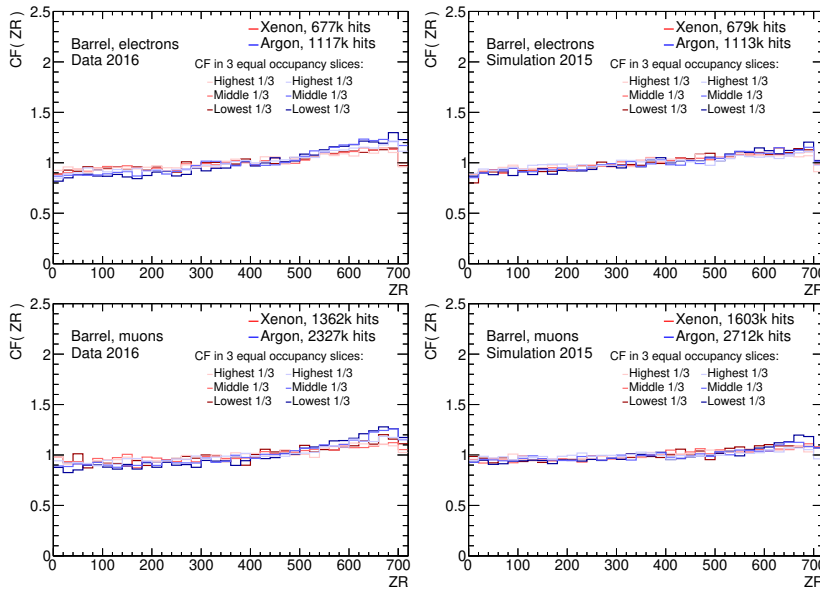


Figure 18.35: Correction factor (SL, TW, or ZR) for the barrel, endcap A, or endcap B. Electrons are on the top sub-figures, while muons are on the bottom sub-figures. The lighter colors show higher occupancy slices. Argon is only present in one wheel in endcap B, leading to very low statistics.

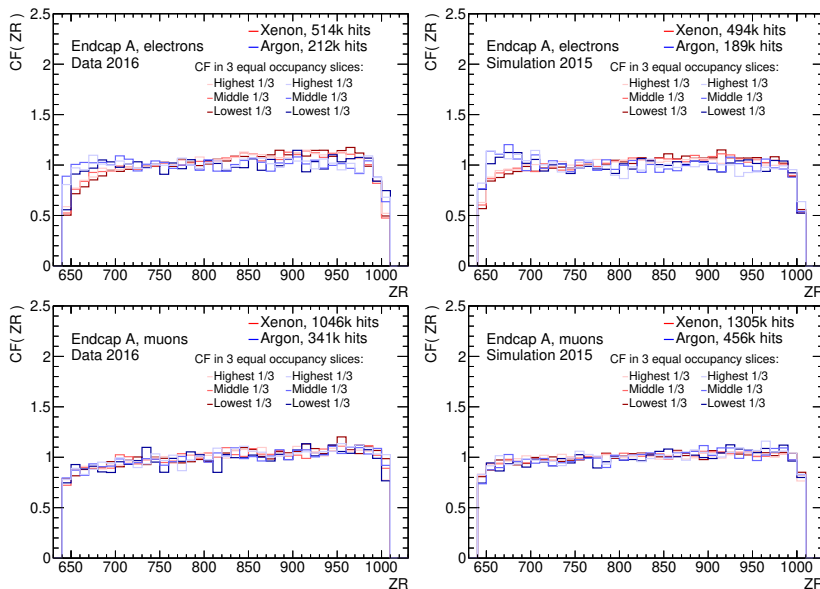
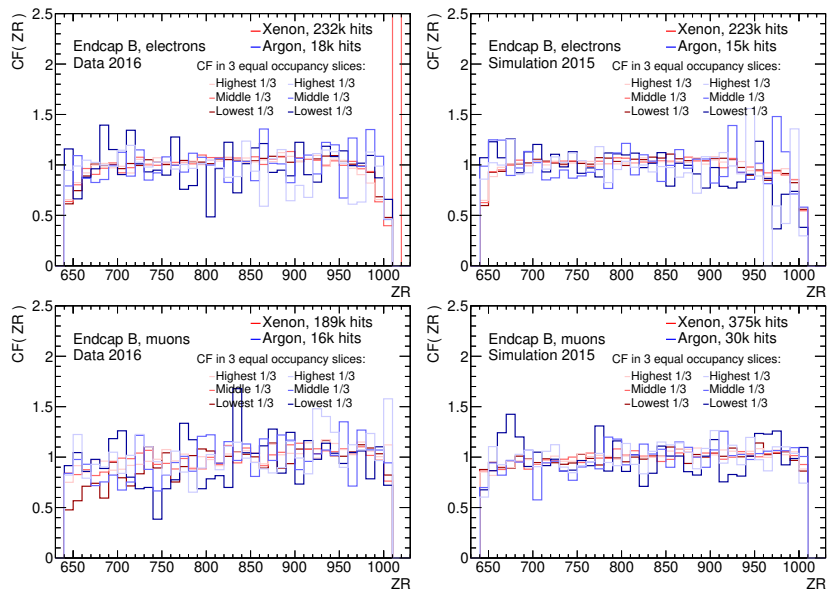


Figure 18.36: Correction factor (SL, TW, or ZR) for the barrel, endcap A, or endcap B. Electrons are on the top sub-figures, while muons are on the bottom sub-figures. The lighter colors show higher occupancy slices. Argon is only present in one wheel in endcap B, leading to very low statistics.

Figure 18.37: Correction factor (SL, TW, or ZR) for the barrel, endcap A, or endcap B. Electrons are on the top sub-figures, while muons are on the bottom sub-figures. The lighter colors show higher occupancy slices. Argon is only present in one wheel in endcap B, leading to very low statistics.



**18.G Performance for different CF configurations**

Referenced in Sect. 6.2 and Sect. 6.3, this appendix shows ROC curves for additional CF configurations. Importantly, truncating  $CF(TW)$  at 2.0 mm (blue vs magenta lines in Figs. 18.38–18.41) shows a decrease in performance in data which warrants its full use in data as well.

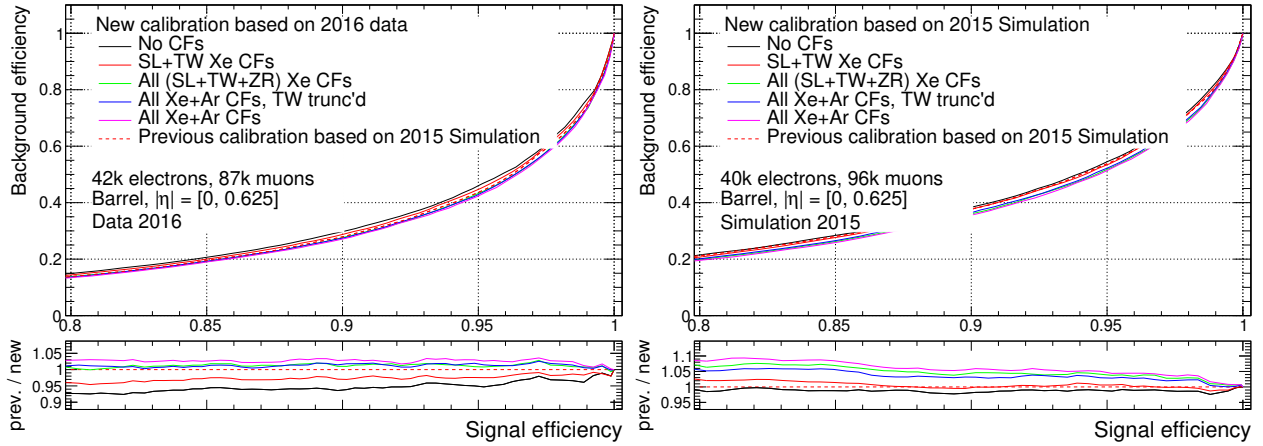


Figure 18.38: ROC curves for additional CF configurations. The

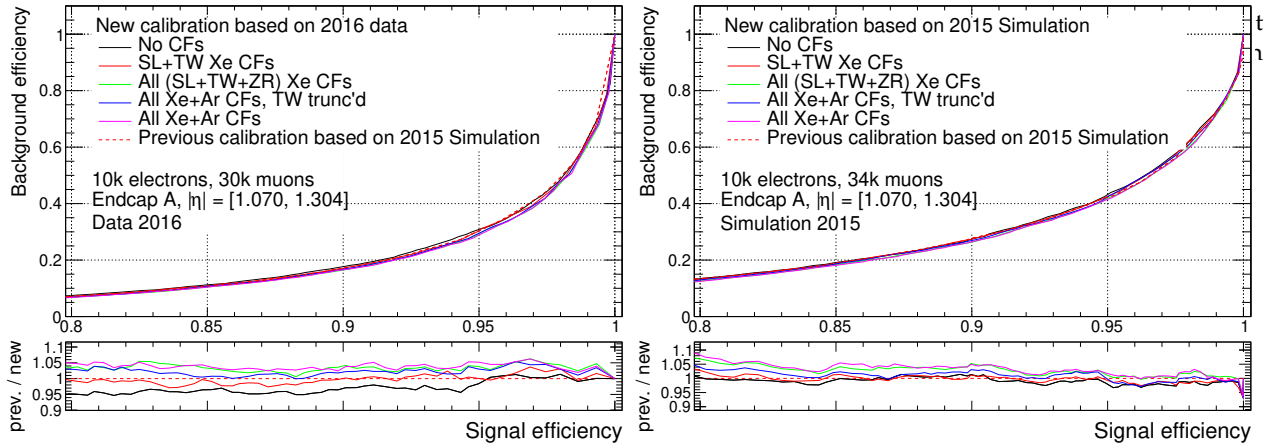


Figure 18.39: ROC curves for additional CF configurations. The blue line has  $CF(TW)$  truncated at 2.0 mm which shows a decrease in performance.

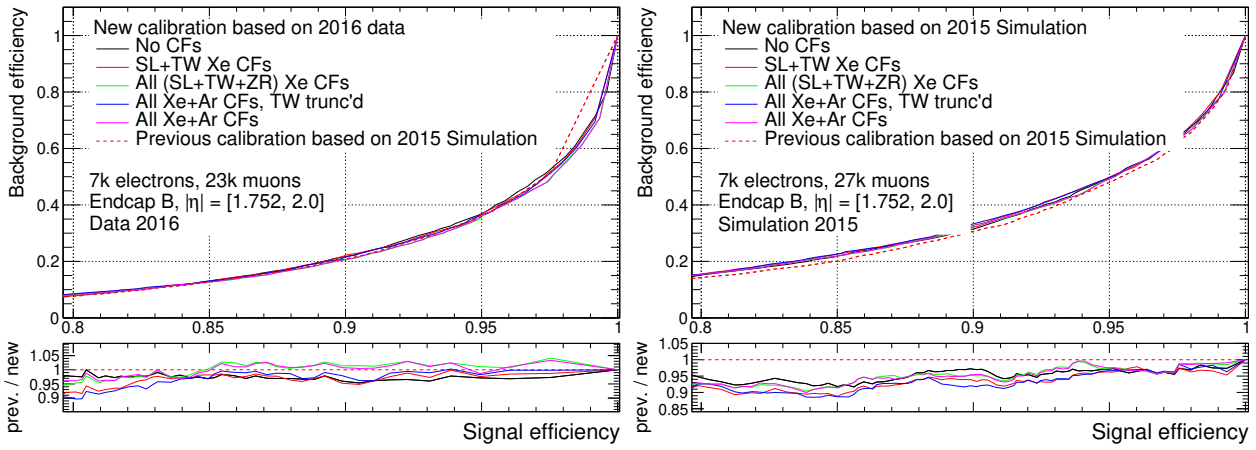


Figure 18.40: ROC curves for additional CF configurations. The blue line has  $CF(TW)$  truncated at 2.0 mm which shows a decrease in performance.

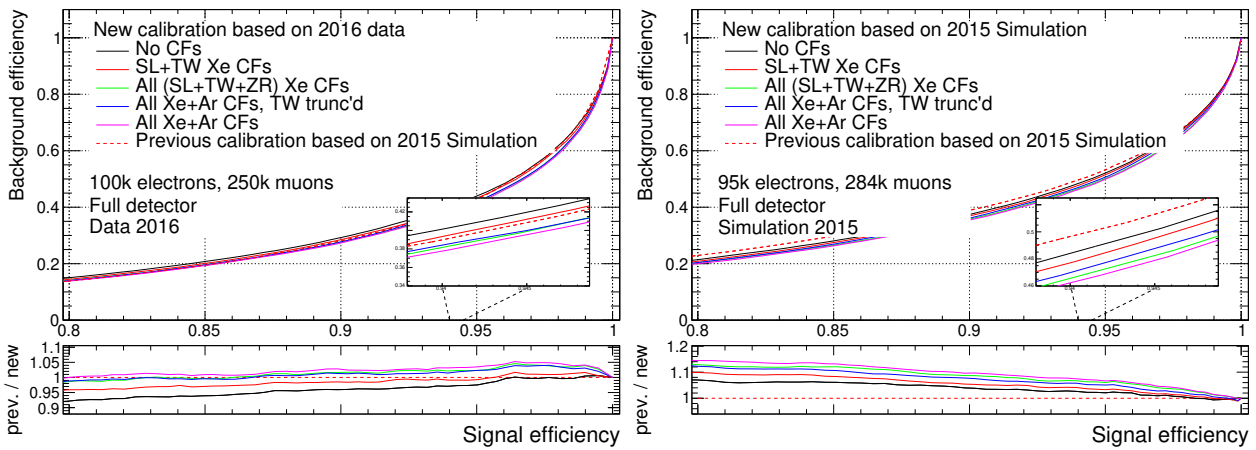


Figure 18.41: ROC curves for additional CF configurations. The blue line has  $CF(TW)$  truncated at 2.0 mm which shows a decrease in performance.

## 18.H Momentum to $\gamma$ factor

This figure is used in Sect. 6.2. Previously, CFs were only calculated for particles with momentum up to 50 GeV. This has been increased to 80 GeV. The vertical, dashed, black line shows that this selection enters the onset of the curve.

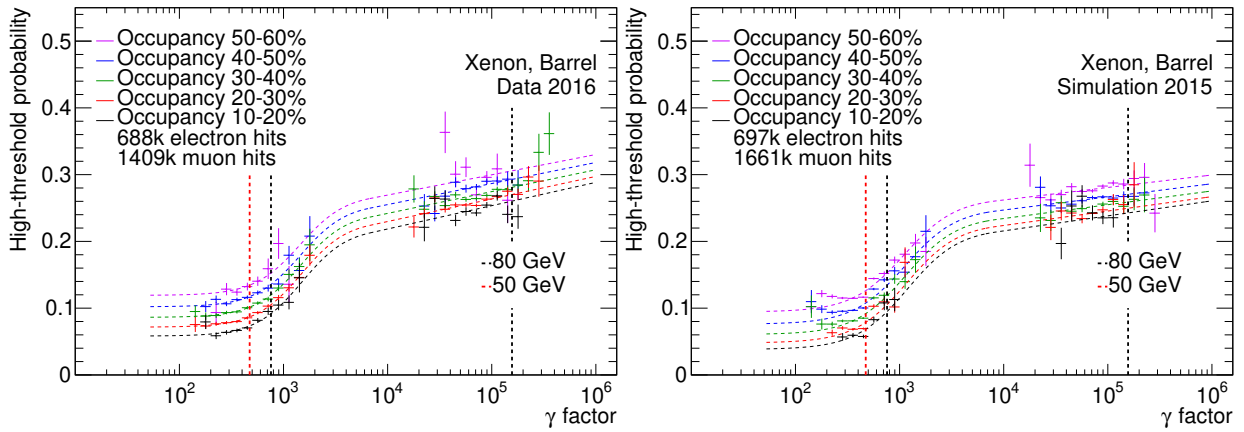


Figure 18.42: Momentum lines for muons and electrons. See text for details.

## 18.1 Track-based $p_{\text{HT}}$ method

For the method in the main text,  $p_{\text{HT}}$  is calculated per hit. The 2D histograms, binned in  $\gamma$  and occupancy, for LT and HT hits are filled with the hits from the tracks. After filling, the two histograms are divided to give the  $p_{\text{HT}}$  per hit:

$$p_{\text{HT}}^{\text{hit-based}}(\gamma, occ) = \frac{\sum_i n_{\text{HT},i}(\gamma, occ)}{\sum_i n_{\text{LT},i}(\gamma, occ)}. \quad (18.2)$$

This method will de-associate the hits from the tracks, and hence tracks with more hits will weight more.

Since the TRT PID tool is for tracks, a track-based approach may seem more appropriate. For each track, calculate the  $p_{\text{HT}}$  from its hits and put it into the corresponding bin. The bins will then contain the average  $p_{\text{HT}}$  per track:

$$p_{\text{HT}}^{\text{track-based}}(\gamma, occ) = \frac{1}{N} \sum_i \frac{n_{\text{HT},i}(\gamma, occ)}{n_{\text{LT},i}(\gamma, occ)}. \quad (18.3)$$

Note that the sum is now outside the fraction.

This way of calculating  $p_{\text{HT}}$  suffers from the fact that the TRT is separated into parts and gases. How is the probability calculated for a track that traverses the barrel and endcap A? If the hits are separated into parts and gases, tracks with few hits in one part will give very uncertain probabilities, unless they are required to have a minimum number of hits. But having a threshold will lead to a significant loss of statistics in endcap B.

For the following figures, at least 1 LT hit has been required for a track's  $p_{\text{HT}}$  to be included in the corresponding part and gas histograms.

The following pages will show Figs. 18.43–18.48. The upper sub-figures show the hit-based histograms from the main text as reference. The middle sub-figures show the fractions obtained through the track-based method. **Note that the hit-based method has a requirement of at least 20 HT hits per bin. This explains the seemingly fewer amount of filled bins in the hit-based histograms.** The bottom sub-figures show the ratio of the two approaches.

For the part/gas histograms with the greatest amount of statistics, the bulk shows little difference and there is only slightly more deviation at the edges. However, for endcap B, more noise is visible with the track-based approach.

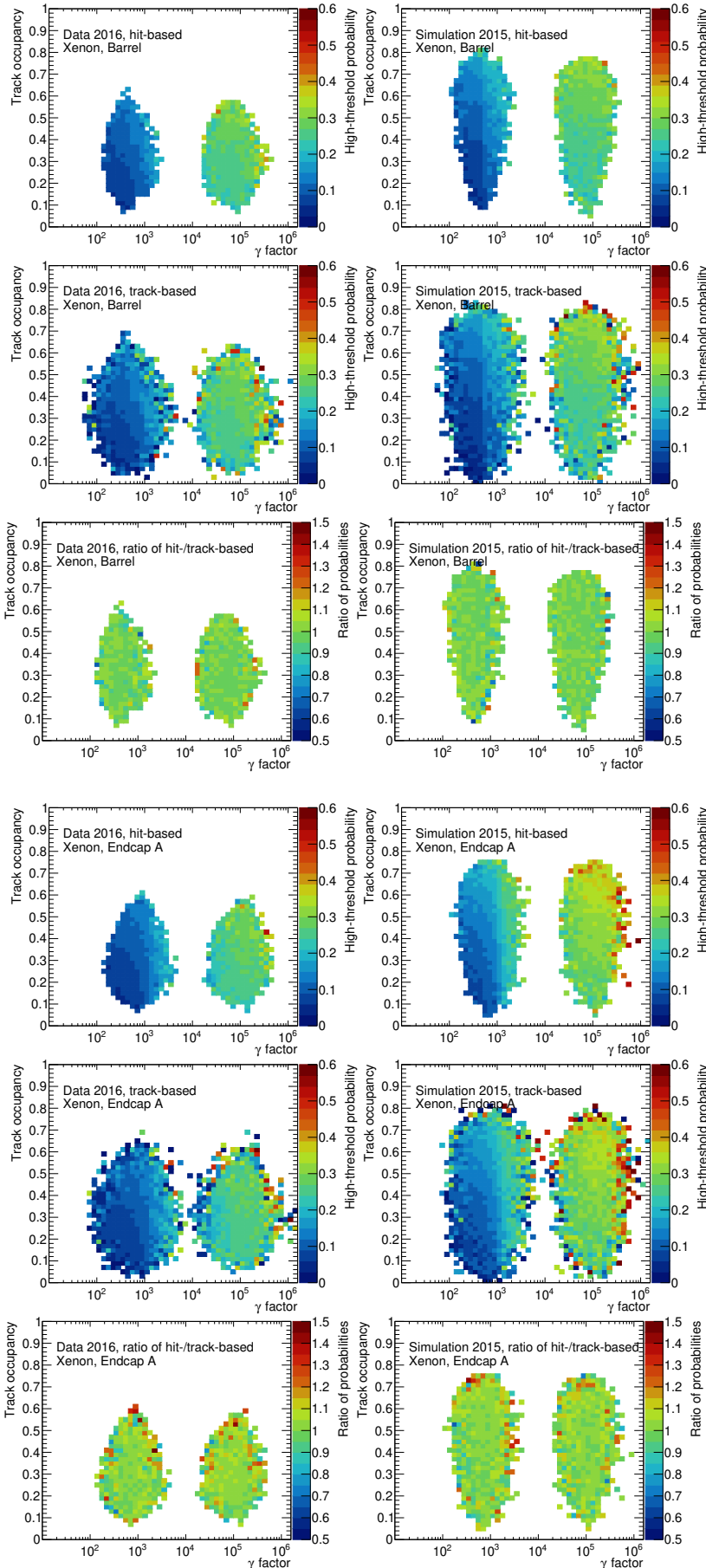


Figure 18.43: Comparison of the hit-based and track-based approaches to calculate the HT fraction ( $p_{HT}$ ). The upper sub-figures show, as reference, the fractions from the main text. The middle sub-figures show the 2D histograms of fractions obtained through the track-based approach. The lower sub-figures show the ratio between the two histograms. Very little deviation is seen between the two histograms.

Figure 18.44: Comparison of the hit-based and track-based approaches to calculate the HT fraction ( $p_{HT}$ ). The upper sub-figures show, as reference, the fractions from the main text. The middle sub-figures show the 2D histograms of fractions obtained through the track-based approach. The lower sub-figures show the ratio between the two histograms. Very little deviation is seen between the two histograms.

Figure 18.45: Comparison of the hit-based and track-based approaches to calculate the HT fraction ( $p_{HT}$ ). The upper sub-figures show, as reference, the fractions from the main text. The middle sub-figures show the 2D histograms of fractions obtained through the track-based approach. The lower sub-figures show the ratio between the two histograms. Very little deviation is seen between the two histograms.

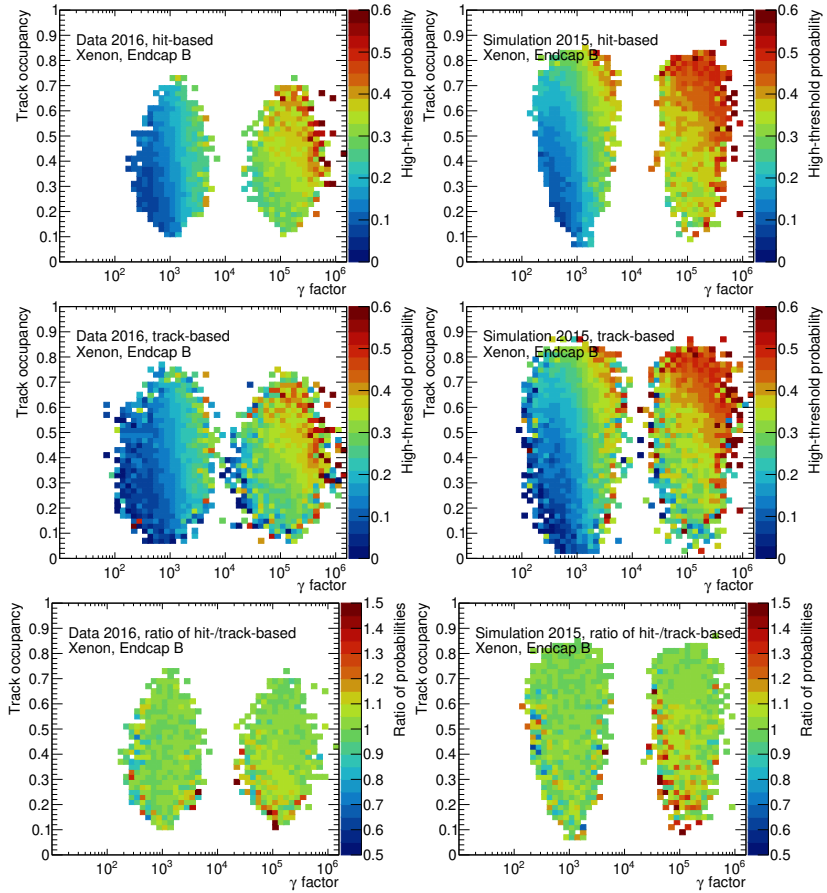
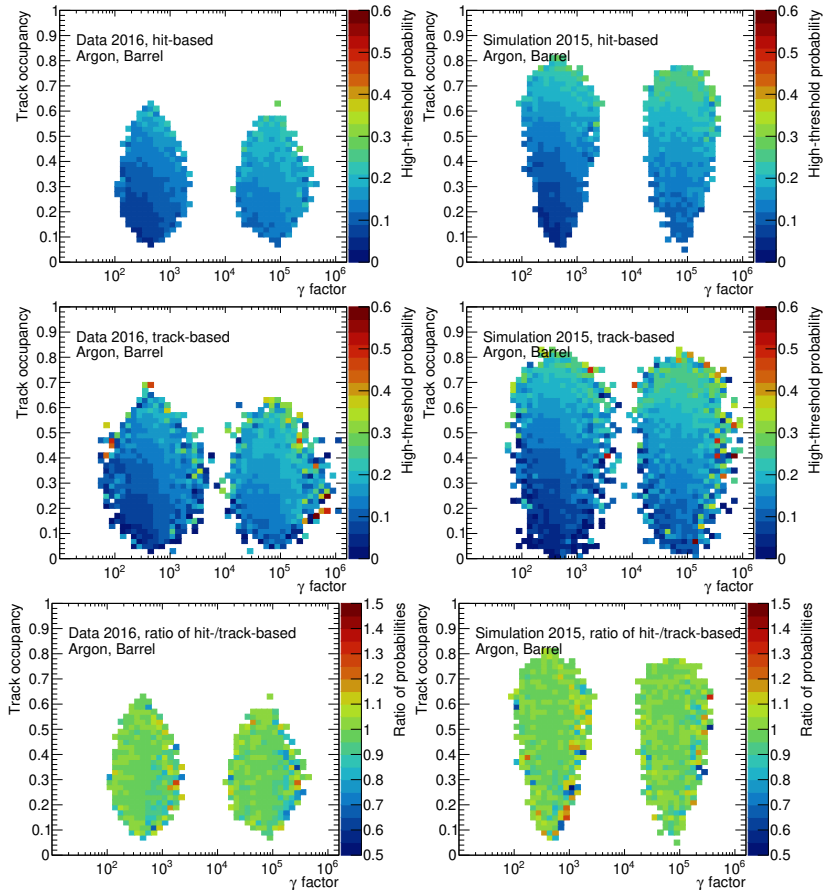


Figure 18.46: Comparison of the hit-based and track-based approaches to calculate the HT fraction ( $p_{HT}$ ). The upper sub-figures show, as reference, the fractions from the main text. The middle sub-figures show the 2D histograms of fractions obtained through the track-based approach. The lower sub-figures show the ratio between the two histograms. Very little deviation is seen between the two histograms.



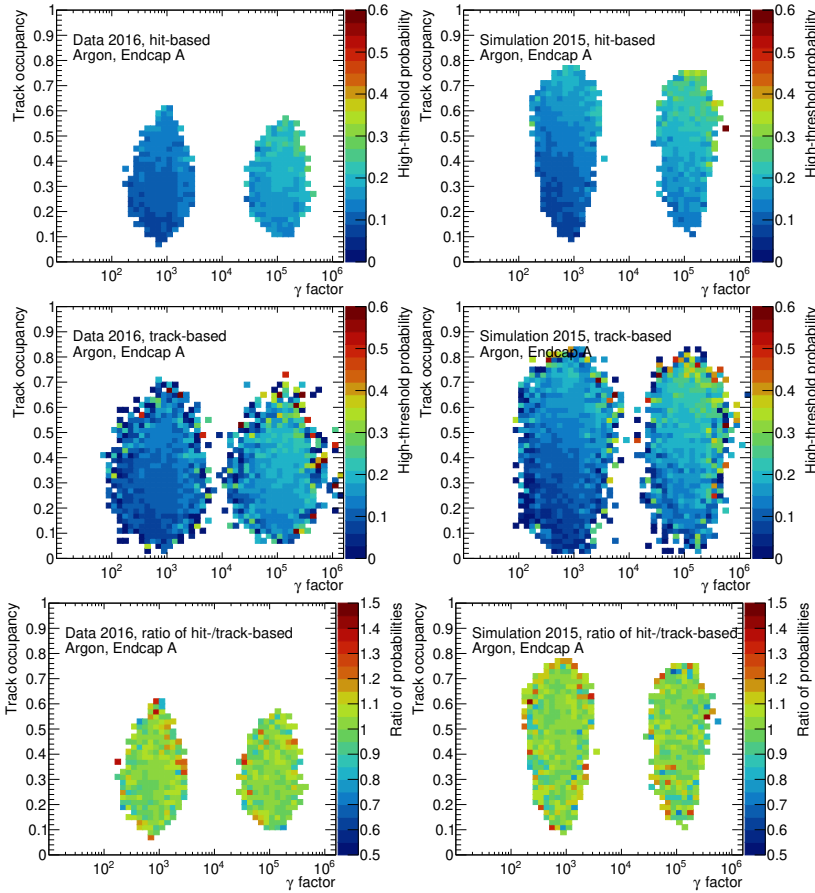


Figure 18.47: Comparison of the hit-based and track-based approaches to calculate the HT fraction ( $p_{HT}$ ). The upper sub-figures show, as reference, the fractions from the main text. The middle sub-figures show the 2D histograms of fractions obtained through the track-based approach. The lower sub-figures show the ratio between the two histograms. Very little deviation is seen between the two histograms.

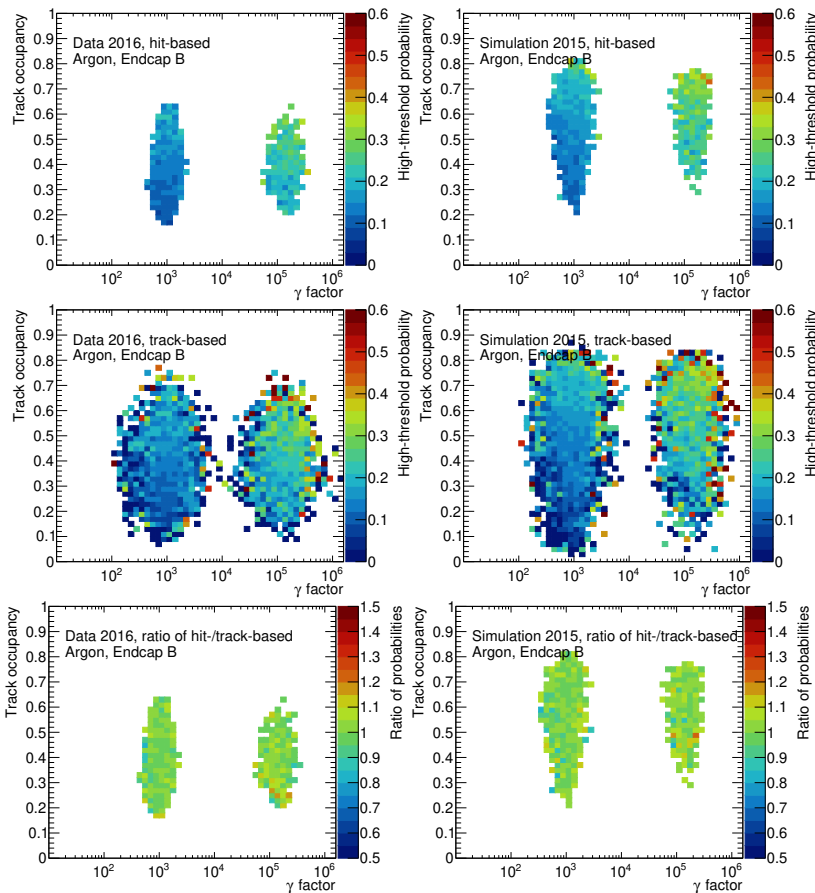


Figure 18.48: Comparison of the hit-based and track-based approaches to calculate the HT fraction ( $p_{HT}$ ). The upper sub-figures show, as reference, the fractions from the main text. The middle sub-figures show the 2D histograms of fractions obtained through the track-based approach. The lower sub-figures show the ratio between the two histograms. Very little deviation is seen between the two histograms.



# 19 Physics analysis

## Contents

---

19.A "Hardest jets" limits . . . . .	220
19.B Kinematic variables . . . . .	220
19.C Fitted parameterized signals . . . . .	223
19.D Asimov pulls and ranks . . . . .	225
19.E Unblinded post-fits, pull plots, and NP ranks . . . . .	232
19.F Unblinded 1D limit slices . . . . .	243

---

### 19.A "Hardest jets" limits

In Chap. 10, the "hardest jets" approach was disregarded in favor of the approach that resolves jet combinatorics before unblinding when systematics and corrections were in place. The expected upper limits on the production cross-section of  $A$  of the two approaches at the time of the decision are shown in Tab. 19.1.

Table 19.1: The upper limits on the production cross-section of  $A$  for the simulated signals using the approach that resolves jet combinatorics ("resolving") and the "hardest jets" approach. The resolving approach gives limits that are 1.4 to 4.1 times lower. The limits are given in the production cross-section times branching ratios for the whole decay chain in units of pb.

$m_A$	$m_H$	Limits		
		resolving	"hardest jets"	resolving $x$ times lower
300	200	0.2169	0.3165	1.5
350	250	0.1018	0.1385	1.4
400	200	0.0776	0.1202	1.5
400	300	0.0421	0.0763	1.8
500	200	0.0360	0.0944	2.6
500	300	0.0284	0.0467	1.6
500	350	0.0215	0.0408	1.9
500	400	0.0115	0.0306	2.7
600	200	0.0206	0.0356	1.7
600	300	0.0171	0.0320	1.9
600	400	0.0098	0.0260	2.6
600	480	0.0062	0.0190	3.0
700	200	0.0114	0.0214	1.9
700	300	0.0143	0.0284	2.0
700	500	0.0049	0.0166	3.4
800	200	0.0070	0.0136	1.9
800	300	0.0069	0.0137	2.0
800	500	0.0039	0.0133	3.4
800	600	0.0031	0.0131	4.1
800	700	0.0022	0.0086	3.9

### 19.B Kinematic variables

The reconstructed masses used in the fits and the corrected variables were shown in Chap. 11. The signal lepton and jet  $p_T$  and  $\eta$  variables are shown here at Levels 1 and 2 to show that no regressive effects are introduced from the corrections.

Figure 19.1: The pseudorapidity and the transverse momentum distributions of the signal leptons at Level 1. Linear scale is shown.

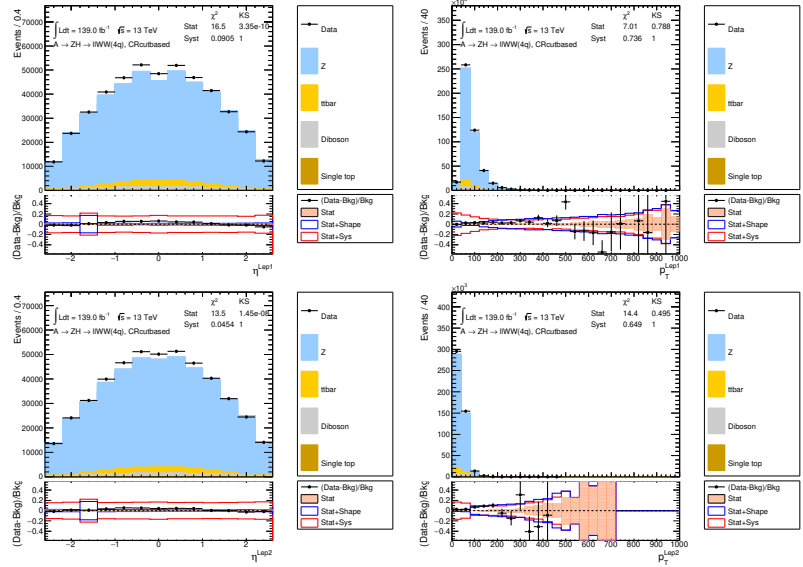


Figure 19.2: The pseudorapidity and the transverse momentum distributions of the signal jets at Level 1. Linear scale is shown.

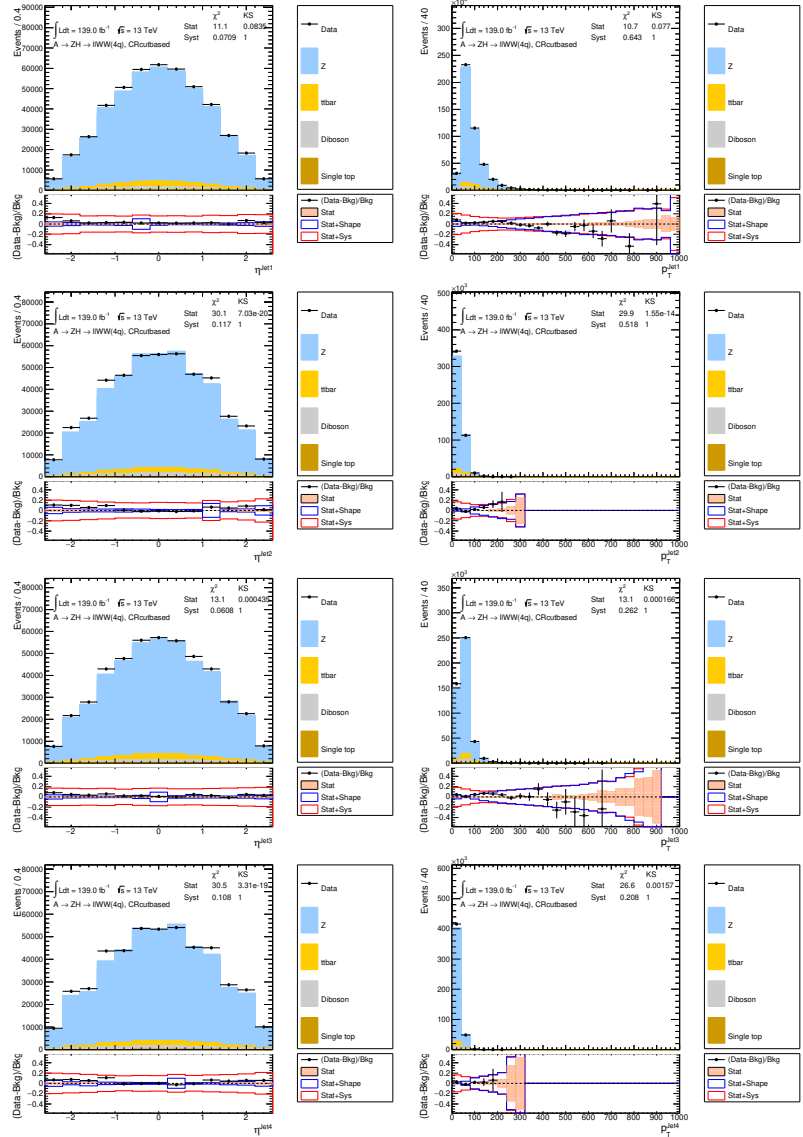


Figure 19.3: The pseudorapidity and the transverse momentum distributions of the signal leptons at Level 2. Linear scale is shown.

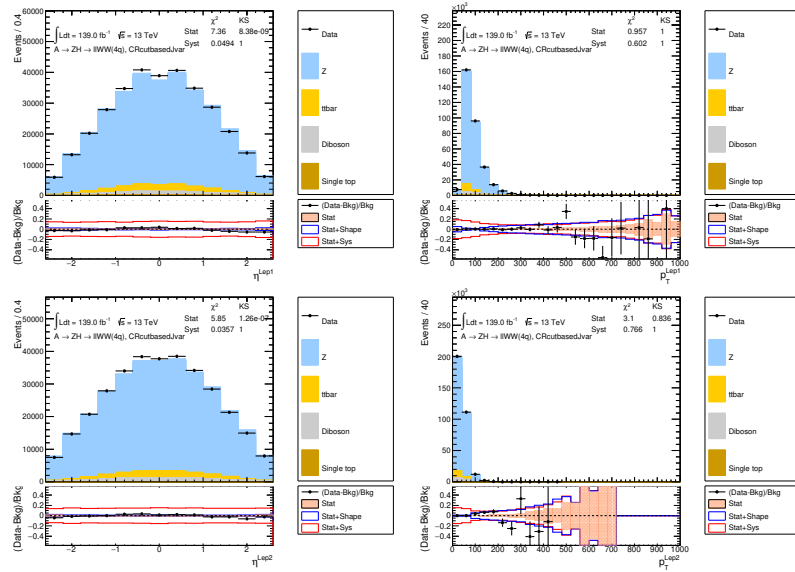
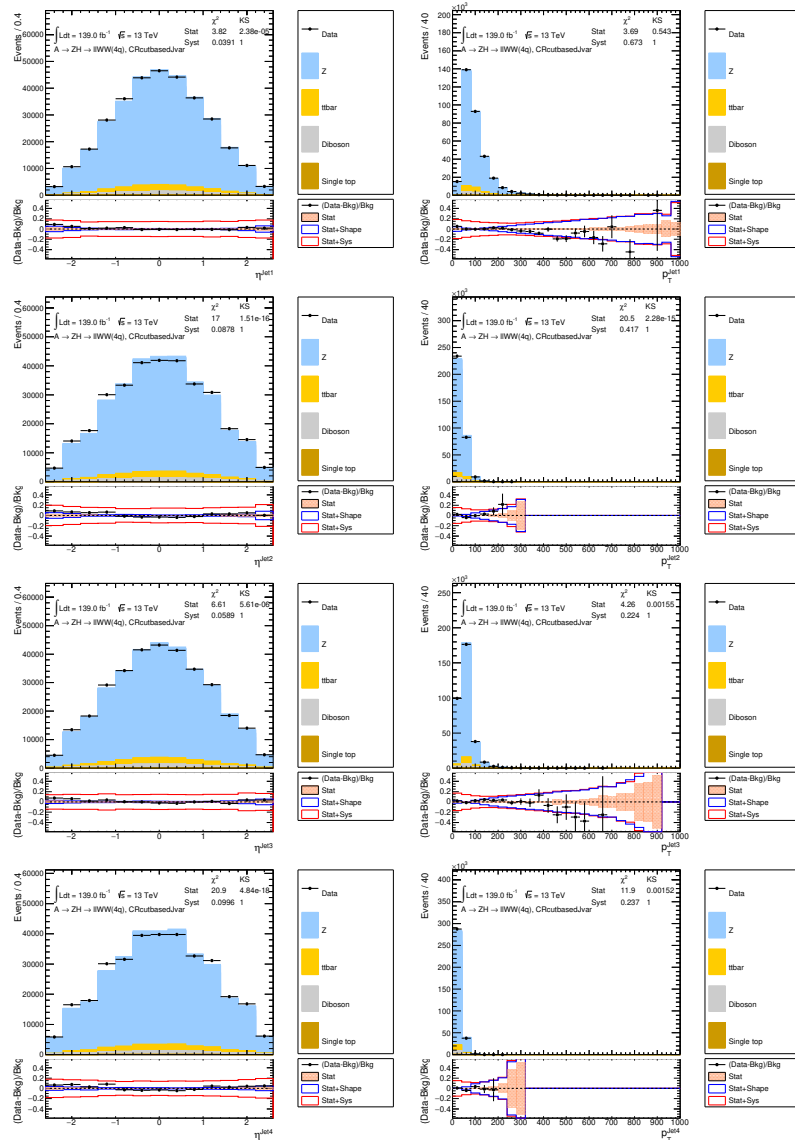


Figure 19.4: The pseudorapidity and the transverse momentum distributions of the signal jets at Level 2. Linear scale is shown.



**19.C Fitted parameterized signals**

The interpolation uncertainty was examined on selected mass points by the end of Sect. 12.1. Mass points for the remaining simulated signals are shown here.

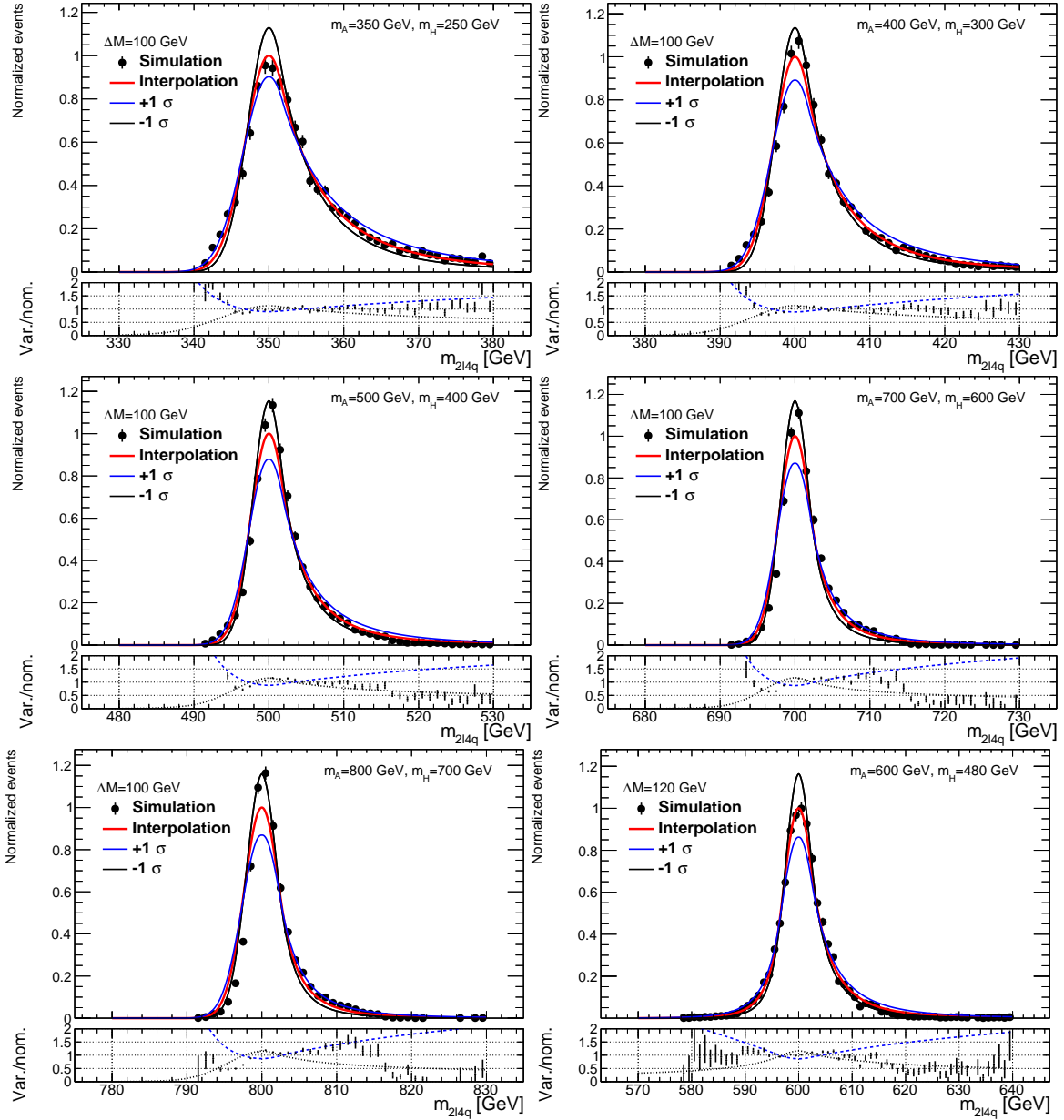


Figure 19.5: Interpolated signals along with their interpolation uncertainties compared against the simulated signals.

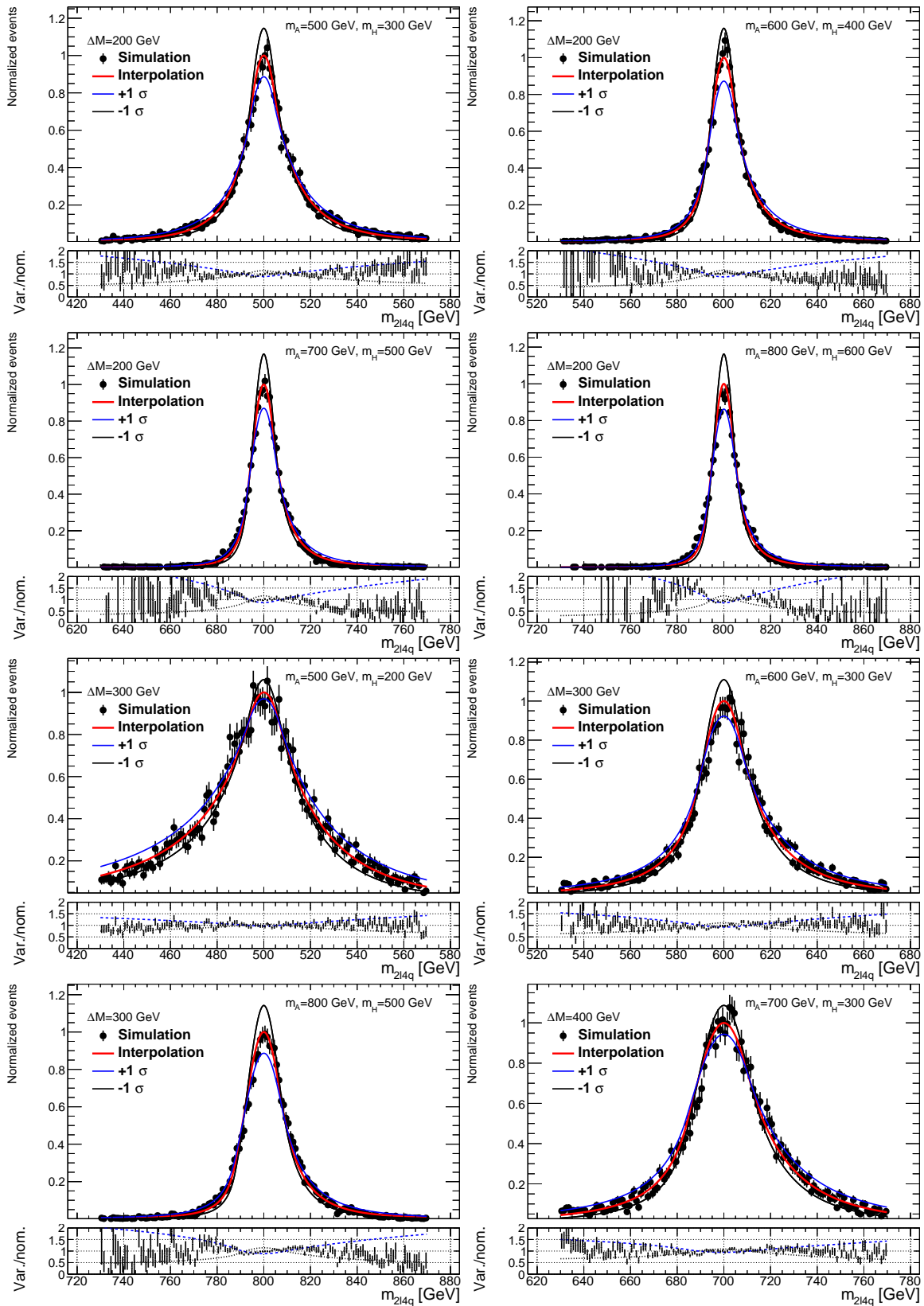


Figure 19.6: Interpolated signals along with their interpolation uncertainties compared against the simulated signals.

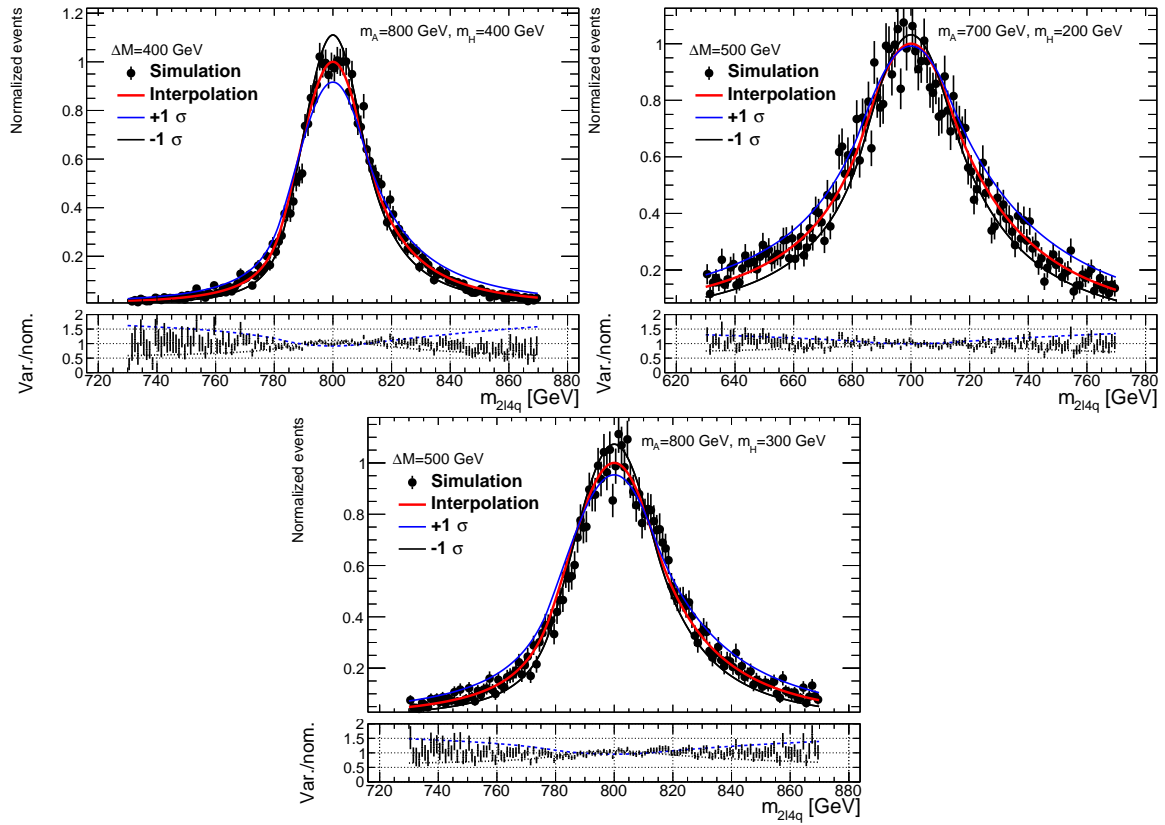


Figure 19.7: Interpolated signals along with their interpolation uncertainties compared against the simulated signals.

## 19.D Asimov pulls and ranks

In Sect. 14.2, the pulls and ranks for Asimov fits to some simulated signals were shown. This appendix contains figures for the remaining signals.



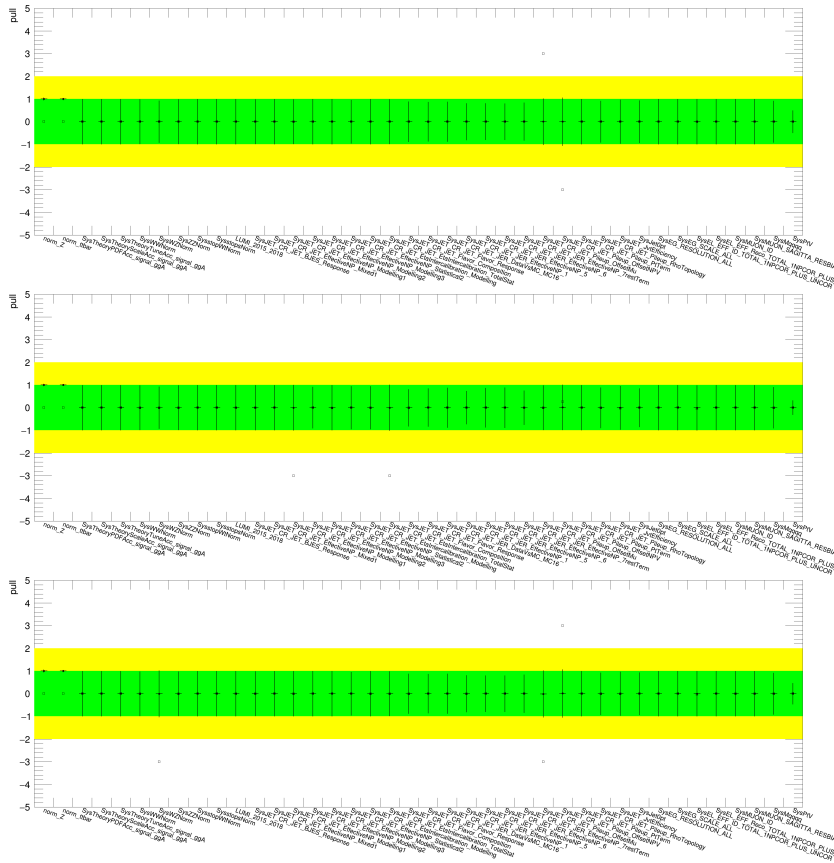


Figure 19.10: The pulls of the nuisance parameters used in the Asimov fits for the (500,400), (600,200), and (600,400) signals, respectively.

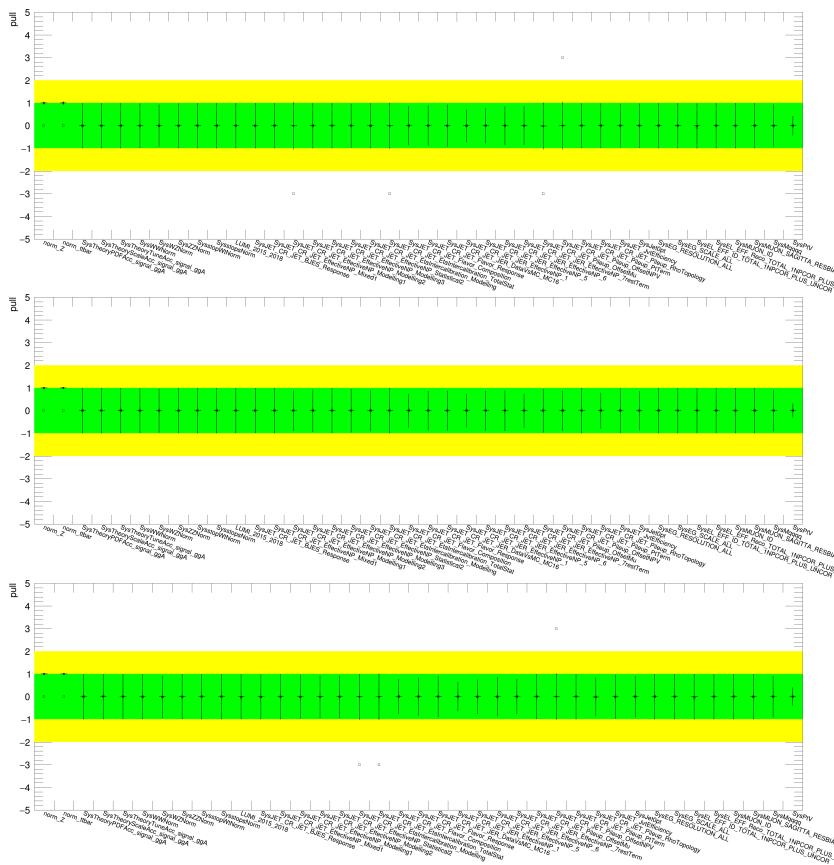


Figure 19.11: The pulls of the nuisance parameters used in the Asimov fits for the (600,480), (700,200), and (700,300) signals, respectively.



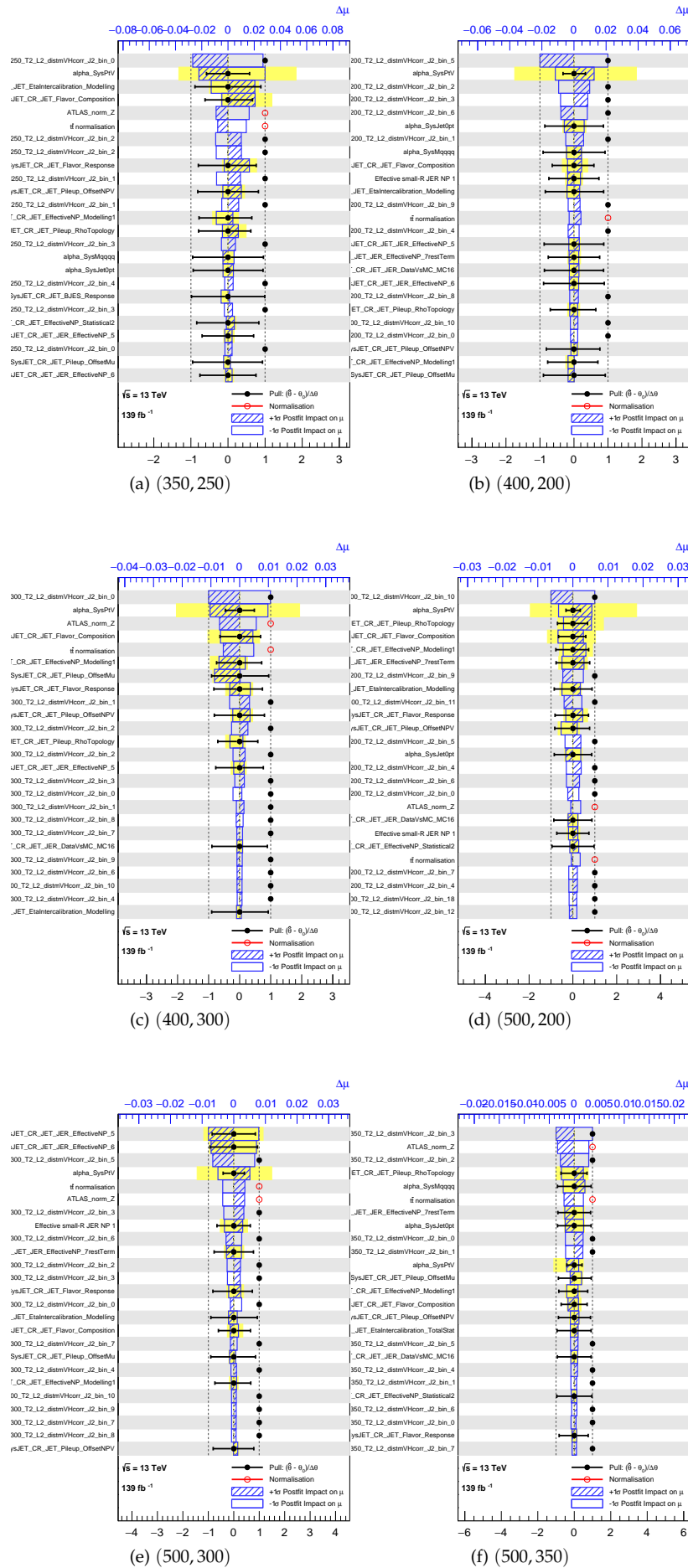


Figure 19.14: The post-fit ranking of the nuisance parameters used in the Asimov fits.

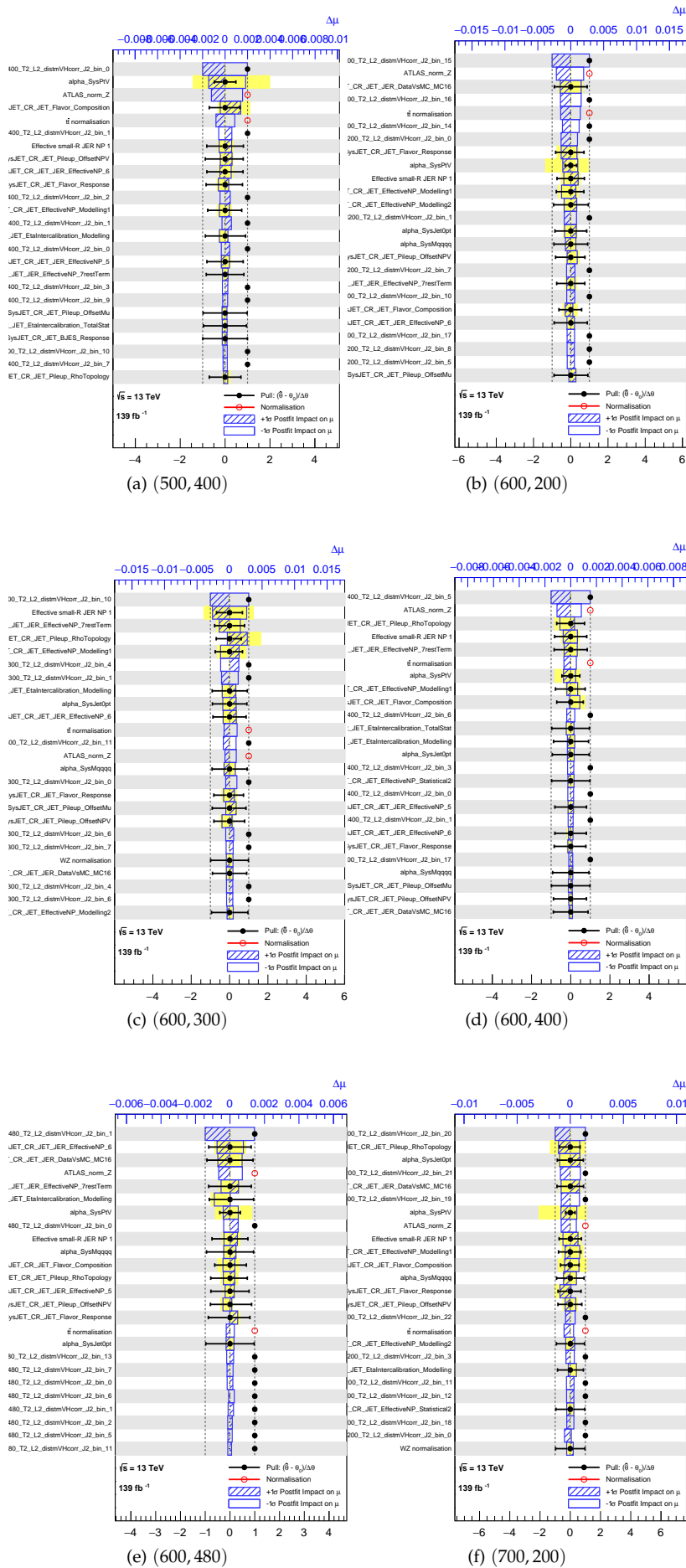


Figure 19.15: The post-fit ranking of the nuisance parameters used in the Asimov fits.

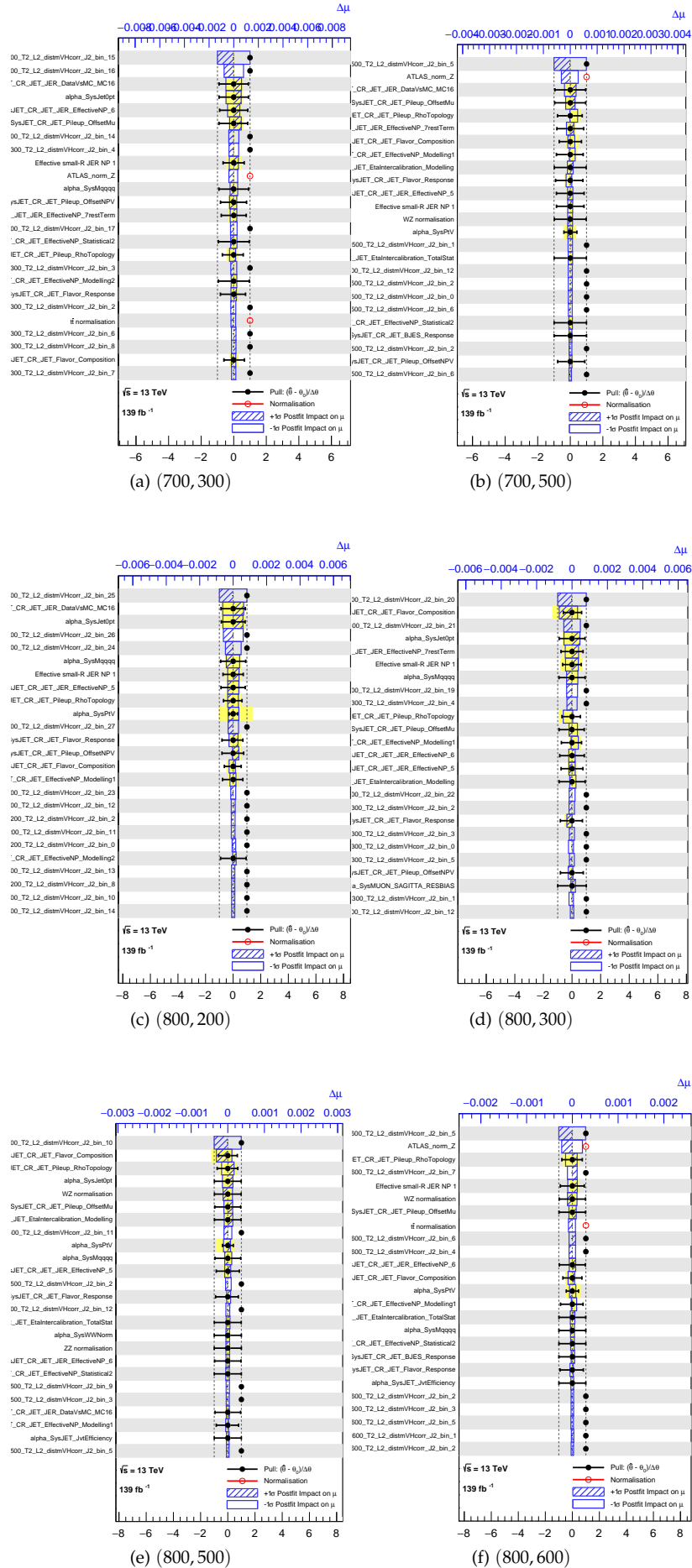


Figure 19.16: The post-fit ranking of the nuisance parameters used in the Asimov fits.

**19.E Unblinded post-fits, pull plots, and NP ranks**

In Sect. 14.4, pull plots and ranks for unblinded fits using interpolated signals for some representative mass points were shown. Chap. 15 showed the unblinded post-fits. This appendix contains figures for the remaining signals.

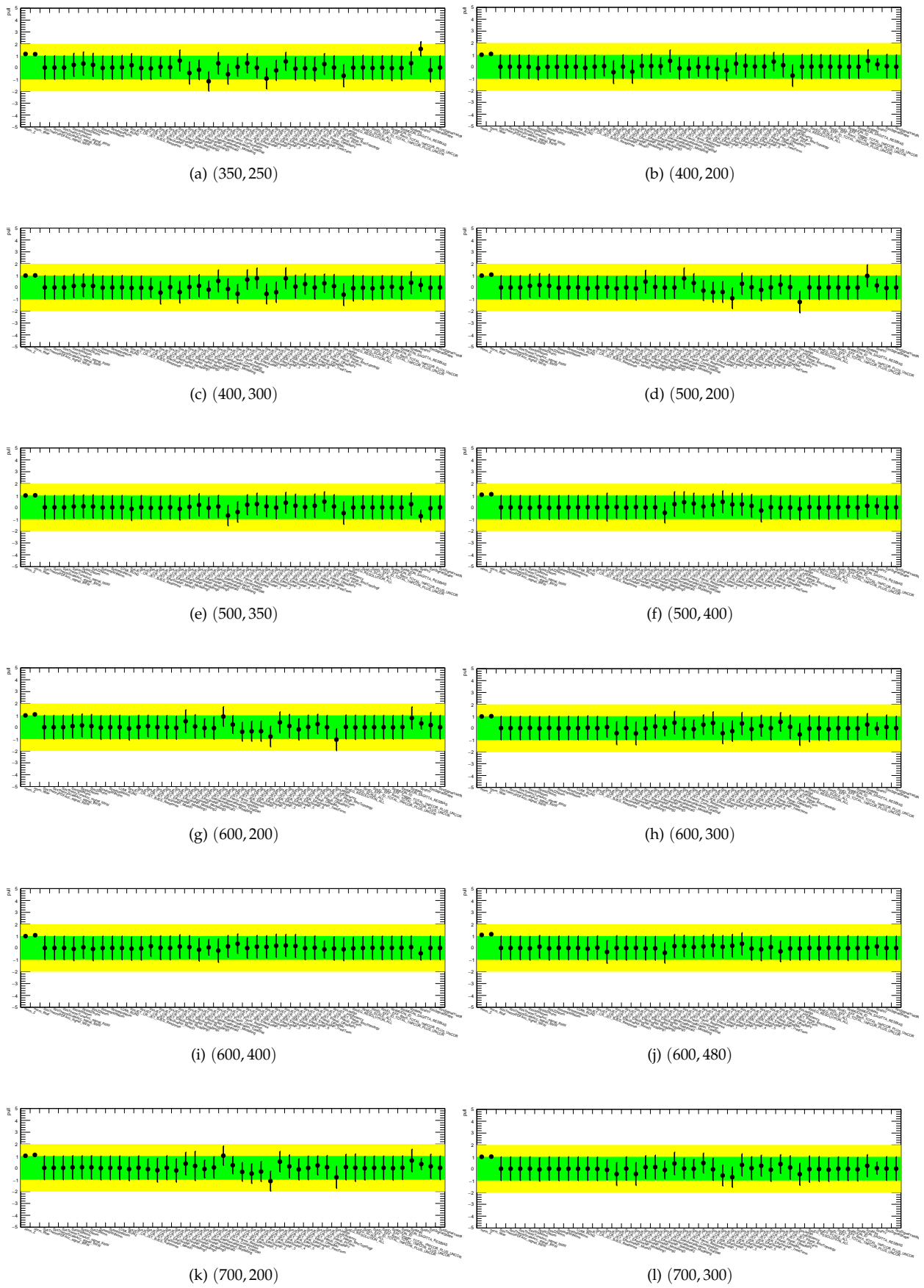


Figure 19.17: The unblinded pull plots.

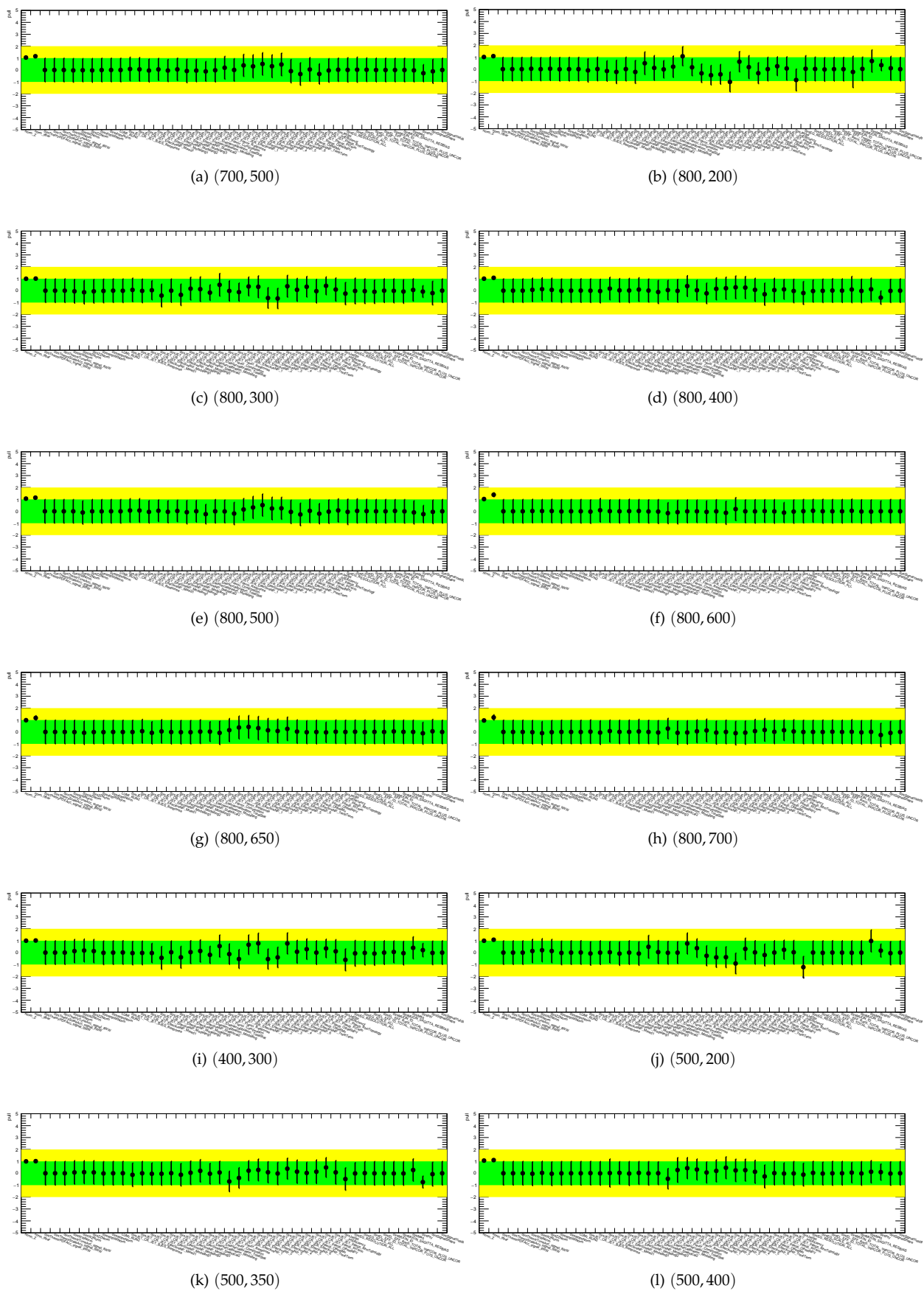


Figure 19.18: The unblinded pull plots.

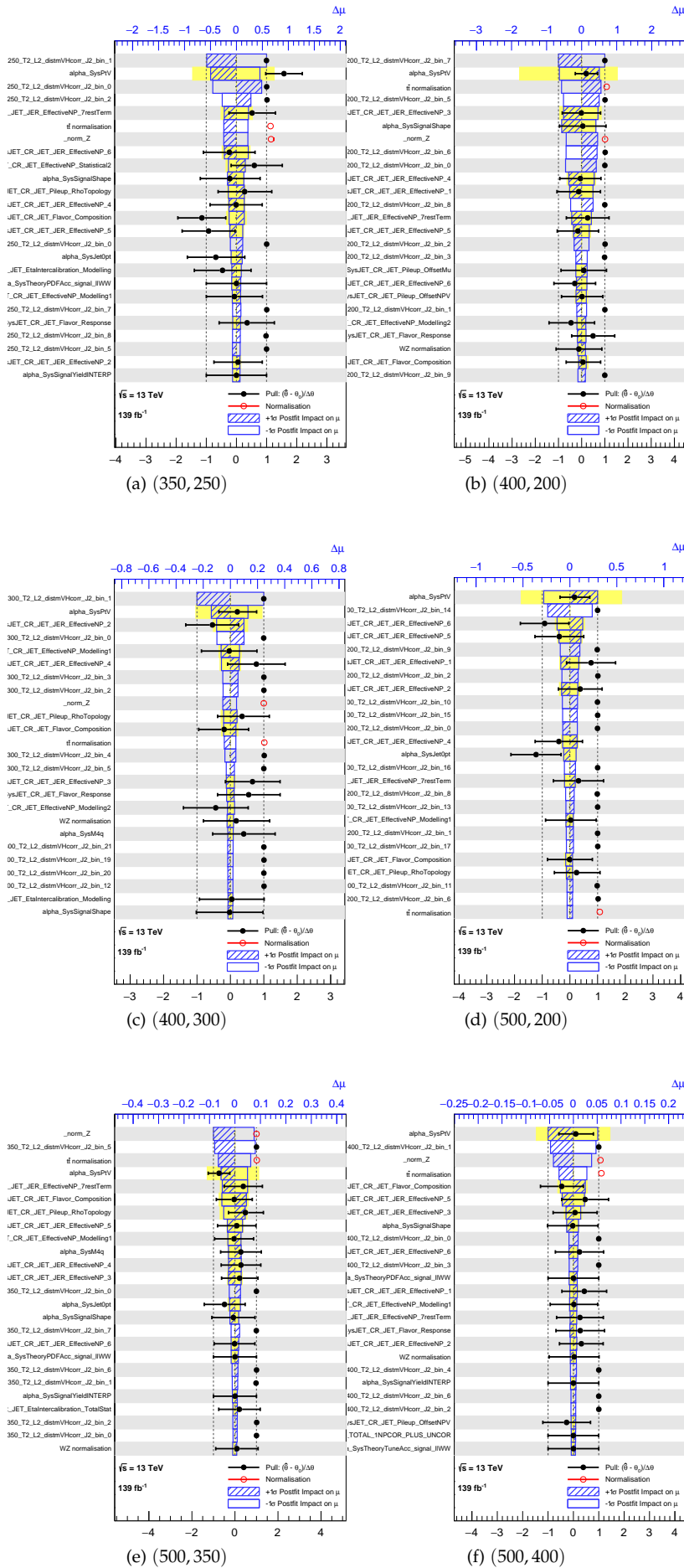


Figure 19.19: The unblinded post-fit ranking of the nuisance parameters used in the fits.

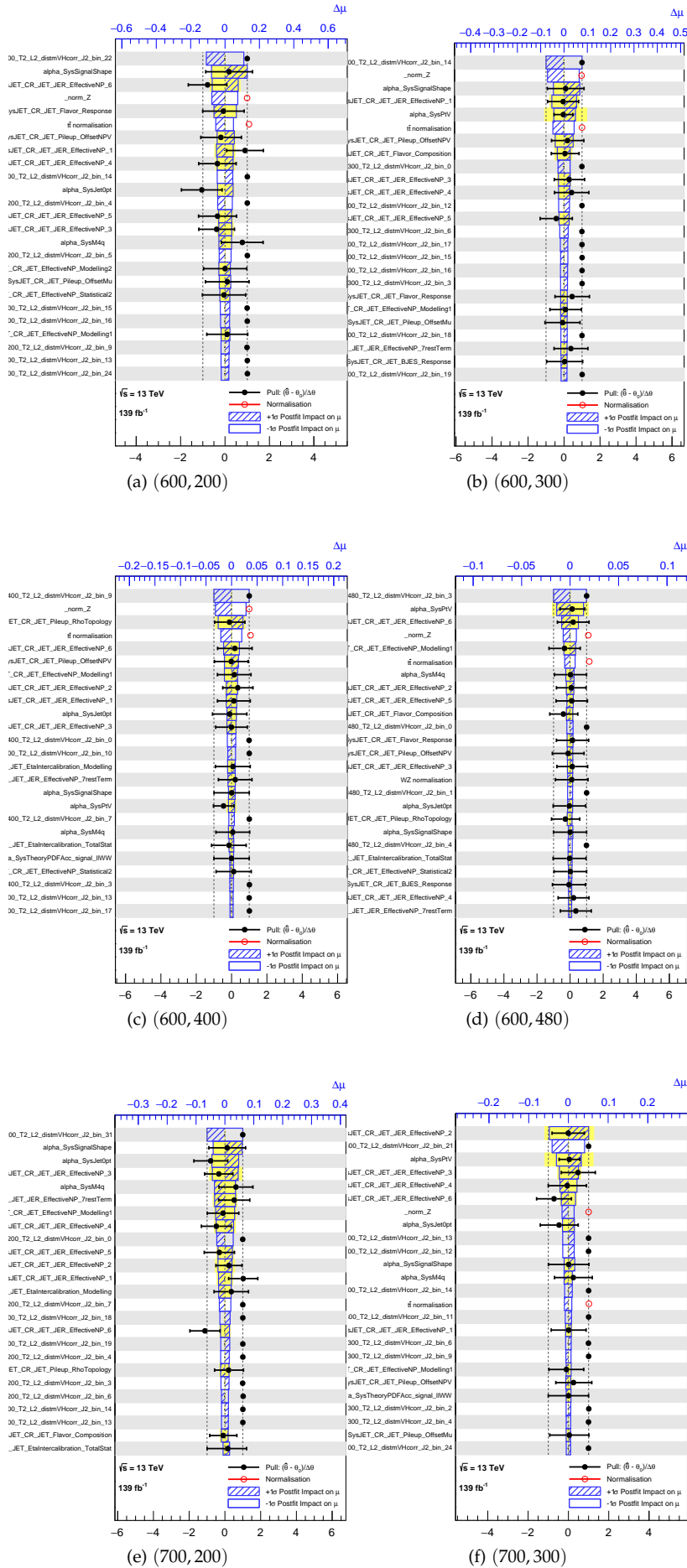


Figure 19.20: The unblinded post-fit ranking of the nuisance parameters used in the fits.

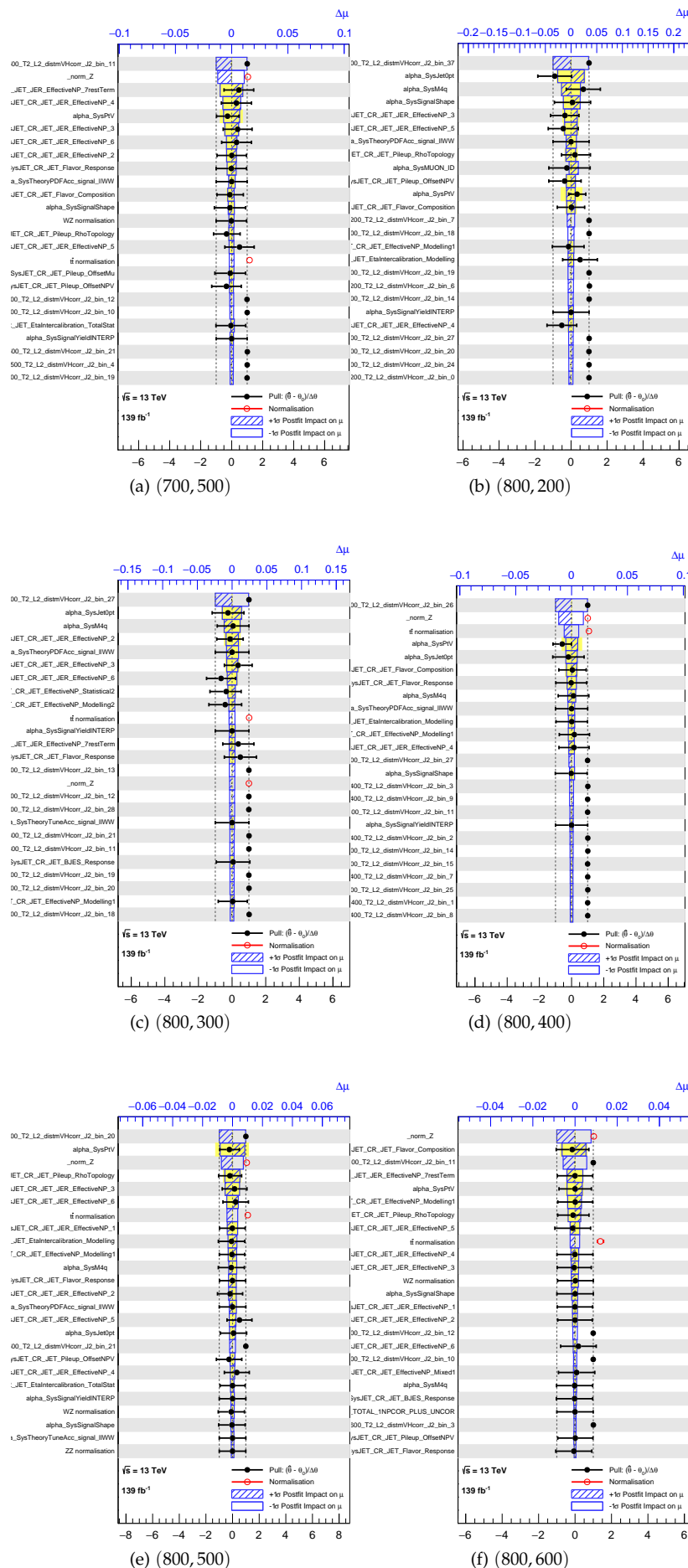


Figure 19.21: The unblinded post-fit ranking of the nuisance parameters used in the fits.

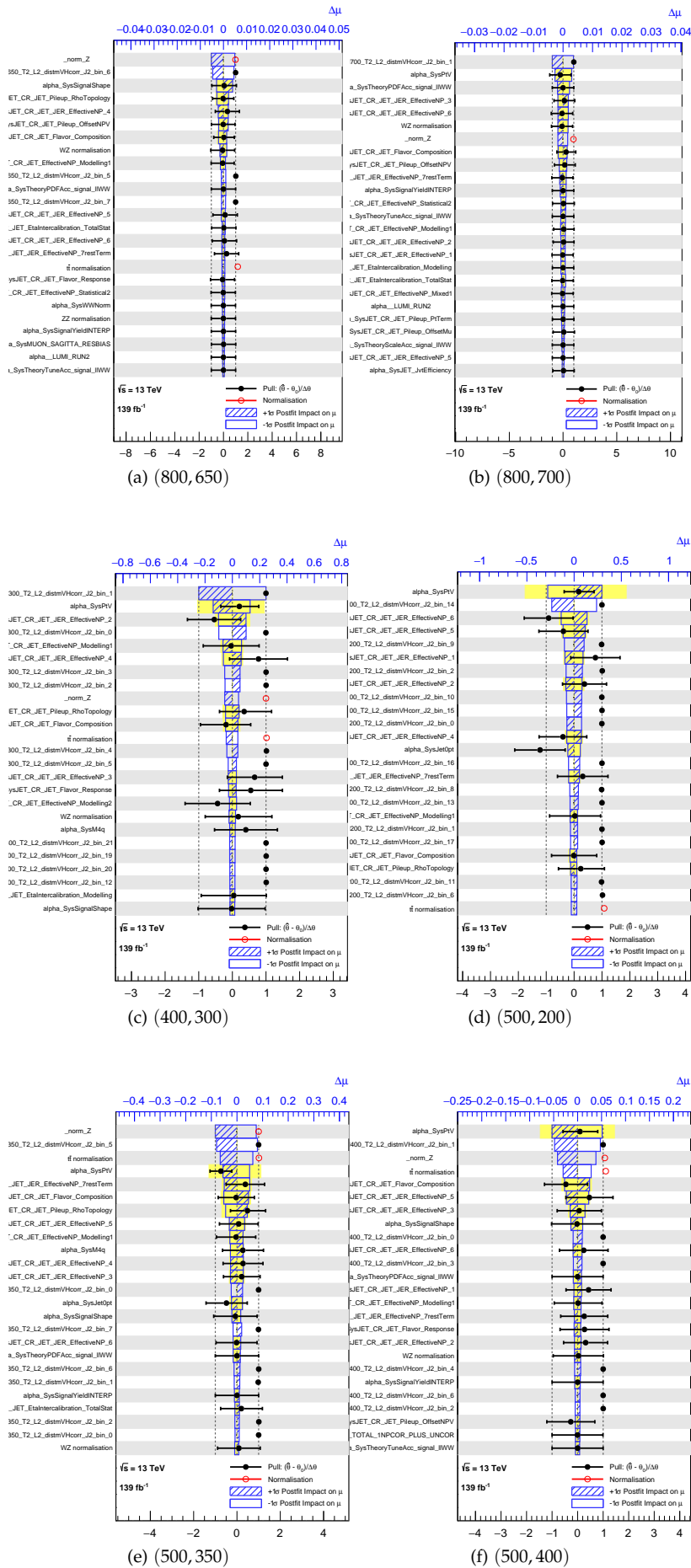


Figure 19.22: The unblinded post-fit ranking of the nuisance parameters used in the fits.

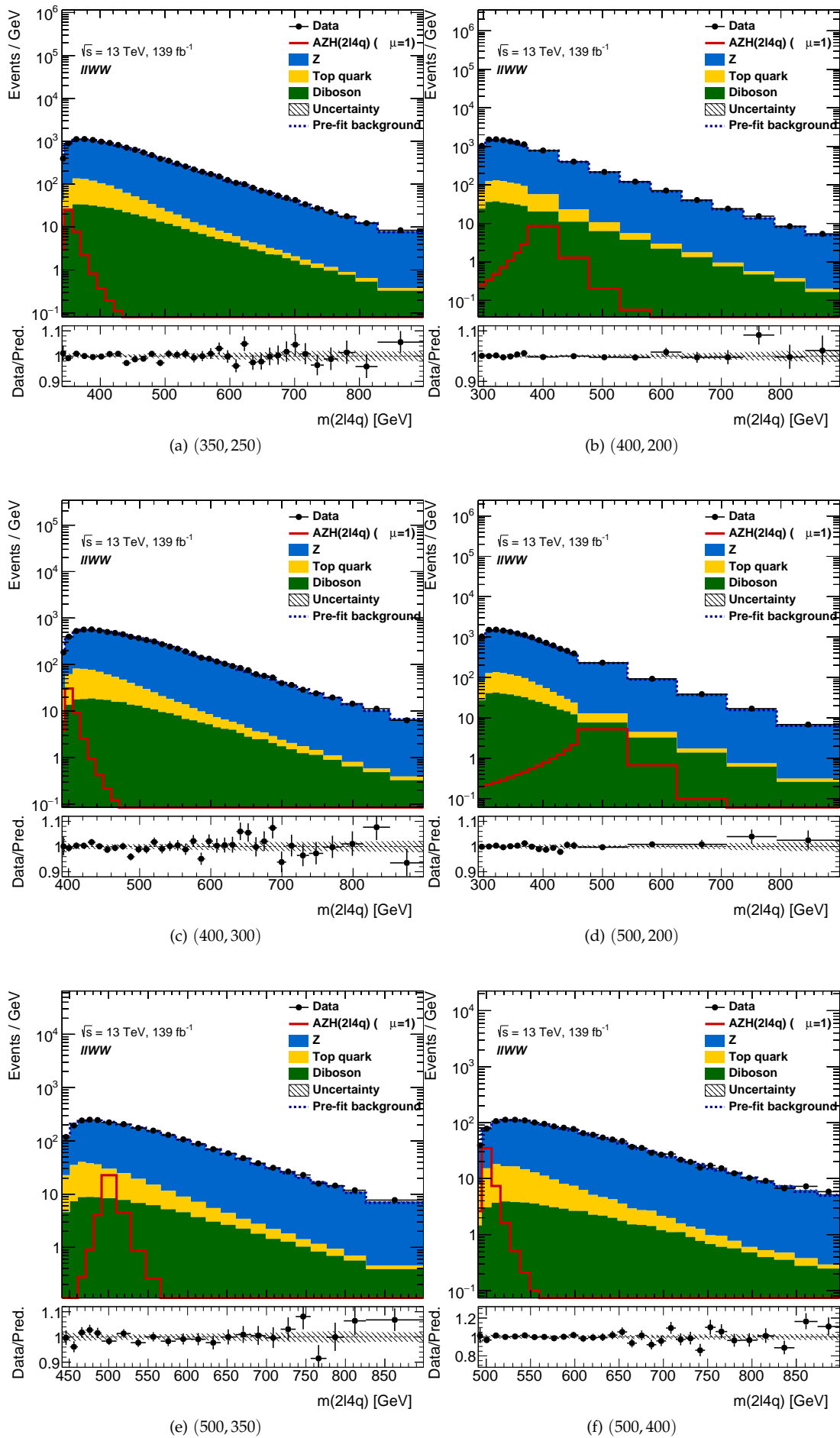


Figure 19.23: Post-fit plots for additional mass points.

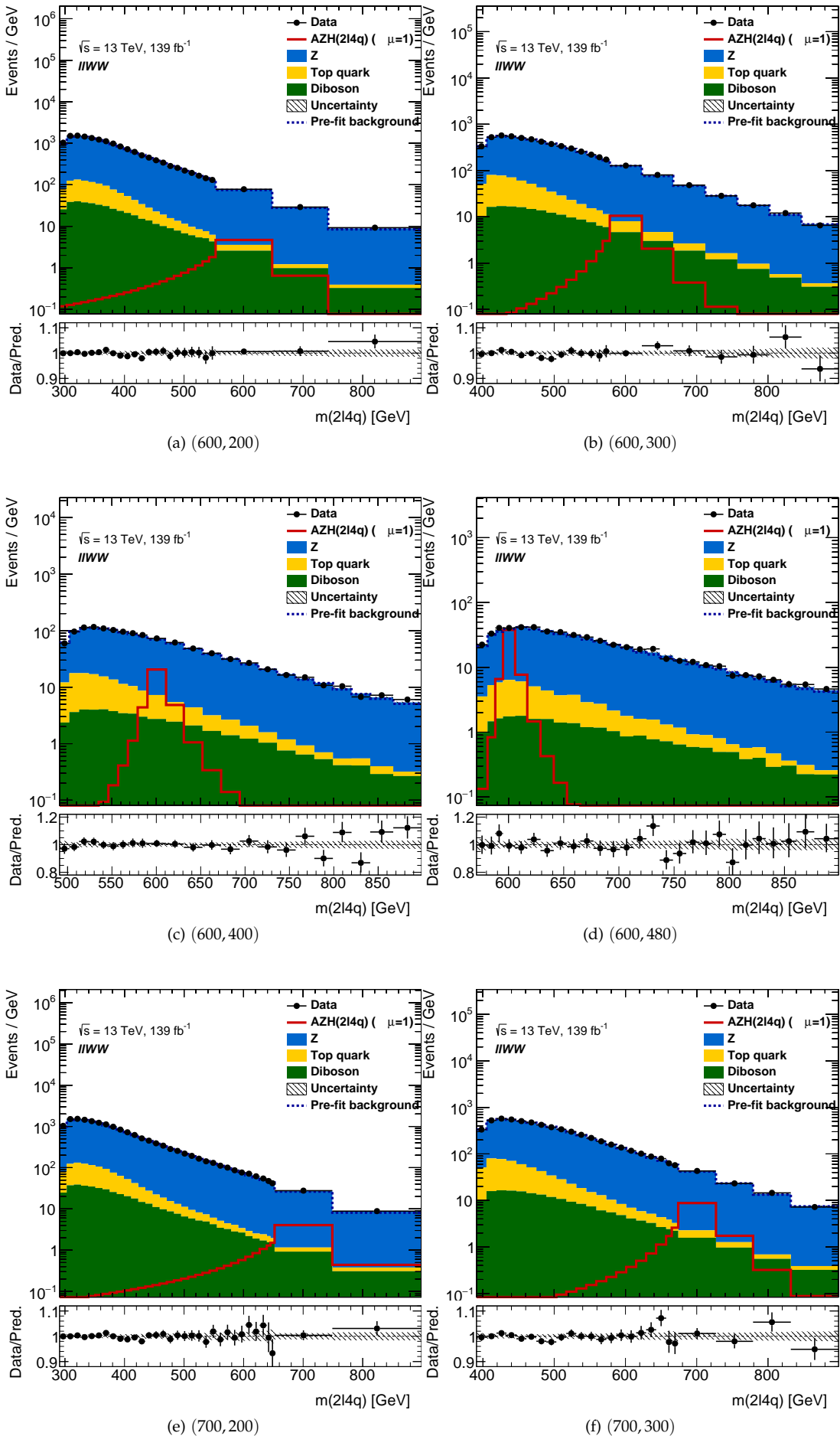


Figure 19.24: Post-fit plots for additional mass points.

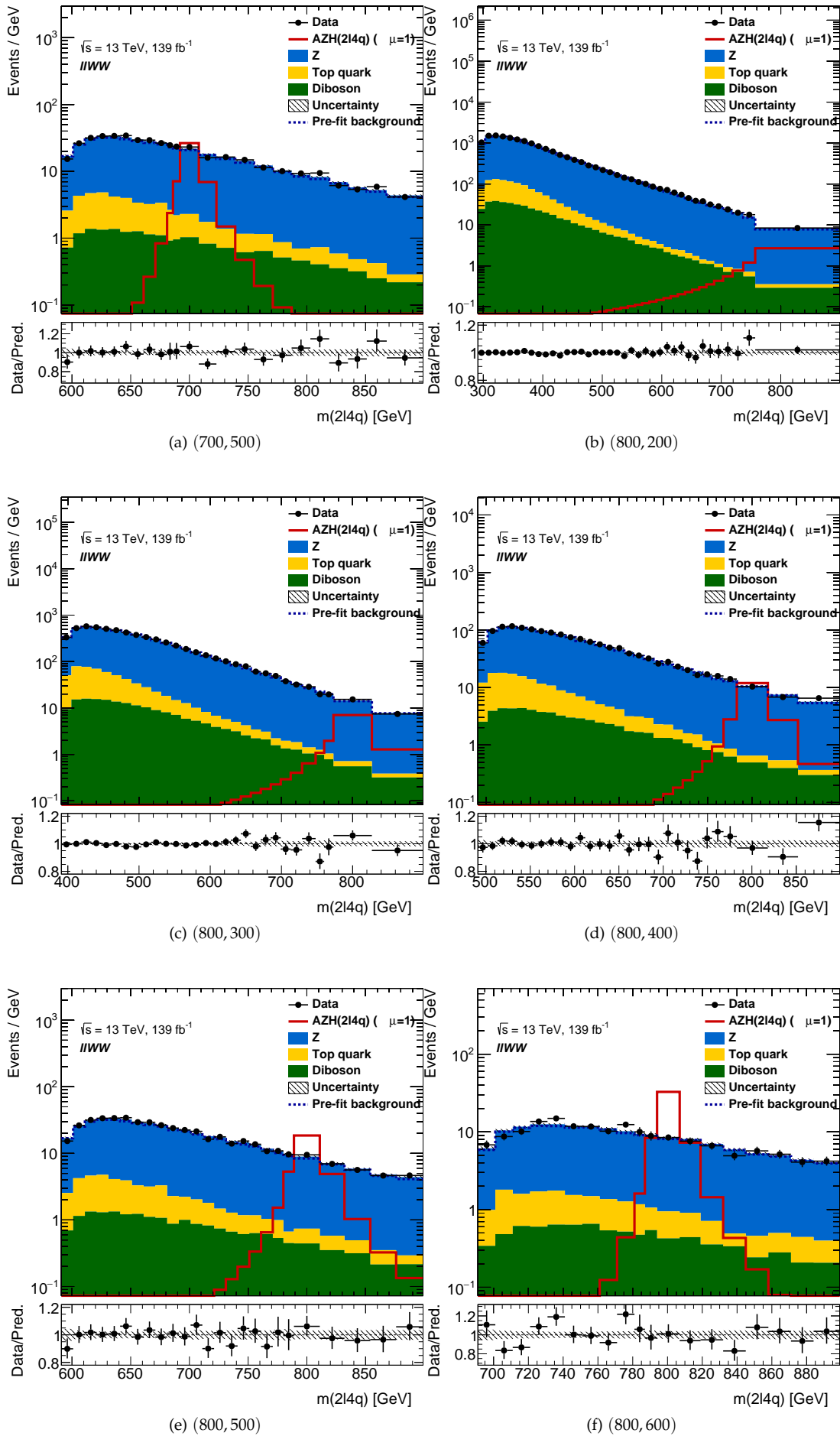


Figure 19.25: Post-fit plots for additional mass points.

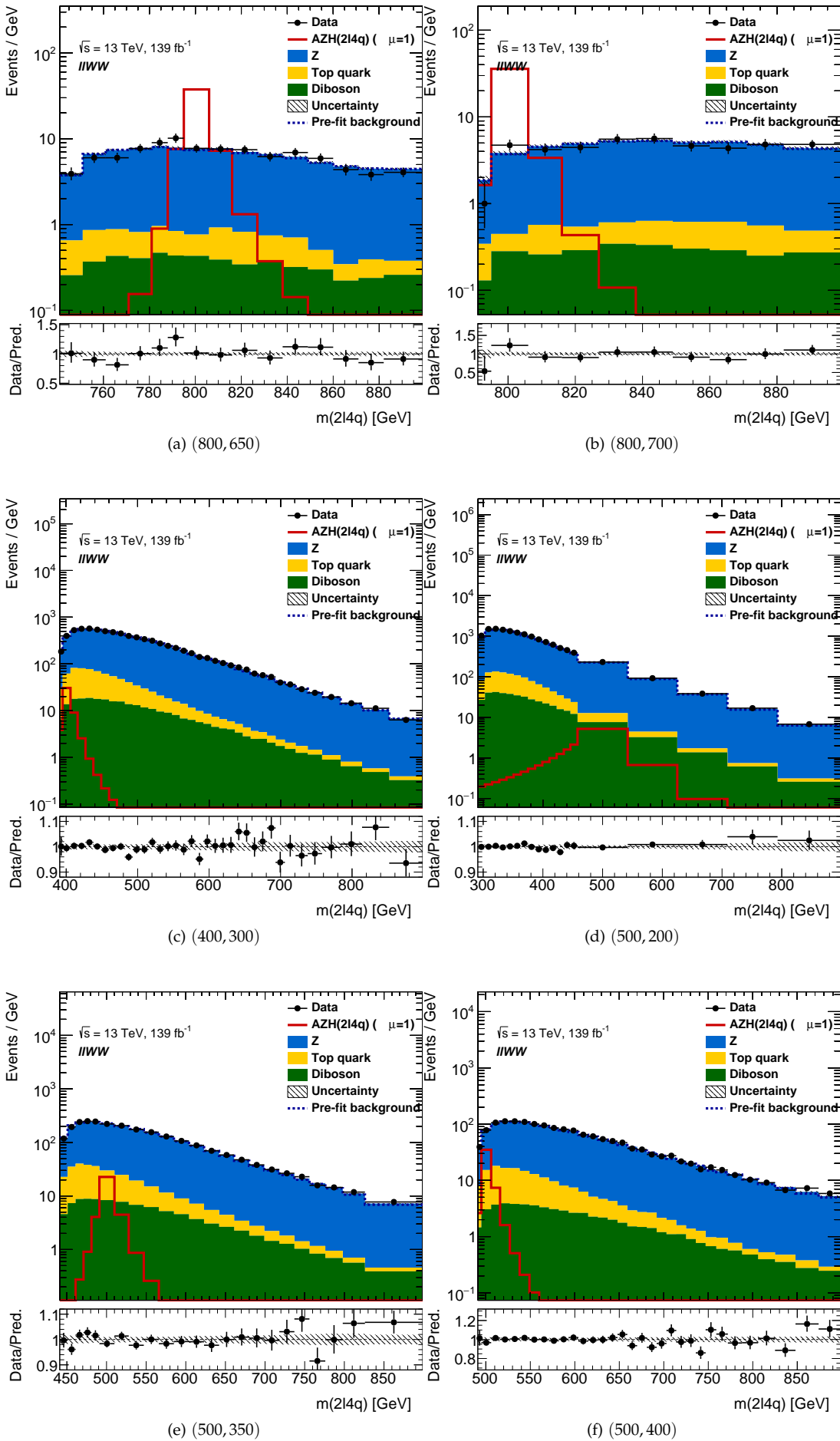


Figure 19.26: Post-fit plots for additional mass points.

**19.F Unblinded 1D limit slices**

In Chap. 15, the limits for some  $m_H$  slices were shown. Here are shown figures for the remaining slices.

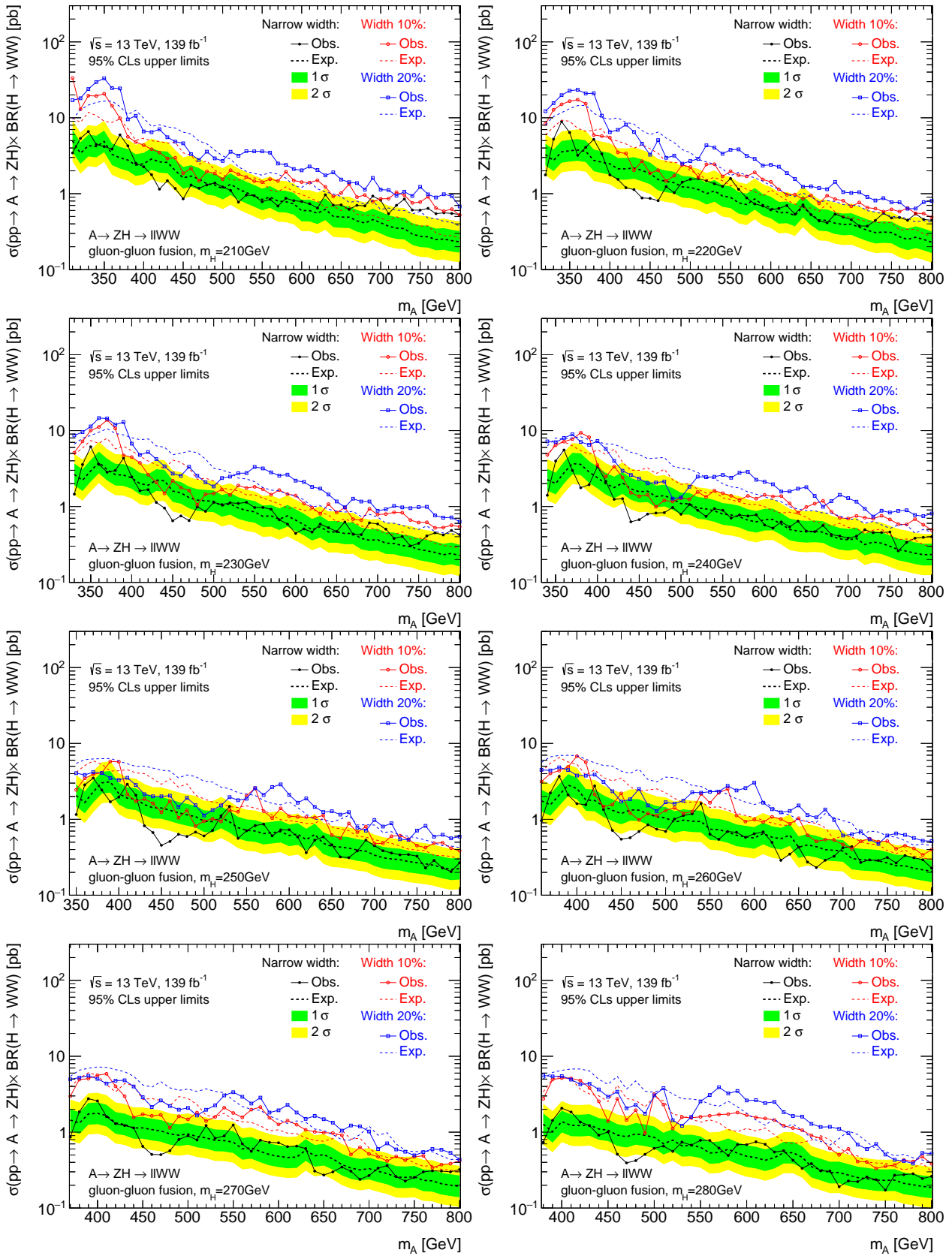
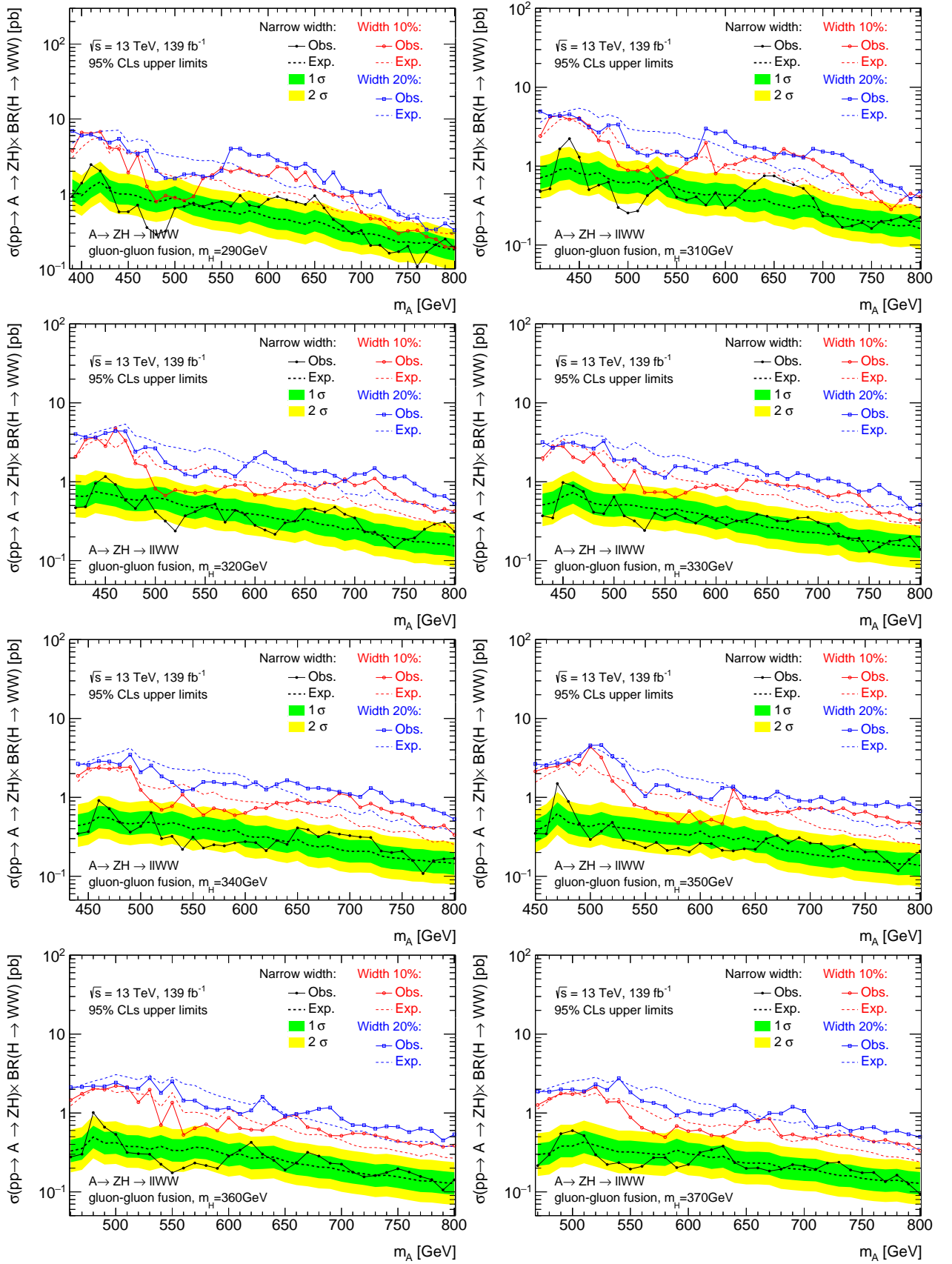


Figure 19.27: The limits for  $A$  for  $m_H$  slices shown in the figures.


 Figure 19.28: The limits for  $A$  for  $m_H$  slices shown in the figures.

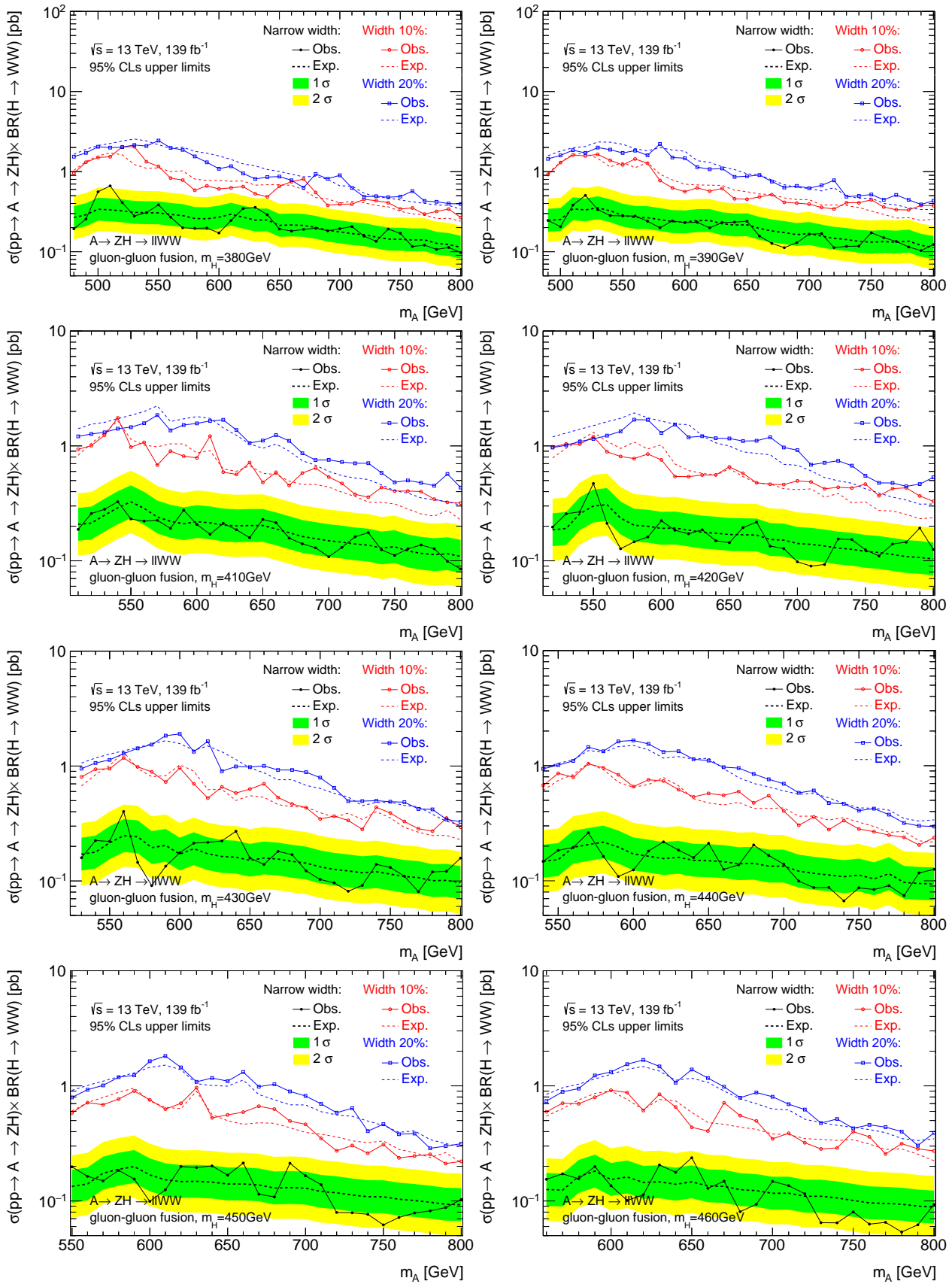
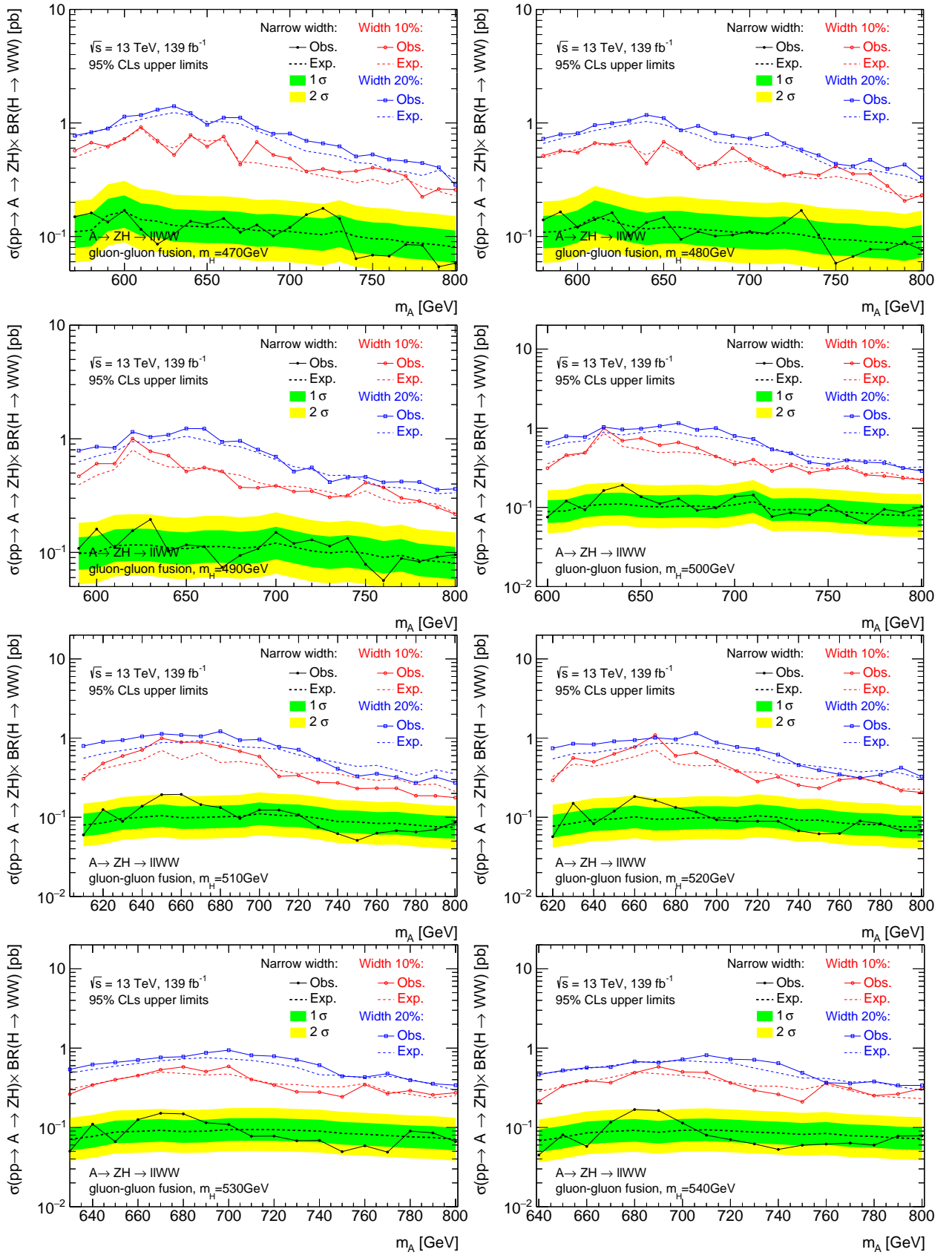


Figure 19.29: The limits for  $A$  for  $m_H$  slices shown in the figures.


 Figure 19.30: The limits for  $A$  for  $m_H$  slices shown in the figures.

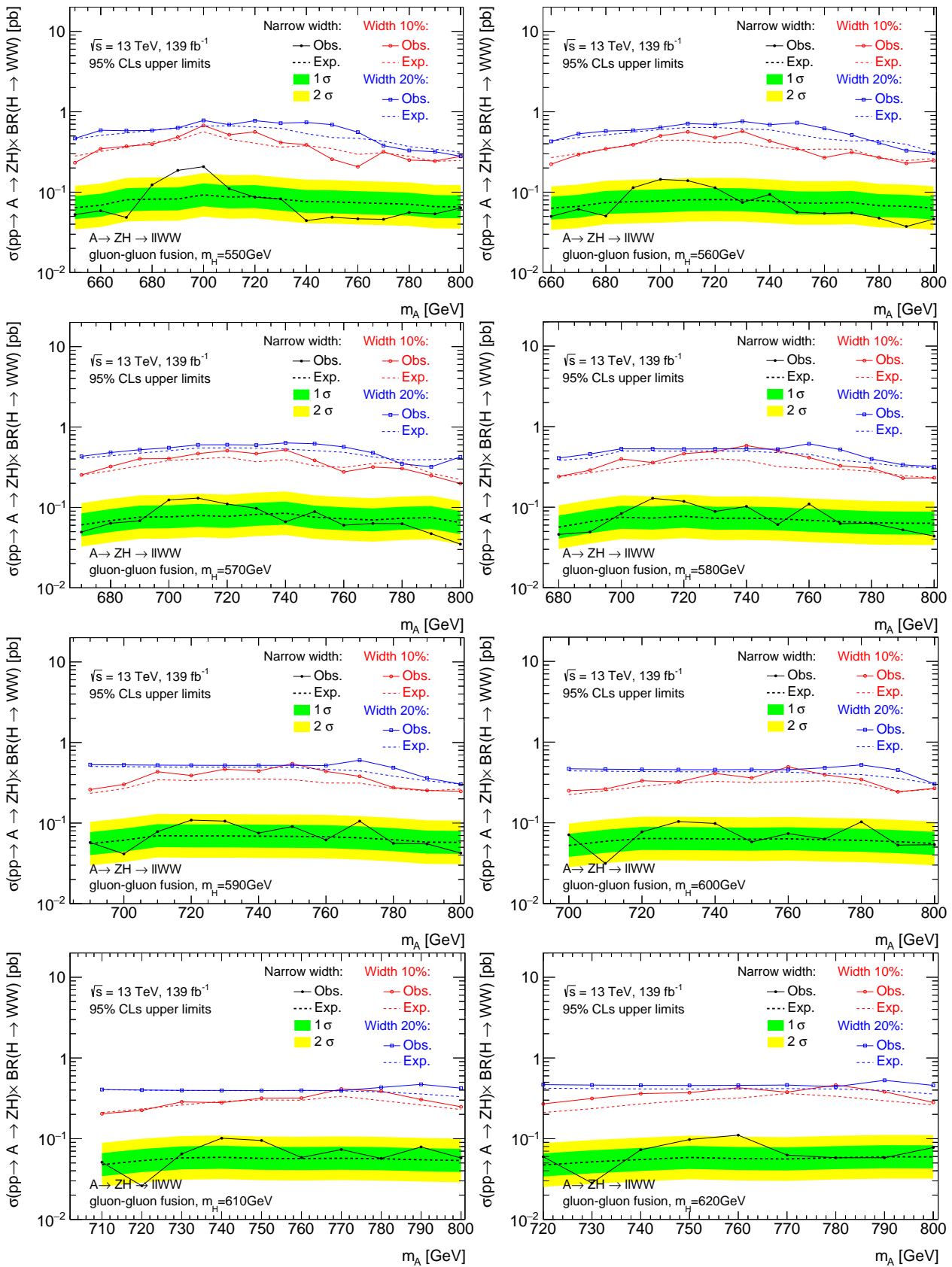


Figure 19.31: The limits for  $A$  for  $m_H$  slices shown in the figures.

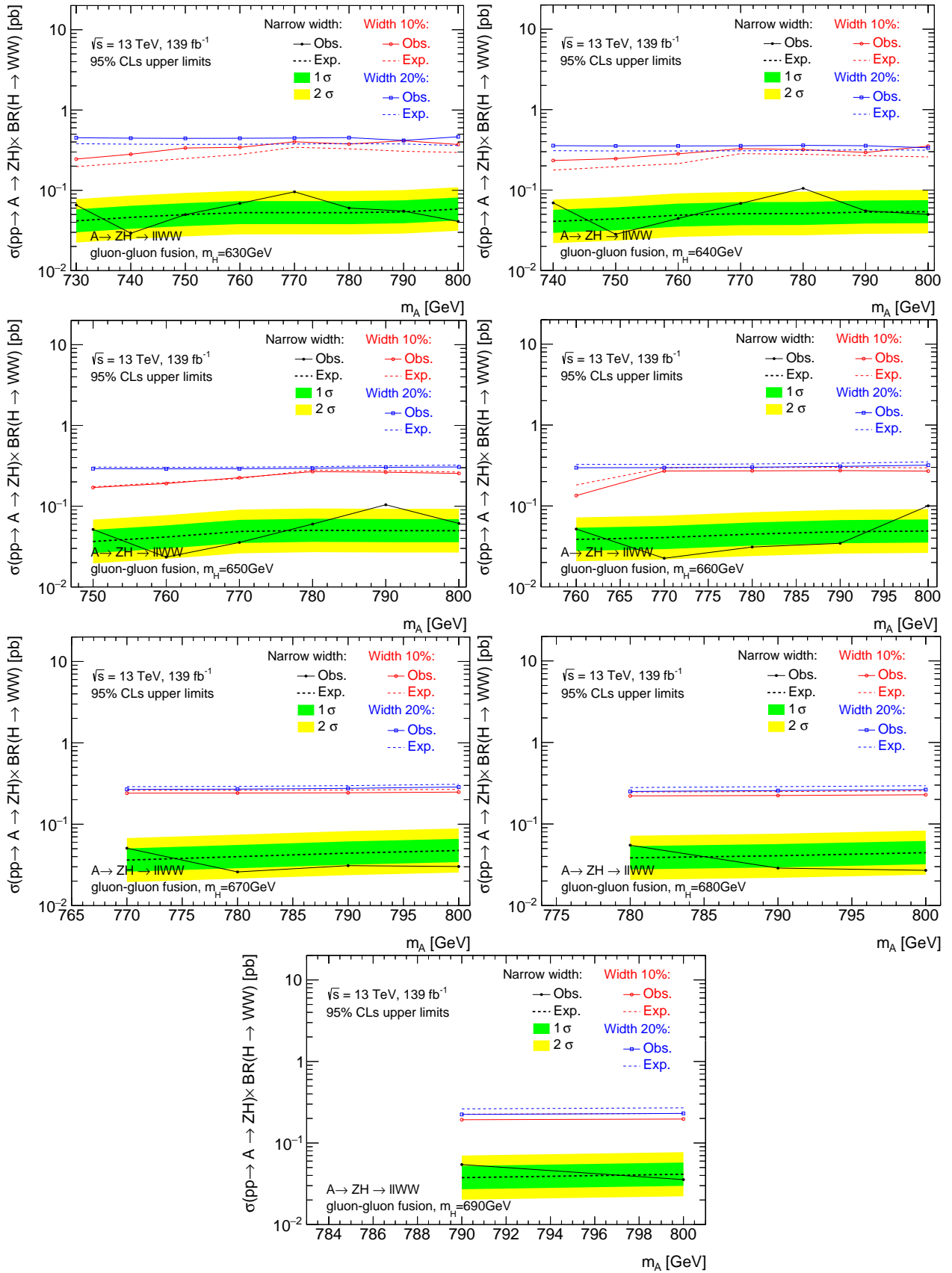


Figure 19.32: The limits for  $A$  for  $m_H$  slices shown in the figures. The slice for  $m_H = 700$  GeV is not shown since it only contains one mass point.

